Development of a differential absorption lidar for remote sensing of water vapor and the isotopologue HDO

Jonas Hamperl

Thèse de doctorat de Sorbonne Université

ED129
École doctorale des sciences de l'environnement d'Ile de France

Soutenue à Paris, le 14 décembre 2022, par :

Jonas Hamperl

Development of a differential absorption lidar for remote sensing of water vapor and the isotopologue HDO

Devant le jury composé de :

François Ravetta Professeur, Sorbonne Université (LATMOS)	**Président**
Patrick Rairoux Professeur, Université Lyon 1	**Rapporteur**
Patricia Segonds Professeure, Université Grenoble Alpes	**Rapporteure**
Caroline Bès Responsable du service sondage de l'atmosphère, CNES	**Examinatrice**
Jean-Baptiste Dherbecourt Ingénieur de recherche, ONERA	**Co-encadrant de thèse**
Cyrille Flamant Directeur de recherche, CNRS (LATMOS)	**Directeur de thèse**

Abstract

Observations of stable water isotopologues in the atmosphere provide valuable insights into the condensation and evaporation history of water vapor. The provision of such data with sufficient vertical resolution in the lower troposphere (0–3 km) helps to improve our understanding of basic processes like cloud formation, moist convection and mixing, and offers the potential to increase the accuracy in the predictions made by atmospheric general circulation models. Despite the progress in remote sensing from the ground and from space, retrievals from passive sensors are prone to biases and lack the vertical resolution required for water cycle studies in the lower troposphere.

The aim of this thesis is to investigate an active remote sensing approach based on the differential absorption lidar (DIAL) method to measure both the water vapor main isotopologue $H_2{}^{16}O$ and the semi-heavy water isotopologue $HD^{16}O$ with high vertical and temporal resolution (100–200 m, 10 min). The expected performance of such an instrument in terms of random and systematic errors was first analyzed using simulations accounting for instrumental and atmospheric parameters. The theoretical analysis showed that the spectral range around 1.98 µm is suitable for DIAL profiling of $H_2{}^{16}O$ and $HD^{16}O$ and that range-resolved measurements require a tunable laser in that wavelength range with pulse energies of tens of mJ. To fulfill this requirement, a parametric laser source based on a nested-cavity optical parametric oscillator and an optical parametric amplification stage using state-of-the-art high-aperture ($5 \times 7\,mm^2$) periodically poled potassium titanyl phosphate (PPKTP) crystals was implemented. It delivers widely tunable (1.95–2.30 µm) single-frequency radiation with energies up to 9 mJ for 12 ns pulses at a repetition rate of 150 Hz. Using the developed laser source, DIAL measurements of $H_2{}^{16}O$ and $HD^{16}O$ in the atmospheric boundary layer were conducted in direct-detection mode in the frame of several measurement campaigns. It was shown that with the developed lidar setup, isotopologue measurements with meaningful precision are limited to the first few hundred meters above the ground. To achieve measurements with range resolution and precision suitable for water cycle studies within the entire boundary layer, further instrumental improvements in terms of laser energy and reduced detection noise are necessary. For this purpose, a further step is proposed for the design and pre-development of a lidar setup capable of achieving a higher sensitivity thanks to an optimized double-stage amplification scheme for the laser transmitter that should allow to reach output energies > 40 mJ.

Acknowledgments

The work presented in this thesis would not have been possible without the great support I received during my PhD project from colleagues, collaborators, friends and my family.

First, I would like to thank my supervisors at ONERA, Myriam Raybaut and Jean-Baptiste Dherbecourt, for their constant support during the entire three years of my PhD. I very much enjoyed working with you — whether it was in the lab or during the long hours we spent for our lidar experiments in the rooftop shelter or in the lidar truck. Second, I would also like to thank Cyrille Flamant, my PhD supervisor at LATMOS, for his support from the beginning to the very end of my thesis.

Since a big part of this work was experimental and involved a lot of instrument integration and sometimes improvisation, I am also very glad for all the help that I received from our technicians at ONERA. So thank you, Cédric, Jean-Pierre and Philippe for helping us out with all kinds of challenges concerning electronics and mechanical issues. And thanks for all the good laughs we had.

Also, I am thankful for being surrounded by wonderful colleagues of the SLM group at ONERA. Special thanks go to Antoine Godard and Jean-Michel Melkonian for having always a door open and bringing in new ideas and valuable feedback. I would also like to thank the rest of the group for their good company, help with lab equipment and all the interesting discussions. Thanks also to everyone who has accompanied me as fellow PhD student, post-doc or intern during my time at ONERA: Elodie, Jeanne, Pier-Henri, Maxime, Noemie, Clément, Romain, Thomas, Eve-Line, Marie, Antoine, Amine, Magdalena, Ghislain, Anaïs, Carlos, Hugo. I will for sure miss chatting over a coffee with you all! I especially wish to thank my office colleague Elodie. Our daily chats about all kinds of things and our shared love (or better, addiction) for coffee definitely helped me get over the more difficult days.

I am also grateful for all the support I received and the fruitful discussions I had with numerous collaborators from both the WaVIL and the LEMON projects. Especially, I would like to thank Julien Totems and Patrick Chazette of LSCE for their help in the WaVIL instrument development, organizing measurement campaigns, and their constructive support in writing papers. Your feedback was always much appreciated! I also want to direct a special thank you to Harald Sodemann, Hans Christian Steen-Larsen and Daniele Zanoni of the University of Bergen for providing us with water isotope profiles from the 2021 field campaign which was very helpful for overcoming some of the problems we still had with the WaVIL instrument at that time.

Furthermore, I would also like to thank all jury members of my PhD defense for having accepted to review my thesis and for their suggestions for further improvements of the manuscript.

And finally, I am very grateful for the support I received from my parents, my girlfriend Marta, as well as old and new friends which made these three years more enjoyable.

Table of contents

List of abbreviations

ABL	atmospheric boundary layer
AERONET	Aerosol Robotic Network
AGL	above ground level
AIRS	Atmospheric Infrared Sounder
AL	aerosol load
AOD	aerosol optical depth
APD	avalanche photodiode
A-SCOPE	Advanced Space Carbon and Climate Observation of Planet Earth
ARMA	Aerosol Reference Model of the Atmosphere
CET	Central European Time
CRDS	cavity ring-down spectroscopy
DCS	dual-comb spectroscopy
DFG	difference frequency generation
DIAL	differential absorption lidar
DOD	differential optical depth
FOV	field of view
FRU	frequency reference unit
FSR	free spectral range
FTIR	Fourier-transform infrared
FWHM	full width at half maximum
GOSAT	Japanese Greenhouse Gases Observing Satellite
HgCdTe	mercury cadmium telluride
HITRAN	high-resolution transmission molecular absorption database
HWHM	half width at half maximum
HyMeX SOP1	Hydrological cycle in Mediterranean Experiment special observation period 1
IASI	Infrared Atmospheric Sounding Interferometer
IP-DIAL	integrated-path differential absorption lidar
InGaAs	indium gallium arsenide
IR	infrared
LEMON	Lidar Emitter and Multispecies greenhouse gases Observation instrument
LR	lidar ratio
L-WAIVE	Lacustrine-Water vApor Isotope inVentory Experiment

MIPAS	Michelson Interferometer for Passive Atmospheric Sounding
MOPA	master oscillator power amplifier
MUSICA	MUlti-platform remote Sensing of Isotopologues for investigating the Cycle of Atmospheric water
NDACC	Network for the Detection of Atmospheric Composition Change
NEP	noise-equivalent power
NesCOPO	nested-cavity optical parametric oscillator
OD	optical depth
OPG	optical parametric generation
OPO	optical parametric oscillator
OPA	optical parametric amplification/amplifier
PBL	planetary boundary layer
PIN	positive intrinsic negative
PPKTP	periodically poled potassium titanyl phosphate
PPLN	periodically poled lithium niobate
PZT	piezoelectric transducer
QPM	quasi-phase matching
RS	radiosounding
RF	radio frequency
RMS	root mean square
RR-DIAL	range-resolved differential absorption lidar
SCIAMACHY	SCanning Imaging Absorption spectroMeter for Atmospheric CHartographY
SHG	second-harmonic generation
SIRTA	Site Instrumental de Recherche par Télédétection Atmosphérique
SNR	signal-to-noise ratio
SROPO	singly resonant optical parametric oscillator
TCCON	Total Carbon Column Observing Network
TES	Tropospheric Emission Spectrometer
TROPOMI	Tropospheric Monitoring Instrument
ULA	ultra-light aircraft
UTC	Coordinated Universal Time
VMR	volume mixing ratio
WaVIL	Water Vapor and Isotope lidar
WF	weight function
WVMR	water vapor mixing ratio

Introduction

In many important aspects, climate and weather depend on the distribution of water vapor in the atmosphere. Water in its vapor phase only accounts for 0.25% of the total mass of Earth's atmosphere (Trenberth and Smith, 2005), but due to its relatively strong absorption of infrared (IR) radiation, water vapor contributes significantly to the radiative budget and is thus key to understand climate change. Knowing exactly how water vapor is distributed in the vertical is essential to understand basic processes like cloud formation, moist convection and mixing. However, the quantification of these processes still comes with large uncertainties that limit the accuracy of climate prediction models (Stevens and Bony, 2013b). A more detailed picture of the processes governing the hydrological cycle, and thus additional constraints for numerical models, can be obtained by incorporating an analysis of the isotopic composition of water vapor. Due to slightly different behaviours during phase changes, stable water isotopologues, or more precisely their ratios, serve as natural tracers giving insights into its condensation and evaporation history (Galewsky et al., 2016).

The observation of the vertical distribution of water vapor isotopologues is challenging. Atmospheric concentrations of water vapor are highly variable in the troposphere but the isotopic ratios are significantly less so. Consequently, this requires measurement techniques that are both sensitive over a large dynamic range and precise enough to detect the small isotopic signals. Much progress has been made in recent years in the observation of water vapor isotopologues enabled by passive remote sensors either from space using spectrometers operating in the thermal IR and short-wave IR, or from the ground using Fourier-transform-IR spectrometers. However, both methods are prone to biases and lack the vertical resolution required for the study of the dynamics of evaporation, condensation and air mass mixing processes in the lower troposphere. To date, the only way to obtain profiles of water vapor isotopologues with high vertical resolution is by in-situ sensors mounted on airborne platforms in the frame of dedicated measurement campaigns.

This thesis proposes an alternative approach based on laser remote sensing. The two most common techniques, Raman lidar and differential absorption lidar (DIAL), have proven as indispensable tools to probe the vertical distribution of water vapor in the troposphere with high spatio-temporal resolution, but were so far not used to address water vapor isotopologues individually. The Water Vapor and Isotope Lidar (WaVIL) developed in the frame of this thesis aims at measuring the water vapor main isotopologue $H_2{}^{16}O$ (hereafter referred to as H_2O) and the semi-heavy water isotopologue $HD^{16}O$ (hereafter referred to as HDO). This makes it the first lidar instrument dedicated to sounding two water vapor isotopologues, potentially enabling the estimation of the isotopic ratio with vertical and temporal resolutions relevant for the study of water-cycle processes in the lower troposphere.

The measurement principle of the WaVIL instrument is based on the DIAL method which consists

in analyzing the elastic backscatter signals from molecules and aerosols at slightly different wavelengths. In the simplest case, two wavelengths are alternately tuned upon and away from an absorption line of the molecule of interest. The key to independently measure H_2O and HDO with a single instrument lies thus in the proper selection of a spectral region which offers well separated absorption lines of the two molecules with similar and adequate absorption for lidar ranges over several kilometers. Such a favorable situation can be found in the short-wavelength IR region at 1.98 µm. A DIAL instrument for range-resolved measurements of H_2O and HDO thus requires a high-energy, narrow-linewidth laser source that is tunable within this wavelength range in order to access the absorption lines of both water vapor isotopologues.

Faced with limited options for tunable high-energy laser sources in the 2 µm spectral region, optical parametric conversion is a fruitful approach as it allows to extend the spectral coverage of mature 1 µm laser sources further into the near- and mid-IR to wavelengths where lasers perform poorly or are simply unavailable. In this context, the Office National d'Etudes et de Recherches Aérospatiales (ONERA) has made significant contributions in the development of coherent sources based on optical parametric oscillators (OPO). These developments have led to the doubly resonant nested-cavity OPO (NesCOPO) architecture allowing for tunable single-longitudinal-mode emission with a relatively compact device and without the need for injection seeding (Hardy et al., 2011). It has been used for various gas sensing applications in the short-wavelength and mid-IR spectral range (Godard et al., 2017), including a high-energy (10–20 mJ) laser source tunable in the spectral range from 1.9 to 2.3 µm capable of addressing CO_2, CH_4 and H_2O (Barrientos Barria et al., 2014).

Recent advances in the fabrication of periodically poled nonlinear materials also allow for more compact and rugged setups with increased output energies due to high-aperture crystals. Moreover, it also opens the path for generic architectures to address different spectral windows while keeping the same components. This concept is the basis for the WaVIL instrument developed in this thesis project and its future successor, the Lidar Emitter and Multispecies greenhouse gases Observation (LEMON) instrument, which aims to add to the H_2O/HDO capability at 1.98 µm the spectral window around 2.05 µm dedicated to CO_2 in a robust setup. The 2.05 µm wavelength region has been identified in several theoretical studies for integrated-path DIAL measurements of CO_2 from space for the quantification of carbon sources and sinks which poses very demanding instrumental requirements in terms of laser energy and absolute frequency stability (Ingmann et al., 2008; Singh et al., 2017b).

Objectives of this thesis

The overarching goal of this thesis was to investigate the feasibility of measuring range-resolved profiles of both water vapor isotopologues H_2O and HDO using the DIAL method. This was addressed both theoretically by the means of simulation and experimentally in the framework of different measurement campaigns with a specifically developed lidar setup.

On the technological side, a key objective was the implementation of a tunable high-energy parametric laser source operating at 1.98 µm to be utilized as the lidar transmitter for DIAL measurements of H_2O and HDO. With the aim of compactness and the prospect of extending the wavelength range towards 2.05 µm, which would additionally allow for DIAL sensing of atmospheric CO_2, the developed laser source is fully oriented around quasi-phase-matched nonlinear materials. Therefore, specifically developed periodically

poled potassium titanyl phosphate (PPKTP) crystals were obtained through a collaboration with the Laser Physics group of the KTH Royal Institute of Technology (Sweden). The objective was to test these crystals in an optical parametric amplification (OPA) setup and to build a versatile amplifier with the aim of achieving mJ-level output energies suitable for DIAL sensing. Additionally, the conducted OPA experiments also contributed to the design and pre-development of the laser transmitter of the future LEMON instrument.

Thesis outline

The structure of this manuscript reflects the work accomplished throughout the three years of this thesis project. The manuscript is thus organized as follows:

Chapter 1 provides the background and scientific motivation for this thesis. It is divided into two parts reflecting the two different scientific objectives on which the presented work is oriented. The first part outlines the role of atmospheric water vapor and its isotopologues for the study of the hydrological cycle and presents an overview of the state of observing methods. The second part of chapter 1 is dedicated to the subject of future CO_2 measurements from space using the DIAL technique and briefly summarizes key requirements that such an instrument must fulfill.

The second chapter introduces the mathematical foundation of the DIAL method and the associated sources of noise and systematic uncertainties. Based on this theory, chapter 3 presents a numerical sensitivity study and an error budget to assess the performance of a DIAL system for ground-based measurements of the water vapor isotopologues H_2O and HDO and to estimate the achievable precision in the isotopologue ratio. The sensitivity analysis investigates the influence of instrument-specific parameters and uses atmospheric models representative of polar, mid-latitude and tropical conditions.

In chapter 4, the design and experimental implementation of a high-energy parametric laser source covering the 2 µm spectral range for H_2O/HDO and CO_2 DIAL measurements is presented. It is based on a master-oscillator-power-amplifier setup consisting of a NesCOPO and a parametric amplification stage based on state-of-the-art high-aperture PPKTP crystals which were tested in different configurations in order to optimize the extracted output energy.

The developed 2 µm parametric laser source was subsequently integrated in a lidar setup in order to perform range-resolved measurements of the water vapor isotopologues H_2O and HDO, which is the subject of chapter 5. The results of different measurement campaigns, including a two-week field campaign with multiple auxiliary measurements for intercomparisons, are presented and discussed in detail. To demonstrate the multi-species capability of the developed lidar transmitter, a preliminary range-resolved DIAL measurement of CO_2 in the atmospheric boundary layer is also presented.

Finally, strategies for instrument improvements are discussed in chapter 6 which are realized in the framework of the LEMON instrument development. First, this concerns the improvement in terms of laser energy enabled by the implementation of a double-stage parametric amplifier. And second, an approach to increase the laser wavelength stability by the implementation of a frequency-locking scheme is presented. Taking these instrument upgrades into account, the expected sensitivity gain for ground-based DIAL measurements of H_2O/HDO and a potential airborne measurement scenario are discussed.

Chapter 1

Scientific background

1.1 Observation of water vapor and stable water vapor isotopologues in the lower troposphere

1.1.1 Atmospheric water vapor

Water vapor in the atmosphere strongly influences our climate and weather as it contributes significantly to the Earth's radiative budget and transports energy in the form of latent heat. Water vapor only accounts for 0.25% of the total mass of the atmosphere (Trenberth and Smith, 2005). Yet, due to the combination of its relatively high number density and the strong molecular absorption of IR-radiation, water vapor is the most important greenhouse gas contributing more than half to the atmospheric greenhouse effect under clear-sky conditions (Kiehl and Trenberth, 1997).

The role of atmospheric moisture in the global water cycle is also key to understand climate change because water vapor leads to an important feedback as it more than doubles the surface warming from atmospheric carbon dioxide (Stevens and Bony, 2013a). However, the processes determining the dynamics of atmospheric moisture are far from being fully understood. For instance, there are still large uncertainties in determining the relative contributions to moisture over land from local evaporation and humidity from oceanic sources (Worden et al., 2007). In fact, the largest source of spread in current climate predictions is caused by variations in the distribution of clouds in the boundary layer (Bony and Dufresne, 2005; Bony et al., 2006). A better understanding of basic processes like cloud formation, moist convection, and mixing is thus essential in order to reduce the uncertainties in these models (Stevens and Bony, 2013b). This will help answer the essential question of how regional and global water and energy cycles are changing due to anthropogenic influences.

Because the amount of water vapor an air parcel can hold is tightly coupled to temperature through the Clausius-Clapeyron relation, water vapor is highly variable in space and time. Figure 1.1 shows the vertical distribution of the absolute humidity for different standard atmospheres. A general decrease of temperature with height in the troposphere (the lowest 10–15 km of the Earth's atmosphere) leads to a vertical variability of 2–3 orders of magnitude. Consequently, about 80% of the water vapor mass is concentrated in the lowest 3 km above the surface. Due to different surface temperatures in different climate zones, the water vapor amount close to the surface can vary by more than an order of magnitude between tropical and arctic

regions. Additional variability of the distribution of water vapor is caused by phenomena such as evapotranspiration from the surface, horizontal advection and condensation (Wulfmeyer et al., 2015). Therefore, knowing exactly how water vapor is distributed in the lower troposphere by the means of high-resolution measurements is essential to understand and predict climate and weather processes.

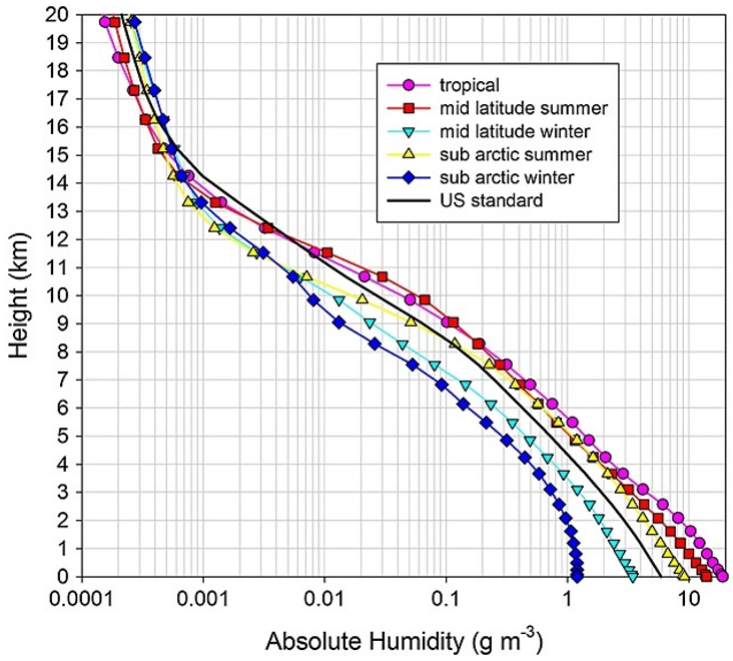

Figure 1.1: Vertical profiles of absolute humidity for the U.S., tropical, midlatitude summer, midlatitude winter, subarctic summer, subarctic winter atmospheres. Figure from Wulfmeyer et al. (2015)

1.1.2 Methods for the observation of tropospheric water vapor

1.1.2.1 Measurement requirements

Requirements on the measurement of atmospheric water vapor vary widely depending on the purpose and application. For climate research, water vapor profiles with moderate spatio-temporal resolution are sufficient, but high and stable accuracy is required over large time scales in order to allow for the analysis of trends (Wulfmeyer et al., 2015). For the purpose of operational weather forecasting, vertical profiles of temperature and humidity should capture changes within a few hours, with a vertical resolution of a few hundred meters, a systematic error (bias) better than 5% and a noise error per range bin better than 10% in the atmospheric boundary layer (Bösenberg, 1998; Weckwerth et al., 1999). Modern numerical prediction systems approaching the nowcasting-range require temporal resolutions of 5–10 min. In the context of verification, i.e. to asses the performance of numerical models or for the intercomparison with other instruments, biases close to 2% are highly desirable as this would eliminate the need for bias corrections. The most demanding requirements, especially in terms of temporal resolution, are needed for mesoscale and microscale process studies. For instance, observation of turbulence and convective transport in the boundary layer require temporal and vertical resolutions of 1–60 s and a few tens of meters (Wulfmeyer, 1999).

1.1.2.2 In situ measurements

Still to date, balloon-borne radiosoundings are the most reliable way to produce measurements with sufficient vertical resolution (in the range of meters) to record the variability of water vapor in the atmospheric boundary layer and the interfacial layers at the boundary layer top. However, radiosoundings are limited to a finite number of sites, mostly over land and a limited number of launches per day (typically two launches per day for stations operated by national meteorological services). In the framework of measurement campaigns, ballon-borne radiosondes or dropsondes launched from an aircraft are considered as a reference standard to which other remote sensing instruments are compared.

1.1.2.3 Passive remote sensing

Ground-based passive sensors, such as IR spectrometers or microwave radiometers, can fill some observational gaps as they allow for continuous monitoring (during daylight) with temporal resolutions of several minutes. However, the density of these observations is even lower than the one of radiosounding networks and retrievals are highly sensitive to instrument calibration, the radiative transfer model chosen, the inversion method and atmospheric conditions (Wulfmeyer et al., 2015). Vertical resolutions vary between a few hundred meters close to the surface to 1–2 km at the top of the atmospheric boundary layer.

Satellite-based passive sounders have the advantage of daily global coverage which makes their retrieval products indispensable for weather forecasting and climate research. However, the vertical resolution is rather coarse with 2 km in the lower troposphere and an accuracy of 20% for the case of the Infrared Atmospheric Sounding Interferometer (IASI) onboard the METOP-A satellite (Pougatchev et al., 2009). Although, future instruments with higher spectral and radiometric resolution are still expected to deliver an overall gain in accuracy and vertical resolution, only marginal improvements are expected for the lower boundary layer (Crevoisier et al., 2014). This makes space-borne passive sounders incapable of resolving the structure and gradients of water vapor which is necessary to study many lower-tropospheric, cloud, and boundary-layer processes (Wulfmeyer et al., 2015).

1.1.2.4 Global Navigation Satellite System Radio Occultation

The Global Navigation Satellite System Radio Occultation (GNSS-RO) technique is based on measuring the bending angle due to refraction of a radio signal that propagates through the Earth's atmosphere along a near-horizontal path from a GNSS satellite to a receiver onboard a low-earth-orbit satellite. The refraction experienced by the radio signal is caused by the vertical gradient of the refractive index of the atmosphere which is a function of pressure, temperature and humidity.

The GNSS-RO measurement technique provides global coverage, high vertical resolution (ca. 100 m), high accuracy and the capability of sounding under all types of weather conditions (Anthes, 2011). However, the accuracy of GNSS-RO is reduced in the lower troposphere due to signal tracking issues and strong horizontal and vertical gradients in the refractivity (Wulfmeyer et al., 2015). The horizontal resolution is in the order of a few hundred kilometers. This makes GNSS-RO products essential inputs for mesoscale weather forecasting and climate monitoring, but they are less appropriate for fine-scale numerical weather predictions needed to foresee extreme weather events.

1.1.2.5 Lidar remote sensing of atmospheric water vapor

In contrast to passive remote sensors, active remote sensing systems such as lidars transmit radiation which is then analyzed with respect to the backscattered signals. One advantage of lidar over passive sensors is the high range resolution enabled by the time-of-flight measurement principle. And because the solution of the equation governing the lidar return signals is unique, higher accuracy is expected in comparison to the retrievals of passive remote sensors. However, this advantage comes at the cost of higher system complexity reflected in more challenging instrument development and operation.

For water vapor profiling, two types of lidar are commonly used: Raman lidar and differential absorption lidar (DIAL). If designed and operated correctly, both methods are recognized by the World Meteorological Organization (WMO) as reference standards for water vapor measurements in the troposphere with an accuracy of $< 5\%$ (Wulfmeyer et al., 2015).

Water vapor Raman lidar

The Raman lidar technique, first demonstrated in 1969 (Melfi et al., 1969), makes use of the inelastic scattering of laser radiation by atmospheric molecules. Raman scattering leads to a shift in wavelength of the scattered radiation with respect to the incident one which depends on the rotational-vibrational energy level structure unique to every molecular species. Since the Raman scattering cross-section is proportional to λ^{-4}, where λ denotes the laser wavelength, short wavelengths between 320 and 550 nm are best suited for Raman lidar measurements (Wandinger, 2005). Owing to the weakness of the Raman scattering cross-sections, the method requires a high-power laser source and is better suited for species with high atmospheric concentrations such as nitrogen, oxygen and water vapor.

Water vapor Raman lidars measure the mixing ratio of water vapor which is defined as the mass of water vapor divided by the mass of dry air in a given volume. Besides the channel of the Raman backscattered water vapor signal, the approach also uses a Raman nitrogen channel as a reference. Since nitrogen is in constant proportion to dry air in the troposphere, the Raman return signal can be used to determine the mass of dry air needed to derive the water vapor mixing ratio (Whiteman et al., 1992). Such type of Raman lidar instruments often use the frequency-tripled radiation of a neodymium-doped yttrium aluminum garnet (Nd:YAG) laser emitting UV laser pulses at 355 nm for which the water vapor and nitrogen Raman signals are observed around 408 nm and 387 nm, respectively.

Raman lidar is a powerful and robust tool to probe the atmosphere as it can give access to several atmospheric state parameters such as temperature, aerosols and water vapor simultaneously. It benefits from widely commercially available high-power visible or UV lasers as well as highly sensitive detectors in that spectral range. However, limitations can arise from parasitic daytime sky radiance and the need for calibration to auxiliary measurements. In the lower troposphere, typical resolutions of Raman lidar measurements are 1–30 min in time and 50–300 m in space (Wandinger, 2005) and it has been shown in theoretical analyses and extensive intercomparisons with in situ sensors that systematic errors better than 5% can be achieved (Wulfmeyer et al., 2015), making these systems a valuable asset in atmospheric research.

Due to their relatively modest experimental complexity and their capability to monitor the vertical water vapor distribution with high spatio-temporal resolution, Raman lidars are regularly used in the framework of

scientific field campaigns (see for example Chazette et al. (2014, 2021), Lange et al. (2019), Di Girolamo et al. (2009, 2020)). Water vapor Raman lidars are also used in continuous operation by meteorological services for monitoring and numerical weather prediction (Goldsmith et al., 1998; Reichardt et al., 2012; Dinoev et al., 2013).

Water vapor differential absorption lidar

The DIAL technique consists in measuring the elastic backscatter signals from molecules and aerosols at slightly different laser wavelengths. In the simplest case of a two-wavelength DIAL, the wavelength of the laser beam probing the atmosphere is alternately tuned to (on-line) and away from (off-line) an absorption line of the atmospheric species of interest and the difference in atmospheric transmission between the on-line and off-line signals allows for the derivation of the species concentration, provided that the spectroscopy of the target molecule is well known (Bösenberg, 2005).

DIAL measurements impose stricter requirements on the laser source than the Raman lidar method as the laser needs to be tunable and its narrow-linewidth emission must be positioned precisely on the absorption line of the molecule to be measured. However, this comes with the significant benefit that the DIAL technique is in principle calibration-free making it one of the most accurate water vapor remote sensing techniques. The accuracy of the the DIAL method is essentially limited by the knowledge of spectroscopic parameters, which can be improved by laboratory measurements (Wulfmeyer et al., 2015).

With respect to water vapor DIAL systems, a lot of effort has been dedicated to the development of airborne instrumentation. Compared to ground-based soundings, measurements from aircraft allow to cover large areas and provide a certain flexibility in choosing a geographical region of scientific interest which might otherwise be inaccessible. Additionally, airborne demonstrations are an important step towards a potential instrument employment in space. Examples of airborne DIAL instruments are the NASA Langley Research Center (LaRC) Lidar Atmospheric Sensing Experiment (LASE, Moore et al., 1997), the Lidar pour l'Etude des interactions Aérosols Nuages Dynamique Rayonnement et du cycle de l'Eau (LEANDRE II, Bruneau et al., 2001) of the Centre National de la Recherche Scientifique (CNRS), the WAter vapour Lidar Experiment in Space (WALES, Wirth et al., 2009) instrument of the Deutsches Zentrum für Luft- und Raumfahrt (DLR) and the LASE-successor instrument High Altitude Lidar Observatory (HALO, Carroll et al., 2022).

Both ground-based and airborne water vapor DIAL systems have been successfully demonstrated for the study of land surface exchange and lower tropospheric transport processes (Späth et al., 2016), the study of the mesoscale water vapor field (Ferrare et al., 2004) and turbulence studies in the convective boundary layer (Muppa et al., 2016), among others. Promising demonstrations have also been reported with respect to routine water vapor monitoring using cost-effective diode lasers (Spuler et al., 2015, 2021). The ultimate goal is to employ such technology in networks which would improve quantitative precipitation forecasts and greatly benefit the capability of forecasting severe weather events.

The majority of water vapor DIAL instruments operate in the near-IR spectral range from 0.7–1 µm, but suitable absorption lines are also found in the atmospheric transparency windows around 1.6 µm and 2 µm. Different technological approaches are used to generate the near-IR laser radiation used for DIAL applications. The airborne LASE system uses a double-pulsed Ti:Sapphire laser generating 30 ns pulses with a

repetition rate of 5 Hz and pulse energies of up to 150 mJ. The Titanium:Sapphire oscillator is pumped by a frequency-doubled Nd:YAG laser and is seeded to operate in the 813 to 819 nm wavelength region using a single-mode diode laser and an absorption reference cell (Moore et al., 1997).

The WALES system employs two identical Nd:YAG lasers followed by two nonlinear conversion stages allowing to generate four wavelengths between 935 and 936 nm. First, the pump laser radiation is frequency doubled by second-harmonic generation and then converted to a wavelength of 935 nm by an optical parametric oscillator. Both stages use potassium titanyl phosphate (KTP) as the nonlinear material. Each OPO is alternately injection-seeded by two distributed-feedback diode lasers. The output energy at 935 nm is 45 J for 5.5 ns pulses at a repetition rate of 50 Hz.

The ground-based DIAL developed at the University of Hohenheim, Germany, consists of an injection-seeded high-power Titanium:Sapphire laser pumped by a frequency-doubled Nd:YAG laser. Output pulses at 820 nm are in the range of 60 ns and have energies of 8 mJ at a repetition rate of 250 Hz (Späth et al., 2016).

DIAL systems operating in wavelength ranges below 1.6 µm mostly use either detectors based on photomultipliers or avalanche photodiodes (APD). Silicon-based APD provide high responsivity in the visible spectral range up to around 1 µm. Maximum responsivity is reached between 0.6 µm and 0.8 µm. For longer wavelengths up to 1.7 µm, APD based on germanium or indium gallium arsenide (InGaAs) are used.

1.1.3 Stable water vapor isotopologues

Humidity observations alone are not sufficient for identifying the variety of processes accounting for the proportions and history of tropospheric air masses (Galewsky et al., 2016). A more detailed picture of the role of atmospheric moisture in the water cycle, and thus additional constraints for numerical prediction models, can be obtained by incorporating an analysis of its isotopic composition. A molecule of water consists of two atoms of hydrogen and one of oxygen. The former has two naturally occurring stable isotopes (^{1}H and ^{2}H, or D) and the latter has three stable isotopes (^{16}O, ^{17}O, ^{18}O). Combinations of isotopes on a molecular level are called isotopologues. For water, there are nine possible isotopologues. The primary isotopologue $H_2{}^{16}O$ is by far the most abundant (99.73098%), followed by $H_2{}^{18}O$, $H_2{}^{17}O$ and $HD^{16}O$ (0.199978%, 0.037888%, and 0.031460%, respectively) (Sharp, 2017). The work presented in this thesis focuses on the main isotopologue $H_2{}^{16}O$ (hereafter referred to as H_2O) and the semi-heavy water isotopologue $HD^{16}O$ (hereafter referred to as HDO).

Isotopic abundances are often expressed using the so-called δ-notation, which compares the ratio of the rare and heavy (HDO) to the most abundant and light isotopologue (H_2O) with the standard abundance ratio of Vienna Standard Mean Ocean Water (VSMOW) (Craig, 1961):

$$\delta D = \left[\frac{[\mathrm{HDO}]_{\mathrm{sample}} / [\mathrm{H_2O}]_{\mathrm{sample}}}{[\mathrm{HDO}]_{\mathrm{VSMOW}} / [\mathrm{H_2O}]_{\mathrm{VSMOW}}} - 1 \right] \cdot 1000, \tag{1.1}$$

with $[\mathrm{HDO}]_{\mathrm{VSMOW}} / [\mathrm{H_2O}]_{\mathrm{VSMOW}} = 3.1152 \times 10^{-4}$. Low values of δD thus indicate that a sample of water contains fewer of the heavy isotopologue and higher values of δD in a sample indicate that it is enriched with the heavy isotopologue.

Due to their subtle difference in mass, different isotopologues behave differently during evaporation and

condensation processes. Heavier water isotopologues evaporate less readily from their liquid phase and the resulting vapor will be depleted in the heavy isotopologues whereas the initial liquid water will experience a net enrichment of molecules containing heavier isotopes. In the opposite case of condensation, the resulting condensate will be richer in heavier isotopologues than the initial vapor. This process of separation of different isotopologues whenever phase changes occur is called fractionation. It takes place at all stages of the hydrological cycle and determines the isotopic composition of atmospheric water vapor at different geographic locations (see Fig. 1.2). This makes stable water isotopologues useful natural tracers helping to identify the origin of water vapor, how it is transported and providing insights into its condensation and evaporation history (Galewsky et al., 2016).

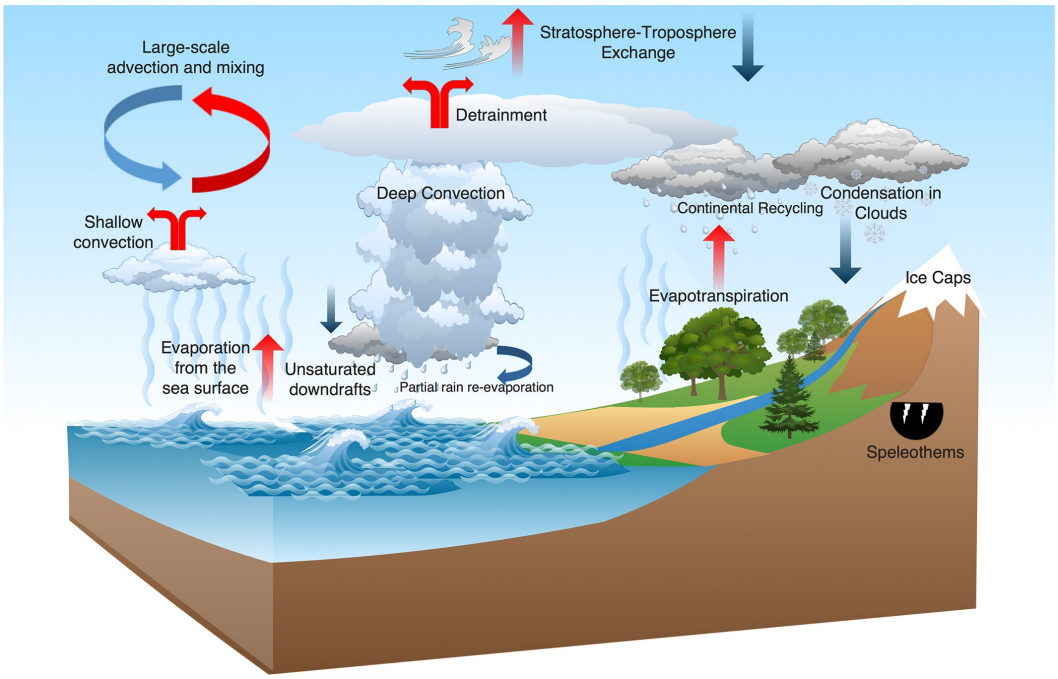

Figure 1.2: Schematic of key processes of the hydrological cycle governing the isotopic compositon of atmospheric water vapor. Blue arrows indicate processes that isotopically deplete water vapor (decrease in δD) and red arrows indicate processes that isotopically enrich water vapor (increase in δD). Illustration from Galewsky et al. (2016)

1.1.4 Methods for the observation of water vapor isotopologues in the atmosphere

Observing atmospheric water vapor isotopologues and their ratios is challenging. Concentrations of water vapor vary widely within the troposphere ranging from 2500 ppm on a cold dry day to more than 25 000 ppm on a warm humid day at sea level for mid-latitude locations. In contrast to this large variability, isotopic ratios are significantly less variable. This requires observational techniques that are both sensitive over the large dynamic range of water vapor concentrations and precise enough to detect the small isotopic signals (Schneider et al., 2012).

The first use of stable isotopes in hydrological studies goes back to the 1950s and 1960s in which the analysis of the water isotopic composition was limited mostly to precipitation (Dansgaard, 1964) giving only access to an integrated history from the evaporation source to the sampled precipitation water. First

studies on the isotopic composition of water in its vapor phase were conducted between 1966 and 1973 in the frame of several airborne campaigns over the United States (Ehhalt, 1974; Ehhalt et al., 2005). The measurements relied on cryogenic and mass spectrometric techniques for which water vapor samples were taken in cold traps and analyzed later in a laboratory by mass spectrometers yielding data with limited spatio-temporal resolution. First space-based measurements were conducted in 1994 in the frame of a space shuttle mission using the Atmospheric Trace Molecule Spectroscopy (ATMOS) instrument (Gunson et al., 1996). This was complemented by the advent of laser absorption spectroscopic techniques in the 1990s (Scherer et al., 1997) enabling in situ isotope measurements with real-time temporal resolution which paved the way for airborne measurement campaigns with laser spectrometers on board in the early 2000s (Webster and Heymsfield, 2003).

In the following, methods for the measurement of water isotopologues in the atmosphere are divided into three categories including in situ observations, as well as ground-based and space-based remote sensing. A brief description is given for each of them highlighting their advantages and limitations.

1.1.4.1 In situ instruments

Today, most in situ instruments are based on laser spectrometry using cavity-ring-down spectrometers (CRDS). The measurement principle is based on comparing the time signal of the decay of a laser pulse with and without a sample inside a high-finesse opitcal resonator. Due to the enhanced interaction path length inside the cavity and the fact that the absorption is evaluated from the time behavior of the signal, and is thus independent of laser intensity fluctuations, CRDS instruments provide highly sensitive measurements of the absorption coefficient of a gas sample on an absolute scale (Maity et al., 2020). There are commercial systems available which can provide real-time measurements of multiple water isotopologues with high precision and accuracy. For instance, reported precision in δD for commercial CRDS analyzers are in the range of 5–10‰ (Johnson et al., 2011), but also precision levels close to 1‰ have been reported (Steen-Larsen et al., 2013). However, the measurement accuracy is highly dependent on a proper calibration procedure which can be based on the injection of liquid water standards into a vaporizer or the use of a reference vapor provided by a dew point generator (Bailey et al., 2015).

In situ observations of water isotopologues in the troposphere are rare. In order to obtain vertically resolved profiles of δD, in situ instruments are employed using airborne platforms in the frame of dedicated measurement campaigns. Figure 1.3a shows an example of H_2O and δD profiles obtained in the frame of the MUlti-platform remote Sensing of Isotopologues for investigating the Cycle of Atmospheric water (MUSICA) airborne campaign conducted in 2013 over the subtropical North Atlantic Ocean near Tenerife with the purpose of collecting accurate reference profiles for the validation of remote sensing data (Dyroff et al., 2015). During several flights over seven days, profiles between 150 m and 7000 m of H_2O and δD were measured with high vertical resolution of 3 m and a total uncertainty in δD of ca. 10‰. The in situ sensor was a specifically developed tunable diode-laser absorption spectrometer which was calibrated during flights with known isotopologue ratios (Dyroff et al., 2010). The δD profiles in Fig. 1.3a show a large variability in the troposphere ranging from -50‰ close to sea level to -500‰ at altitudes above 6 km. Most of the measured profiles also show strong gradients in δD at the top of the marine boundary layer. Figure 1.3b shows another example of an airborne campaign where profiles of δD were obtained in the

frame of the HyMeX SOP1 (Hydrological cycle in Mediterranean Experiment special observation period 1) field campaign in the western Mediterranean above Corsica using a CRDS isotope analyzer onboard an aircraft (Sodemann et al., 2017). And more recently, Chazette et al. (2021) deployed a CRDS, among other sensors, onboard an ultra-light aircraft to gain insights into the vertical distribution of stable water isotopologues above an Alpine mountain lake in order to analyze its links with the isotopic composition of the lake water and with location-characteristic small-scale dynamics.

In situ observations based on laser spectrometry have evolved as the state-of-the-art method to provide profiles of water isotopologues with high vertical resolution which is essential to study processes in the atmospheric boundary layer. Due to highly accurate measurements, such profiles are also in great need for the validation of ground-based and satellite-based remote sensing instruments.

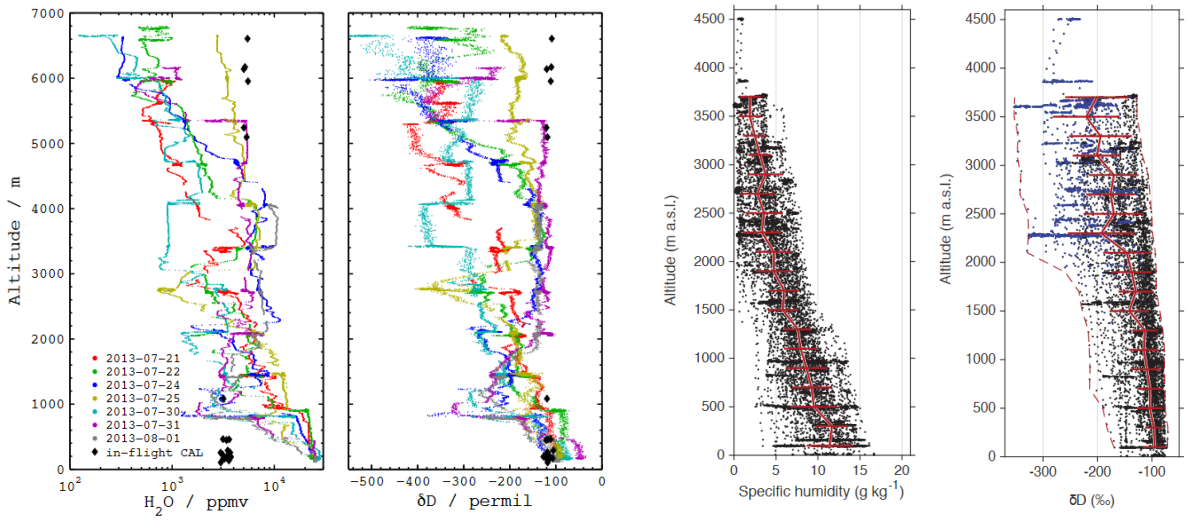

Figure 1.3: Examples of vertical δD profiles obtained by in situ aircraft measurements. (a) Vertical profiles of H_2O (left) and δD (right) over the subtropical North Atlantic Ocean near Tenerife measured in the frame of the MUSICA airborne campaign (Dyroff et al., 2015). Colors indicate different flights. (b) Profiles of H_2O (left) and δD (right) in the western Mediterranean above Corsica obtained from the HyMeX SOP1 campaign (Sodemann et al., 2017). Data points from all valid flights. Red solid line shows the mean profile (200 m bins) and dashed red lines indicate minimum and maximum values.

1.1.4.2 Ground-based Fourier transform infrared spectrometers

Remote sensing instruments operated on the ground are usually Fourier transform infrared (FTIR) spectrometers which analyze the spectrum in the near- and mid-infrared of direct sun light. These measurements yield total-column averages of H_2O and HDO above the instrument location. FTIR instruments are often organized in networks such as the Total Carbon Column Observing Network (TCCON, Wunch et al., 2011) and the Network for the Detection of Atmospheric Composition Change (NDACC, De Mazière et al., 2018) which can provide reliable long-termn data sets. The coverage of ground-based FTIR is limited by the number of ground stations (20–30 locations) which, however, play a crucial role in the validation of space-borne retrieval products (Scheepmaker et al., 2015).

Reported precision levels in δD columns retrieved from ground-based FTIR are between 5‰ and 35‰

(see Table 4 of Risi et al., 2012 and references therein). However, due to the complex nature of the retrieval methods, the resulting δD columns can be biased and thus themselves rely on validation profiles obtained from airborne in situ observations. Schneider et al. (2015) conducted an extensive empirical validation for the ground-basesd NDACC/FTIR instrument on the island of Tenerife using well calibrated in situ profiles obtained from multiple aircraft flights and nearby ground sensors. The observed positive bias in δD ranged from 25‰ in the lower troposphere to 70‰ in the middle troposphere. In another study, Schneider et al. (2020) compared the retrieval outputs for co-located measurements by seven stations which are part of both the TCCON and NDACC networks revealing a difference in δD of 58‰ on average.

1.1.4.3 Spaced-borne infrared spectrometers

Satellite-borne measurements have paved the way for water isotopologue observations on a global scale. From space, H_2O and HDO are observed using spectrometers operating in the thermal infrared spectral range. Since the early 2000s, there have been several satellite missions with the capability of retrieving water isotopologues in the stratosphere and troposphere. Examples are the Tropospheric Emission Spectrometer (TES) onboard the Earth Observing System (EOS) Aura satellite (Worden et al., 2006), the Michelson Interferometer for Passive Atmospheric Sounding (MIPAS) onboard the European Space Agency (ESA)'s environmental satellite (ENVISAT) (Steinwagner et al., 2007), the SCanning Imaging Absorption spectroMeter for Atmospheric CHartographY (SCIAMACHY) instrument on ENVISAT (Frankenberg et al., 2009; Scheepmaker et al., 2015; Schneider et al., 2018), the Infrared Atmospheric Sounding Interferometer (IASI) onboard the MetOP satellites (Herbin et al., 2009; Schneider and Hase, 2011), the Japanese Greenhouse Gases Observing Satellite (GOSAT) (Frankenberg et al., 2013), the Atmospheric Infrared Sounder (AIRS) onboard the NASA Aqua satellite (Worden et al., 2019) and the more recent Tropospheric Monitoring Instrument (TROPOMI) onboard the Sentinel-5 Precursor (S5P) satellite (Schneider et al., 2020, 2022). Instruments analyzing spectra in the thermal infrared (TES, MIPAS, IASI and AIRS) are mostly sensitive in the stratosphere and free troposphere while short-wave infrared sensors (SCIAMACHY, GOSAT and TROPOMI) have good sensitivity in the lower troposphere which contains the majority of atmospheric water vapor.

Figure 1.4 shows a plot of the global water vapor column and δD averaged over September 2018 as observed from space using the TROPOMI instrument (Schneider et al., 2022). It clearly shows the so-called latitude effect, meaning that water vapor becomes more depleted with higher latitudes as heavier isotopologues condense to form rain during poleward transit towards lower-temperature regions (Dansgaard, 1964).

Typical precision levels for space-borne measurements of δD vary widely from 10‰ to 100‰ (see Table 2 of Risi et al., 2012 and references therein) depending on the averaging used in the retrieval. Similarly to ground-based FTIR column measurements, special care has to be dedicated to the quantification of biases in the retrieved H_2O/HDO data. Scheepmaker et al. (2015) observed a mean negative bias in δD retrieved from SCIAMACHY of -30‰ compared to ground-based FTIR of TCCON and -69‰ copmpared to NDACC-MUSICA FTIR instruments. Bias in δD derived from TROPOMI-retrieved H_2O/HDO columns was determined to be around -20‰ (median value) validated against different TCCON sites (Schneider et al., 2022). Both studies reveal a dependency of the observed bias with latitude with high-latitude observations giving rise to larger biases due to less favorable measurement geometries with typically high solar

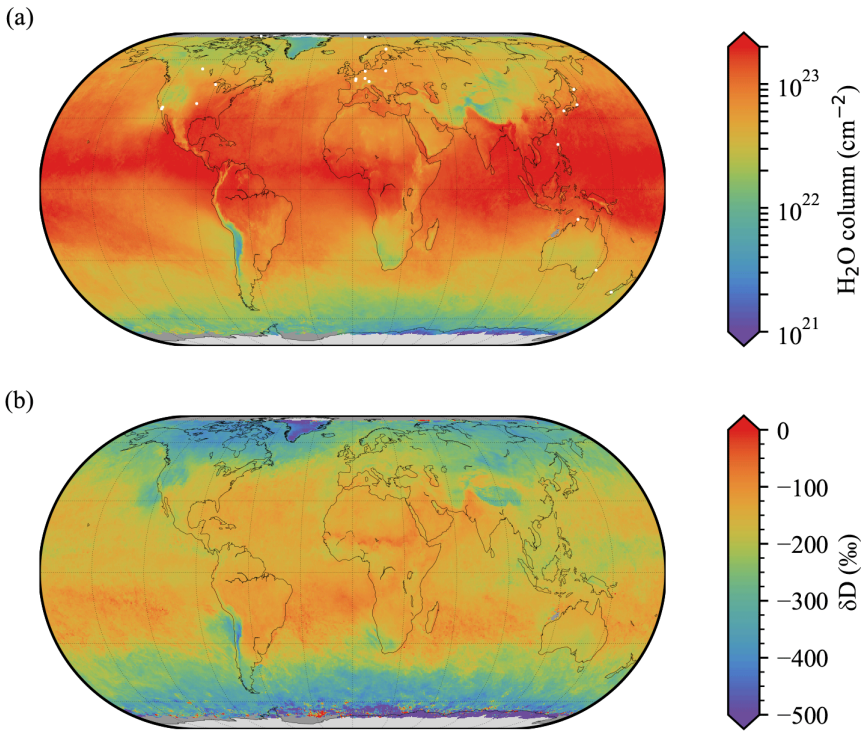

Figure 1.4: Map of global distribution of H_2O (a) and δD (b) averaged over September 2018 observed from TROPOMI on a 0.5° × 0.5° grid. Figure from Schneider et al. (2022)

zenith angles and low surface albedos.

The increased availability of H_2O/HDO data products from satellite-borne observations has significantly contributed to improve our understanding of the tropical water cycle (Worden et al., 2007) and to assess the role of plants in global evapotranspiration (Good et al., 2015). However, due to their lack of vertical resolution, oftentimes reduced sensitivity in the boundary layer and insufficient temporal coverage, they are ill-suited for the study of the dynamics of evaporation, condensation, and air mass mixing processes on local or regional scales.

1.1.4.4 Remote sensing based on dual-frequency-comb spectroscopy

Dual-comb spectroscopy (DCS) is based on the interference of two synchronized frequency combs, i.e. laser radiation with a spectrum consisting of a series of discrete, equally spaced frequency lines, with slightly different repetition rates (Schiller, 2002). The interference signal is detected by a single photoreceiver generating a radio frequency (RF) comb composed of unique heterodyne beating signals between pairs of the optical comb teeth. To obtain a spectroscopic measurement, either one or both optical combs pass through a sample volume and the resulting absorption spectrum is obtained from the RF spectrum which is easily accessible by RF electronics. DCS combines the advantages of conventional FTIR spectrometers, such as broad spectral coverage for multi-species detection, with the strengths of laser spectrometers where high sensitivity is achieved by using a high-brightness diffraction-limited source and kilometer-long interaction paths (Coddington et al., 2016).

The application of the DCS technique to open-path remote sensing of greenhouse gases and other

atmospheric species has been intensively driven by different teams of the National Institute of Standards and Technology (NIST) in Boulder, USA. For instance, Rieker et al. (2014) deployed a dual-frequency comb system to probe absorption features from CO_2, CH_4, H_2O and HDO in the spectral range from 1.60 to 1.67 µm over a 2 km-long path. A mid-IR dual-comb system (3.1–4.2 µm) specifically dedicated to water vapor isotopologues was demonstrated recently in a field experiment over a 760 m long open path (Herman et al., 2022). From the acquired spectra of H_2O and HDO, the isotopic abundance δD was determined with a precision of less than 2‰ over 17 min.

Open-path measurements based on DCS have several advantages over point sensors, such as CRDS analyzers. First, they do not rely on calibration procedures via a reference gas cell. Second, open-path measurements avoid representation errors as they are better suited than point sensors to capture processes on large scales, for example, evaporation above reservoirs. This characteristic makes these measurements also better adapted to the spatial resolution of synoptic and mesoscale atmospheric models.

1.1.5 The Water Vapor and Isotope Lidar (WaVIL)

As outlined in the previous section, the only way to obtain vertical profiles of the water vapor isotopologues H_2O and HDO with high vertical resolution is by in situ CRDS analyzers mounted on airborne platforms. Active remote sensing using lidar provides similar vertical resolution and even better temporal resolution, but is so far only capable of measuring the water vapor main isotopologue H_2O. Adding a capability to sound HDO to a lidar system would thus provide a unique remote sensing instrument to complement the airborne in situ sensor approach and to allow for more continuous observations of water vapor isotopologues. The idea has been studied for the Raman lidar technique, but first calculations reported in the literature indicate that a H_2O/HDO Raman lidar with reasonable performance is hindered by the low Raman scattering cross-section (Liberti et al., 2018). In a multiple-wavelength lidar approach for probing CO_2 at 1.6 µm, Yu et al. (2021) were able to obtain range-resolved measurements of HDO since it interferes slightly with the probed CO_2 R16 line. But no lidar system is so far reported capable of providing range-resolved measurements of HDO together with the main isotopologue H_2O which would enable the estimation of δD with high spatio-temporal resolution.

The development of such an instrument and first proof-of-concept experiments were pursued in the framework of the Water Vapor and Isotope Lidar (WaVIL) project which is the main topic of this thesis. The overarching goal was to develop a transportable DIAL prototype instrument capable of measuring both water vapor isotopologues H_2O and HDO with vertical and temporal resolution on the order of 100 m and 10 min for ground-based measurements in the atmospheric boundary layer. To resolve characteristic gradients in δD between the boundary layer and the free troposphere, the precision should ideally be on the order of 10–20‰. High vertical and temporal resolution combined with high precision in δD would make such a lidar a unique instrument compared to existing state-of-art measurement technologies (see Fig. 1.5). Compared to passive space-borne sensors, which provide total-column averages or few-level measurements with km-resolution at best, the potential gain of the WaVIL instrument would come from its significantly higher temporal (ca. 10 min) and vertical (ca. 100 m) resolution as well as better precision. In comparison to ground-based FTIR spectrometers, precision in δD and time resolution would be comparable, but the WaVIL instrument would provide a vertical resolution which these passive sounding methods lack.

Figure 1.5 also contains a point representing δD measurements based on laser spectrometers, which are characterized by a precision as low as 1‰ and sub-minute temporal resolution. However, these instruments only provide a measurement at a single point in space and an aircraft is required to obtain a vertical profile of δD, making this approach rather unsuitable for continuous long-term measurements.

A lidar capable of measuring both water vapor isotopologues H_2O and HDO would thus provide a novel and unique instrument to complement existing technologies in the framework of scientific field campaigns for the study of the water cycle.

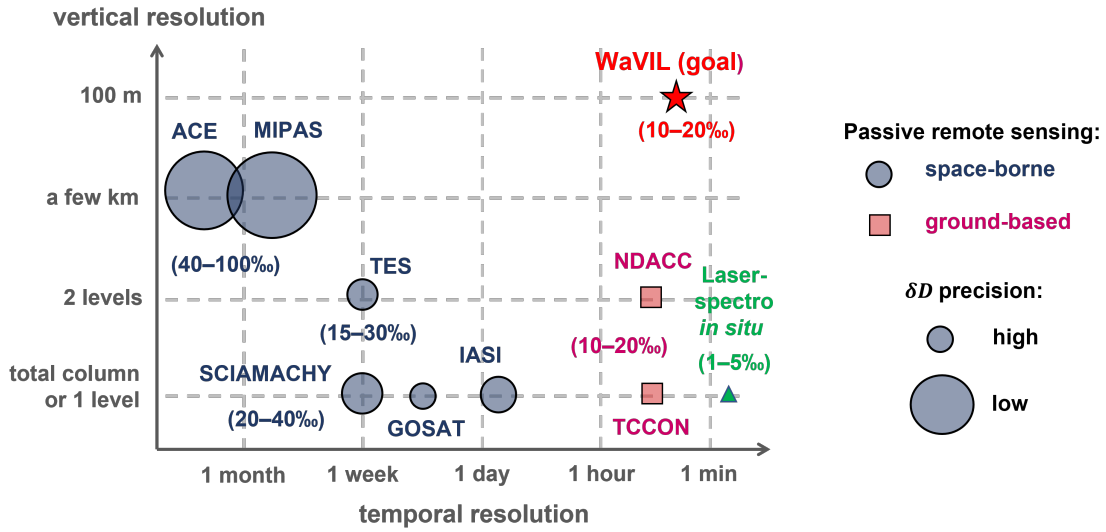

Figure 1.5: Comparison of the performance in terms of vertical (y-axis) and temporal (x-axis) resolution as well as precision in the HDO abundance δD (values in parentheses; symbol size inversely proportional to precision) between examples of existing instruments and the novel WaVIL instrument. Space-borne passive sensors (blue circles): ACE – Aerosol-Cloud-Ecosystems mission, MIPAS – Michelson Interferometer for Passive Atmospheric Sounding, TES – Tropospheric Emission Spectrometer, SCIAMACHY – SCanning Imaging Absorption spectroMeter for Atmospheric CHartographY, GOSAT – Japanese Greenhouse Gases Observing Satellite, IASI – Infrared Atmospheric Sounding Interferometer. Violet rectangles stand for ground-based FTIR spectrometer from the Total Carbon Column Observing Network (TCCON) and the Network for the Detection of Atmospheric Composition Change (NDACC).

1.2 Lidar remote sensing of carbon dioxide from space

1.2.1 Scientific background

Carbon dioxide is the most prominent greenhouse gas the atmospheric concentration of which has increased significantly due to human activity since the industrial revolution. Due to its importance as a key contributor to global warming – among all anthropogenic greenhouse gases CO_2 causes the strongest radiative forcing (Myhre et al., 2013) – it is an essential task to gain a more accurate understanding of the sources and sinks of CO_2 and their role in the global carbon cycle.

Similar to water vapor, atmospheric CO_2 is monitored from the ground using in situ sensors and FTIR spectrometers organized in networks, such as the TCCON (Wunch et al., 2011). These measurements are complemented by airborne in situ field campaigns, which are however sparse in space and time. The identification of CO_2 sources and sinks on a regional and global scale can thus only be achieved from space for which there are a variety of active and planned instruments. Examples for passive remote sensing instruments are the Japanese Greenhouse Gases Observing Satellite (GOSAT) and the NASA developments Orbiting Carbon Observatories 2 and 3 (OCO-2 and OCO-3). With these instruments a relative precision in the measured column-averaged atmospheric CO_2 dry air mole fraction better than 0.5% has been demonstrated (Kuze et al., 2016; Wunch et al., 2017), fulfilling the precision requirement necessary for identifying CO_2 surface fluxes by means of inverse models that describe atmospheric transport and mixing (Buchwitz et al., 2015).

However, achieving measurements with sufficient total accuracy on a regular basis is still challenging. Major limitations arise due to interference of clouds and aerosols, low sensitivity in the troposphere and unfavourable sun angles at high latitudes. Active remote sensors like lidar are a potential complement to passive remote sensing as they can overcome some of the limitations. This is why a lot of research efforts have been dedicated to the development of future space-borne integrated-path DIAL systems.

1.2.2 Requirements on a space-based IP-DIAL instrument

Multiple feasibility studies have been carried out by several groups and space agencies in order to define the technical requirements for a potential space mission employing an integrated-path DIAL instrument. For instance, the ASCEND program from NASA (Kawa et al., 2018) or the A-SCOPE study from ESA (Ingmann et al., 2008) have driven technological developments and mission concepts for CO_2 probing in the wavelength ranges around 1.6 µm and 2.1 µm. Indeed, feasibility studies indicate that the stringent requirements on accuracy and precision in the column-averaged CO_2 dry air mixing ratio are achievable by using the IP-DIAL method (Ehret et al., 2008; Singh et al., 2017b).

However, the accuracy requirements on column-averaged CO_2 measurements from space give rise to demanding challenges in the development of a space-borne lidar instrument. The first main requirement concerns the laser output energy in order to achieve sufficiently high signal-to-noise ratios to achieve the demanded precision in the CO_2 mixing ratio. In the A-SCOPE study, a baseline energy value of 55 mJ was derived for a detector noise-equivalent power of 100 fW $Hz^{-1/2}$ and a telescope aperture of 1.2 m diameter in direct-detection mode (Ingmann et al., 2008).

For IP-DIAL measurements at 2.05 µm, the on-line wavelength needs to be tuned to the wing of the R30

absorption line in order to optimize the measurement sensitivity for the lower troposphere. This increases the potential bias due to laser wavelength fluctuations and thus imposes a high level of frequency stability of the lidar transmitter. Indicative values from the A-SCOPE study are in the order of 200 kHz over averaging times of 10 s. The laser emission also needs to be spectrally pure. A spectral purity better than 99.9% is highly desirable for space-borne IP-DIAL sounding (Singh et al., 2017b).

1.2.3 The Lidar Emitter and Multispecies greenhouse gases Observation instrument

In order to fulfill the technological requirements with the prospect of a space-borne DIAL, using a laser transmitter based on parametric conversion is an appealing approach because it allows for the extension of the spectral coverage of mature 1 µm laser sources further into the near- and mid-infrared. It also opens the path for generic architectures that could be transferred from one spectral window to another while keeping the same core components. For instance, using a laser source based on a nested-cavity optical parametric oscillator (NesCOPO) developed at ONERA, Barrientos Barria et al. (2014) demonstrated an IP-DIAL setup capable of addressing the three main greenhouse gases CO_2, CH_4 and H_2O at the wavelengths suitable for space-borne soundings of 2.05 µm, 2.29 µm, and 2.06 µm, respectively.

The Lidar Emitter and Multispecies greenhouse gases Observation instrument (LEMON) developed in the framework of the European Union Horizon 2020 research and innovation program builds on the NesCOPO technology of ONERA with the aim of realizing a multi-species DIAL instrument capable of addressing CO_2 and both water vapor isotopologues H_2O and HDO in a ruggedized setup with the prospect of an airborne instrument demonstration. In the frame of the thesis research project, two main development aspects were addressed:

- The demonstration of high-energy operation of a 2 µm laser transmitter based the NesCOPO architecture combined with parametric amplification. The goal is set in line with the requirements for CO_2 IP-DIAL measurement from space while keeping a fairly compact footprint for airborne operation. For this purpose, the design is fully oriented around quasi-phase-matched nonlinear materials, including state-of-the-art periodically poled Potassium Titanyle Phosphate crystals (PPKTP). Preliminary tests were conducted using the WaVIL setup in order to validate this design approach.

- The demonstration of high frequency stability in line with the requirement for CO_2 IP-DIAL measurement from space. A technique for locking the NesCOPO-emitted frequency was developed and the resulting frequency stability was characterized.

Table 1.1 provides an overview of instrument requirements for space-borne IP-DIAL sounding of CO_2 and the development goals for the LEMON lidar. Since the A-SCOPE study, several developments on avalanche photodiodes have been carried out in recent years (Dumas et al., 2017; Sun et al., 2017; Tan et al., 2019) and detectors with record noise-equivalent powers down to 0.5 fW $Hz^{-1/2}$ have been reported (Beck et al., 2014). Taking into account these recent developments, the aim for the LEMON instrument is to generate 40 mJ of output pulse energy, at a repetition rate of 75 Hz, in double-pulse operation. The foreseen laser energy level would also fulfil the requirement for range-resolved DIAL measurement from the ground using commercially available detectors (e.g., InGaAs photodiodes). In terms of laser frequency stability, stringent values for IP-DIAL measurements of CO_2 from space at 2.05 µm are taken as the objective for the

frequency accuracy in the LEMON instrument development while adding the capacity to address also the water vapor isotopologue spectral range at 1.98 µm.

While the major goal is to demonstrate the technological readiness of the LEMON lidar instrument in a challenging environment such as an airplane, the expected upgrades in laser energy and frequency stability compared to the WaVIL instrument will also improve the capability of ground-based, range-resolved DIAL measurements of H_2O and HDO.

Table 1.1: Laser transmitter specifications for space-borne IP-DIAL measurement of CO_2 as stated in the framework of the A-SCOPE mission assessment (Ingmann et al., 2008; Fix et al., 2017) and performance objectives for the LEMON instrument. Values in parentheses indicate threshold values.

Parameter	**Requirement**	**Objective for LEMON lidar**
On-line wavelength	4875.59 cm^{-1} (2051.0328 nm)	3 cm^{-1} tunability around line center at:
		4875.59 cm^{-1} for CO_2
		5045.41 cm^{-1} for H_2O/HDO
Pulse energy	55 mJ (> 30 mJ) for λ_{ON}	40 mJ (> 30 mJ)
Frequency stability	< 0.2 MHz (1 MHz) RMS over 10 s	same values for both spectral windows
Spectral purity	99.93%	experimental verification

Chapter 2

Theory of the differential absorption lidar method

In this chapter, the overall principle and the mathematical foundations of the differential absorption lidar method are introduced. On the one hand, the presented theoretical concepts serve to simulate lidar signals with the associated noise contributions in order to asses the expected performance of a given lidar setup under certain atmospheric conditions (see chapter 3). On the other hand, this chapter lays the foundation for the retrieval of the water vapor isotopologue mixing ratios from experimentally measured lidar signals which is the subject of chapter 5.

2.1 Interaction of laser radiation with the atmosphere

A laser beam sent into the atmosphere interacts with its constituents (molecules, aerosols, water droplets, etc.) leading to an attenuation of the laser beam intensity. For a given laser wavelength and for a travelling distance r, this attenuation can be expressed in the form of the optical depth defined as:

$$\tau = \int_0^r \alpha(\lambda, r')dr', \tag{2.1}$$

where $\alpha(\lambda, r)$ is the extinction coefficient (unit: m^{-1}). The atmospheric transmission is obtained from the optical depth according to the law of Beer-Lambert:

$$T(\lambda, r) = e^{-\tau(\lambda, r)}. \tag{2.2}$$

Extinction can occur because of scattering and absorption of light by molecules and particles. The total extinction coefficient can thus be expressed as the sum of extinction coefficients due to scattering and absorption with contributions from molecules and aerosols:

$$\alpha(\lambda) = \alpha_{\mathrm{sca}}^{\mathrm{mol}}(\lambda) + \alpha_{\mathrm{abs}}^{\mathrm{mol}}(\lambda) + \alpha_{\mathrm{sca}}^{\mathrm{aer}}(\lambda) + \alpha_{\mathrm{abs}}^{\mathrm{aer}}(\lambda) \tag{2.3}$$

2.1.1 Scattering

Throughout this manuscript, the term scattering is used in the context of elastic scattering meaning that the wavelength remains unchanged during the scattering process. Depending on the size of the scattering particles and the laser wavelength, it is common to differentiate between Rayleigh and Mie scattering.

Rayleigh scattering is defined as the scattering due to particles that are small compared to the wavelength of the radiation. It is thus a synonym for scattering on molecules (principally oxygen and nitrogen). Rayleigh scattering is characterized by a λ^{-4} spectral dependence and is consequently more pronounced at at shorter wavelengths (the scattered intensity of a green laser at 0.5 µm is 256 times larger than that of a 2 µm laser).

Even though Mie scattering theory (Mie, 1908) is not limited to a certain size of the scatteing particles (it is a general formulation for scattering by spherical particles of arbitrary radius), the term is often used in the context of scattering from particles with sizes similar to the wavelength of the radiation or larger. Atmospheric particles from air pollution (sulfates, soot, organic compounds), dust or pollen fall into this category.

In the context of lidar, an important quantity related to scattering is the backscatter coefficient β (unit: $m^{-1}\,sr^{-1}$). It is a measure of the amount of radiation that is scattered in the backward direction. Assuming that N_j is the number density of scattering particles of type j, the backscatter coefficient is the sum of the contributions from all scatterers according to:

$$\beta(\lambda,r) = \sum_j N_j(r)\frac{d\sigma_{j,\mathrm{sca}}}{d\Omega}(\pi,\lambda), \tag{2.4}$$

where $d\sigma_{j,\mathrm{sca}}(\pi,\lambda)/d\Omega$ is the backscatter cross-section per unit of solid angle of particle type j which depends on the particle size and shape as well as the the wavelength of the scattered radiation.

The backscatter coefficient can be decomposed into components due to molecular (Rayleigh) scattering and due to aerosol (Mie) scattering:

$$\beta(\lambda,r) = \beta_{\mathrm{mol}}(\lambda,r) + \beta_{\mathrm{aer}}(\lambda,r). \tag{2.5}$$

As molecular scattering depends primarily on the air density, it decreases with altitude. It can be calculated as a function of wavelength and altitude z according to (Cezard, 2008):

$$\beta_{\mathrm{mol}}(\lambda(\mu\mathrm{m}),z) = 10^{20}\exp\left(-\frac{z}{z_0}\right)\frac{4\pi^2}{n_0\lambda^4}\left(\frac{5.79}{238-(1/\lambda)^2}+\frac{0.17}{57-(1/\lambda)^2}\right)^2 \mathrm{m}^{-1}\,\mathrm{sr}^{-1}, \tag{2.6}$$

with $z_0 = 8000\,\mathrm{m}$ and $n_0 = 2.55\times10^{25}$ is the air number density under standard atmospheric conditions. The aerosol backscatter coefficient is highly variable as it strongly depends on the presence and types of aerosols in the atmosphere. The scattered intensity depends on the ratio of particle radius to wavelength and on the complex refractive index of the scatterers. Figure 2.1 shows a comparison between the molecular backscatter coefficient calculated according to Eq. 2.6 for a wavelength of 2 µm and two profiles of the aerosol backscatter coefficient also calculated for a wavelength of 2 µm following the ESA ARMA model (European Space Agency, 1999) constrained to different aerosol loads (see chapter 3 for more details).

As clearly demonstrated in Fig. 2.1, aerosol scattering is the most dominant scattering contribution for wavelengths around 2 µm in the lower part of the atmosphere, mostly in the atmospheric boundary layer where aerosols are trapped. A sharp decline of the aerosol backscatter is usually observed in the free troposphere at 2–3 km where values approach the molecular backscatter coefficient. For larger altitudes, the backscatter coefficient is principally determined by the molecular contribution. However, the presence of particles in the free troposphere, for example due to long-range transport of dust, can lead to significant deviations from the backscattering profiles shown in Fig. 2.1.

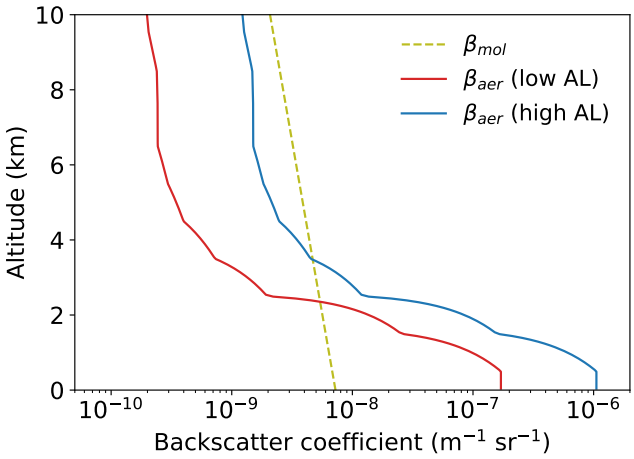

Figure 2.1: Vertical profiles of molecular (β_{mol}) and aerosol (β_{aer}) scattering coefficients calculated for a laser wavelength of 2 µm. Profiles of β_{aer} were derived from the ESA ARMA model (European Space Agency, 1999) constrained by aerosol optical depth measurements at a mid-latitude site (Palaiseau, France). The plot shows cases of low and high aerosol loads (AL). See chapter 3 for more details.

Backscatter and extinction coefficient are related through the extinction-to-backscatter ratio (lidar ratio) defined as:

$$LR = \frac{\alpha}{\beta}. \tag{2.7}$$

For Rayleigh scattering, the extinction coefficient is related to the backscatter coefficient according to:

$$\alpha_{\text{mol}} = \frac{8\pi}{3}\beta_{\text{mol}}. \tag{2.8}$$

For aerosol scattering the determination of the lidar ratio is more complex because it depends on the size distribution, shape and chemical composition of the particles.

2.1.2 Absorption

Absorption of near- and mid-infrared radiation takes place on a molecular level when an incoming photon changes the rotational-vibrational state of the interacting molecule. For a mixture of j absorbing species, the extinction coefficient due to absorption, or simply the absorption coefficient, can be expressed as follows:

$$\alpha_{\text{abs}}(\lambda, r) = \sum_j n_{\text{air}}(r) X_j(r) \sigma_j(\lambda, r), \tag{2.9}$$

where $n_{\text{air}}(r)$ is the total air number density, $X_j(r)$ is the volume mixing ratio of gas species j and $\sigma_j(\lambda, r)$ is the wavelength-dependent absorption cross-section of species j.

The shape and width of an absorption line is determined by the motion and collisions of the gas molecules. Depending on pressure and temperature conditions, two regimes are differentiated giving rise to two different line shape functions:

- Pressure (collisional) broadening due to collisions of molecules giving rise to a Lorentz line shape function.
- Doppler broadening under low-pressure conditions due to the Doppler shifting of frequencies interacting with molecules caused by their velocity distribution resulting in a Gaussian line shape.

2.1.2.1 Lorentz line shape

Under high-pressure conditions such as in the lower part of the atmosphere (0–15 km), molecular collisions are the dominant broadening mechanism and the absorption line shape is described by a Lorentz profile as a function of wavenumber $\tilde{\nu}$ according to

$$\sigma_L = \frac{S}{\pi} \frac{\gamma_L}{\gamma_L^2 + (\tilde{\nu} - \tilde{\nu}_0)^2}, \tag{2.10}$$

where $\tilde{\nu}_0$ is the line center position, S is the line intensity, and γ_L the pressure-broadened half width at half maximum (HWHM) line width. The line intensity depends on the temperature T and the energy of the lower molecular state E" according to:

$$S = S_0 \left(\frac{T_0}{T}\right)^j \exp\left[-\frac{E"hc}{k}\left(\frac{1}{T} - \frac{1}{T_0}\right)\right], \tag{2.11}$$

where k is the Boltzmann constant and S_0 is the line intensity under reference conditions for temperature $T_0 = 296$ K and pressure $p_0 = 1013.25$ hPa. The exponent j takes the values of $j = 1$ for CO_2 and $j = 3/2$ for H_2O. The temperature and pressure dependence of the linewidth can be expressed as:

$$\gamma_L = \gamma_{L0} \frac{p}{p_0} \left(\frac{T_0}{T}\right)^n \tag{2.12}$$

with γ_{L0} as the HWHM line width under the above mentioned reference values for pressure and temperature and n as the coefficient of the temperature dependence of the pressure-broadened half width. Note that the pressure-broadened line width results from collisions of molecules of the same type (self-broadening) and from collisions with other gas molecules (air broadening). Under standard atmospheric conditions, pressure-broadened are half widths are in the order of a few GHz for wavelengths around 2 µm.

2.1.2.2 Doppler line shape

Under conditions of low pressure, the spectral shape of absorption lines is due to Doppler broadening. Assuming a Maxwell-Boltzmann distribution for the velocities of the molecules, the absorption cross-sections

follow a Gaussian profile according to:

$$\sigma_D = \frac{S}{\gamma_D}\sqrt{\frac{\ln 2}{\pi}}\exp\left[-\ln 2\frac{(\tilde{\nu}-\tilde{\nu}_0)^2}{\gamma_D^2}\right], \tag{2.13}$$

and the Doppler-broadened HWHM depends on the gas temperature T according to:

$$\gamma_D = \frac{\tilde{\nu}_0}{c}\sqrt{\frac{2N_A kT\ln 2}{M}}, \tag{2.14}$$

where N_A is the Avogadro constant, M is the molar mass of the molecule and c is the speed of light. Contrary to pressure broadening, the Doppler-broadened half width depends on the frequency of the incoming radiation. Doppler-broadened half widths are in the order of a few hundreds of MHz at 2 µm under standard atmospheric conditions.

2.1.2.3 Voigt line shape

In the general case in which both collisional and Doppler broadening contribute, the absorption line shape can be described by a Voigt profile resulting from the convolution of a Lorentzian function and a Gaussian function. The absorption cross-section can then be written as:

$$\sigma(\nu) = \sigma_0\frac{y}{\pi}\int_{-\infty}^{+\infty}\frac{\exp(-t^2)}{y^2+(x-t)^2}dt, \tag{2.15}$$

with

$$\sigma_0 = \frac{S}{\gamma_D}\left(\frac{\ln 2}{\pi}\right)^{1/2},$$
$$y = \frac{\gamma_L}{\gamma_D}(\ln 2)^{1/2},$$
$$x = \frac{\tilde{\nu}-\tilde{\nu}_0}{\gamma_D}(\ln 2)^{1/2},$$

where S is the line intensity according to Eq. 2.11, γ_D and γ_L are the Doppler-broadened and pressure-broadened line widths (HWHM), respectively, and $\tilde{\nu}_0$ is the line center position.

Absorption line parameters for different molecules and isotopologues can be accessed through spectroscopic databases such as HITRAN or GEISA. In the framework of this thesis, HITRAN2016 (Gordon et al., 2017) and the more recent version HITRAN2020 (Gordon et al., 2022) were used (no significant difference between both versions for the in this thesis investigated wavelength range and isotopologues).

2.2 Principle of differential absorption lidar

Figure 2.2 shows the basic setup of a lidar system. It consists of a laser source (transmitter) and a receiver part. The laser emits pulses in the ns-regime which are sent into the atmosphere in the form of a low-divergence beam. The receiver comprises a telescope collecting the backscattered photons from the atmosphere and in some cases from some kind of distant target. The collected radiation is then directed

onto a detector which converts the received optical signal into an electrical signal which is digitized and stored on a computer. The peculiarity of a DIAL is that the laser transmitter emits pulses with at least two different wavelengths that experience different attenuations due to absorption of the target gas. In the simplest case, one wavelength, the so-called on-line wavelength, is tuned to a strong absorption feature of the target gas while the second (off-line) wavelength is tuned such as to experience only weak absorption along the lidar path. The difference in atmospheric transmission between the on-line and off-line signals is then used to determine the target gas concentration.

Depending on the origin of the lidar return signals, there are two types of measurements. If the backscattered signal is due to molecular and aerosol scattering along the lidar line of sight, a range-resolved measurement (RR-DIAL) of the target gas concentration is obtained. In the case where the return signal originates from a hard target (reflector, vegetation, clouds, etc.) at a certain distance, the concentration of the target gas is determined as the path-integrated average value between the lidar and the target (integrated-path DIAL or in the following IP-DIAL).

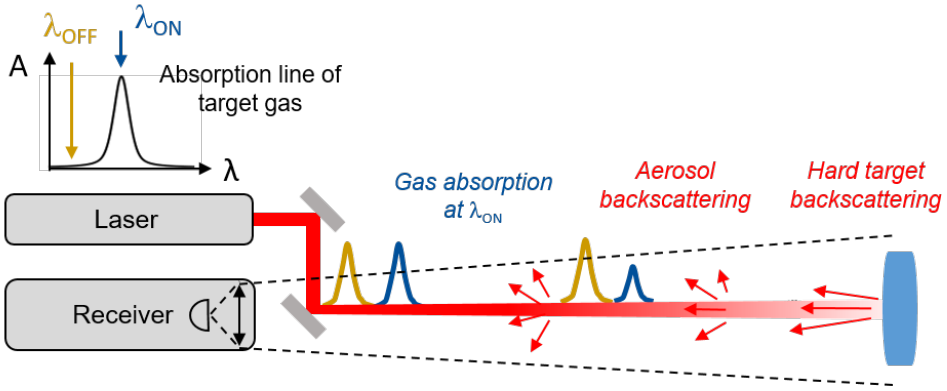

Figure 2.2: Schematic illustration of the DIAL measurement principle.

2.3 Lidar equation

The backscattered power signal for a given wavelength λ arriving at the detection unit as a function of range r is expressed in form of the lidar equation (Collis and Russell, 1976), which can be written as:

$$P_{\mathrm{r}}(\lambda,r) = T_{\mathrm{r}}(\lambda)\frac{A}{r^2}O(\lambda,r)\frac{c}{2}\beta(\lambda,r)E_{\mathrm{p}}(\lambda)\cdot\exp\left(-2\int_0^r \alpha(\lambda,r')dr'\right), \tag{2.16}$$

where:

- $T_{\mathrm{r}}(\lambda)$ is the transmission of the lidar receiver,
- A is the effective area of the receiving telescope,
- $O(\lambda,r)$ is the laser-beam receiver-field-of-view overlap function,
- $\beta(\lambda,r)$ is the total backscatter coefficient,
- $\alpha(\lambda,r)$ is the total atmospheric extinction coefficient accounting for molecular absorption as well as Mie and Rayleigh scattering,

- $E_p(\lambda)$ is the laser pulse energy and
- c is the speed of light.

The validity of Eq. 2.16 is based on the assumptions that (i) the scattering is incoherent, (ii) multi-scattering processes do not contribute significantly to the received signal, (iii) the time constant of the scattering process is small compared with the laser pulse length, (iv) the laser radiation is monochromatic and (v) the wavelength remains unchanged during the scattering process (Bösenberg, 1998).

2.4 DIAL method and derivation of the mixing ratio

The DIAL method consists in measuring the differential optical depth defined as:

$$\Delta\tau(0,r) = \tau_{\text{on}}(0,r) - \tau_{\text{off}}(0,r), \tag{2.17}$$

where $\tau_{\text{on}}(0,r)$ and $\tau_{\text{off}}(0,r)$ are the single-path optical depths for a path length r of the on- and off-line signals, respectively. Using Eq. 2.16 for both the on- and off-line signals and after some algebraic manipulations the differential optical depth can be calculated from the received power signals and laser energies according to:

$$\Delta\tau(0,r) = \frac{1}{2}\ln\left(\frac{P_{\text{off}}(r)E_{\text{on}}}{P_{\text{on}}(r)E_{\text{off}}}\right) + C, \tag{2.18}$$

where C is a constant containing the spectral dependence of the remaining parameters of the lidar equation Eq. 2.16:

$$C = \frac{1}{2}\left[\ln\left(\frac{T_r(\lambda_{\text{on}})}{T_r(\lambda_{\text{off}})}\right) + \ln\left(\frac{O(\lambda_{\text{on}})}{O(\lambda_{\text{off}})}\right) + \ln\left(\frac{\beta(\lambda_{\text{on}})}{\beta(\lambda_{\text{off}})}\right)\right]. \tag{2.19}$$

For the case of a two-wavelength DIAL, it is assumed that the on-line and off-line laser pulses are emitted sufficiently close in wavelength and time to consider the backscatter coefficient β as equal. Similarly, assuming that the receiver transmission $T_r(\lambda)$ and the overlap function $O(\lambda)$ are wavelength-independent within the spectral range of the DIAL wavelengths, the constant C in Eq. 2.18 vanishes. The final assumption is that on- and off-line pulses experience identical extinction due to scattering. Consequently, the difference in transmission between the on- and off-line pulses depends only on the wavelength-dependent absorption along the line of sight.

Considering now an atmospheric column between distances r and $r+\delta r$, one obtains the local differential optical depth between r and $r+\delta r$ according to:

$$\Delta\tau(r,r+\delta r) = \int_r^{r+\delta r} X(r')n_{\text{air}}(r')[\sigma_{\text{on}}(r') - \sigma_{\text{off}}(r')]dr' \tag{2.20}$$

where $X(r)$ is the volume mixing ratio of the gas of interest, $\sigma_{\text{on/off}}(r)$ are the on- and off-line absorption cross-sections, and $n_{\text{air}}(r)$ is the total air number density calculated from the ideal gas law according to:

$$n_{\text{air}}(r) = \frac{p(r)}{kT(r)}, \tag{2.21}$$

where $p(r)$ and $T(r)$ are atmospheric pressure and temperature and k is the Boltzmann constant.

From Eq. 2.20, the local mean volume mixing in the atmospheric column between distances r and $r+\delta r$ can be obtained:

$$\overline{X}(r, r+\delta r) = \frac{\Delta\tau(r, r+\delta r)}{\int_r^{r+\delta r} WF(r')dr'}, \tag{2.22}$$

where the nominator is calculated according to Eq. 2.18 and now reads as:

$$\Delta\tau(r, r+\delta r) = \frac{1}{2}\ln\left(\frac{P_{\text{off}}(r+\delta r)P_{\text{on}}(r)}{P_{\text{on}}(r+\delta r)P_{\text{off}}(r)}\right), \tag{2.23}$$

and

$$WF(r) = n_{\text{air}}(r)[\sigma_{\text{on}}(r) - \sigma_{\text{off}}(r)] \tag{2.24}$$

is the so-called weight function evaluated between r and $r+\delta r$.

2.4.1 Range-resolved DIAL measurement

Range-resolved DIAL measurements rely on aerosol backscattering of short laser pulses (typically a few tens of ns). The distance r from the lidar to the scattering volume is simply obtained from the time delay Δt between the emission and reception of the laser pulse and the time-of-flight principle according to $r = 1/2\,c\,\Delta t$. Due to the finite bandwidth of the detection system, the backscattered signal is received in temporal gates δt giving rise to a spatial resolution of $\delta r = 1/2\,c\,\delta t$. Assuming that the range resolution is sufficiently small, the weight function can be considered as constant between the distances $r - \delta r/2$ and $r + \delta r/2$ and one obtains a range-resolved profile of the volume mixing ratio from the local differential optical depth at range r according to:

$$X(r-\delta r, r+\delta r) = \frac{\Delta\tau((r-\delta r, r+\delta r)}{WF(r)\cdot\delta r}. \tag{2.25}$$

In practice, the mixing ratio is often evaluated over several range gates in order to reduce the associated random error. Finding the volume mixing ratio at a distance r is then equivalent to calculating the local slope of the measured differential optical depth according to:

$$X(r) = \frac{1}{WF(r)}\frac{\mathrm{d}}{\mathrm{d}r}\Delta\tau(r). \tag{2.26}$$

2.4.2 Integrated-path DIAL measurement

With an integrated-path measurement between two distances r_1 and r_2, one obtains a columnar average of the volume mixing ratio according to:

$$\overline{X}(r_1, r_2) = \frac{\Delta\tau(r_1, r_2)}{\int_{r_1}^{r_2} WF(r)dr}. \tag{2.27}$$

Integrated-path measurements are usually applied when the backscatter signal is due to the reflection on a hard target. Examples are air-borne or space-borne DIAL measurements that use the laser backscatter caused by the Earth's surface or the top layer of clouds.

For the case of vertical DIAL measurements, the weight function of Eq. 2.24 is range-dependent since air number density and absorption cross-sections depend on the vertical profiles of pressure and temperature. This requires at least some a priori knowledge of these two quantities either by using an atmospheric model based on measurements at ground level or by relying on auxiliary observations along the lidar line of sight (radiosondes, Raman lidar). The error from the uncertainty in the temperature and pressure profiles should be minimized by selecting temperature-insensitive absorption lines.

2.5 DIAL measurement errors

2.5.1 Noise in direct-detection DIAL measurements

2.5.1.1 Shot noise

In direct-detection mode, the incoming photon flux entering the detector surface is converted to an electrical signal current through the generation of charge carriers due to internal and external amplification processes. Due to the discrete nature of the generated electric charges, the process can be described by Poisson statistics and it can be shown that the variance in the generated photocurrent for an incident optical power P can be expressed as:

$$\langle i^2_{\mathbf{shot}} \rangle = 2eM^2F\Delta f \left(\frac{\eta e}{h\nu}\right) P, \tag{2.28}$$

where e is the elementary charge, h is the Planck constant, ν is the frequency of the frequency of the incoming photons, Δf is the detector bandwidth, and η is the quantum efficiency of the detector (the conversion efficiency of photons to electrons). In the case that the detector uses an internal gain mechanism (avalanche photodiodes or photomultipliers), the factor M describes the internal gain of the detector and F is the so-called excess noise factor describing the additional noise due to the internal amplification statistics. The term $\eta e(h\nu)^{-1}$ is the detector responsivity (unit: A/W) that describes the amount of photocurrent generated per unit optical power incident on the dector.

In a lidar setup, shot noise is mostly due to the laser backscatter signal. However, an additional contribution also comes from background radiation such as solar backscatter which passes the optical filter of the receiver. This sky background radiation strongly depends on the position of the sun relative to the telescope axis and other factors such as clouds and aerosol load.

2.5.1.2 Thermal noise

Thermal noise (Johnson-Nyquist noise) is the electronic noise generated by the thermal agitation of the charge carriers affecting all parts of an electric circuit with a resistance regardless of any applied voltage. The noise expressed as variance in the electrical current depends on the temperature T according to:

$$\langle i^2_{\mathbf{th}} \rangle = \frac{4kT}{R}\Delta f, \tag{2.29}$$

where k is the Boltzmann constant, R is the resistance and Δf the bandwidth.

2.5.1.3 Shot noise due to dark current

Dark currents are small electric currents in a photosensitive device which are present even in the absence of incident radiation entering the detector. In detectors based on p-i-n-junctions, such dark current can arise from thermal excitation of charge carriers due to crystal defects or impurities. This process depends critically on temperature, but also on band gap energy and operation voltage. The dark current in a photosensitive device is technically no noise but an offset. However, it gives rise to shot noise even in the absence of an optical power. Dark currents can be reduced by operating the device at low temperatures.

In general, the contribution of the dark-current induced shot noise to the total noise of a detector is taken into account in the noise-equivalent power (NEP) of the device.

2.5.1.4 Noise due to electrical amplification

For many applications, the induced photocurrent is weaker than the thermal noise of the load impedance and thus needs to be amplified before the load. This can be realized using a transimpedance amplifier that amplifies the low-level photodiode current to a usable voltage output. Figure 2.3 shows a simple model of a current-amplifier setup consisting of the photodiode, the transimpedance amplifier with the resistance R_a determining the amplifier gain and the digitizer card with resistance R_c.

The noise in the amplification chain shown schematically in Fig. 2.3 can be broken down into a thermal noise contribution generated by the thermal agitation of charge carriers and a noise due to the electrical amplification process which depends on the input current noise density i_a^2 and the input voltage noise density e_a^2. It can be calculated according to (Ehret et al., 2008):

$$\langle i_{\text{amp}}^2 \rangle = \left(i_a^2 + \frac{e_a^2}{R_a^2} + \frac{4kT}{R_a} + \frac{(2\pi C_p \Delta f)^2}{3} e_a^2 \right) \Delta f, \tag{2.30}$$

where R_a is the amplifier resistance, C_p is the photodiode capacitance and Δf is the bandwidth.

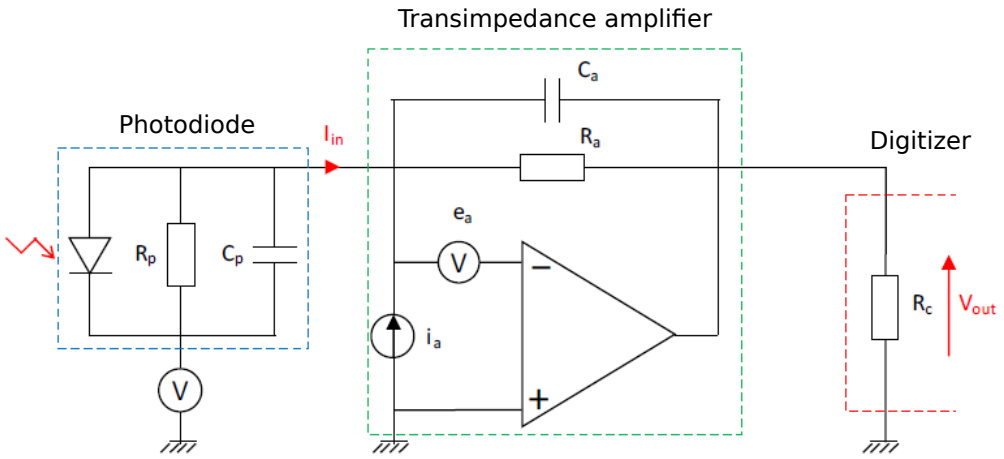

Figure 2.3: Schematic of the analog detection chain based on a transimpedance amplifier. e_a and i_a represent the voltage and current noise spectral densities of the transimpedance amplifier. The amplifier gain is determined by the resistance $R_a = V_{\text{out}}/I_{\text{in}}$. The bandwidth is given by $\Delta f = (2\pi R_a C_a)^{-1}$. Schematic from Cadiou (2017)

2.5.2 Laser speckle

In lidar measurements, variations of the microphysical properties in the backscatter volume or in the reflectivity of a hard target surface lead to spatial fluctuation of irradiance on the detecotor surface. This effect is called speckle and results from the interference of many different reflected portions of the laser beam beam with random relative optical phases. It can be shown that laser speckle exhibit a probability density of the form (Goodman, 1976):

$$p(I) = \frac{1}{\langle I \rangle} \exp\left(-\frac{I}{\langle I \rangle}\right), \tag{2.31}$$

where $\langle I \rangle$ denotes the average intensity.

The influence of speckle on the measured intensity can be estimated by analyzing the number of statistically independent spatial and temporal speckle cells falling on the receiver aperture. In a lidar setup, laser speckle is thus integrated spatially over the the detector surface and temporally over the integration time leading to a reduction in speckle noise.

In direct detection, the electrical current generated by the detector is directly proportional to the incoming optical power. The relative error in the measured power can thus be derived from the relative standard deviation on the detected photoelectron number which can be calculated by (Saleh, 1978):

$$\frac{\sigma(P)}{P} = \sqrt{\frac{1+N/M}{N}}, \tag{2.32}$$

where N is the average number of detected photoelectrons in the range gate and $M = M_s M_t$ is the product of the number of spatial and temporal speckle cells. For a Gaussian beam it can be shown that the number of spatial speckles can be estimated according to (Saleh, 1978) :

$$M_s = \left(1 + \frac{\pi A \theta^2}{4\lambda^2}\right), \tag{2.33}$$

where λ is the laser wavelength, A is the telescope area, and θ is the full beam divergence angle. The number of temporal speckles within a time gate $\Delta t = (2\Delta f)^{-1}$ determined by the detection bandwidth Δf can be calculated from:

$$M_t = \sqrt{1 + \left(\frac{\Delta t}{\tau_c}\right)^2}, \tag{2.34}$$

where τ_c is the coherence length of the laser pulse which is approximately the laser pulse duration in the case of a Fourier-transform-limited laser pulse (single longitudinal mode, no chirp). Note that in the case of an IP-DIAL using a hard target, the number of temporal speckle approaches unity as $\Delta t = 2\delta R/c$ becomes small compared to the coherence length of the laser pulse for small range intervals δR.

For range-resolved lidar measurements using direct detection, the number of speckle cells M is usually quite large. For instance, a 2 µm laser beam with a divergence full angle of 500 mrad and a coherence length of 10 ns combined with a telescope of 10 cm in diameter and 1 MHz detection bandwidth give rise to M in the order of 10^4.

2.5.3 Statistical DIAL measurement error

By applying an error propagation on Eq. 2.18 and assuming that the uncertainties on the emitted energies can be neglected with respect to the errors on the returned power signals, the relative error in the differential optical depth, and consequently in the wanted gas mixing ratio, is given by (Killinger and Menyuk, 1981):

$$\frac{\sigma(\tau)}{\tau} = \frac{1}{2\tau}\sqrt{\frac{\sigma^2(\langle P_{\text{off}}\rangle)}{(\langle P_{\text{off}}\rangle)^2} + \frac{\sigma^2(\langle P_{\text{on}}\rangle)}{(\langle P_{\text{on}}\rangle)^2} - 2\rho(\langle P_{\text{on}}\rangle, \langle P_{\text{off}}\rangle)\frac{\sigma(\langle P_{\text{on}}\rangle)\cdot\sigma(\langle P_{\text{off}}\rangle)}{\langle P_{\text{on}}\rangle\cdot\langle P_{\text{off}}\rangle}}, \tag{2.35}$$

where $\sigma(\langle P\rangle)$ is the standard deviation on the power signal $\langle P\rangle$ accounting for power fluctuations due to the detection noise, speckle noise and atmospheric backscatter variability. $\rho(\langle P_{\text{on}}\rangle, \langle P_{\text{off}}\rangle)$ is the cross-correlation coefficient between the return signals $\langle P_{\text{on}}\rangle$ and $\langle P_{\text{off}}\rangle$ which is defined as follows:

$$\rho(\langle P_{\text{on}}\rangle, \langle P_{\text{off}}\rangle) = \frac{\text{cov}(\langle P_{\text{on}}\rangle, \langle P_{\text{off}}\rangle)}{\sigma(\langle P_{\text{on}}\rangle)\sigma(\langle P_{\text{off}}\rangle)}. \tag{2.36}$$

Equation 2.35 shows that the optical depth error is reduced if the on- and off-line signals are correlated. In practice, the cross-correlation coefficient is quite difficult to estimate. Therefore, it is often chosen to overestimate the optical depth error by setting the covariance term to zero. Equation 2.35 then reduces to:

$$\frac{\sigma(\tau)}{\tau} = \frac{1}{2\tau}\sqrt{\frac{1}{\text{SNR}_{\text{on}}^2} + \frac{1}{\text{SNR}_{\text{off}}^2}}, \tag{2.37}$$

with $\text{SNR}_{\text{on}} = \langle P_{\text{on}}\rangle/\sigma(\langle P_{\text{on}}\rangle)$ and $\text{SNR}_{\text{off}} = \langle P_{\text{off}}\rangle/\sigma(\langle P_{\text{on}}\rangle)$ as the on- and off-line signal-to-noise ratios, respectively.

From the lidar equation (Eq. 2.16) it follows on the one hand that a high optical depth leads to a strong decrease in the measured on-line return power and thus to a drop in its SNR. On the other hand, the relative error expressed in Eq. 2.37 is inversely proportional to the differential optical depth accounting for the method sensitivity. This is the so-called DIAL dilemma: a small differential optical depth leads to low sensitivity in the measurement whereas high optical depth deteriorates the SNR of the on-line signal. It is thus clear that a balance has to be struck by finding an optimum optical depth that minimizes the measurement error. In practice, this is achieved by choosing suitable absorption lines or by tuning the on-line wavelength to the flank of a strong absorption line. Given a fixed total laser energy, optimizing the energy ratio between on- and off-line pulses may also be an option if technically feasible. For a complete mathematical treatment regarding the problematic of finding the optimum optical depth and energy ratio for DIAL measurements the reader is referred to the analysis by Bruneau et al. (2006). It shows that for a direct-detection DIAL (integrated-path DIAL, but range-resolved case is quite similar) that is only limited by shot noise the lowest possible error is achieved for an optical depth of 1.28 and an on-line-to-off-line energy ratio of 3.6. These values decrease if detection noise is also relevant. Fortunately, the optima are relatively broad and errors not exceeding the ideal-case error by a few percent can still be achieved for considerable ranges in optical depth and on-line-to-off-line energy ratio.

2.5.4 Systematic DIAL measurement errors

Systematic errors in the DIAL-retrieved volume mixing ratio occur due to uncertainties in the parameters which are used to calculate the weight function in Eq. 2.26 and due to instrumental and environmental factors directly influencing the optical depth measurement. In the following, only a brief list of systematic error sources is given as some of them are treated in more detail in the sensitivity analysis presented in chapter 3.

Sources of systematic error in DIAL measurements are:

- Uncertainties in the the profiles of pressure and temperature along the lidar path. These meteorological parameters are only known with a certain accuracy. This error can be reduced by selecting absorption lines with low sensitivity to pressure and temperature. The accuracy in the meteorological parameters can be increased by means of auxiliary measurements of pressure and temperature using radiosondes or a temperature Raman lidar.
- Uncertainties in spectroscopic line parameters. Line parameters listed in spectroscopic databases such as HITRAN or GEISA are the result of experimental observations (and theoretical models). Depending on the molecule, wavelength range and quality of the experimental data, each parameter has an uncertainty range. For instance, the line intensity parameter is often known with an accuracy of 1–2%.
- Uncertainty in emitted laser wavelength. The exact knowledge of the emitted laser wavelengths is critical for the calculation of the on- and off-line absorption cross-sections. In the DIAL experiments conducted in the framework of this thesis, the laser wavelength was measured on a shot-to-shot basis with a wavelength-meter. The uncertainty in the measured wavelength depends thus on the accuracy of the wavelength-meter which is essentially determined by the calibration procedure used and the measurement stability over time.
- Finite laser linewidth. Laser emission is never monochromatic but has a certain spectral width. If the laser linewidth is perfectly known, it can be taken into account in the calculation of the absorption cross-sections. Otherwise, the uncertainty of the laser linewidth translates into a systematic error in the retrieved mixing ratio.
- Spectral purity of the emitted laser radiation. The laser spectrum can contain frequencies which are outside of the spectral linewidth range due to, for example, the presence of higher-order longitudinal modes or amplified spontaneous emission depending on the laser.
- Laser beam pointing fluctuations. Variations in the laser beam angle can lead to different overlap functions for the on- and off-line shots. This creates a bias in the measured signals. The effect of beam pointing fluctuations is more pronounced at short ranges where the overlap has not yet reached unity.
- Spectral dependence of the receiver transmission (optical elements, detector sensitivity). This can in principal be characterized experimentally.
- Spectral dependence of atmospheric backscatter and extinction coefficients. This error should be minimized by choosing on- and off-line wavelengths that are spectrally close to each other. This

error is generally lower in the near- and mid-IR region where Mie scattering is predominant which has a weaker wavelength dependence than Rayleigh scattering.

- Temporal variability of the aerosol backscatter and extinction coefficients (and target reflectivity in the case of an IP-DIAL measurement) between two laser shots. Minimization of this error requires minimal on/off-pulse separation time.
- Temporal response of the detector. Parasitic tails in the detector impulse response can lead to biased power measurements (see for example in Dumas et al. (2017)).
- Nonlinearity of the detection chain. For DIAL this can lead to large biases if the on- and off-line pulses have different signal dynamics. The linearity of the detection setup should ideally be characterized experimentally under well controlled conditions.

Chapter 3

Sensitivity study for ground-based DIAL measurements of water vapor isotopologues with respect to instrumental and atmospheric parameters

This chapter presents a numerical sensitivity study and an error budget for ground-based DIAL measurements of the water vapor isotopologues H_2O and HDO. The aim of this analysis is to derive precision estimates of the DIAL-retrieved mixing ratios as a function of instrument-specific and environmental parameters. Because the presence of water vapor and aerosols in the troposphere can vary significantly at different latitudes, atmospheric models representative for polar, mid-latitude and tropical conditions are taken into account. On the instrument side, simulations were carried out for a commercial InGaAs PIN photodiode and a state-of-the-art HgCdTe avalanche photodiode. Additionally, using vertical isotopologue profiles derived from a previous field campaign, precision estimates of the HDO isotopic abundance δD are provided for that specific case.

The content of this chapter was the subject of an article in the peer-reviewed journal *Atmospheric Measurement Techniques* published in October 2021 (Hamperl et al., 2021a).

3.1 Choice of the sensing spectral range

Remote sensing by DIAL relies on the alternate emission of at least two closely spaced laser wavelengths, one coinciding with an absorption line of the molecule of interest (λ_{on}) and the other tuned to the wing of the absorption line (λ_{off}) to retrieve a given species concentration. The key to independently measuring H_2O and HDO abundances with a single instrument lies thus in the proper selection of a spectral region where *(i)* the two molecules display well-separated, significant absorption lines while minimizing the interference from other atmospheric species and *(ii)* the selected lines preserve a relatively equal lidar signal dynamic and relative precision ranges for both isotopologues. This makes the line selection rather limited. Using spectroscopic data from the HITRAN2016 database (Gordon et al., 2017), the possibilities for HDO sound-

ing were investigated up to 4 µm, where robust pulsed nanosecond lasers or optical parametric oscillator sources based on mature lasers or nonlinear crystal components can be developed (Godard, 2007).

Figure 3.1a shows that HDO lines are strong in the 2.7 µm region but overlap with an even more dominant H_2O absorption band. Considering the state of possible commercial photodetector technologies, it was chosen to limit the range of investigation to 2.6 µm, corresponding to the possibilities offered by InGaAs photodiodes. In the telecom wavelength range, which offers both mature laser sources and photodetectors, HDO absorption lines are too weak to be exploited for DIAL measurements over 1–3 km. The same argumentation holds for wavelengths towards 2.05 µm (see Fig. 3.1b) which have been extensively studied for future space-borne CO_2 lidar sensing (Singh et al., 2017b; Ehret et al., 2008). However, the 2 µm region seems to offer an interesting possibility in terms of absorption strength as well as technical feasibility of pulsed, high-energy, single-frequency laser sources (Geng and Jiang, 2014). The spectral window between 1982–1985 nm is well suited to meeting the mentioned requirements as illustrated in Fig. 3.1c.

This thesis focuses on the H_2O absorption line at 5043.0475 cm^{-1} (1982.93 nm) and the HDO lines at 5044.2277 cm^{-1} (1982.47 nm) and 5040.4937 cm^{-1} (1983.93 nm), hereafter referred to as HDO options 1 and 2, respectively, allowing for a sufficiently high absorption over several kilometers with negligible interference from other gas species. Additionally, a second option for H_2O slightly detuned from the absorption peak at 1982.97 nm will be discussed as a possibility for reducing the temperature sensitivity of the DIAL measurement (hereafter referred to as H_2O option 2). Wavelength switching has to be realized on a shot-to-shot basis to consecutively address the chosen on-line wavelengths and the off-line wavelength at 1982.25 nm for H_2O (options 1 and 2) and HDO (1) or the off-line wavelength at 1983.72 nm for HDO (2). As shown in Fig.3.1c, the HDO absorption line at 1982.47 nm is accompanied by a non-negligible H_2O absorption feature which has to be corrected for when retrieving the volume mixing ratio and thus adds a bias dependent on the accuracy of the H_2O measurement at 1982.93 nm. Furthermore, the interfering H_2O line has a ground-state energy of 2756 cm^{-1} (see Table 3.1) which makes it highly temperature sensitive. Probing HDO at 1982.47 nm thus requires highly accurate knowledge of the H_2O profile to limit biased measurements. The alternative second option for HDO at 1983.93 nm avoids any H_2O interference, however with slightly weaker absorption optical depth it gives rise to smaller signal-to-noise ratios and consequently increased random uncertainty.

Table 3.1: Spectroscopic parameters for selected water isotopologue absorption lines

	ν	λ	S	E"	γ_{air}	n_{air}
H_2O (1)	5043.0476	1982.928	$2.17 \cdot 10^{-24}$	920.21	0.0367	0.49
HDO (1)	5044.2277	1982.464	$1.17 \cdot 10^{-24}$	91.33	0.1036	0.71
HDO (2)	5040.4937	1983.933	$9.38 \cdot 10^{-25}$	116.46	0.1003	0.71
H_2O at HDO (1)	5044.2300	1982.463	$2.29 \cdot 10^{-25}$	2756.42	0.0456	0.37

ν (cm^{-1}): wavenumber; λ (nm): vacuum wavelength; S (cm^{-1}(molecule x cm^{-2})$^{-1}$): line intensity at 296 K; E" (cm^{-1}): lower-state energy; γ_{air} (cm^{-1} atm^{-1}): air-broadened Lorentzian half width at half maximum (HWHM) at 1 atm and 296 K; n_{air}: temperature exponent for γ_{air}

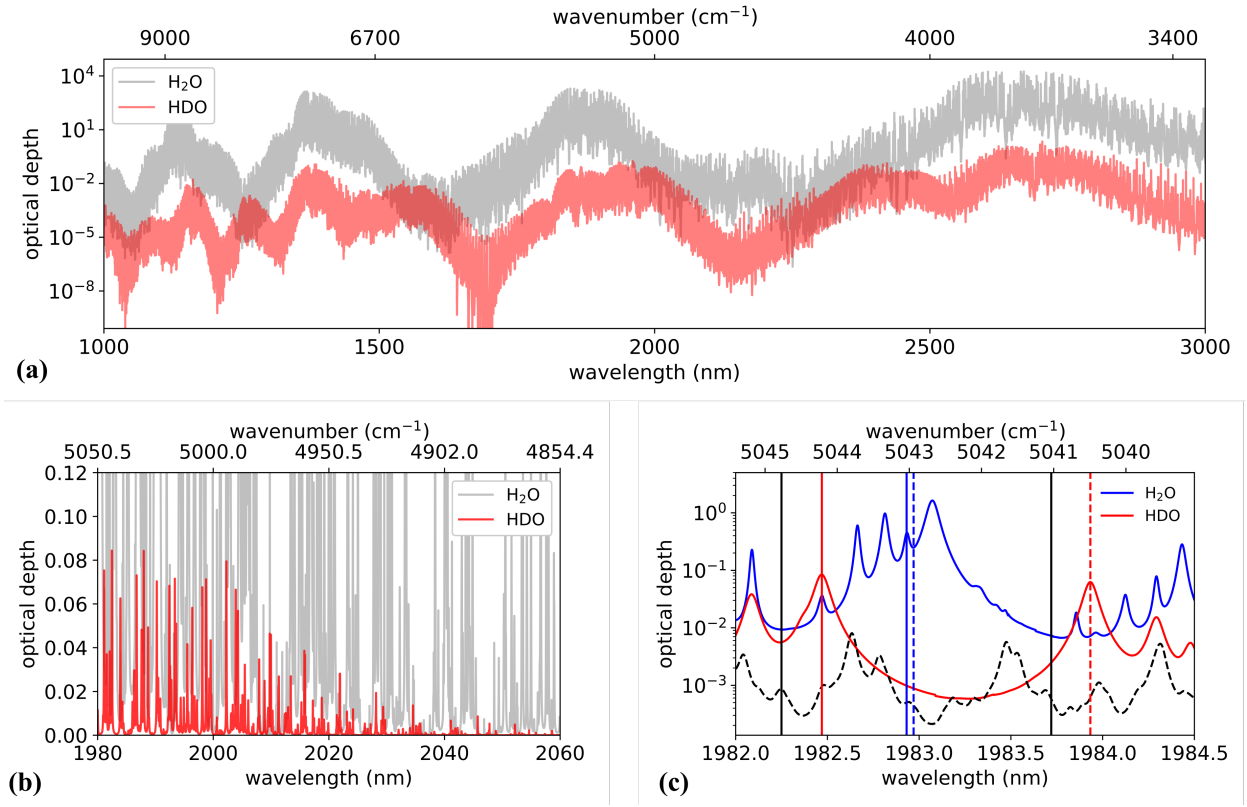

Figure 3.1: Optical depth over 1 km for H_2O and HDO with uniform volume mixing ratios of 8400 ppmv and 2.6 ppmv, respectively (relative humidity of 50% at 15°C). (a) Spectral overview between 1 µm and 3 µm. (b) Close-up window for wavelengths around 2 µm with decreasing HDO absorption towards 2.05 µm. (c) Spectral range of interest for simultaneous H_2O and HDO sounding. The dashed black line represents the total optical depth of other species (CO_2, CH_4, N_2O) with standard atmospheric concentrations. Vertical black lines indicate the positions of possible off-line wavelengths. On-line wavelengths are indicated for H_2O (vertical blue line for option 1 at 1982.93 nm, dashed blue line for option 2 at 1982.97 nm) and HDO (vertical red line for option 1 at 1982.47 nm, dashed red line for option 2 at 1983.93 nm). Spectra calculations are based on the HITRAN2016 database assuming a temperature of 15°C and standard atmospheric pressure of 1013.25 hPa.

3.2 Methodology of the sensitivity analysis

As schematically depicted in Fig. 3.2, the DIAL simulator consists of three sub-models describing atmospheric properties, lidar instrument parameters and detector properties. Each model will be explained in more detail in the following paragraphs. The atmosphere model is based on a set of vertical profiles of temperature, pressure and humidity representative of different climate regions along with aerosol optical depth data of the AERONET database (https://aeronet.gsfc.nasa.gov/, last access: 2 October 2021). Those data are exploited to calculate the atmospheric transmission using absorption cross-sections computed with the HITRAN2016 spectroscopic database (Gordon et al., 2017). Together with the model describing the lidar instrument, the calculated transmission data are used to feed the lidar equation in order to calculate the received power at each selected on-line and off-line wavelength. In a subsequent step, noise contributions arising from the detection unit are taken into account to estimate the signal-to-noise ratio (SNR). From the SNR of the on- and off-line signals, the random error $\sigma(X)$ in the measured isotopologue mixing ratio X is

calculated according to:

$$\sigma(X) = \frac{\Delta f}{\sqrt{2}\mathrm{WF}c}\left(\frac{1}{\mathrm{SNR}_{\mathrm{on}}^2} + \frac{1}{\mathrm{SNR}_{\mathrm{off}}^2}\right)^{1/2}, \tag{3.1}$$

where Δf is the measurement bandwidth, c the speed of light and $WF = n_{\mathrm{air}}(\sigma_{\mathrm{on}} - \sigma_{\mathrm{off}})$ is the weight function accounting for the differential absorption cross-section. Finally, the random error in the HDO abundance δD is obtained from the relative errors of the H_2O and HDO mixing ratio measurements according to:

$$\sigma(\delta D) = (\delta D + 1)\left[\left(\frac{\sigma(X_{\mathrm{H_2O}})}{X_{\mathrm{H_2O}}}\right)^2 + \left(\frac{\sigma(X_{\mathrm{HDO}})}{X_{\mathrm{HDO}}}\right)^2\right]^{1/2}. \tag{3.2}$$

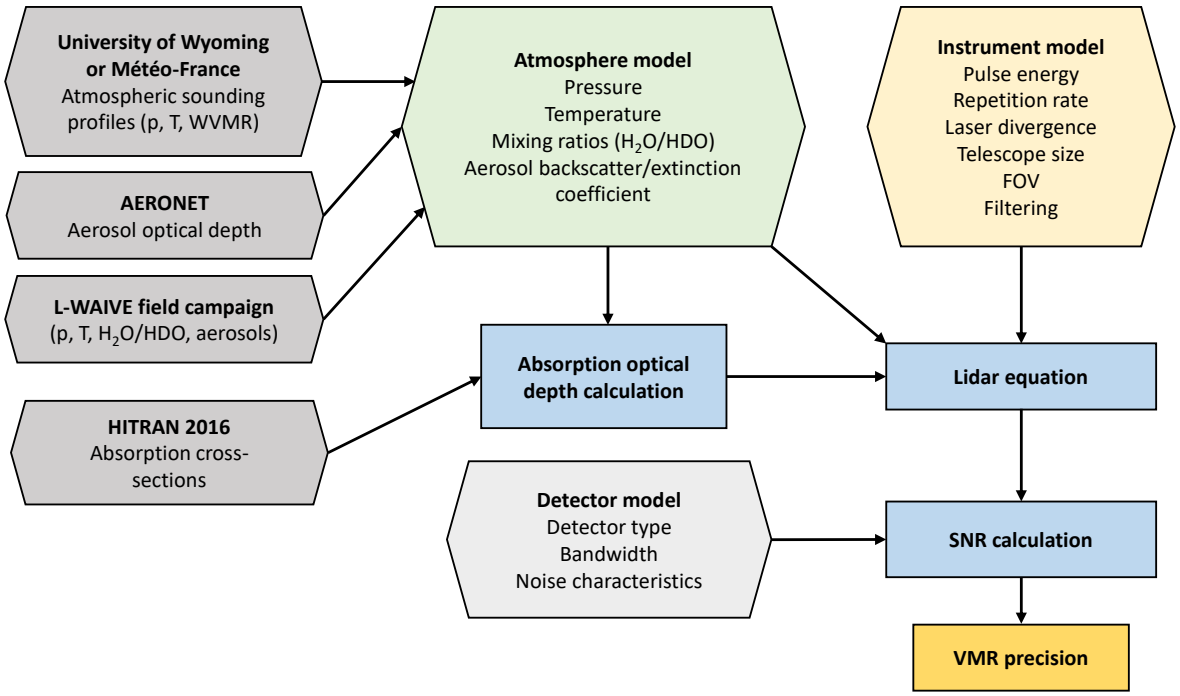

Figure 3.2: Block diagram of the DIAL simulator. Input models and databases are in hexagons, and principal calculations are indicated by rectangles. p: pressure; T: temperature; WVMR: water vapor mixing ratio; FOV: telescope field of view. The signal-to-noise ratio (SNR) is used to calculate the statistical noise error (precision) of the volume mixing ratios (VMR) of H_2O and HDO.

3.2.1 Instrument and detector model

In order to estimate the feasibility of water vapor isotopologue DIAL measurements, calculations were performed for the transmitter and receiver parameters summarized in Table 3.2. Laser energies at 1.98 µm of 20 mJ and 10 mJ are used for the calculations as a baseline case and a more conservative estimation, respectively. The receiver part consists of a Cassegrain-type telescope with a primary mirror of 40 cm in diameter. For the detection part, calculations were performed for a direct-detection setup with a commercial InGaAs PIN photodiode and a HgCdTe avalanche photodiode (APD) specifically developed for DIAL applications in the 2 µm range, which is presented in Gibert et al. (2018a). The telescope field of view is de-

termined by an aperture in the telescope's focal plane. For better comparability, the same aperture diameter of 1.2 mm for both the PIN photodiode and the APD is assumed. Given the small active area of the APD, imaging of the field of view on the detector might, however, prove extremely challenging in practice. The measurement bandwidth of the DIAL system is effectively determined by an electronic low-pass filter in the detection chain. In the simulations, a bandwidth of 1 MHz is used corresponding to a spatial resolution of the retrieved isotopologue concentrations of 150 m. All calculations are based on signal averaging over 10 min (45 000 laser shots for the on- and off-line wavelengths each).

Table 3.2: DIAL instrument parameters used for the sensitivity analysis

Transmitter		**Receiver**		
Energy	10–20 mJ		(i)	(ii)
Pulse duration	10 ns	Telescope aperture	40 cm	40 cm
Repetition rate	150 Hz	Detector type	InGaAs PIN	HgCdTe APD
H_2O on (1)	1982.93 nm	Detector diameter	300 µm	180 µm
H_2O on (2)	1982.97 nm	FOV	630 µrad	630 µrad
HDO on (1)	1982.47 nm	NEP	600 fW $Hz^{-1/2}$	75 fW $Hz^{-1/2}$
HDO on (2)	1983.93 nm	Bandwidth	1 MHz	1 MHz
Divergence	270 µrad		R: 1.2 A W^{-1}	η: 0.8
				F: 1.2

R: Responsivity; η: Quantum efficiency; F: Excess noise factor

In order to quantify the measurement uncertainty in the retrieved isotopologue mixing ratios, random and systematic sources of errors are taken into account. Random errors in measuring the differential optical depth, and thus the species mixing ratio, are related to different noise contributions arising from the detection setups. For a single return-signal pulse, the associated noise power P_n consists of a constant detector and amplifier noise expressed as noise-equivalent power NEP, shot noise due to background radiation P_sky, shot noise dependent on the pulse power $P(\lambda)$ and speckle noise $P_\mathrm{sp}(\lambda)$:

$$P_\mathrm{n} = \sqrt{(\mathrm{NEP}^2 + 2 \cdot e \cdot [P_\mathrm{sky} + P(\lambda)] \cdot F/R) \cdot \Delta f + P_\mathrm{sp}^2(\lambda)}, \tag{3.3}$$

where e is the elementary charge, F the excess noise factor (in the case of the APD), R the detector responsivity (depending on quantum efficiency in the case of the APD) and Δf the measurement bandwidth. The NEP of 600 fW $Hz^{-1/2}$ for configuration (i) featuring the InGaAs PIN photodiode is a conservative estimate by calculations based on the specifications of the photodiode and amplifier utilized in the framework of this thesis (G12182-003K InGaAs PIN photodiode from Hamamatsu combined with a gain-adjustable DHPCA-100 current amplifier from FEMTO). The background power P_sky depends on the background irradiance S_sky and the receiver geometry according to:

$$P_\mathrm{sky} = \frac{\pi}{4} \cdot S_\mathrm{sky} \cdot \Delta\lambda_\mathrm{f} \cdot A_\mathrm{eff} \cdot \theta_\mathrm{FOV}^2, \tag{3.4}$$

where $\Delta\lambda_f$, A_{eff} and θ_{FOV} are the optical filter bandwidth, effective receiver telescope area and field of view angle, respectively. A constant background irradiance of 1 W m^{-2} µm^{-1} sr^{-1} and an optical filter bandwidth of 50 nm are used for all calculations. Assuming Gaussian beam characteristics, the speckle-related noise power is approximately calculated as in Ehret et al. (2008):

$$P_{sp} = P(\lambda) \cdot \frac{\lambda \cdot 2\sqrt{\Delta f \cdot \tau_c}}{\pi \cdot R_{tel} \cdot \theta_{FOV}}, \tag{3.5}$$

where R_{tel} denotes the telescope radius and τ_c the coherence time of the laser pulse corresponding to the pulse duration for a Fourier-transform-limited pulse. Finally, the overall time-averaged signal-to-noise ratio is given as the ratio of received power P_r calculated from the lidar equation (see Eq. 2.16) and the total noise power from Eq. 3.3 multiplied by the square root of the number of laser shots N:

$$\mathrm{SNR} = \frac{P_r}{P_n}\sqrt{N}. \tag{3.6}$$

3.2.2 Atmosphere model

The distribution of water vapor and aerosols in the troposphere can vary significantly at different geographic regions. To study the sensitivity of the DIAL instrument with respect to varying atmospheric conditions, the analysis includes models for mid-latitude, arctic and tropical locations. To build these representative models, three locations were identified for which both radio-sounding data (pressure, temperature and relative humidity) as well as sun-photometer products were available. Table 3.3 gives an overview of the chosen locations and origins of the data sets used. For each location, a baseline model was constructed by using the columns of pressure, temperature and volume mixing ratios averaged over the year of 2019. To account for seasonal variations in the sensitivity analysis, profiles with the lowest and highest monthly averages of temperature and humidity are used (Figs. 3.3a–c). For the sake of simplicity, HDO mixing ratios were obtained from water vapor profiles simply by considering their standard abundance value of $3.11 \cdot 10^{-4}$; i.e., variability in terms of the isotopic ratio δD is not included in the model.

Table 3.3: Overview of atmospheric sounding and AERONET sites used to derive an atmosphere model for the sensitivity analysis. For all sites data from 2019 were used.

	Radio sounding profiles	**AERONET**
	Pressure, temperature, humidity	Level 2.0 aerosol optical depth
Mid-latitude location	Trappes	Palaiseau
Paris region, France	48.77° N, 2.01° E	48.71° N, 2.22° E
	Météo-France data	
Arctic location	Ittoqqortoormiit	Ittoqqortoormiit
Greenland, Denmark	70.49° N, 21.95° W	70.49° N, 21.95° W
	University of Wyoming data	February–September 2019
Tropical location	Réunion (Gillot)	Réunion (Saint-Denis)
Réunion, France	20.89° S, 55.51° E	20.90° S, 55.49° E
	Météo-France data	

To complement the atmospheric model, data of level 2.0 aerosol optical depth (AOD) from AERONET (https://aeronet.gsfc.nasa.gov/, last access: 2 October 2021) were used. AERONET sun-photometer products are usually available for wavelengths between 340 and 1640 nm. For extrapolation to the 2 µm spectral region, the wavelength dependence of the AOD described by a power law (Ångström, 1929) is used:

$$\frac{\mathrm{AOD}(\lambda)}{\mathrm{AOD}(\lambda_0)} = \left(\frac{\lambda}{\lambda_0}\right)^{-\alpha}, \tag{3.7}$$

where $\mathrm{AOD}(\lambda)$ is the optical depth at wavelength λ, $\mathrm{AOD}(\lambda_0)$ is the optical depth at a reference wavelength and α represents the Ångström exponent. The Ångström exponent was obtained by fitting Eq. 5.1 to the available AOD data in the above-mentioned spectral range in order to extrapolate further to 1.98 µm. Histograms of the yearly distribution of the extrapolated AOD at 1.98 µm are shown in the panels (g)–(i) of Fig. 3.3. Median values of the AOD are used for the baseline model. The lowest (AOD_{10}) and highest (AOD_{90}) decile values serve as input for the sensitivity analysis to model conditions of low and high aerosol charge, respectively. As a next step, vertical profiles of aerosol extinction are constructed by making basic assumptions about their shape and constraining their values by the extrapolated AOD.

In the baseline model, the vertical distribution of aerosols is represented by an altitude-dependent Gaussian profile of the extinction coefficient with varying half-width depending on the location (Fig. 3.3 d–f). This type of profile roughly corresponds to the ESA Aerosol Reference Model of the Atmosphere (ARMA) (European Space Agency, 1999) which is plotted for each region normalized to the (AOD_{90})-derived extinction profile maximum. However, the distribution of tropospheric aerosols varies widely from region to region (Winker et al., 2013). To broadly reflect the different boundary layer characteristics for each environment, the extinction profile was adapted accordingly.

In mid-latitude regions, vertical aerosol distributions vary widely due to regional and seasonal factors (Chazette and Royer, 2017). The planetary boundary layer (PBL) height can range from a few hundred meters up to 3 km (Matthias et al., 2004). Assuming that aerosols are mostly confined to the PBL and that the free tropospheric contribution to aerosol extinction is weak, the half-Gaussian-shaped baseline model used for the simulations gives rise to 85% of AOD within the first 1.5 km. Since high aerosol loads in the free troposphere due to long-range dust transport are not uncommon over western Europe (Ansmann et al., 2003), a dust scenario profile constrained by the highest-decile AOD was also investigated. Dust aerosols are represented by a Gaussian profile above the PBL extending well up to a height of 5 km. For this case, aerosol extinction in the PBL below 1.5 km accounts for half of the total AOD, while dust in the free troposphere accounts for the other half.

At high latitudes, the boundary layer tends to be stable and extends from a few meters to a few hundred meters above ground. The baseline Arctic extinction profile thus contains 95% of the AOD within the first 1.5 km since most aerosols are confined within the first kilometer of the troposphere as observed by space-borne lidar during long-term studies of the global aerosol distribution (Di Pierro et al., 2013). The occurrence histogram in Fig. 3.3h shows very low values of AOD for most of the time in the available photometer products from February to September. The long-tailed wing of the asymmetric distribution towards higher values can be explained by seasonally occurring episodes of arctic haze due to anthropogenic aerosols transported from mid-latitude regions (winter to spring) and boreal forest fire smoke during the summer season (Tomasi et al., 2015; Chazette et al., 2018). Similarly to the dust scenario for the mid-

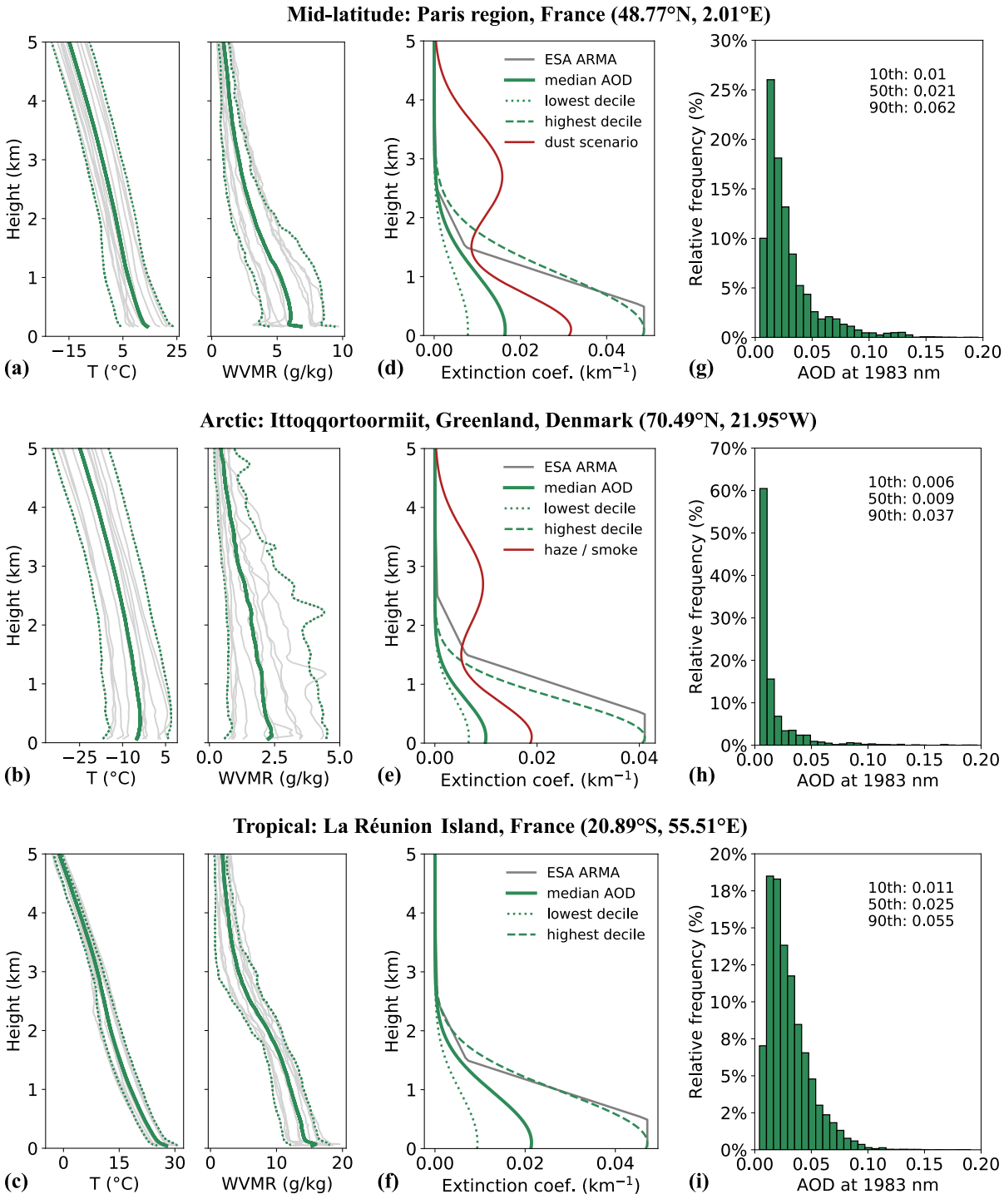

Figure 3.3: Atmosphere models: (a–c) vertical sounding profiles of temperature and the water vapor mixing ratio (WVMR). Grey lines indicate monthly averages; solid green line is the yearly average of 2019 (baseline profile). Dotted lines indicate profiles of the lowest and highest monthly temperatures and WVMR; (d–f) model profiles of aerosol extinction coefficient; (g–i) distribution of the aerosol optical depth at 1983 nm for AERONET level 2.0 data of 2019.

latitude model, these haze and smoke events are modeled by an additional Gaussian profile in the free troposphere constrained by the highest-decile AOD.

Extinction profiles representing the tropical environment of the island of Réunion, where sea salt aerosols can be assumed to be the dominant aerosol species, are chosen such that 90% of the AOD is attributed to the first 1.5 km.

Vertical profiles of the aerosol backscatter coefficient were calculated assuming, for the sake of simplicity, a constant extinction-to-backscatter ratio (lidar ratio) of 50 sr throughout all sets of extinction profiles.

3.3 Simulation results and discussion

This section discusses the expected instrument performance for the atmospheric models presented in the previous section in terms of random errors and systematic errors. Different noise sources contributing to the signal-to-noise ratio are presented and compared with respect to the detector used in the simulation. For each environment, the precision in the HDO abundance δD is calculated for different levels of humidity and varying aerosol loads. The analysis of systematic errors includes uncertainties in atmospheric, spectroscopic and instrumental parameters used for the derivation of the isotopologue mixing ratio profiles.

3.3.1 Instrument random error

The random error of the isotopologue mixing ratio measurement was investigated depending on instrument parameters such as laser pulse energy and the type of detector employed. For this case, all calculations are based on the mid-latitude baseline atmosphere model (yearly average profiles of temperature and WVMR, median AOD) assuming vertical sounding of the lower troposphere with aerosols confined to the lowest 2 km. Considering a simple calculation of random errors, the implications for the precision of the measurement of range-resolved δD profiles are discussed.

Figure 3.4 shows the individual noise contributions for a single on-line pulse (20 mJ pulse energy) for both detector configurations. As expected, the electronic noise level is significantly reduced by roughly an order of magnitude for the HgCdTe APD combined with a transimpedance amplifier due to a low combined NEP of 75 fW Hz$^{-1/2}$ compared to 600 fW Hz$^{-1/2}$ for the amplifier of the InGaAs PIN detector. In fact, shot noise and speckle are predominant for the APD for the first kilometer of range, whereas the electronic noise of the transimpedance amplifier is the predominant contribution over the entire range for the commercial PIN detector. Due to the lower NEP of the APD, the signal-to-noise ratio (SNR) is slightly higher at low ranges compared to the InGaAs PIN photodiode and decreases more slowly at long ranges where the shot-noise and speckle-contributions become insignificant.

The expected relative random errors in the mixing ratios of H_2O and HDO are shown separately for each detector in the upper and lower panels of Fig. 3.5. Two scenarios with different laser pulse energies of 10 and 20 mJ are compared. All calculations are based on a measurement bandwidth of 1 MHz (150 m range cell resolution), and signal averaging over 10 min for a repetition rate (on–off rate) of 150 Hz. The simulation based on the 20 mJ configuration gives an estimation of the best-case precision limit of the DIAL system. The second configuration with 10 mJ pulse energy can be understood as a lower limit on the precision of measuring mixing ratios of H_2O and HDO and finally the isotopic ratio.

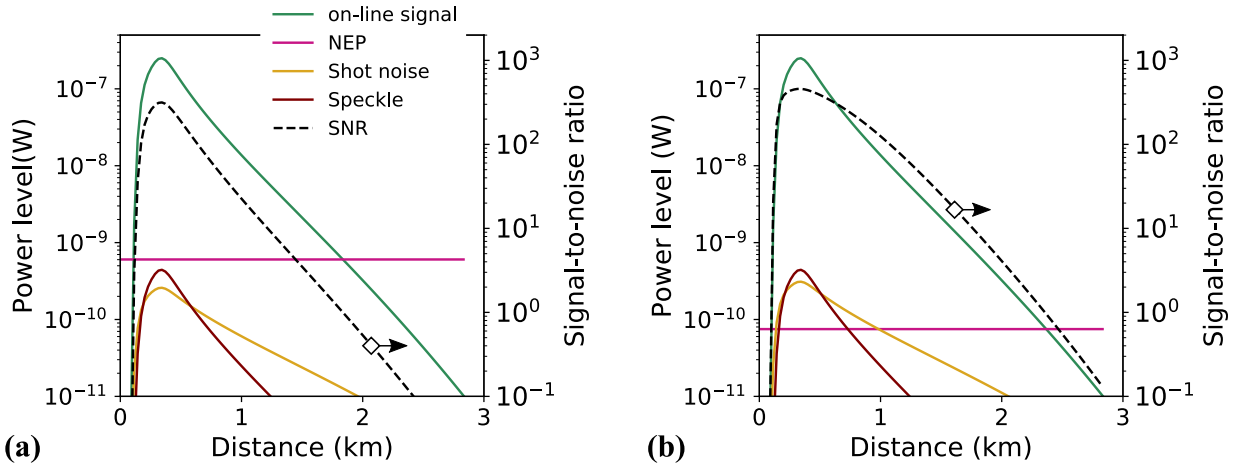

Figure 3.4: Received power according to the lidar equation (Eq. 2.16) (solid green line) and power-equivalent levels of major noise contributions related to the H_2O on-line signal for a single 20 mJ pulse and resulting signal-to-noise ratio (SNR, dashed black line, right vertical axis) as function of lidar range: (a) InGaAs PIN detector, (b) low-noise HgCdTe APD.

As shown in Figure 3.5, a relative random error of well under 1% in the mixing ratio of both isotopologues can be achieved within the first kilometer for both detectors and 20 mJ pulse energy. The degraded precision for measuring HDO is due to its lower differential absorption. The slight difference in optical depth for the two HDO options leads only to a small loss in precision for wavelength option 2. For the low-noise APD shown in the bottom panel of Fig. 3.5, the simulations show that even for the conservative assumption of 10 mJ pulse energy, the relative error stays below 1% for both isotopologues over a range of 1.5 km corresponding to typical heights of the planetary boundary layer. H_2O uncertainties were calculated for sounding at the peak of the absorption line (option 1). The simulation results also reveal a sharp rise in the random uncertainty towards longer distances which is attributed to the drastic decline in aerosol backscattering in the free troposphere assumed in the underlying model. The sharp fall of the random error within the first 200–300 m is due to the increasing overlap between the laser beam and telescope field of view imaged onto the detector described by the overlap function $O(r)$ in Eq. 2.16. This overlap term is zero directly in front of the lidar instrument and reaches unity after around 450 m for the here-described telescope configuration. It should be noted that for the range zone of non-uniform overlap, slight differences between the on- and off-line overlap, for example due to laser beam pointing, can induce significant systematic errors. From a practical point of view, the expected lowest instrument range is thus closer to 0.5 km than the distance suggested by the location of the random error minima around 250 m.

Since the main interest of the here evaluated DIAL system is the derivation of a vertical profile of the isotopic ratio from the H_2O and HDO measurements, panels (c) and (f) of Fig. 3.5 show the expected precision of that ratio expressed as δD which depends on the relative random errors in the volume mixing ratios for H_2O and HDO (see Eq. 3.2). For the commercial InGaAs PIN photodiode it is found for the most favorable configuration (20 mJ pulse energy) that the absolute uncertainty in δD is below 5‰ within a range of 1 km and close to 30‰ at 1.5 km. The 10 mJ configuration allows for measurement of δD with an absolute precision of up to 10‰ within the first kilometer. For greater ranges, precision levels decline rapidly and are not sufficient to resolve naturally occurring variations in δD on the order of a few tens of per

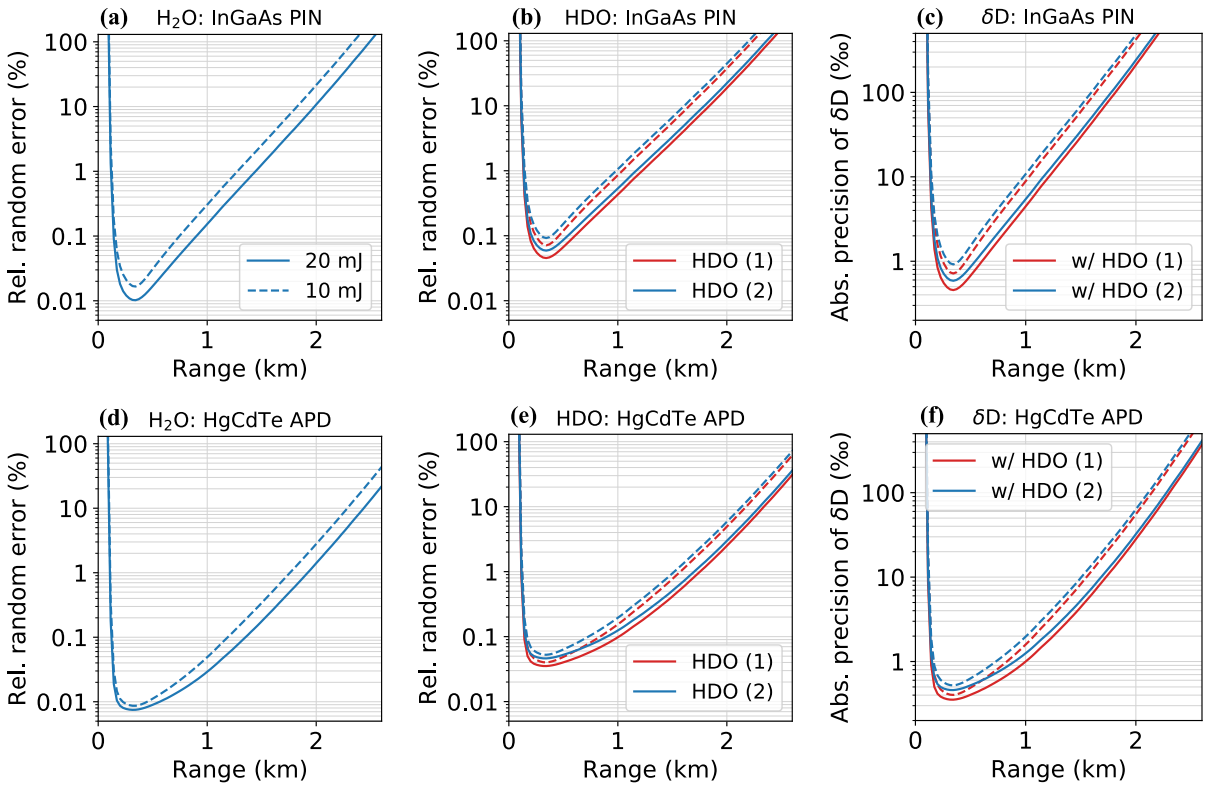

Figure 3.5: Expected relative random error in the volume mixing ratio of H_2O and HDO for different pulse energies (solid lines: 20 mJ; dashed lines: 10 mJ) and detectors: (a,b) InGaAs PIN detector, (d,e) HgCdTe APD. (c, f) Corresponding absolute uncertainty (standard deviation) in δD as a function of range

mil. The use of a HgCdTe APD detector can overcome this limitation for which the calculations indicate that an absolute precision better than 10‰ within a range of 1.5 km can be achievable.

3.3.2 Sensitivity to atmospheric variability

The sensitivity of the DIAL measurement to the variability of humidity and aerosol load was investigated for the mid-latitude, arctic and tropical atmosphere models. In the following analysis, the relative random error (precision) is used to compare the influence of each atmospheric parameter under investigation. All simulations were conducted assuming a measurement of H_2O at 1982.93 nm (option 1) and of HDO at 1983.93 nm (option 2), a measurement bandwidth of 1 MHz (150 m range cell resolution) and signal averaging over 10 min for a repetition rate of 150 Hz (45 000 shots per DIAL wavelength). All calculations were performed with the InGaAs PIN detector and assuming a laser pulse energy of 20 mJ.

In Figure 3.6, the three baseline models of mid-latitude, tropical and arctic environments are compared with respect to relative random error in the H_2O mixing ratio (Fig. 3.6a) and absolute precision in δD (Fig. 3.6b). For the mid-latitude atmospheric model, DIAL measurements of water vapor are expected to deliver mixing ratios with relative precision better than 0.2% in the first kilometer of atmosphere growing to ca. 10% at 2 km above the ground at the boundary layer top. Taking also the HDO random error into account, the absolute precision in δD is better than 5‰ in the lower boundary layer (< 1 km), but reaches values close to 100‰ between 1.5 and 2 km which is in the order of the naturally occurring values of δD

in the mid-latitudes. Under tropic conditions, the precision in the H_2O mixing ratio deteriorates faster with increasing height due strong absorption of the on-line signal. Under very humid conditions, it is thus worth considering to tune the on-line wavelength slightly away from the absorption peak. With respect to HDO, a high content of water vapor is beneficial for DIAL soundings as it increases the measurement sensitivity which is reflected in the increased precision in δD compared to the mid-latitude model.

The random error for the arctic environment is almost one order of magnitude higher due to rather dry conditions in terms of water vapor content and low aerosol content observed at the eastern Greenland AERONET station of Ittoqqortoormiit used to construct the arctic model. The expected precision in δD is better than 30‰ in the lowest first kilometer of atmosphere.

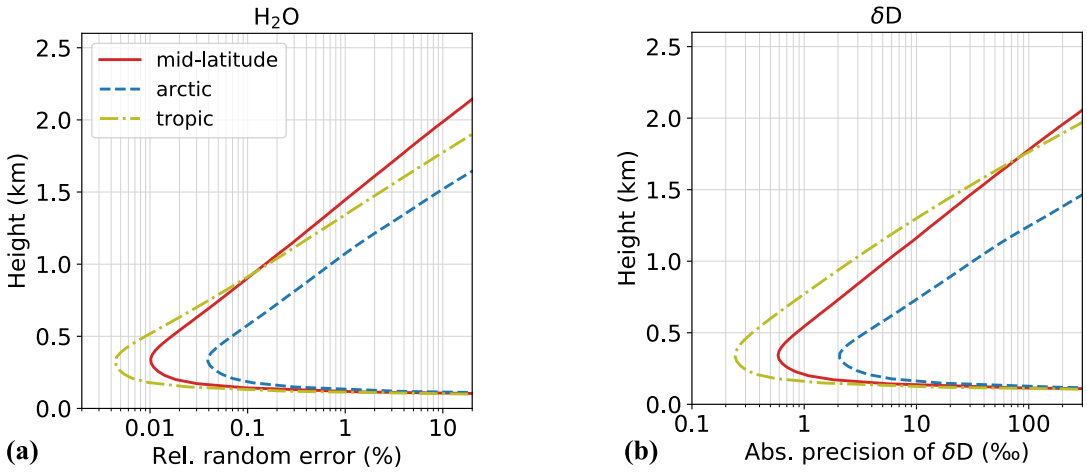

Figure 3.6: (a) Relative random error for H_2O and (b) absolute random error for δD with respect to different atmospheric models (yearly average temperature and WVMR profile, median AOD). Instrument parameters: 20 mJ pulse energy, 1 MHz bandwidth (150 m range resolution), 45 000 shots per wavelength, InGaAs PIN detector.

Figure 3.7 shows the calculated precision in δD with respect to variations in humidity for each atmospheric model. Differences in the precision for the mid-latitude model are due to humidity variations throughout the seasons characterized by higher water vapor content in the summer (ca. 6–10 g/kg at ground level) and rather dry conditions during winter (ca. 3–5 g/kg). A high sensitivity to seasonal variability in the humidity profile was also observed for the arctic model where the water vapor mixing ratio can be as low as 0.1 g/kg during winter and close to 5 g/kg during summer. For the tropical environment, the water vapor content is generally high throughout the year and variations are smaller in relative terms (ca. 12–20 g/kg at ground level) and thus only slightly affect the expected measurement precision.

In Fig. 3.8, the simulations clearly show the influence of the aerosol distribution and its backscatter coefficient on the expected precision of the DIAL-measured HDO abundance. For all three locations, the precision gain between the low-charge (lowest-decile AOD) and high-charge (highest-decile AOD) aerosol model is roughly one order of magnitude. The presence of aerosols in the free troposphere, for example due to long-range dust transport in the mid-latitudes and arctic haze or boreal forest fire smoke in the Arctic, leads to significant improvements in the precision at altitudes beyond the atmospheric boundary layer. Under such conditions, DIAL measurements of δD at the interface between the boundary layer and the free troposphere would be possible with a precision of a few tens of per mil.

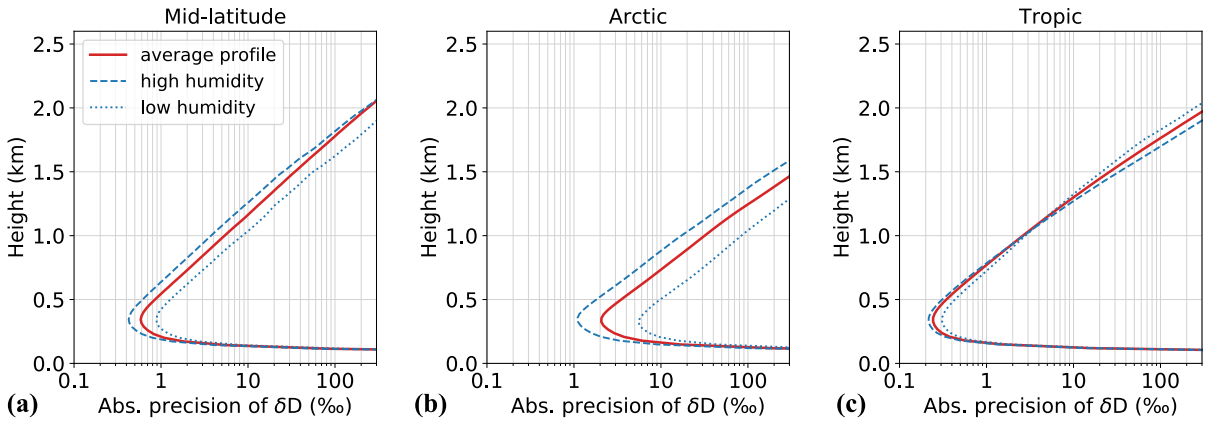

Figure 3.7: Absolute random error in δD with respect to humidity for the (a) mid-latitude, (b) arctic and (c) tropic atmospheric model. Instrument parameters: 20 mJ pulse energy, 1 MHz bandwidth (150 m range resolution), 45 000 shots per wavelength, InGaAs PIN detector.

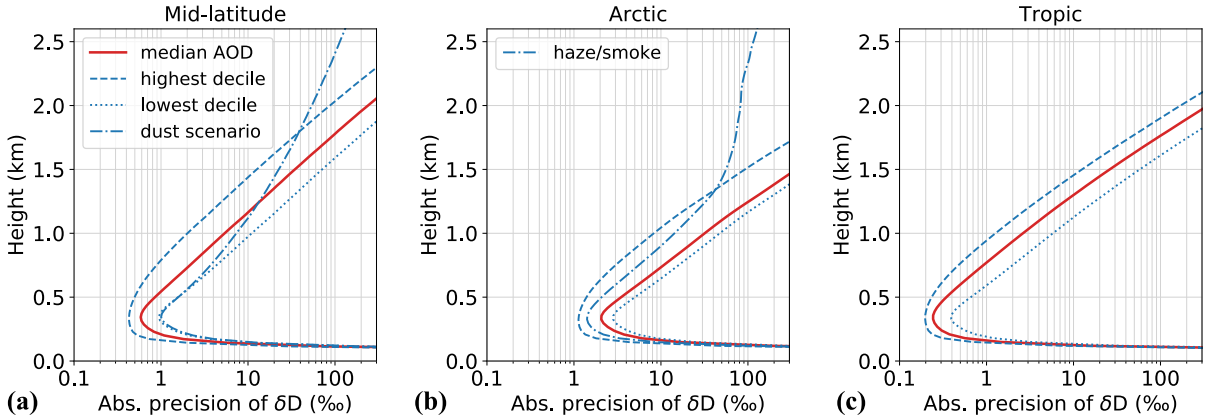

Figure 3.8: Absolute random error in δD with respect to aerosol load for the (a) mid-latitude, (b) arctic and (c) tropic atmospheric model. Aerosol loads include the median, highest and lowest aerosol optical depths (AOD) and a scenario of elevated dust for the mid-latitude model and haze/smoke for the arctic model. Instrument parameters: 20 mJ pulse energy, 1 MHz bandwidth (150 m range resolution), 45 000 shots per wavelength, InGaAs PIN detector.

3.3.3 Systematic errors

Systematic errors arise from uncertainties in the knowledge of atmospheric, instrumental and spectroscopic parameters to compute the weight function WF used in the derivation of the volume mixing ratio from the measured differential optical depth (see Eq. 2.26). Additionally, a DIAL measurement of HDO at 1982.47 nm requires a correction of the H_2O absorption which thus presents another source of error. In the following, systematic errors are evaluated for each category and a final error budget for the isotopic abundance δD is presented.

3.3.3.1 Error due to temperature and pressure

The sensitivity of the weight function WF to the uncertainty in the temperature profile is estimated by generating a random set of numbers δT that follow a normal distribution with a mean of zero and a standard

deviation ΔT representing the assumed temperature uncertainty. This random seeding is used to calculate $WF(T+\delta T)$ for each δT and the relative temperature error ε_T in WF, and thus in the retrieved mixing ratio, is evaluated from the mean of the perturbed weight function $\overline{WF}(T+\delta T)$ according to:

$$\varepsilon_T = \max\left(\frac{|WF(T)-\overline{WF}(T+\delta T)|}{WF(T)}\right). \tag{3.8}$$

The systematic error due to temperature is calculated for uncertainties in the temperature profile ΔT ranging from ± 0.5 K to ± 4 K. The lower end of this range can be obtained by auxiliary in situ sensors or an additional lidar instrument for temperature profiling. The upper end of the uncertainty range corresponds to the situation where a temperature measurement is only available on the ground and a vertical model profile is used. Figure 3.9a depicts the calculated temperature errors for the mid-latitude atmospheric model and a maximum range up to 2 km. Due to the higher temperature sensitivity of the H_2O absorption line, sounding H_2O at the absorption peak is especially sensitive to temperature uncertainties. A measurement with the on-line wavelength shifted off the absorption peak (H_2O option 2) significantly reduces the error.

Similarly, the sensitivity to uncertainties in the pressure profile Δp ranging from ± 0.5 hPa to ± 8 hPa are calculated according to:

$$\varepsilon_p = \max\left(\frac{|WF(p)-\overline{WF}(p+\delta p)|}{WF(p)}\right). \tag{3.9}$$

In this case, H_2O wavelength option 2 is more sensitive to such an uncertainty as shown in Fig. 3.9b. The resulting error in the measurement of HDO is found to be negligible. Note the difference between the two options for probing H_2O. Shifting the on-line wavelength off the absorption peak (option 2) results in a noticeable reduction in the temperature error. However, this comes at the expense of increased pressure error and a lower signal-to-noise ratio and thus increased random error for unchanged laser energy, averaging time and bandwidth. Considering the mentioned systematic error contributions, option 2 for H_2O proves to be the preferred wavelength choice with the intention of reducing the systematic error, especially if the temperature profile along the line of sight is not known with an accuracy better than ± 0.5 K.

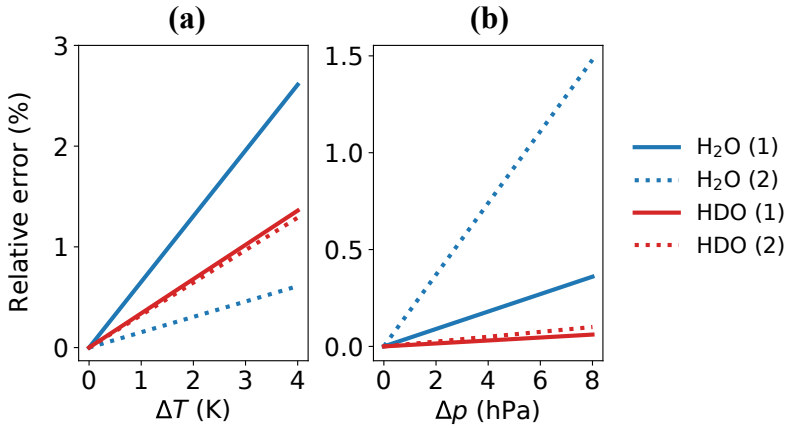

Figure 3.9: Maximal relative error in the H_2O and HDO mixing ratios (over 2 km range, mid-latitude baseline) due to uncertainties in the profiles of (a) temperature and (b) atmospheric pressure. The parenthetical numbers (1) and (2) denote the two potential on-line wavelength options.

3.3.3.2 Error due to laser wavelength and linewidth

The systematic error related to the laser wavelength accuracy is estimated by introducing a random seeding to the on-line and off-line wavelengths. From the sensitivity of the weight function to wavelength uncertainties $\delta\lambda$ the relative error is calculated according to:

$$\varepsilon_\lambda = \max\left(\frac{|WF(\lambda_{\text{on/off}}) - \overline{WF}(\lambda_{\text{on/off}} + \delta\lambda)|}{WF(\lambda)}\right). \tag{3.10}$$

Figure 3.10a shows the relative error for laser wavelength deviations $\Delta\lambda$ up to 120 MHz (1.5 pm). Due to the narrower absorption line of H_2O at 1982.93 nm, a wavelength detuning results in a larger error compared to the spectrally larger HDO line. Option 2 for H_2O reduces the wavelength error.

The systematic error due to the finite laser linewidth is estimated numerically by substituting the absorption cross-sections σ by the effective absorption cross-sections defined as:

$$\sigma_{\text{eff}} = \frac{\int L(\nu, r) \cdot \sigma(\nu, r) \cdot d\nu}{\int L(\nu, r) \cdot d\nu} \tag{3.11}$$

where L represents the spectral intensity distribution of the laser transmitter and ν denotes the wavenumber. The laser spectral distribution L is assumed to be an altitude-independent Gaussian function with full width at half maximum values up to 200 MHz. Note that a value of 50 MHz corresponds roughly to the 10 ns pulse duration assuming transform-limited pulses. For comparison, the air-broadened Lorentzian widths of the absorption lines under standard atmospheric conditions are in the order of a few gigahertz. The systematic error due to linewidth is calculated according to:

$$\varepsilon_{\text{LW}} = \max\left(\frac{|\sigma(\lambda_{\text{on}}) - \sigma_{\text{eff}}(\lambda_{\text{on}})|}{\sigma(\lambda_{\text{on}})}\right). \tag{3.12}$$

Figure 3.10b shows the calculated errors for both H_2O and HDO wavelength options. The calculated relative error is in the order of 0.1% for the narrowest (thus most critical) H_2O line at 1982.93 nm and practically negligible for HDO assuming a laser linewidth of 50 MHz.

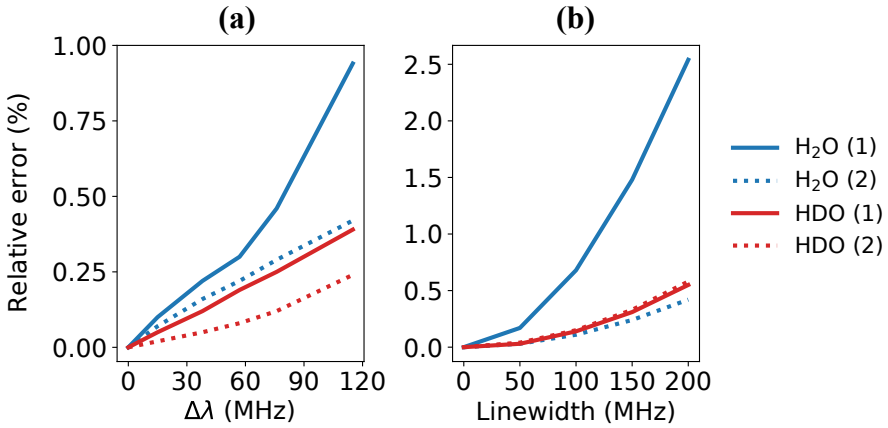

Figure 3.10: Maximal relative error in the H_2O and HDO mixing ratios (over 2 km range, mid-latitude baseline) due to (a) uncertainties in the on- and off-line wavelength and (b) due to finite linewidth. The parenthetical numbers (1) and (2) denote the two potential on-line wavelength options.

3.3.3.3 Error due to spectroscopic line parameters

Systematic errors due to uncertainties in spectroscopic parameters are analyzed by introducing normally distributed deviations δY with mean zero and standard deviation ΔY to the weight function and calculating its sensitivity according:

$$\varepsilon_Y = \max\left(\frac{|WF(Y) - \overline{WF}(Y+\delta Y)|}{WF(Y)}\right), \tag{3.13}$$

where Y is representative of the HITRAN parameters of line intensity S, air-broadened width γ_{air}, temperature coefficient of the air-broadened width n_{air} and the pressure shift parameter δ_{air}. Figure 3.11 shows the resulting errors for each line parameter. In the HITRAN database, the uncertainty of the line intensity is stated as 2% for both isotopologues giving rise to a relative error of 1.6%. As shown in Fig.3.11b, the HDO measurement is more sensitive to an uncertainty in the air-broadened-width parameter. Values stated in the error code of the HITRAN line list are 2% for H_2O and 10% for HDO giving rise to relative errors of 0.5% and close to 9%, respectively. The uncertainty in the air-broadened-width parameter is thus a major contribution to the error budget for HDO. Uncertainties in the remaining parameters of n_{air} and δ_{air} are typically in the range of 10–20%, but result in only minor error contributions as shown in panels (c) and (d) of Fig. 3.11.

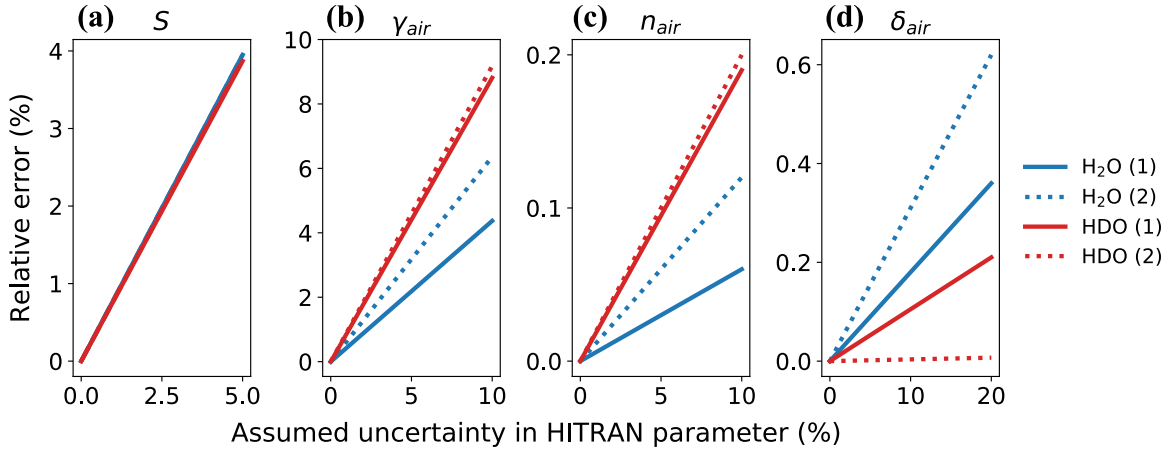

Figure 3.11: Maximal relative error in the VMR retrieval (over 2 km range, mid-latitude baseline) due to uncertainties in HITRAN parameters. S : line intensity; γ_{air}: air-broadened half width; n_{air}: coefficient of the temperature dependence of γ_{air}; δ_{air}: pressure shift. The parenthetical numbers (1) and (2) denote the two potential on-line wavelength options.

Uncertainties in the line intensity and air-broadened width parameters largely contribute to the error budget, highlighting the importance of having accurate knowledge of these quantities. Improvements are expected through ongoing spectroscopic studies which are carried out by the GSMA laboratory of Reims in the framework of the WaVIL project (Régalia et al., 2021).

3.3.3.4 HDO error due to H_2O interference

Another systematic error arises for sounding HDO at 1982.47 nm (option 1) from the uncertainty in the optical depth due to the non-negligible H_2O absorption feature. The DIAL-measured differential optical

depth $\Delta\tau$ must be corrected for the H_2O contribution $\Delta\tau_{H2O}$ according to $\Delta\tau_c = \Delta\tau - \Delta\tau_{H2O}$. The relative error is estimated by introducing a normally distributed set of deviations δX_{H2O} to the profile of the H_2O mixing ratio X_{H2O} used to calculate $\Delta\tau_{H2O}$ and by evaluating the mean of the perturbed corrected differential optical depth $\overline{\Delta\tau_c}(X_{H2O} + \delta X_{H2O})$:

$$\varepsilon_{H2O} = \max\left(\frac{|\Delta\tau_c(X_{H2O}) - \overline{\Delta\tau_c}(X_{H2O} + \delta X_{H2O})|}{\Delta\tau_c(X_{H2O})}\right). \tag{3.14}$$

Figure 3.12 depicts the resulting relative error in the HDO mixing ratio as a function of the uncertainty in the H_2O mixing ratio profile used for the calculation of $\Delta\tau_c$. This type of error varies with the atmospheric water vapor content and thus differs widely between arctic and tropic environment, the latter giving rise to the highest systematic error.

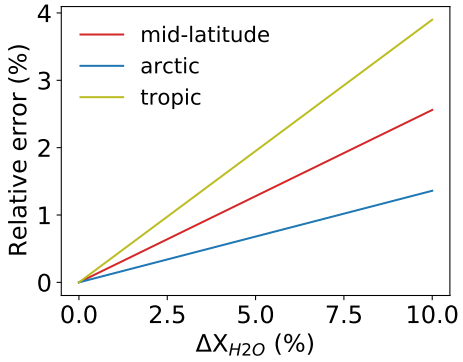

Figure 3.12: Maximal relative error in the DIAL-retrieved HDO volume mixing ratio as a function of the uncertainty in the H_2O mixing ratio profile used to correct the measured differential optical depth at HDO wavelength option 1 (over 2 km range). Baseline profiles of mid-latitude, arctic and tropic models were used.

3.3.3.5 Budget of systematic errors and implications for δD

Table 3.4 provides a summary of systematic errors for the measurements of H_2O and HDO and the resulting errors in the isotopic abundance δD. For the sake of simplicity, only wavelength options 1 are shown for both H_2O and HDO and the calculated errors are representative of mid-latitude conditions. Main sources of systemic error arise from uncertainties in the temperature profile used to calculate the altitude-dependent weight function. For instance, a temperature uncertainty of ± 2 K gives rise to an absolute error in δD of 15‰. This is mainly due to the temperature sensitivity of the H_2O absorption line and can be reduced by shifting the on-line wavelength away from the line center as discussed previously. Systematic errors due to wavelength accuracy and laser linewidth are in the order of a few per mil and thus relatively small if the laser wavelengths are well known through proper calibration. The main contributions to the error budget arise from uncertainties in spectroscopic parameters. An assumed uncertainty in the line intensity parameter leads to an absolute error in δD of 22‰. The largest systematic error for the HDO measurement, and thus δD, is due to the uncertainty in the air-broadened with parameter which is stated with a relative uncertainty of 10% in the HITRAN2020 line list. This results in an absolute error in δD of nearly 90‰ which is in the order of the natural variability of δD in the lower troposphere under mid-latitude conditions. This clearly shows the importance for additional spectroscopic studies in order to reduce these uncertainties.

Table 3.4: Budget of systematic errors for DIAL measurements of H_2O and HDO (wavelength options 1) up to a height of 2 km under mid-latitude baseline model. (*) marks uncertainties with no estimates in HITRAN for which case an assumed value is used.

Error source	**H_2O (1)**		**HDO (1)**		**δD**
	Uncertainty	Rel. error	Uncertainty	Rel. error	Abs. error
Atmosphere					
Temperature	±2 K	1.4%	±2 K	0.7%	15‰
Pressure	±5h Pa	0.2%	±5h Pa	negligible	2‰
H_2O bias	-	-	±5%	1.3%	13‰
Transmitter					
Wavelength	±1 pm (75 MHz)	0.5%	±1 pm (75 MHz)	0.1%	5‰
Linewidth	50 MHz	0.2%	50 MHz	negligible	2‰
Spectroscopy					
Line intensity	±2%	1.6%	±2%	1.6%	22‰
Air-broadened width γ_{air}	±2%	0.5%	±10%	9.3%	89‰
T-exponent of γ_{air}	±10%*	0.1%	±10%	0.4%	4‰
Pressure shift	±20%*	0.4%	±20%*	negligible	4‰
Total systematic error		2.3%		9.6%	98‰

3.3.4 Precision estimate applied to field campaign data

In order to complete the numerical analysis and to include a specific case using a realistic vertical profile of the HDO abundance δD based on observational data, DIAL performance simulations were applied to observations obtained during the L-WAIVE (Lacustrine-Water vApor Isotope inVentory Experiment) field campaign at the Annecy lake in the French Alpine region (Chazette et al., 2021). The data include profiles of pressure and temperature as well as vertical profiles of H_2O and HDO isotopologue concentrations which were obtained by an ultra-light aircraft equipped with an in situ cavity-ring-down-spectrometer (CRDS) isotope analyzer. The chosen example case is from 14 June 2019, where aerosols were present above the planetary boundary layer extending up to an elevation of more than 2.5 km. To simulate atmospheric conditions during the measurement campaign as realistically as possible, aerosol extinction data from the lidar WALI (Weather and Aerosol Lidar) (Chazette et al., 2014), operated during the L-WAIVE campaign on the same day, was used (see Fig. 3.13a). The backscatter coefficient was estimated with a lidar ratio of 50 sr and extrapolated to a wavelength of 2 µm using the Ångström exponent derived from sun-photometer measurements. Panels (b) and (c) of Fig. 3.13 show the in-situ-measured δD profile from the field campaign and the hypothetical precision of δD represented by the shaded area depending on detector characteristics and laser energy if that same profile was measured with the here-presented DIAL system (precision estimate based on wavelength option 1 for H_2O and option 2 for HDO).

For the commercial InGaAs PIN photodiode, the simulations show for the optimum case of 20 mJ laser energy that the uncertainty related to noise is sufficiently low for the characteristic variations in the experimentally obtained δD profile, ranging from -90‰ on the ground to -125‰ at a height of 2 km, to be fully resolved with the DIAL system. In terms of absolute precision, which is visualized as the width of

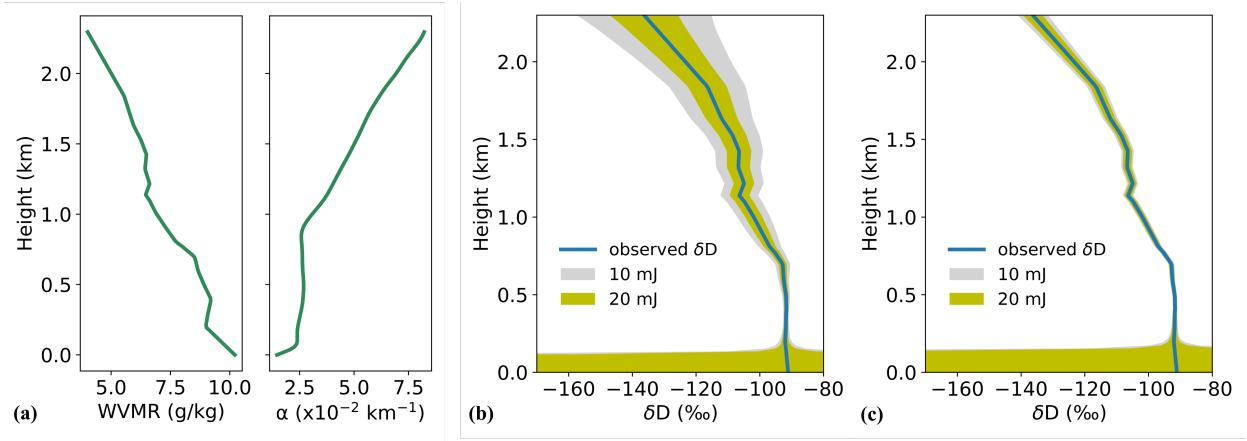

Figure 3.13: (a) Experimental profiles of the water vapor mixing ratio (WVMR) and aerosol extinction coefficient α obtained from the L-WAIVE field campaign. Expected precision in the isotopic ratio in terms of δD for the InGaAs PIN photodetector (b) and the low-noise HgCdTe avalanche photodiode detector (c). Shaded areas indicate the absolute uncertainty based on random noise in terms of standard deviation for laser energies of 10 mJ and 20 mJ. Calculations are based on a measurement bandwidth of 1 MHz and signal averaging over 45 000 shots per wavelength.

the shaded error band around the in situ profile, δD could be determined with a precision better than 5‰ within the first 1.5 km and better than 10‰ at a range height of 2 km. A setup with 10 mJ would deliver an absolute precision close to 20‰ at that height.

Simulations performed with the HgCdTe APD indicate extremely promising precision levels over the entire range of under 3‰ and 5‰ (in absolute terms) for 20 mJ and 10 mJ, respectively. It should be noted that the presented profiles represent a rather favorable case as the aerosol backscatter coefficient increases with altitude (due to the presence of an elevated dust layer) which is contrary to the baseline atmospheric models described in the previous numerical analysis. These simulations incorporating observed water isotopologue profiles clearly show the potential of a ground-based DIAL instrument to measure isotopic mixing ratios with high spatio-temporal resolution in the lower troposphere.

3.4 Conclusion of the sensitivity study

This chapter provided a sensitivity analysis for a DIAL system aiming to probe the water vapor isotopologues H_2O and HDO in the lower troposphere. The spectral window between 1982–1984 nm has been identified to perform such measurements. The selected H_2O absorption line has a sufficiently high line strength to probe the atmospheric boundary layer with low noise error and a range resolution of 100–200 m in the tropics and mid-latitude regions with high water vapor concentrations. The HDO absorption lines are substantially weaker which imposes stricter requirements on the laser source (higher pulse energy) and the lidar receiver (low-noise detector) if a similar relative precision is required. The selected H_2O absorption line is slightly temperature sensitive, requiring an accurate knowledge of the temperature profile along the line of sight for the mixing ratio retrieval. Ideally, such a profile would have to be provided by auxiliary measurements, for example by using a temperature Raman lidar.

A sensitivity analysis with an error budget was performed taking instrument-specific and environmental parameters into account. The numerical analysis included models of mid-latitude, polar and tropical

environments with realistic aerosol loads derived from the AERONET database extrapolated to the 2 µm spectral region. It was shown that the retrieval of water vapor mixing ratios is possible with relative random errors better than 1% within the atmospheric boundary layer (< 1.5 km) in mid-latitude and tropical conditions due to favorable differential absorption and aerosol load.

Based on the noise errors of the H_2O and HDO mixing ratio measurements, the expected precision in the HDO isotopic abundance δD was evaluated for different atmospheric conditions. The calculations revealed differences in precision of almost 1 order of magnitude between the tropical and arctic model. Reduced precision under arctic conditions is due to low water vapor content and reduced aerosol load. For the tropic and mid-latitude environment, the precision in δD ranges from better than 10‰ in the first kilometer of atmosphere to 20–40‰ at the boundary layer top at around 1.5 km. The expected precision values are in the order of or better than the columnar measurements obtained with other remote sensing techniques deployed from the ground (between 5‰ and 35‰ for a Fourier transform infrared spectrometer of the Total Carbon Column Observing Network) or from space (ca. 40‰ for the Tropospheric Emission Spectrometer (TES) and the Infrared Atmospheric Sounding Interferometer (IASI); see Table 4 in Risi et al. (2012)) but with a much greater resolution on the vertical. On the other hand, the expected precision is roughly 2 to 4 times lower than for in situ airborne CRDS measurements with a similar vertical resolution (see Table 3 in Sodemann et al. (2017)). These findings have been obtained for laser pulse energies of 20 mJ, a measurement bandwidth of 1 MHz (150 m range resolution), a signal averaging time of 10 min and a commercial InGaAs PIN photodiode.

As an interesting perspective option, the theoretical performance of a state-of-the-art HgCdTe avalanche photodiode featuring a NEP reduced roughly by 1 order of magnitude was also investigated. The use of such a detector would enable range-resolved measurement of the isotopic ratio with a precision close to CRDS analyzers.

An error budget was presented to outline systematic errors due to uncertainties in atmospheric, spectroscopic and instrument-related parameters. The H_2O on-line wavelength at 1982.93 nm shows a pronounced temperature sensitivity imposing strict requirements on accurate temperature profiles for the mixing ratio retrieval. This can be mitigated by tuning the on-line wavelength to 1982.97 nm which, however, comes at the cost of slightly increased pressure sensitivity and slightly reduced differential absorption. For the HDO isotopologue, two wavelength options were studied. Option 2 with the on-line wavelength at 1983.93 nm was found to be more suitable since it has no H_2O interference (as is the case for HDO option 1 at 1982.47 nm). The slightly smaller differential absorption for option 2 is a price worth paying, and the resulting increase in random error can be offset by longer signal averaging. Systematic errors due to uncertainties in spectroscopic parameters contribute significantly to the error budget which demonstrates that having an accurate knowledge of these parameters is crucial for DIAL measurements. This is addressed by laboratory measurements conducted by the GSMA laboratory of the university of Reims in the framework of the WaVIL project (Régalia et al., 2021).

Finally, using a measured H_2O/HDO profile obtained during the L-WAIVE field campaign, the presented calculations showed that sufficient precision in the isotopic mixing ratios can be achieved with the presented system parameters so that characteristic, vertical variations in the isotopic content δD observed during the field campaign could be resolved with the DIAL system under study, showing the potential to complement existing methods.

Chapter 4

Implementation and characterization of a 2 µm parametric laser source

As indicated in the sensitivity analysis of the previous chapter, range-resolved detection of water vapor isotopologues using a ground-based DIAL setup requires a laser source capable of emitting ns-pulses with energies in the mJ-range with adequate tunability in a spectral window around 1.98 µm. This chapter presents the design and the experimental realization of such a laser source based on a master-oscillator-power-amplifier setup consisting of a nested-cavity optical parametric oscillator (NesCOPO) and a parametric amplification stage. After an overview of the state of the art in 2-µm laser sources and a brief review of relevant concepts of nonlinear optics, the NesCOPO architecture is presented. In order to amplify the NesCOPO output radiation to the mJ-level, a parametric amplification chain based on a combination of specifically developed high-aperture PPKTP crystals is used. Different configurations of crystals were experimentally investigated in order to optimize the extracted output energy. Finally, measurements of the beam propagation factor of the final configuration as well as of the angular beam pointing stability are presented.

4.1 Pulsed laser sources in the 2 µm spectral range

The development of laser sources in the 2 µm spectral range has been driven by a variety of applications. Strong absorption of radiation by water and human tissue around 2 µm makes this spectral range interesting for laser surgery. Low atmospheric absorption and eye-safe properties have given rise to applications like materials processing, range-finding and remote sensing. Additionally, lasers operating around 2 µm can serve for pumping Ho-based and Cr-based lasers or mid-IR OPOs for which 1 µm pump lasers are not an option (Godard, 2007).

In the context of lidar remote sensing, technological developments have been driven by the need for high-energy pulsed lasers for DIAL measurements of greenhouse gases, especially CO_2, as well as wind measurements potentially from space based on heterodyne detection (Singh et al., 2015). The majority of these systems use bulk-crystal or fiber lasers with doping of thulium (Tm) or holmium (Ho), or both. Another possibility for generating tunable, high-energy radiation at 2 µm is offered by optical parametric sources. In the following, examples are given for both technologies which are summarized in Table 4.1.

4.1.1 Thulium/holmium-doped lasers

Infrared laser emission in the 1.9–2.1 µm spectral range can be achieved using laser materials doped with Tm^{3+} or Ho^{3+} ions. While the former can be pumped using laser diodes operating at 790 nm, the latter requires a pump wavelength of 1.9 µm making it less suitable for pumping by commercially available high-power laser diodes. This issue can be circumvented by using Tm-Ho co-doping in which Tm^{3+} acts as sensitizer ion strongly absorbing the pump radiation and transferring it to Ho^{3+} as the active ion. However, power scaling using this technique leads to large thermal loads in the laser medium which severely limits the achievable pulse repetition rate in Q-switched systems or requires special cooling if higher repetition rates are desired. With the increasing availability of high-power Tm:fiber lasers emitting around 1.94 µm in recent years, a common approach today is to use these lasers as pumping sources for Ho-doped yttrium lithium fluoride (Ho:YLF) bulk lasers leading to a significant reduction of the thermal load in the rod.

Pioneering work in the development of 2-µm Tm:Ho co-doped lasers has been carried out by the NASA Langley Research Center (LaRC) with a focus on applications to both global wind and CO_2 active remote sensing from space (Singh et al., 2015). In the framework of the NASA ASCENDS program, a laser-diode-pumped Tm,Ho:YLF laser was developed for integrated-path DIAL measurements of CO_2 at 2051 nm (Refaat et al., 2016). It operates in double-pulse operation in order to minimize the effect of ground reflectivity variations between the on-and off-line shots when used for airborne measurements. The laser delivers pulses of at the on- and off-line wavelengths of 90 and 45 mJ, respectively, with a pulse separation of 200 µs and a repetition rate of 10 Hz. More recently, the same group also demonstrated a triple-pulse Tm,Ho:YLF laser transmitter for simultaneous measurements of CO_2 and H_2O (Singh et al., 2017a).

Also at the NASA LaRC, another development path has led to the use of lutetium lithium fluoride (LuLiF) as host material. Compared to YLF, LuLiF allows for the extraction of higher pulse energies which is why it is especially suitable for long-range wind measurements using the coherent Doppler lidar technique. Using a diode-pumped Ho,Tm:LuLiF laser emitting close to 100 mJ per pulse at 2053 nm, Koch et al. (2007) demonstrated ground-based Doppler lidar wind measurements. The same laser was also used for ground-based, range-resolved DIAL measurements of CO_2 (Koch et al., 2008).

Significant work in advancing Tm:Ho co-doped laser oscillators has also been carried out by the National Institute of Information and Communications Technology (NICT) in Japan. Using a diode-side-pumped laser oscillator with a Tm,Ho:YLF rod conductively cooled to -80°C, Q-switched pulse energies of 125 mJ with near-diffraction-limited beam quality were obtained when operated at a repetition rate of 50 Hz (Sato et al., 2017). More recently, the group also investigated a Tm:fiber-laser-pumped Ho:YLF laser motivated by the aforementioned advantage of reduced thermal load due to pumping at 1.94 µm and thus higher possible repetition rates which is desired for coherent Doppler wind lidar. The developed laser system achieves pulse energies of 21 mJ at a repetition rate of 200 Hz and was used for Doppler wind lidar measurements (Mizutani et al., 2018).

Ho:YLF crystal lasers pumped by Tm-fiber laser have also been developed at the Laboratoire de Météorologie Dynamique (LMD) in France for coherent DIAL sensing of CO_2. A Q-switched Ho:YLF oscillator end-pumped by a commercial Tm-fiber laser delivering 10-mJ pulses with a duration of 40 ns at 2 kHz was used for atmospheric CO_2 profiling (Gibert et al., 2015). The system was later improved to respond to the requirements of a potential CO_2 space lidar. In its latest version, it can operate in double-pulse

mode generating energies of 42 mJ for the on-line pulse and 12 mJ for the off-line pulse at a repetition rate of 303.5 Hz (Gibert et al., 2018b).

A drawback of the presented solid-state laser systems is that they rely on free-space optics which are prone to thermal and mechanical alignment issues. All-fiber laser architectures overcome this problem allowing for more compact and robust designs. Additionally, a fiber-based lidar transmitter generally facilitates the use coherent detection for range-resolved Doppler wind measurements. In this context, a 2.05 µm all-fiber laser source designed for CO_2 and wind coherent lidar measurements was developed at the Optics and Associated Techniques Department (DOTA) of ONERA (Lahyani et al., 2021). It is based on a succession of four Tm-doped fiber amplifiers pumped at 793 nm and seeded with a narrow-linewidth distributed feedback laser diode (DFB-LD) resulting in 120 µJ pulses with a duration of 200 ns at a repetition rate of 20 kHz with close-to-diffraction-limited beam quality ($M^2 = 1.12$). The same group later added a crystalline Ho:YLF amplifier pumped by a Tm-doped fiber laser at 1940 nm resulting in a pulse energy of 9 mJ at 1 kHz repetition rate (Lahyani, 2022).

4.1.2 Optical parametric sources

Optical parametric sources based on optical parametric oscillators (OPO) and optical parametric amplifiers (OPA) are very versatile devices that can be tailored to generate coherent radiation in wavelength ranges not accessible with other laser sources. Based on a nonlinear three-wave mixing process, an OPO down-converts a pump radiation into two tunable frequencies, called signal and idler (see section 4.2). The 2-µm spectral range can be accessed by using bulk and periodically-poled ferroelectric oxides as nonlinear media. These materials include lithium niobate ($LiNbO_3$), potassium titanyl phosphate (KTP), potassium titanyl arsenate (KTA) and lithium tantalate ($LiTaO_3$) which can all be pumped by mature and reliable 1 µm laser sources. Depending on the selected nonlinear material and laser architecture, parametric sources can be tuned over hundreds of nanometers and are able to deliver pulse energies of a few hundreds of milijoule in the nanosecond low-repetition-rate regime. For instance, Mennerat and Kupecek (1998) used an OPO based on a bulk $LiNbO_3$ and demonstrated 430 mJ pulse energy (signal and idler) near degeneracy ($\lambda \approx 2\,\mu m$) from a Q-switched Nd:YAG pump laser (950 mJ, 15 ns, 10 Hz), but with a rather broad linewidth (ca. 900 GHz). A narrower linewidth of 1.8 GHz was achieved by using a combination of an intra-cavity etalon and a dispersive grating, although with a reduction the achieved output energy (250 mJ).

An alternative approach to achieve narrow-linewidth emission, which is an important instrument requirement for DIAL gas sensing, is the use of a dual-cavity doubly resonant OPO architecture. This path has been investigated at ONERA and has led to the nested-cavity OPO (NesCOPO) design which is described in more detail in section 4.3.2. Using a PPLN-based NesCOPO as master oscillator and an amplifier stage consisting of a PPLN pre-amplifier and four bulk KTP amplifiers, output energies of 20 mJ (12 ns, 30 Hz) were achieved at signal wavelengths tunable bewtween 2.05 and 2.3 µm making it a suitable laser source for DIAL measurements of the three greenhouse gases CO_2, CH_4 and H_2O (Barrientos Barria et al., 2014).

Table 4.1: Examples of nanosecond-laser sources in the 2 µm spectral range.

Lab	Reference	Laser type	Application	Specifications
NASA LaRC USA	Refaat et al. (2016)	Tm,Ho:YLF pumped by DFB-LD	IP/RR-DIAL of CO_2	$\lambda = 2051$ nm, $E_{on/off} = 90/45$ mJ, $P = 1.35$ W, $f_r = 10$ Hz (d-p), $\tau_{on/off} = 200/350$ ns
NASA LaRC USA	Koch et al. (2007; 2008)	Tm,Ho:LuLiF pumped by DFB-LD	Doppler wind lidar RR-DIAL of CO_2	$\lambda = 2053$ nm, $E = 90$ mJ, $P = 0.45$ W, $f_r = 5$ Hz, $\tau = 140$ ns
NICT Japan	Sato et al. (2017)	Tm,Ho:YLF pumped by LD	Doppler wind lidar	$\lambda = 2050$ nm, $E = 125$ mJ, $P = 6.25$ W, $f_r = 50$ Hz, $\tau = 800$ ns
NICT Japan	Mizutani et al. (2018)	Ho:YLF pumped by Tm:fiber-laser	Doppler wind lidar	$\lambda = 2064$ nm, $E = 21$ mJ, $P = 4.2$ W, $f_r = 200$ Hz, $\tau = 150$ ns
LMD France	Gibert et al. (2015)	Ho:YLF pumped by Tm:fiber-laser	coherent RR-DIAL of CO_2	$\lambda = 2051$ nm, $E = 10$ mJ, $P = 20$ W, $f_r = 2$ kHz, $\tau = 40$ ns
LMD France	Gibert et al. (2018b)	Ho:YLF pumped by Tm:fiber-laser	future space-based CO_2 IP-DIAL	$\lambda = 2051$ nm, $E_{on/off} = 42/12$ mJ, $P = 16.4$ W, $f_r = 303.5$ Hz (d-p), $\tau_{on/off} = 33/74$ ns
ONERA, DPHY France	Barrientos Barria et al. (2014)	NesCOPO, OPA	DIAL of CO_2, CH_4 and H_2O	$\lambda = 2050 - 2300$ nm, $E = 20$ mJ, $P = 0.6$ W, $f_r = 30$ Hz, $\tau = 12$ ns
ONERA, DOTA France	Lahyani et al. (2021)	Tm-doped fiber laser	CO_2 DIAL and wind coherent lidar	$\lambda = 2051$ nm, $E = 120$ µJ, $P = 2.4$ W, $f_r = 20$ kHz, $\tau = 200$ ns
DOTA / LMD France	Lahyani (2022)	Tm-doped fiber laser amplified in Ho:YLF crystal	CO_2 DIAL and wind coherent lidar	$\lambda = 2051$ nm, $E = 9$ mJ, $P = 9$ W, $f_r = 1$ kHz, $\tau = 200$ ns

λ: wavelength, E: pulse energy, P: average power, f_r: pulse repetition rate, τ: pulse length
DFB-LD: distributed-feedback laser diode
d-p: double-pulse operation

4.2 Relevant concepts of nonlinear optics

4.2.1 Nonlinear frequency conversion

Parametric laser sources are based nonlinear frequency conversion in non-centrosymmetric materials that exhibit a second-order susceptibility $\chi^{(2)}$. For the generation of near- and mid-IR wavelengths, two processes are of interest:

- Difference frequency generation (DFG): Nonlinear mixing of two incoming photons at frequencies ω_3 and ω_2 results in the difference frequency $\omega_1 = \omega_3 - \omega_2$ (see Fig. 4.1a). By convention, the laser beam with the highest frequency ω_3 is called the pump beam, the one with the lowest frequency ω_1 is the idler beam and the remaining one is called signal beam at frequency ω_2.
- Optical parametric generation (OPG): An incoming pump photon at frequency ω_3 generates two photons at lower frequencies ω_1 and ω_2 (see Fig. 4.1b).

For both processes, the energy is conserved, i.e. $\hbar\omega_1 + \hbar\omega_2 = \hbar\omega_3$, where $\hbar = h/2\pi$ is the reduced Planck constant.

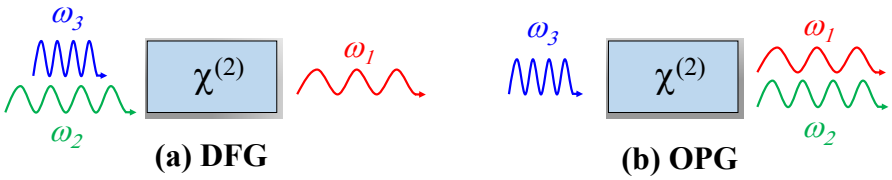

Figure 4.1: Schematic illustration of (a) difference frequency generation (DFG) and (b) optical parametric generation

From the coupled wave equations for the process of difference frequency generation it can be shown that the intensity of the generated idler wave can be calculated according to (Byer and Herbst, 1977):

$$I_{1,\mathrm{DFG}} = 2\frac{\omega_1^2 d_{\mathrm{eff}}^2 L^2 I_2 I_3}{c^3 \varepsilon_0 n_1 n_2 n_3} \mathrm{sinc}^2\left(\frac{\Delta k L}{2}\right), \tag{4.1}$$

where ω_1 is the frequency of the generated idler wave, n_3, n_1 and n_2 are refractive indices of the pump, idler and signal beams, respectively, c denotes the speed of light in vacuum, ε the dielectric constant, d_{eff} is the effective nonlinear coefficient, L is the interaction length in the nonlinear material, I_2 and I_3 are the intensities of the signal and pump beams, respectively, and Δk denotes the wavevector mismatch of the interacting waves.

Equation 4.1 reveals several fundamental characteristics of three-wave mixing by difference frequency generation. First, the generated idler intensity depends on the product of signal and pump intensity, so it is indeed a quadratic nonlinear process. Second, one can define $\mathrm{FM} = d_{\mathrm{eff}}^2/n_1 n_2 n_3$ as the so-called figure of merit accounting for the linear and nonlinear properties of the crystal. For an efficient frequency conversion, a large effective nonlinear coefficient is desired. And third, the efficiency of the nonlinear mixing process also depends on the phase mismatch factor $\mathrm{sinc}^2(\Delta k L/2)$, which is plotted in Fig. 4.2. As the product $\Delta k L$ increases, the efficiency decreases with some oscillations occurring. This behavior is explained by the fact that if L approaches the so-called coherent build-up length of the interaction $L_c = \pi/\Delta k$, the generated

wave gets out of phase with its driving polarization leading to a backconversion of power to the initial pump and signal waves until L reaches twice the coherence length and the cycle of constructive and destructive interference repeats itself again. From Fig. 4.2 it is also evident that processes with $\Delta k \approx 0$ are highly desirable in order to achieve high conversion efficiency, but there is an acceptance bandwidth for which nonlinear DFG still takes place as long as the coherent interaction length is larger than or equal to the length of the nonlinear crystal used.

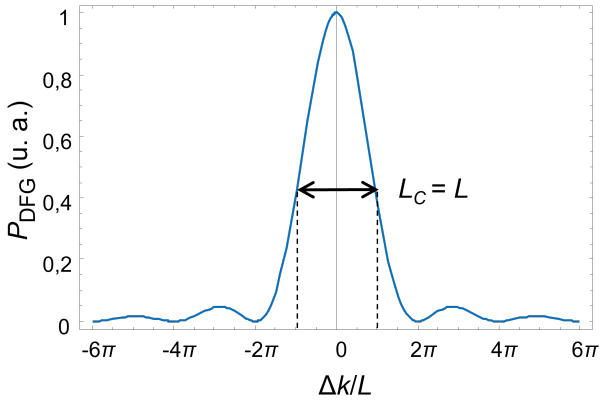

Figure 4.2: Output power resulting from difference frequency generation as a function of wavevector mismatch Δk. The acceptance bandwidth of the nonlinear process if defined by the condition for which the crystal length L is equal to the coherent build-up length of the nonlinear interaction L_c.

4.2.2 Phase matching

An efficient energy transfer between the waves propagating in the nonlinear crystal requires that they are in phase with the nonlinear polarization generating them. In other words, the phase-matching condition (momentum conservation) has to be fulfilled which can be expressed as:

$$\Delta\vec{k} = \vec{k}_3 - \vec{k}_1 - \vec{k}_2 = 0 \tag{4.2}$$

where $\Delta\vec{k}$ is the so-called phase mismatch and $\vec{k}_3$, $\vec{k}_1$ and $\vec{k}_2$ denote the wavevectors of the pump, idler and signal beam, respectively. Due to its vector nature, the phase matching condition stated in Eq. 4.2 can be fulfilled in collinear and noncollinear configuration as depicted in Fig. 4.3. In the case that the wave vectors of the involved beams propagate in the same direction (collinear case), Eq. 4.2 becomes

$$n_3\omega_3 = n_1\omega_1 + n_2\omega_2, \tag{4.3}$$

where n_3, n_1 and n_2 are refractive indices of the pump, idler and signal beam. It can be fulfilled by exploiting the refractive index dependency on temperature, polarization and crystal axis orientation of birefringent materials to compensate the chromatic dispersion of the interacting waves.

However, a major drawback of birefringence phase matching is that it can only be used in materials that are birefringent, thus excluding some other materials with interesting nonlinear properties. Additionally, the orientation of a birefringent crystal satisfying the phase-matching condition does not generally yield the highest possible nonlinear coefficient.

Figure 4.3: Schematic of (a) collinear and (b) noncollinear (angular) phase matching

In order to overcome these limitations, the technique of quasi-phase matching (QPM) was introduced (Fejer et al., 1992). In this case, the three interacting waves can propagate with parallel polarization (type 0) allowing to make use of the highest nonlinear coefficient (typically the d_{33} tensor element). In such a configuration, phase matching is not locally satisfied, but the modulation of the sign of d_{eff} realized by periodic poling of the nonlinear material gives rise to an average macroscopic net exchange of energy between the interacting waves. Figure 4.4 illustrates the principle of QPM in a periodically poled nonlinear medium. In the case that the phase-matching condition is not satisfied ($\Delta k \neq 0$), the newly generated wave after each coherence length $l_c = \pi/\Delta k$ interferes destructively with the wave created in the previous coherence length leading to a net destruction after twice the coherence length. However, if the nonlinear crystal is designed such that its polarization is changed by 180° after each coherence length, the nonlinear coefficient changes its sign and constructive interference occurs leading to a build-up of the generated wave. This implies that the periodicity of crystal poling Λ must be twice the coherence length ($\Lambda = 2l_c$).

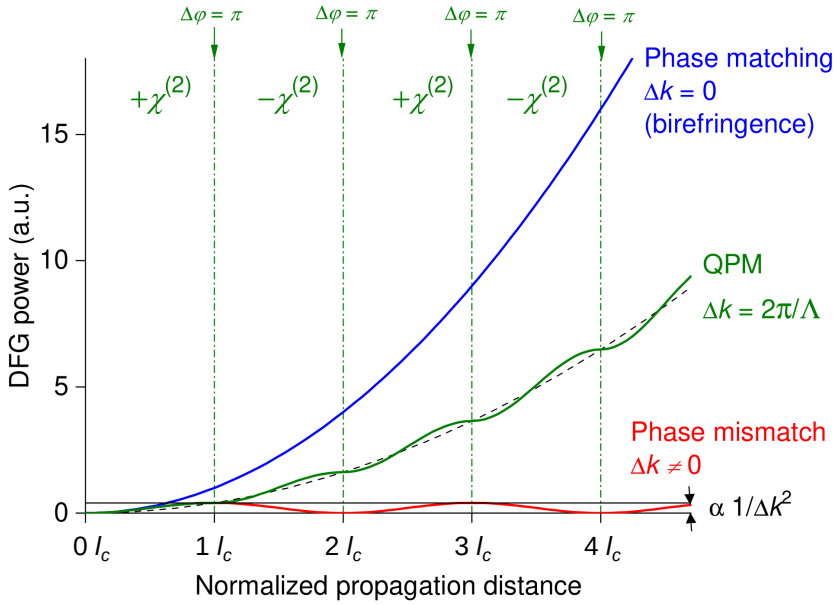

Figure 4.4: Power generated in the process of difference frequency generation (DFG) as a function of distance propagated in a nonlinear crystal normalized to the nonlinear coherence length l_c in the case of perfect phase matching, quasi-phase matching and phase mismatch.

For a quasi-phase matching process, the phase matching equation now includes the momentum contribution from the periodic poling and reads:

$$\Delta k = k_3 - k_1 - k_2 - \frac{2\pi}{\Lambda}. \tag{4.4}$$

It should be noted that, compared with phase matching by birefringence, the effective nonlinearity d_{eff} is reduced by a factor of $2/\pi$. But this is often compensated by the already mentioned fact that type-0 configurations can be used for which the nonlinear coefficient is the largest. Additionally, since all interacting waves have the same polarization, no spatial beam walk-off occurs.

4.2.3 Optical parametric amplification

Optical parametric amplification (OPA) is similar to DFG, except for the amplitudes of the interacting waves. While DFG arises when the laser beams incident on a nonlinear crystal have comparable intensities, OPA occurs when one beam (seed) is much weaker. As illustrated in Fig. 4.5, a strong pump beam at ω_3 transfers energy to the initial seed beam with the idler frequency ω_1 and generates a signal wave at ω_2. Note that also the signal can be used to seed the OPA leading to its amplification while creating an idler field in the process.

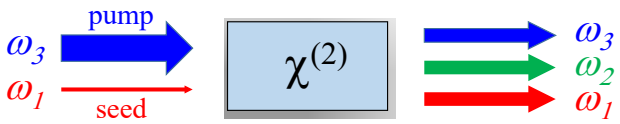

Figure 4.5: Schematic of optical parametric amplification

Solving the coupled-waves equations for the case of an idler seeding, assuming the pump beam with intensity I_3 is not depleted in the OPA process (constant-pump approximation) and allowing for phase mismatch Δk, the intensities of the signal and idler beams (I_2 and I_1) depending on the interaction length L can be expressed as follows:

$$\begin{aligned} I_1(L) &= I_1(0)\left[1 + \left(\frac{\Gamma}{g}\sinh(gL)\right)^2\right] \\ I_2(L) &= I_1(0)\frac{\omega_2}{\omega_1}\left(\frac{\Gamma}{g}\sinh(gL)\right)^2 \end{aligned} \tag{4.5}$$

with

$$\Gamma^2 = \frac{2\omega_1\omega_2 d_{\text{eff}}^2 I_3}{\varepsilon_0 c^3 n_1 n_2 n_3} \quad \text{and} \quad g = \sqrt{\Gamma^2 - \frac{\Delta k^2}{4}} \tag{4.6}$$

Figure 4.6 shows the evolution of the signal and idler intensities with increasing interaction length L according to Eqs. 4.5. The parametric gain of the OPA process can be defined as:

$$G(L) = \frac{I_1(L)}{I_1(0)} = 1 + \left(\frac{\Gamma}{g}\sinh(gL)\right)^2. \tag{4.7}$$

In the case that the gain is large ($gL \gg 1$), Eq. 4.7 can be approximated to:

$$G(L) \approx \left(\frac{\Gamma}{g}\right)^2 \frac{e^{2gL}}{4} \tag{4.8}$$

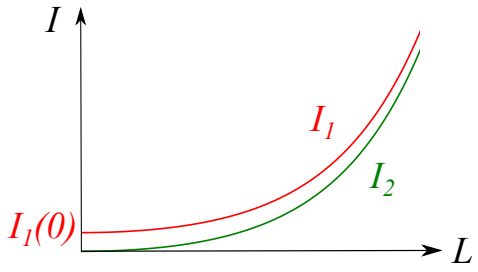

Figure 4.6: Spatial evolution of the signal and idler intensities (I_2 and I_1) generated in an idler-seeded OPA process under the constant-pump approximation.

Consequently, both signal and idler intensities grow exponentially with L assuming that the pump is not depleted. The gain G depends strongly on the parameter g and is maximum if the phase-matching condition is perfectly fulfilled ($\Delta k = 0$) and decreases rapidly for non-zero values of Δk. In the case of $\Delta k = 0$, the OPA gain scales exponentially with the square root of the figure of merit FM. It also depends exponentially on the square root of the pump intensity, which in pulsed regime depends on the pulse duration and energy as well as the beam size.

In reality, the OPA process can become much more complex. The approximated equations stated above are based on the assumption of plane waves and change for more realistic Gaussian beams where the intensity has a radial dependency which causes the gain to vary in the transverse plane. Deviations in the overlap of the interacting beam also lead to an overall gain reduction. Furthermore, the constant-pump approximation is an idealization and in experiments the pump may well deplete significantly. Competing nonlinear processes can also deteriorate the OPA gain, for example if the signal and idler waves recreate light of the pump wavelength in the process of sum-frequency conversion.

4.2.4 Optical parametric oscillators

The gain resulting from the OPA process can in the presence of feedback produce oscillation which is the basic principle of a device known as the optical parametric oscillator (OPO). Similar to a laser, it consists of a resonator and a gain medium, but instead from stimulated emission, the gain in an OPO is derived from parametric amplification. Starting from quantum noise, parametric generation builds up and the resulting signal and idler waves are amplified during each round trip in the cavity until the gain exceeds the losses. Due to the presence of three interacting wavelengths which are governed by the phase-matching condition, large tuning ranges can be achieved.

Since the parametric conversion process generates two wavelengths (signal and idler) from a pump wavelength, different OPO architectures are possible. Figure 4.7 shows an example of a singly resonant OPO (SROPO) for which the cavity is arranged such that only the signal wave resonates. The advantage of the SROPO configuration is its simplicity allowing for the design of robust coherent sources. One drawback of the SROPO architecture is the relatively high oscillation threshold which requires strong pumping. Another disadvantage is that it does not allow for stable single-longitudinal mode emission in pulsed regime due to inefficient mode competition on short time scales. However, single-frequency emission is highly desirable for many spectroscopic applications which has led to the implementation of several spectral-narrowing techniques which are also used in classic lasers.

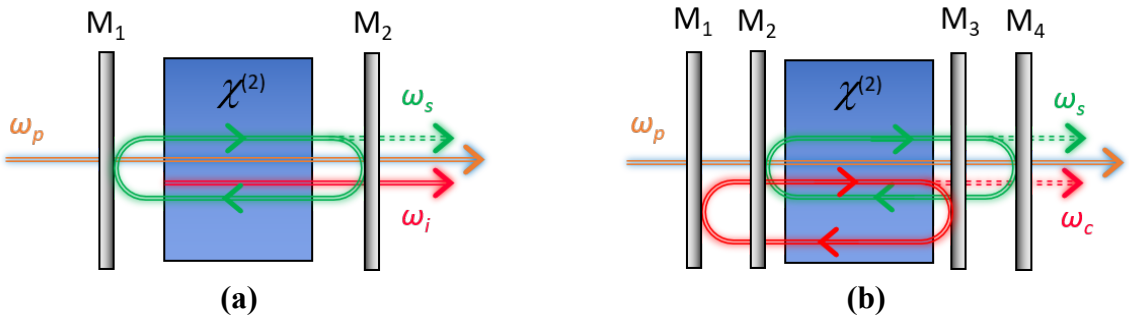

Figure 4.7: Schematic of a singly resonant OPO (a) and a dual-cavity doubly resonant OPO (b)

One strategy consists in introducing Fabry-Perot étalons inside the cavity (Kreuzer, 1969). However, this often leads to insertion losses limiting the achievable performance. Another approach is based on the use of intra-cavity diffractive gratings which has been successfully used to achieve single-longitudinal-mode emission in dye lasers under the so-called Littman configuration (Littman, 1978). However, in OPOs the low reflectivity of a grating is a severe impediment to reaching the oscillation threshold without optical damage. An alternative to overcome the limitations due to optical losses is the injection-seeding technique (Bjorkholm and Danielmeyer, 1969). It consists of injecting light from a seed laser, which is usually a single-frequency laser in continuous-wave operation, into the OPO. If the injected seed frequency is close to one particular resonator mode of the OPO, that mode starts to deplete the pump and to oscillate before the adjacent modes leading to a drastically reduced emission bandwidth compared with unseeded, free-running emission. Since no optical losses are introduced compared to intra-cavity étalons or gratings, the injection-seeding technique offers benefits in terms of lower oscillation threshold and higher conversion efficiency. The injection-seeding technique was successfully implemented in the laser transmitter of the CHARM-F lidar system of the German DLR for sounding CO_2 and CH_4 in the 1.6 µm range (Amediek et al., 2008, 2017). A major drawback of the technique is the limited tunability due to the restricted tuning range of the seed laser.

To overcome this limitation and make use of the full tuning capability provided by the parametric process, a dual-cavity doubly resonant OPO can be used. In such a configuration, which is schematically illustrated in Fig. 4.7b, signal and idler waves oscillate in two distinct cavities whose lengths can be independently adjusted in order to meet the resonance condition for each wave. This approach has been taken by ONERA and has led to the current nested-cavity OPO (NesCOPO) design which serves as the frequency converter of the WaVIL setup and is explained in more detail in section 4.3.2.

4.2.5 Nonlinear optical materials

The choice of the nonlinear optical material is essential for the implementation of a parametric laser source. In order to ensure an efficient nonlinear interaction, the material should have the following properties:

- the transparency window of the nonlinear medium has to cover the spectral range of the interacting wavelengths;
- birefringent or quasi-phase-matching need to be possible for the desired wavelengths;
- the nonlinear coefficient must be non-zero (and ideally of high value) for the chosen configuration;

- the spatial separation of the interacting beams due to birefringence should be minimal;
- the optical damage threshold of the material has to withstand the applied intensities. If high average-powers are involved, high thermal conductivity is also desirable;
- it must be possible to fabricate crystals in the desired lengths and apertures with sufficient quality.

Figure 4.8 gives an overview of nonlinear materials with their transparency ranges and highest possible figure of merit. For the 2 µm wavelength range, common materials are $LiNbO_3$ (LN), $LiTa_3$ (LT), $KTiOPO_4$ (KTP) and $KTiOAsO_4$ (KTA) which can all be pumped by well matured 1 µm lasers. Additionally, these materials are ferroelectric which means that they can be periodically poled by the application of a strong electric field via patterned electrodes on the crystal surface (ferroelectric domain engineering). The process is very challenging for thicker crystals (more than 1 mm) as high electric field strengths are required and the poling quality is sometimes only sufficient near the electrodes.

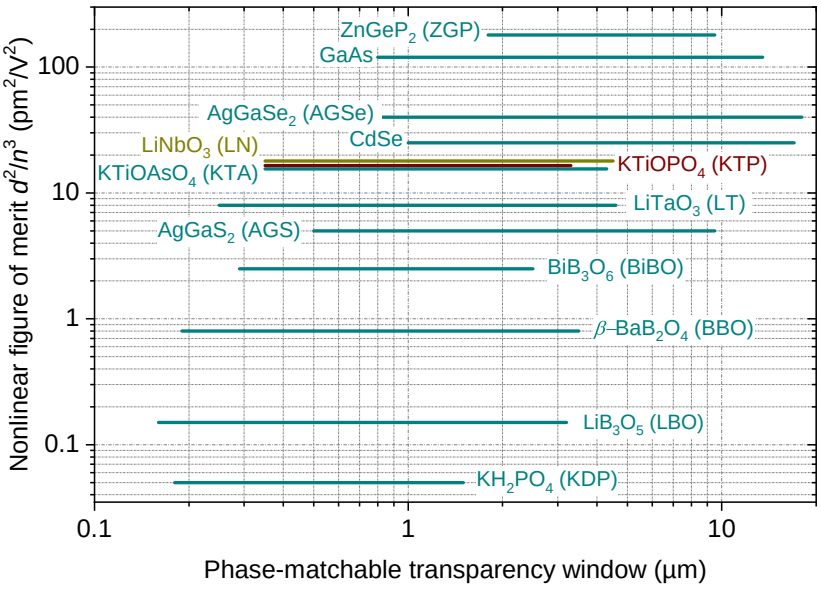

Figure 4.8: Selection of nonlinear crystals with their nonlinear figure of merit (FM) and transparency window. Values of FM are plotted for the highest possible nonlinear coefficient. If QPM is the most efficient process, the corrective factor $2/\pi$ was applied to the nonlinear coefficient. Data from Dmitriev et al. (1999)

In this thesis, periodically poled KTP (PPKTP) is of special interest as it is the nonlinear material of the developed amplification stage. The material KTP offers many advantages. It possesses a high nonlinear susceptibility, has a high damage threshold and has favorable mechanical and thermal properties (Zukauskas et al., 2011). Additionally, the possibility to produce high-aperture periodically poled crystals (several mm in width and height) enables the implementation of high-energy pumping schemes. Moreover, PPKTP crystals have been shown to have low susceptibility to radiation damage, which is an essential consideration for the design of space-based instrumentation (Coetzee et al., 2017).

The PPKTP crystals used for this thesis work were obtained through a collaboration with the KTH Laser Physics group of Stockholm and were specifically tailored for the application as a broadband amplifier. The KTH group is one of the few teams capable of producing high-aperture periodically poled ferroelectric crystals using the electric field poling technique (Zukauskas et al., 2011; Ishizuki and Taira, 2005).

4.3 Implementation of a nested-cavity optical parametric oscillator

This section provides a brief theoretical background of the NesCOPO architecture and outlines the characteristics of the implemented device as the parametric frequency converter of the WaVIL transmitter setup to transfer the 1 µm pump wavelength to the 2 µm range.

4.3.1 Background

Since the 1990s, the group Sources Laser et Métrologie (SLM) of ONERA has been developing dual-cavity OPOs with the aim of providing single-frequency IR laser sources that are tunable over several 100 nm. The latest version of this development is based on a nested-cavity arrangement. This nested-cavity OPO (NesCOPO) is a versatile frequency synthesizer based on parametric down-conversion of near-IR primary radiation (for which laser technology is well matured) to wavelengths in the 2–10 µm range offering the potential for various gas sensing applications (Godard et al., 2017; Cadiou et al., 2017). Due to its doubly resonant nested-cavity design, it enables the emission of single-longitudinal-mode radiation over a wide tuning range without the need of any injection seeding device (Hardy et al., 2011).

4.3.2 NesCOPO architecture

The NesCOPO architecture was studied in detail in the thesis of Betrand Hardy (Hardy-Baransky, 2011). It is based on a three-mirror-dual-cavity design making it relatively simple and compact. Figure 4.9a shows a schematic representation of the NesCOPO architecture. It consists two spherical mirrors M1 and M3 that make up the cavity for the idler wave and a plane mirror M2 deposited on the crystal facet on the pump side which together with mirror M3 makes up the signal cavity. The other side of the nonlinear crystal is anti-reflection coated. Mirrors M1 and M3 are mounted on piezoelectric transducers (PZT) allowing for the adjustment of the cavity lengths. The signal and idler cavity lengths are slightly different (so-called dissociation, around 5-10%) resulting in slightly different free-spectral ranges (FSR) as illustrated in Fig. 4.9b. Under the condition that the parametric gain bandwidth of the nonlinear crystal is narrow

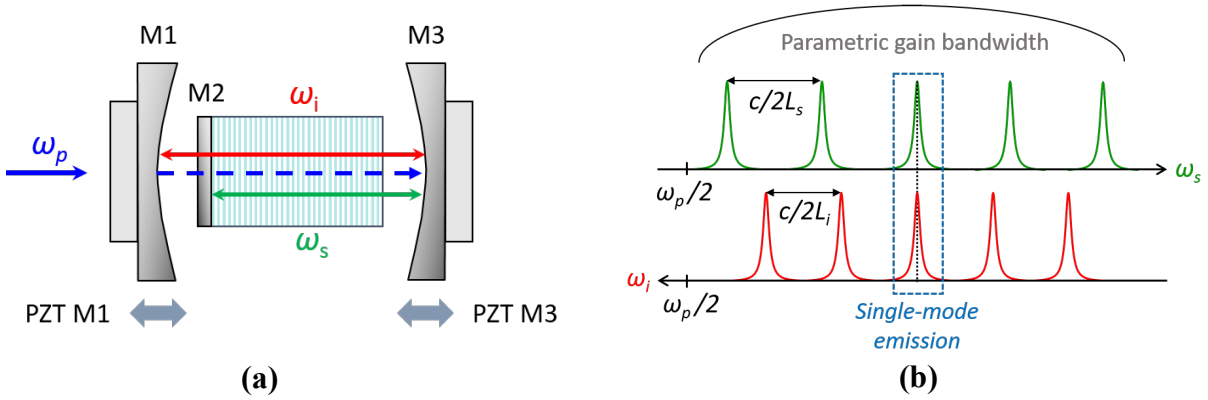

Figure 4.9: (a) Schematic of the NesCOPO architecture with mirrors M1, M2 and M3. Piezoelectric transducers (PZT) translate mirrors M1 and M3 to adjust the signal and idler cavity lengths. (b) Schematic representation of the NesCOPO spectrum with frequency combs of the signal (top) and idler (bottom) cavity modes. The signal and idler cavity lengths L_s and L_i are chosen such that only a single coincidence of signal and idler modes exists within the parametric gain bandwidth leading to single-longitudinal-mode emission.

enough, the signal and idler frequency combs can be adjusted such that only a single pair of modes coincides within the gain bandwidth leading to single-longitudinal-mode emission. Another advantage of the doubly-resonant design is that it decreases the oscillation threshold allowing for pumping with lower energies.

4.3.3 Phase-matching considerations

The nonlinear crystal of the NesCOPO used in the WaVIL laser setup is a PPLN crystal. Because the NesCOPO operates close to degeneracy (1.06 µm pump wavelength and 1.98 µm or 2.05 µm signal wavelength) it is not suitable to exploit type-0-phase matching (similar polarization for all three interacting waves), which would enable the highest nonlinear efficiency. The parametric gain bandwidth in either PPLN or PPKTP would be too broad to achieve single-longitudinal-mode emission with a NesCOPO architecutr. Two alternatives can be implemented to avoid this issue: (i) the use of a volume-Bragg grating (VBG) mirror to reduce the bandwidth by introducing losses outside the VBG bandwidth (Kabacinski et al., 2020) or (ii) the use of type-2 periodically poled crystals (with orthogonal signal and idler polarization directions) resulting in a narrow linewidth but lower nonlinear efficiency (Raybaut et al., 2009). Option (ii) was finally chosen for the NesCOPO used in the framework of this thesis because it allows tuning capabilities over several tens of nanometers to address both the H_2O/HDO spectral window at 1.98 µm and the CO_2 window at 2.05 µm.

In order to obtain the desired signal wavelengths around 1.98 µm and 2.05 µm, the utilized PPLN crystal has four zones with different QPM poling periods. They can be accessed by translating the crystal in transverse direction within the NesCOPO. Figure 4.10 shows the signal wavelengths resulting from the QPM condition as a function the crystal temperature for the four different poling periods. The crystal zones with poling periods of 14.54 µm and 14.59 µm are dedicated for generating a signal wavelength at 1.98 µm suitable for water vapor isotopologue measurements. The CO_2 spectral window at 2.05 µm can be accessed by utilizing the crystal zones with poling periods of 14.30 µm or and 14.26 µm.

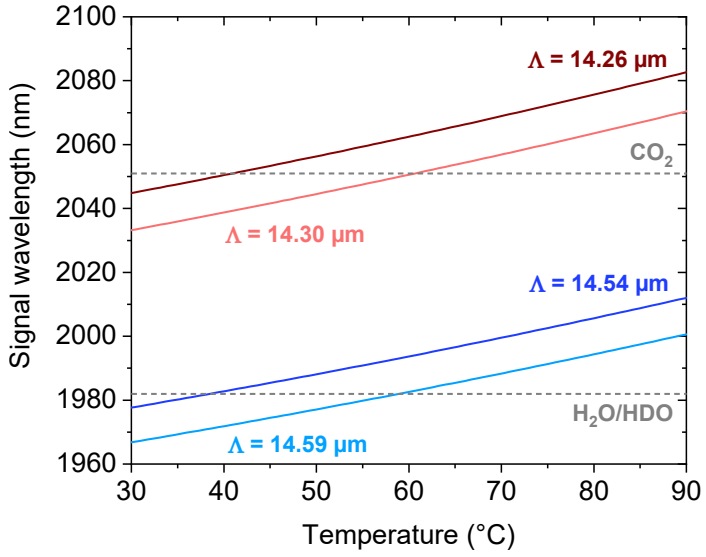

Figure 4.10: Temperature dependency of the signal wavelength in the type-2 PPLN crystal used in the NesCOPO setup for different QPM poling periods.

4.3.4 NesCOPO characteristics

Table 4.2 provides an overview of key parameters of the NesCOPO design that was used in the framework of this thesis. The NesCOPO is pumped by 15 ns-pulses at 1064 nm with energies close to 0.5 mJ per pulse. For the 10 mm-long PPLN crystal used, the resulting output signal and idler energies are in the range of 20 µJ. A coarse tuning of the NesCOPO-emitted wavelengths is achieved by changing the QPM conditions via the poling period of the PPLN crystal or by varying the crystal temperature (see Fig. 4.10). For a fixed poling period and constant temperature, a finer wavelength tuning capability is provided by varying the signal and idler cavity lengths via the PZT-mounted mirrors M1 and M3 in order to adjust the coincidence of modes within the parametric gain bandwidth. Figure 4.11 demonstrates a mode-hop tuning of the NesCOPO signal wavelength over a 1 nm at window at 1.98 µm. The 1 nm tuning range is determined by the parametric gain bandwidth. It is sufficiently large to access multiple absorption lines of water vapor between 1982 nm and 1983 nm that are of interest for DIAL measurements.

Table 4.2: NesCOPO parameters. RoC: radius of curvature

Parameter	**Value**
Reflectivity M1 (idler)	0.8
Reflectivity M2 (signal)	0.98
Reflectivity M3 (signal, idler, pump)	0.99
RoC M1	500 mm
RoC M3	500 mm
Pump beam diameter ($1/e^2$)	460 µm
Distance M1 – M2	2 mm
Distance M3 – crystal output facet	0.5 mm
Crystal type / length	PPLN / 10 mm
Quasi-phase matching (QPM)	Type 2

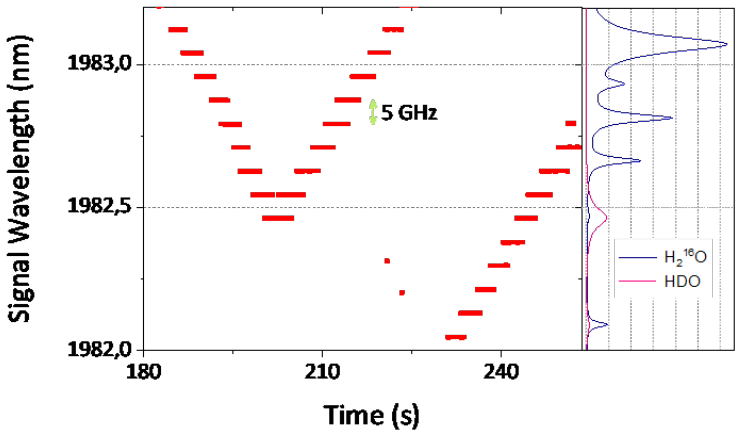

Figure 4.11: Coarse tuning of the NesCOPO signal wavelength over a 1 nm window with steps of one free-spectral range FSR (5 GHz). The presented 1 nm tuning range is determined by the parametric gain bandwidth and allows to access multiple absorption lines of the water vapor isotopologues H_2O and HDO between 1982 nm and 1983 nm.

4.4 Implementation and characterization of an optical parametric amplification setup based on high-aperture PPKTP crystals

This section presents the development of an optical parametric amplifier (OPA) setup with the aim of scaling the energy of the 2 µm radiation generated in the NesCOPO from the microjoule to the millijoule. With the additional objective of achieving amplification in both spectral windows at 1.98 µm and 2.05 µm in the context of a multi-species lidar, the amplifier stage is based on innovative high-aperture PPKTP crystals that were specifically developed by the Laser Physics group of KTH in Sweden. In the following, the experimental results of using different combinations of crystals that led to the final WaVIL transmitter design are presented. The conducted OPA experiments also served as an experimental validation for the performance simulations that were carried out in the framework of the LEMON lidar development which are presented in chapter 6. A characterization of the final WaVIL transmitter in terms of beam quality and beam pointing stability is also presented.

4.4.1 Test of different nonlinear-crystal configurations

In a previous setup realized at ONERA for ground-based DIAL measurements of CO_2, the parametric amplification stage consisted of commercial bulk KTP crystals (Cadiou et al., 2017). In such a configuration, critical phase matching has to be realized by tuning the crystal angle. This would be a feasible approach for a laboratory-bench system operating at a fixed spectral range (as it is the case for the WaVIL instrument at 1.98 µm.) However, critical phase-matching is not practical in the prospect of a multi-species instrument which has to cover both the 1.98 µm and 2.05 µm spectral regions and the design of which is oriented towards high integration and robustness (LEMON instrument). The solution thus consists in utilizing periodically-poled nonlinear materials and exploiting the temperature dependence of the QPM condition. Among possible materials, PPKTP is a good candidate as it offers high nonlinearity, high damage threshold and favorable mechanical and thermal properties (Zukauskas et al., 2011). Additionally, the possibility to produce high-aperture periodically-poled crystals (several mm in width and height) enables pumping with high energy inputs.

4.4.1.1 PPKTP crystals characteristics

The available nonlinear crystals are listed in Table 4.3. Three identical, 12 mm-long Rb-doped PPKTP crystals with an aperture of $5 \times 7\,mm^2$ were used in the OPA experiments. These crystals were fabricated with a poling period of 38.85 µm. Figure 4.12a shows the temperature tuning curve of the PPKTP crystals. These crystals were initially designed for a signal wave at the CO_2 wavelength at 2.05 µm which is reached at a temperature of around 45°C. In order to access wavelengths around 1.98 µm for H_2O/HDO DIAL measurements, the PPKTP crystals would ideally have to be operated at a temperature around 15°C. However, due to the sufficiently large temperature bandwidth of the parametric gain (see Fig. 4.12b), amplification is still possible under room-temperature conditions so that no heating or cooling of the crystals is required.

In addition to the PPKTP crystals, two bulk KTP crystals with lengths of 20 mm and 25 mm were also available and were tested in combination with the PPKTP crystals.

Table 4.3: Nonlinear crystals used in the OPA experiments

Label	Material	Length	Aperture	Poling period	Provider
G10	PPKTP	12 mm	$5 \times 7\,mm^2$	38.85 µm	developed by KTH
G12	PPKTP	12 mm	$5 \times 7\,mm^2$	38.85 µm	developed by KTH
G15	PPKTP	12 mm	$5 \times 7\,mm^2$	38.85 µm	developed by KTH
KTP1	KTP	20 mm	$5 \times 7\,mm^2$	angle tuning	commercial
KTP2	KTP	25 mm	$5 \times 7\,mm^2$	angle tuning	commercial

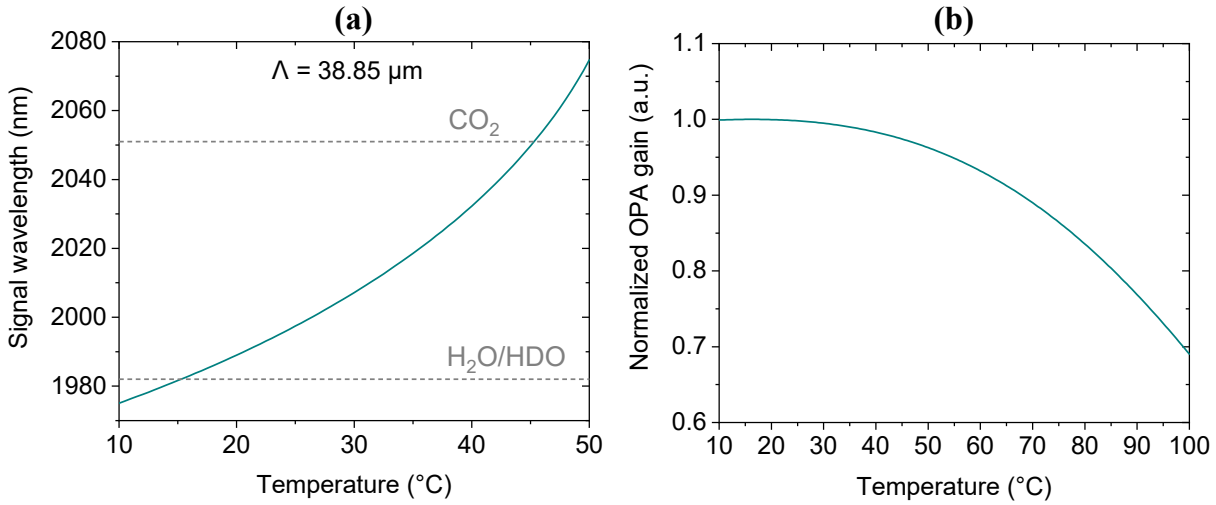

Figure 4.12: (a) QPM curve for the signal wavelength as a function of temperature for PPKTP with a 38.85 µm poling period. (b) OPA gain as a fucntion of temperature for a 12 mm long PPKTP crystal with a 38.85 µm poling period and a signal wavelength of 1982 nm.

4.4.1.2 Experimental setup

The OPA test setup is schematically shown in Fig. 4.13. It is a master-oscillator-power-amplifier (MOPA) architecture consisting of the NesCOPO specified in section 4.3.4 and an OPA stage in which the PPKTP crystals are tested. The pump laser is an injection-seeded Q-switched Nd:YAG laser (1064 nm) emitting 15 ns-pulses at a repetition rate of 150 Hz with an energy per pulse of close to 200 mJ. A small fraction of around 0.5 mJ is used to pump the NesCOPO which generates the signal and idler radiation at 1.98 µm and 2.30 µm, respectively.

As shown in the thesis of J. Barrientos-Barria (Barrientos-Barria, 2014), the generation of the signal and idler pulses in the NesCOPO takes a certain build-up time on the order of a few nanoseconds. For subsequent amplification, it is thus necessary to implement a delay line for the pump beam in order to optimize the temporal superposition of the pump and idler pulses. The pulse-build-up time of the NesCOPO used is ca. 10 ns, thus a delay line with the length of 3 m is used. Prior to the OPA line, the pump beam diameter is reduced by implementing a beam expander (BE). The lenses of the BE (focal lengths $f_1 = 175$ mm and $f_2 = -75$ mm) were chosen such that the pump enters the OPA crystals with maximum beam diameter without being clipped by the crystal edges. This allows for pumping with higher energies while keeping the peak fluence below the damage threshold of the anti-reflection coatings on the crystal facets. The camera

image in Fig. 4.13 shows the transverse profile of the pump beam prior to the OPA stage. To avoid damaging the crystal coatings, the pump energy was limited to 70 mJ. For this energy, the peak fluence was estimated as 2.5 J cm^{-2}, which is below the value of 5 J cm^{-2} that resulted in damages in earlier tests with smaller pump beam diameters. However, that essentially means that over half of the available pump laser energy is unused.

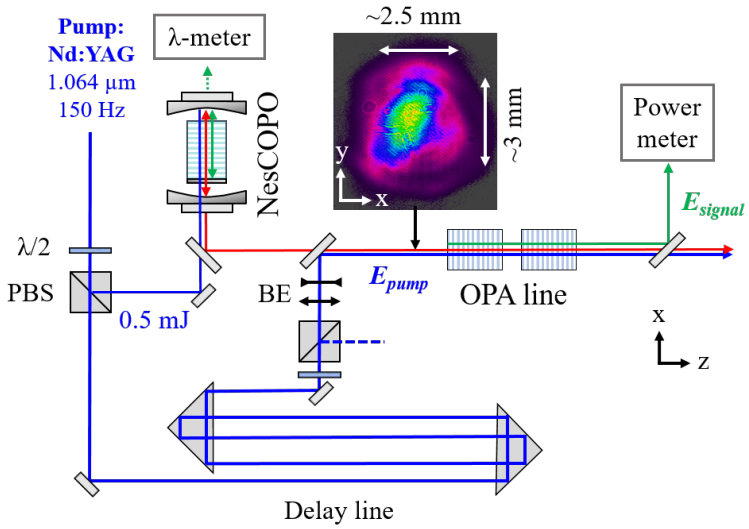

Figure 4.13: Experimental setup of the PPKTP-OPA tests. A small fraction the pump energy is used to pump the NesCOPO master-oscillator. The remaining pump energy passes a 3 m delay line (10 ns) to compensate the pulse build-up time in the OPO before being directed to the idler-seeded OPA line (type 0 phase-matching). The camera image shows the transverse pump beam profile at the OPA entrance. Indicated dimensions are 1/e^2 beam diameters. PBS: polarizing beam splitter; BE: beam expander.

The different PPKTP-crystal configurations that were tested in order to maximize the signal output energy are presented schematically in Fig. 4.14. The OPA line is seeded by the NesCOPO-emitted idler wave featuring pulse energies of ca. 20 µJ. Configurations (a) and (b) are successions of two and three PPKTP crystals, respectively. However, by using such a simple amplifier chain, high gain can lead to a depletion of the pump at the intense parts of the beam before the low-intensity parts are efficiently converted. A further increase in gain might improve the conversion in low-intensity parts of the pump beam, but it may to lead back-conversion (sum frequency generation of signal and idler transfers energy back to the pump) in the high-intensity part which in effect leads to a reduction of the overall conversion efficiency.

In order to reduce such gain saturation effects and enhance the signal conversion efficiency, a fruitful approach is to filter out the idler beam (Arisholm et al., 2004). Two different options were investigated: One consists in coupling out the idler between two PPKTP crystals as is shown in Fig. 4.14c. This approach was used in previous work of the SLM group at ONERA but with bulk KTP crystals (Barrientos Barria et al., 2014). The second option uses the polarization for filtering the idler by implementing bulk KTP crystals realized in configurations (d) and (e). The advantage is that it does not require additional filter optics which can be subject to optical damage. And finally, a combination of idler-out-coupling and polarization filtering was tested with configuration (f).

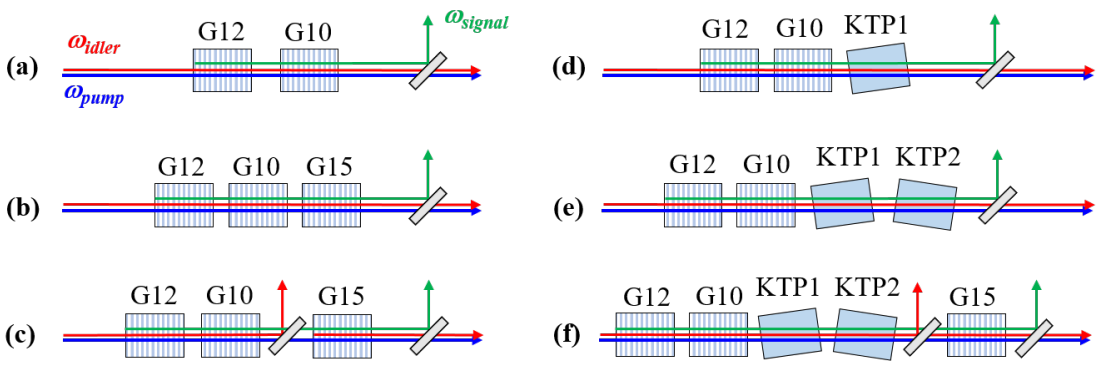

Figure 4.14: Schematic illustration of the tested PPKTP-crystal combinations

4.4.1.3 Phase considerations

An import aspect to consider when combing two or more periodically poled nonlinear crystals for quasi-phase matching is what happens to the phase mismatch in the transition from the last poling period of the first crystal to the first period of the second crystal. After fabrication, the crystal facets are coated with an anti-reflection layer. This additional processing can affect the last poling domain in an unknown manner. Two experimental measures were thus tested to optimize the conversion efficiency:

- Changing the crystal orientation: In some cases, large differences in the achieved output energies were observed if the second crystal was turned by 180°. Consequently, the experimental results presented below were all obtained with crystal orientations optimized in each case.
- Using a wedge phase plate as shown in Fig. 4.15: vertically translating a wedged plate changes the phase mismatch as a function of thickness of the plate and the different refractive indices at the interacting wavelengths. While an effect was indeed observed when translating the wedge, it rather led to a decrease in the generated signal energy compared to the configuration without the phase plate, suggesting that the phase mismatch was already sufficiently small without this measure. For that reason and the disadvantage of added complexity, this option was not further investigated.

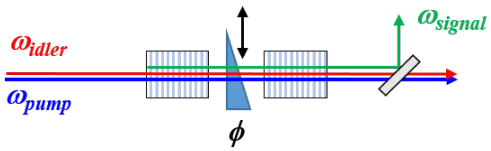

Figure 4.15: Illustration of the use of a wedge phase plate to adjust the phases of the interacting waves between two PPKTP crystals

4.4.1.4 Amplification results

The different amplifier configurations of Fig. 4.14 were characterized for pump energies ranging from 25 mJ to 70 mJ. The measured signal energies are plotted in Fig. 4.16a with the corresponding pump-to-signal conversion efficiency depicted in Fig. 4.16b. With respect to configurations (a) and (b) based on two and

three successive PPKTP crystals, the above mentioned saturation effect starts to appear. The use of two PPKTP crystals leads to an increase in the extracted signal energy according to a quadratic relation to the pump energy. The signal energy is further increased by adding a third PPKTP crystal. However, this leads to a saturation effect due to backconversion for higher pump energies as can be clearly observed in the flattening of the signal conversion efficiency curve.

The configurations that employ an idler filtering either by coupling out the idler between two crystals or by exploiting the polarization-dependent phase-matching in bulk KTP show indeed an improvement in the extracted signal energies for higher pump energies. For instance, the implementation of the idler-outcoupler prior to the third PPKTP crystal in configuration (c) results in a signal energy of 9 mJ for a pump energy of 70 mJ compared to 6.8 mJ for three PPKTP amplifiers with no idler filtering. The highest signal output energy of 10 mJ is achieved with configuration (f) employing both the idler outcoupler and the two bulk KTP crystals. However, considering the marginal improvement in signal energy and the added complexity of two critically phase-matched KTP crystals, the simpler configuration (c) featuring three PPKTP amplifiers and the idler outcoupler prior to the last crystal was the configuration of choice for the subsequent lider experiments.

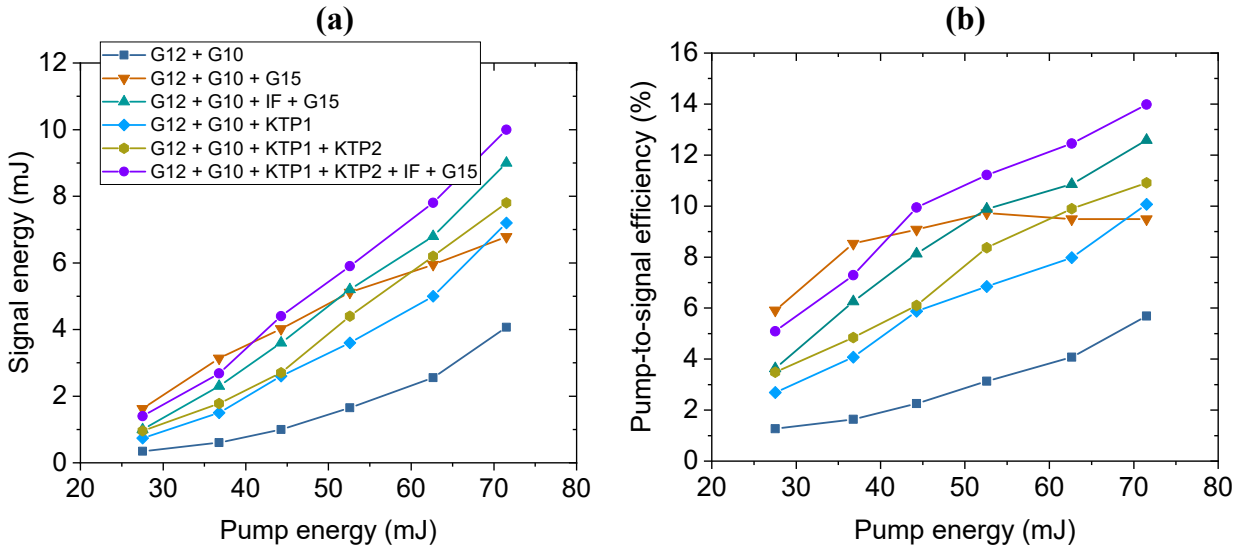

Figure 4.16: Measured signal energy (a) and pump-to-signal conversion efficiency (b) dependent on pump energy for different OPA configurations. IF: idler filtering

It should be noted that the signal energies close to 10 mJ achieved in the framework of the here presented OPA experiments can be considered as an upper limit. During the subsequent DIAL measurement campaigns (see chapter 5), the achieved output energies were substantially lower (3–5 mJ). A part of the lower output energy is due to losses on mirrors and the lenses of the transmitter telescope that were installed after the OPA experiments. Additionally, a degradation of the pump laser beam profile was observed over time due to multiple transports of the setup for the purpose of different measurement campaigns.

4.4.1.5 Comparison with previous work at ONERA

With an output signal energy close to 10 mJ, the current setup based on PPKTP crystals results in lower energy as was demonstrated previously at the SLM group of ONERA. Figure 4.17 shows the MOPA setup

previously realized by Barrientos Barria et al. (2014). In contrast to the current setup based on PPKTP, it consists of a two-step amplifier architecture. In the first step, the NesCOPO-emitted idler beam is amplified in a 25 mm-long 2 mm-thick type-0 PPLN crystal bringing the idler energy close to 1 mJ. In a second step, the idler is further amplified in a chain of three 25 mm-long bulk KTP crystals and an additional 20 mm-long KTP with an idler outcoupling implemented after the third crystal. Furthermore, the entire pump energy of 100 mJ was used for pumping the OPA stage and the transverse beam profile of the pump was of higher quality. All this resulted in a signal output energy of 20 mJ (pump-to-signal efficiency of 20%) compared to 9 mJ of signal for pumping at 70 mJ (pump-to-signal efficiency of 13%) achieved with the current setup based on three PPKTP crystals with idler outcoupling. Table 4.4 summarizes the key characteristics of both systems. It should be noted that although the current setup delivers just around half of the signal energy achieved with the previous development, it is notably more compact due to the use of PPKTP crystals which do not need to be placed in bulky angle-tuning mounts.

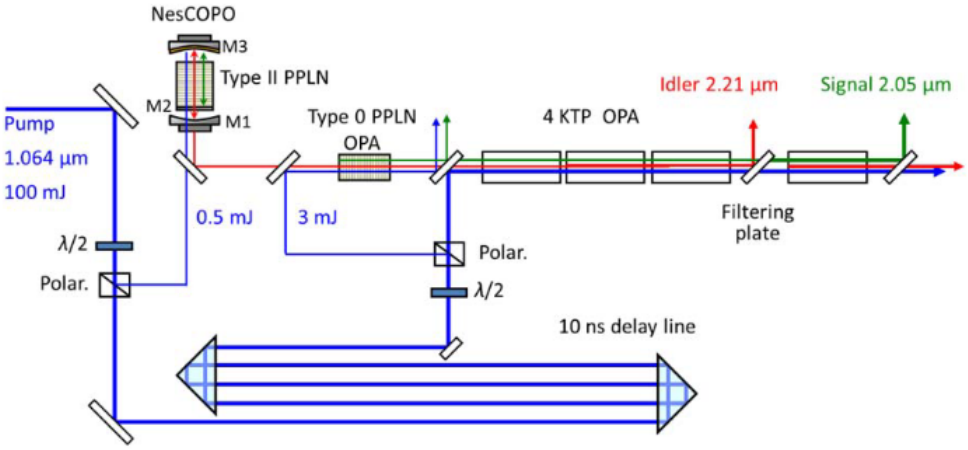

Figure 4.17: Schematic of the MOPA setup previously realized at ONERA (Barrientos Barria et al., 2014)

Table 4.4: Comparison between this work and previous work at ONERA presented in Barrientos Barria et al. (2014)

	Previous work	**This work**
OPA setup	Type-0 PPLN pre-amplifier (25 mm) 4 bulk KTP (20/25 mm) Idler outcoupler after 3rd KTP crystal	3 type-0 PPKTP (12 mm) Idler outcoupler after 2nd crystal
Pump energy	100 mJ	70 mJ
Signal energy	20 mJ	9 mJ
Pump-to-signal efficiency	20%	13%

4.4.2 Measurement of the signal beam propagation factor

An important quantity for assessing the quality of a laser beam is the beam propagation factor M^2 (often called beam quality factor). It is defined as the ratio of a beam's divergence angle and that of an ideal Gaussian beam with identical waist. With an ideal diffraction-limited laser beam having a beam parameter product of λ/π, the M^2 factor can also be expressed as the following ratio in terms of wavelength λ, beam waist radius w_0 and divergence half angle θ:

$$M^2 = \frac{w_0 \cdot \theta}{\lambda/\pi}. \tag{4.9}$$

In the context of lidar, a low value of M^2 is desired in order to achieve a low beam divergence angle for a given beam diameter. The beam divergence must be smaller than the field of view of the receiving telescope to guarantee that the all of the backscattered radiation from the sounded atmospheric volume reaches the detector surface (overlap function of unity).

The beam propagation factor of the amplified signal beam of the setup shown in Fig. 4.13 with the amplifier configuration (c) was determined by measuring the beam diameter (4σ-criterium) at different positions along the propagation direction in the vicinity of the focal plane created by a lens with a focal length of 500 mm. The M^2 value can then be obtained by a fitting function of the following form to the measured beam radius data:

$$w(z) = w_0 \sqrt{1 + \frac{(z - z_0)^2 \lambda^2 (M^2)^2}{\pi^2 w_0^4}} \tag{4.10}$$

where z_0 is the position of the beam waist with radius w_0. The measured beam caustic and the obtained fit are depicted in Fig. 4.18. The resulting M^2 value is 1.33 ± 0.02. The found value is in good agreement with the value used in the simulations for the sensitivity study.

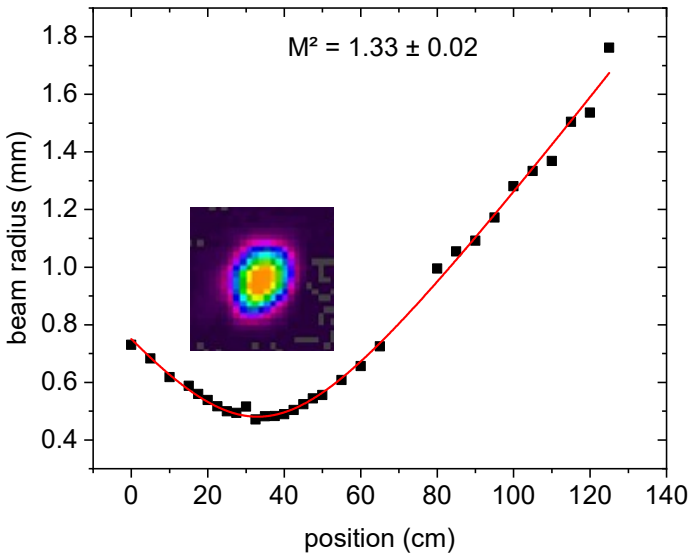

Figure 4.18: Measured beam caustic of the 1.98 µm signal and fit according to Eq. 4.10 to determine the beam propagation factor M^2. Beam diameter was measured according to 4σ-definition. The inlet image shows the transverse profile of the beam waist at the focus of the lens.

4.4.3 Measurement of laser beam pointing fluctuations

The direction of the beam of a laser is subject to beam pointing fluctuations which are of particular concern for many applications. In the context of lidar remote sensing, the transmitter beam should exhibit no or only small pointing fluctuations since the laser beam has to be kept within the field of view of the receiving telescope. Beam pointing fluctuations can be caused by mechanical vibrations and temperature-induced drifts affecting the alignment of critical optical components such as cavity mirrors. Thermal lensing in the gain medium of a laser can also slightly modify the orientation of a laser beam due to focusing and deflection.

In order to quantify the pointing stability of the signal beam amplified in the OPA stage, the position of the beam centroid was monitored using an IR camera (Spiricon Pyrocam III-HR). The camera was located in the focal plane of a focusing lens with focal length of $f = 1000\,\text{mm}$ so that only angular displacements are detected. From the displacement of the beam centroid δy along the y-axis in the focal plane, the angular change in y-direction is found to be:

$$\delta\theta = \frac{\delta y}{f}. \tag{4.11}$$

Figure 4.19 the measured variation of the signal beam centroid position over a duration of 28 min while the NesCOPO was operated on a single longitudinal mode. With a standard deviation of 87 µrad, the angular beam pointing is slightly higher in vertical direction compared to 64 µrad along the horizontal axis. The measured pattern also reveals a drift which is more pronounced in vertical direction. For the MOPA setup of Fig. 4.13, the laser beam pointing of the generated signal beam is expected to follow the pump laser pointing (which was unfortunately not measured in parallel here). This explains the larger fluctuations observed in vertical direction as this was generally noticed for the Nd:YAG pump laser during the experiments.

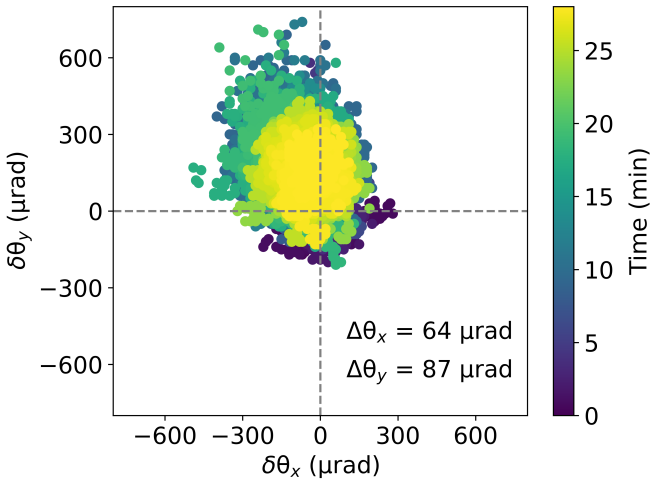

Figure 4.19: Measurement of the signal beam centroid position over a duration of 28 min. $\Delta\theta_x$ and $\Delta\theta_y$ indicate the standard deviations of the angular displacement in in horizontal and vertical orientation.

It is worth mentioning that the presented measurement was obtained with the pump laser frequency well stabilized. The frequency stabilization of the pump laser is realized by a servo-loop integrated within the commercial laser seeder. A minimization of the Q-switch build-up time is used to lock the Nd:YAG

resonator length to the seed wavelength. Under conditions that require a high degree of stabilization (large temperature fluctuations for example), abrupt changes of the pointing direction can be caused by the piezo transducer inside the laser cavity when the build-up time stabilization approaches the end of the voltage range and the piezo voltage is reset. Furthermore, the influence of applying a voltage modulation to one of the NesCOPO cavity mirrors, which is the necessary during DIAL measurements in order to switch between on- and off-line wavelengths, was also not investigated here.

Finally, the measured values of beam pointing represent the angular fluctuations at the level of the OPA line. For lidar measurements, the amplified signal beam diameter is increased using a beam expander with a magnification factor of around 8. Consequently, this results in an 8-times reduction of the angular beam pointing fluctuations downstream of the beam-expander telescope. Based on a measurement of the beam diameter at the transmitter output and the M^2 value of 1.3 determined in the previous section, the full divergence angle of the signal beam sent into the atmosphere for DIAL measurements is estimated as 300 µrad. As a consequence, the relative angular pointing stability of the lidar beam, defined as the beam angular stability divided by the divergence angle, is better than 5% (RMS) for the investigated half-hour duration under the conditions that the pump laser is very stable and no wavelength switching is applied.

4.5 Conclusion

In this chapter, the setup of a parametric laser source developed to serve as the transmitter of the WaVIL system capable of sounding the water vapor isotopologues H_2O and HDO at 1.98 µm was outlined. It is based on a MOPA-architecture consisting of a nested-cavity OPO and a parametric amplification stage in order to achieve mJ-level pulse energies necessary for range-resolved DIAL measurements. Bearing already in mind the desired multi-species capability of the future LEMON instrument, the amplifier stage is based on innovative, state-of-the-art high-aperture PPKTP crystals as quasi-phase matching allows for high integration and robustness compared to critical phase-matching and because PPKTP offers a high effective nonlinear coefficient, high damage threshold and favorable mechanical and thermal properties.

An experimental approach was taken to maximize the extracted signal energy from different combinations of PPKTP crystals and a clear improvement in signal output energy was demonstrated for configurations that used an idler filtering to reduce gain saturation effects. Signal energies up to 10 mJ were achieved with a 70 mJ pump beam. The achieved signal energy is limited by the damage threshold of the anti-reflection coatings on the PPKTP crystal facets which means that more than half of the available pump energy is unused. A way to overcome this issue is pursued in the framework of the LEMON lidar development where two separate OPA stages will be used which is discussed in more detail in chapter 6.

The conducted experiments also served as a means to validate and adjust numerical calculations that were performed by Fraunhofer ILT in the framework of the LEMON project. Based on the experimental data, the effective nonlinear coefficient of the utilized PPKTP crystals was determined which helped the design process of the future LEMON lidar transmitter.

Chapter 5

DIAL measurements of water vapor isotopologues and carbon dioxide using the 2 µm parametric source

This chapter presents a selection of ground-based, direct-detection DIAL measurements of the water vapor isotopologues H_2O and HDO conducted in the framework of the WaVIL project utilizing the 2 µm parametric laser transmitter presented in the previous chapter. The presented DIAL measurements are divided into three campaigns for H_2O/HDO and an additional one for the vertical sounding of CO_2 at 2.05 µm that were conducted between April 2021 and April 2022. The different lidar architectures used throughout the measurement campaigns are introduced and the DIAL retrieval results are discussed and compared to auxiliary measurements if available.

5.1 Overview of measurement campaigns

The parametric laser source described in the previous chapter served as lidar transmitter in the framework of four measurement campaigns which are listed in Table 5.1. The first campaign was conducted in the spring of 2021 with the lidar installed in a provisional laboratory on the rooftop of a five-storey building at the ONERA facilities in Palaiseau. The lidar receiver for this campaign consisted of a Newton telescope with an aperture of 25 cm which was mounted in a horizontal orientation, thus enabling DIAL measurements along a horizontal line of sight for preliminary DIAL soundings of the water vapor isotopologues H_2O and HDO. The second measurement campaign was a field campaign in the Ardèche region in southern France with the aim of testing the setup in such an environment with the possibility to compare the DIAL-measured profiles with auxiliary in situ measurements. The laser bench was integrated into a mobile lidar truck and was transported to the site of the field campaign. The lidar receiver consisted of a zenith-looking Cassegrain-type telescope (40 cm aperture) which was the originally-planned telescope configuration for the WaVIL instrument. Due to challenging experimental conditions during the field campaign and an alignment issue with the telescope, the obtained lidar signals are characterized by rather low signal-to-noise ratios.

For both the first and the second measurement campaigns, a commercial calibration source (852 nm) was used to calibrate the wavelength meter. However, this approach resulted in a substantial wavelength

bias (roughly 10 pm) at the DIAL wavelength range around 1.98 µm, which was only discovered afterwards giving rise to the need for an a posteriori correction of the DIAL wavelengths in the mixing ratio retrievals.

After the field campaign and some additional tests conducted in November 2021, the lidar truck was relocated to ONERA with the aim of conducting vertical measurements of H_2O and HDO with an improved setup. Due to the alignment issues with the Cassegrain telescope utilized at the field campaign, the most convenient and quick solution consisted in replacing it with the Newton telescope which was already utilized in the framework of the first measurement campaign. Additionally, the wavelength meter calibration was also improved by calibrating with a laser diode emitting at 1.58 µm and then checking the measured wavelength against a well known reference at 2.05 µm. This improved lidar setup finally enabled the collection of several data sets of H_2O and HDO measurements in the atmospheric boundary layer in the spring of 2022 of which a selection is presented in section 5.5. The DIAL-retrieved profile of H_2O is compared to an in situ radiosonde measurement.

And finally, in order to demonstrate the versatility of the NesCOPO-based lidar transmitter, a last and short measurement campaign conducted within a few days in April 2022 was dedicated to sounding CO_2 at 2.05 µm.

Table 5.1: Overview of different measurement campaigns

No.	Time period	Location	Description
1	April–June 2021	ONERA, Palaiseau	horizontal DIAL of H_2O and HDO at 1.98 µm Newton telescope (⌀ 25 cm) calibration λ: erroneous
2	September 2021	Ardèche, southern France	vertical DIAL of H_2O and HDO at 1.98 µm Cassegrain telescope (⌀ 40 cm) calibration λ: erroneous
3	January–March 2022	ONERA, Palaiseau	vertical DIAL of H_2O and HDO at 1.98 µm Newton telescope (⌀ 25 cm) calibration λ: OK
4	April 2022	ONERA, Palaiseau	vertical DIAL of CO_2 at 2.05 µm Newton telescope (⌀ 25 cm) calibration λ: OK

5.2 Lidar architectures

In this section, the lidar architectures that were used throughout the different measurement campaigns are presented. While the laser transmitter was principally the same for all measurements, there are two receiver configurations based on two different telescopes. A summary of key parameters of the WaVIL lidar system is provided in Table 5.2 at the end of this section.

5.2.1 Lidar transmitter

The DIAL transmitter is based on the master-oscillator-power-amplifier architecture consisting of an OPO and an OPA stage presented in chapter 4. A schematic setup of the DIAL transmitter is shown on the left side of Fig. 5.1. For most of the conducted DIAL measurements, the OPA stage consisted of three high-aperture PPKTP crystals pumped by the Nd:YAG laser with 12 ns pulses carrying 70 mJ of energy per pulse. Based on this configuration and by filtering the idler beam prior to the last crystal for enhanced conversion efficiency, signal output energies for DIAL operation ranged from 3–9 mJ. The amplified signal beam is then filtered and passes a beam expander resulting in a divergence full-angle of approximately 300 µrad. The wide range in achieved energies is due to the experimental conditions and probably a deterioration of the pump beam quality over the course of time. Higher energies were achieved during the first measurement campaign with the lidar installed in a container on the rooftop at ONERA, whereas during the field campaign under challenging experimental conditions (temperature changes over 10 K from morning to afternoon) the extracted pulse energies were on the lower end of the given range.

The signal wavelength is monitored (pulse-to-pulse) with a commercial wavelength meter (High Finesse WS6 IR) which was calibrated prior to measurements. For measurement campaigns 1 and 2, the calibration was done using a commercial 852 nm calibration source (High Finesse SLR 852), which however did not result in a proper calibration of the wavelength meter. Only for DIAL experiments in the framework of the third and fourth measurement campaign an improved calibration procedure was applied which also allowed to quantify the resulting wavelength accuracy. More details on the wavelength meter calibration are given in each corresponding section.

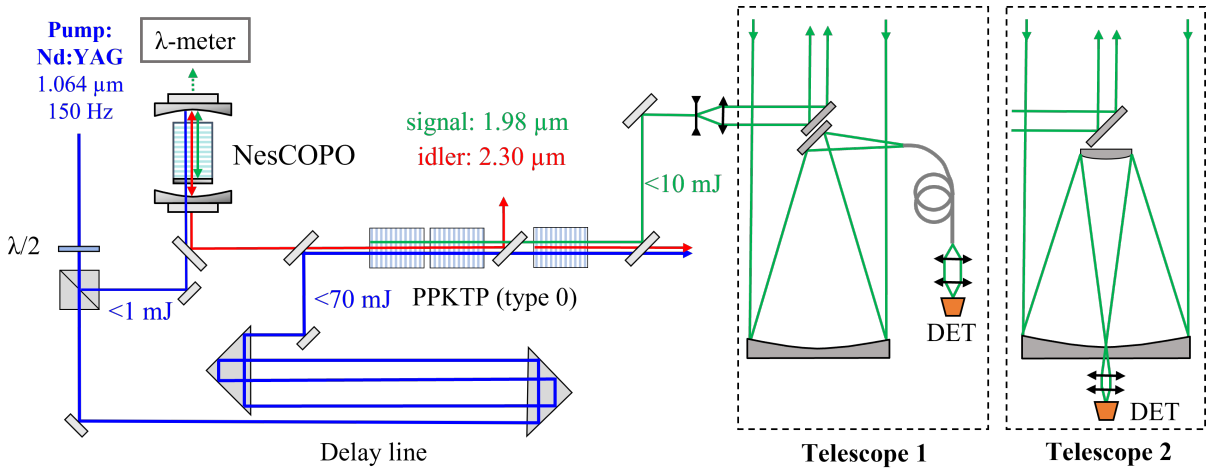

Figure 5.1: Schematic WaVIL instrument architecture. NesCOPO: nested-cavity optical parametric oscillator, PPKTP: periodically poled Potassium Titanyl Phosphate crystals, DET: detector and amplifier. Telescope 1: Newton telescope (25 cm aperture) combined with multi-mode fiber (900 µm diameter) coupled to separate detection unit. Telescope 2: Cassegrain telescope (40 cm aperture) with integrated detection unit. Telescope geometries are only schematic and do not reflect length proportions.

5.2.2 Telescope configurations

Two different telescope configurations were used throughout the measurement campaigns which are both schematically shown on the right in Fig. 5.1. Telescope 1 consists of a 10-inch-aperture Newton telescope which collects the in the atmosphere backscattered radiation and focuses it onto a 900 µm-diameter multi-mode fiber in the focal plane resulting in a full field-of-view angle of 1.2 mrad. The fiber output mode is then imaged onto the detector (300 µm diameter) resulting in a reduction of the transverse mode size by a factor of 0.25. Illuminating the detector with a mode diameter smaller than the size of its active zone is important in order to prevent distortions of the detector response (Cadiou, 2017). Using such a fiber-based approach has the advantage of decoupling the detector alignment from the alignment of the telescope. This comes with the advantage that the detector can be aligned before being integrated into the lidar setup. Such a pre-alignment of the separate detector bench was done by coupling the output of a laser diode emitting at 2051 nm into the multi-mode fiber and by maximizing the detected signal.

The second telescope configuration consists of a Cassegrain-type telescope with an aperture of 40 cm. Figure 5.2a shows a drawing of the telescope design. From the primary mirror side, a tubular component is inserted through an opening in the primary. This tube contains a lens doublet to correct for spherical aberrations and a pinhole (1.2 mm diameter) acting as a field stop. The pinhole is imaged (by a pair of lenses with a magnification of 0.25) onto the detector which is placed at the end of the tube on the backside of the primary mirror. The field of view of 0.63 mrad is defined by the field stop placed 5 mm behind the telescope focal plane. The position of the field stop aperture also determines the lidar overlap function. A pre-alignment of telescope 2 was done in the laboratory before it was installed in the lidar truck. More details on the alignment are given in Section 5.4.4 describing the field campaign for which this telescope configuration was utilized.

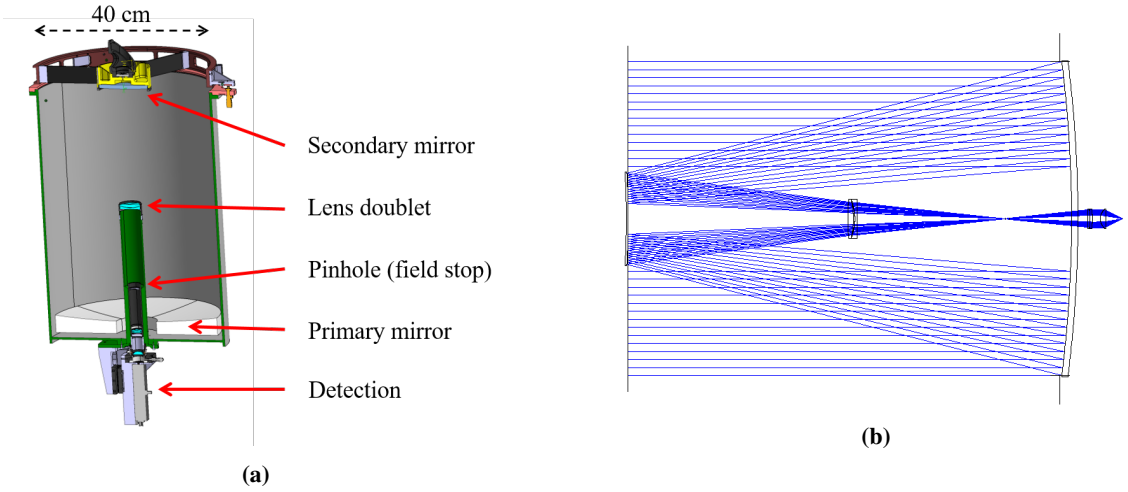

Figure 5.2: (a) 3D drawing of telescope 2. (b) Schematic illustrating the beam path of telescope 2.

Figure 5.3 shows the overlap functions calculated for both telescope configurations. Full overlap is reached at around 250 m for telescope 1 whereas this is the case at around 450 m for telescope 2. An overlap function smaller than unity can be the source of biases in combination with laser beam pointing fluctuations.

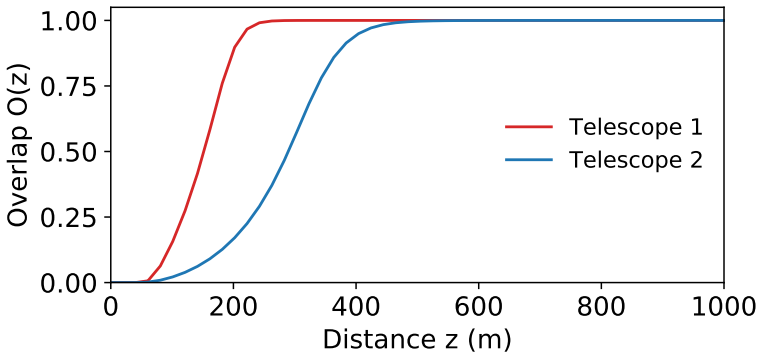

Figure 5.3: Overlap functions for telescope configurations 1 and 2

5.2.3 Detector and data acquisition

The detector used is a commercial InGaAs PIN photodiode (Hamamatsu G12182-003K) with a diameter of 300 µm operated under room-temperature. The photodiode-generated current is amplified by a transimpedance amplifier with a gain setting of 10^6 V A^{-1}, a bandwidth of 3.5 MHz and a noise-equivalent power (NEP) of 1.3 pW $Hz^{-1/2}$. The amplified signals are digitized using an 8-bit high-speed digitizer (Agilent U1084A) featuring a 500 MHz sampling rate and a bandwidth of 20 MHz.

Table 5.2: Key parameters of the WaVIL transmitter and receiver

Transmitter		
Pulse repetition frequency	150 Hz	
Pulse energy	5–9 mJ	depending on conditions
Pulse length	12 ns (FWHM)	
Linewidth	< 100 MHz (FWHM)	
Full beam divergence	0.3 mrad	estimate based on measured M^2
Wavelength monitoring	wavelength meter	High Finesse WS-6-200-IR2
Receiver		
Telescope 1		
Aperture / focal length	25.4 cm / 75 cm	Newton design
Field of view	1.2 mrad	defined by 900 µm fiber
Telescope 2		
Aperture / focal length	40 cm / 190 cm	Cassegrain design
Field of view	0.63 mrad	
Detector		
Detector type	PIN InGaAs photodiode	Hamamatsu G12182-003K
Detector diameter	300 µm	
Transimpedance amplifier gain	10^6 V/A	FEMTO DHPCA-100
Bandwidth	3.5 MHz	
Noise-equivalent power (NEP)	1.3 pW $Hz^{-1/2}$	
Digitizer	8 bits, 500 MHz sampling	Agilent U1084A

5.3 Measurement campaign 1: preliminary horizontal DIAL measurements of H_2O and HDO

In this section, preliminary DIAL tests using telescope configuration 1 (Newton telescope combined with multi-mode fiber) in a horizontal orientation are presented. To conduct these tests, the WaVIL laser bench was transferred to a provisional laboratory container on the rooftop of the J3 building at ONERA in Palaiseau. Examples of a range-resolved measurement of H_2O and HDO along the horizontal line of sight obtained on 16 April 2021 are presented.

5.3.1 Lidar setup and DIAL wavelength selection

Figure 5.4a shows a photograph of the lidar setup with the final path of the 1.98 µm-beam (indicated by the red arrow) leaving the laboratory through the open window in a southwest path as indicated in Fig. 5.4b. A summary of the instrument parameters for all measurements presented in this section is given in Table 5.3. Laser output energies ranged from 6 to 9 mJ, often depending on the temperature stability in the room. The lidar receiver is based on telescope configuration 1 featuring the 25 cm-aperture Newton telescope combined with the 900 µm-diameter multi-mode fiber. The full field-of-view angle of this setup is 1.2 mrad, which is approximately four times larger than the estimated laser beam divergence. The amplified InGaAs PIN photodiode used for the here-presented DIAL experiments was operated at a 10^6 gain setting and a bandwidth of 3.5 MHz.

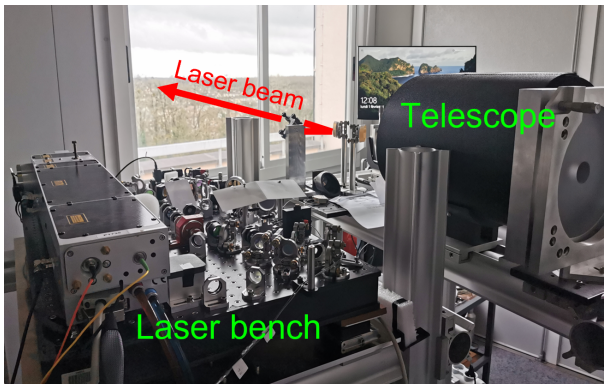

(a)

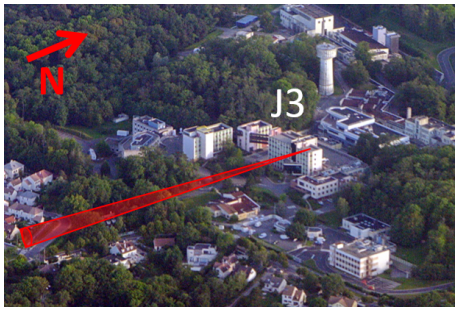

(b)

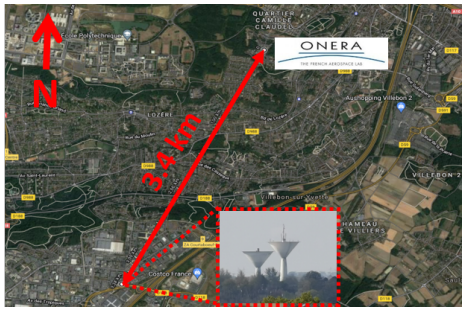

(c)

Figure 5.4: (a) Photograph of the WaVIL instrument with telescope in horizontal orientation. (b) Aerial view of the ONERA site and visualization of the laser beam direction. (c) Line of sight from ONERA to a water tower at a distance of 3.4 km serving as hard target for the alignment.

Table 5.3: DIAL system parameters for preliminary DIAL measurements in horizontal configuration on 16.04.2021.

Laser energy	6–9 mJ
Telescope configuration	Telescope 1 (25 cm Newton-type)
Detector	InGaAs PIN
Gain / bandwidth setting	10^6 V/A / 3.5 MHz
Wavelength calibration	852 nm (erroneous)

Although less interesting in a scientific context, the horizontal measurement configuration comes with some practical advantages. First, the alignment between the laser beam and the telescope axis can be done by aiming at a physical, distant object. This was done by targeting a water tower at 3.4 km distance as shown in Fig. 5.4c. By adjusting carefully the position of the entire lidar setup, it was possible to position the image of the water tower produced in the focal plane of the telescope well centered at the fiber. This ensured that the water tower was centered in the field of view. Then, by steering the laser beam through the field of view and by optimising the return signal from the water tower, the overlap function was optimized prior to DIAL measurements. And second, due to a relatively constant aerosol backscatter coefficient expected along a horizontal path, effects of misalignments on the the geometric overlap can be more easily identified.

Prior to the here-presented measurements, the wavelength meter was calibrated using a 852 nm calibration source (High Finesse SLR 852). This calibration protocol turned out to be erroneous due to the large difference between the calibration wavelength and the DIAL wavelengths at 1.98 µm. Consequently, all wavelength measurements were biased by approximately 10 pm which is large enough to be partly detuned from the on-line absorption peak.

Figure 5.5 shows the expected optical depth of H_2O and HDO for a 1 km path under the atmospheric conditions of 16 April 2021. The on-line wavelength of the main isotopologue is at 1982.93 nm (wavelength option 1 as discussed in the sensitivity study of chapter 3). The on-line wavelength of HDO is at 1982.47 nm (HDO wavelength option 1) meaning that the measured optical depth has to be corrected by a small H_2O bias.

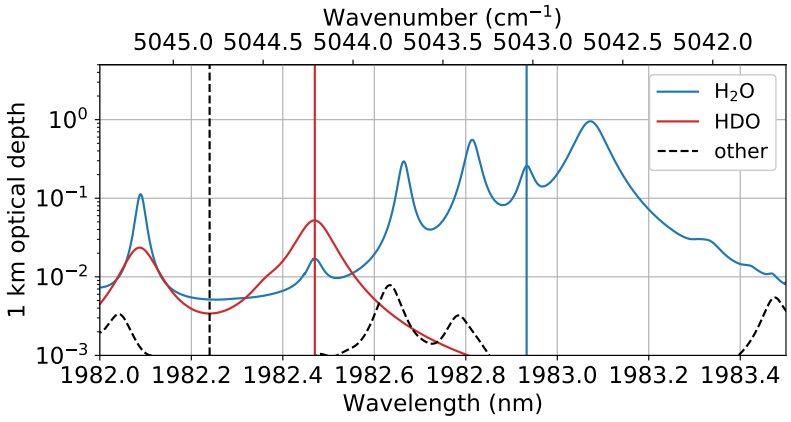

Figure 5.5: (a) Spectrum of the H_2O and HDO optical depths over 1 km under atmospheric conditions of 16.04.2021 (8°C and 1004.25 hPa, 47% relative humidity). Vertical solid lines indicate the DIAL on-line wavelengths, the vertical dahsed line the off-line wavelength.

5.3.2 Lidar signals

Figure 5.6a shows the raw-data (no energy normalization) on- and off-line lidar signals of the H_2O measurement. The signals are averaged over a time duration of ca. 30 min with roughly 73 000 valid on/off-shot pairs were selected in the data post-processing. Each lidar signal is composed of three characteristic features. The initial peak is due to diffusion of the output laser beam on the optics of the setup. The following part of the signal is the aerosol backscatter return with a peak at around 150 m due to the obscuration of the primary mirror by the secondary mirror of the telescope. The signals then fall off according to the inverse of the squared range (R^{-2}). And finally, the signal peak at a range of 3.4 km corresponds to the return from the water tower that served for the alignment between laser beam and telescope axis. Note that both the initial peak and the tower return are at least an order of magnitude higher than the aerosol return leading to a saturation of the digitizer card (or even the detector).

Figure 5.6b depicts the range-corrected (PR^2) representation of the on- and off-line signals. It is obtained by multiplying the lidar signals with the square of the range R resulting in a correction for the R^{-2} signal decrease. The PR^2 representation is helpful to identify a misalignment between the laser beam and the receiver field of view. It is also used to analyze the aerosol structure along the line of sight. In the case of small attenuation, the amplitude of the PR^2 signals is roughly proportional to the density of aerosols. Note that the range-corrected signals in Fig. 5.6b clearly show the difference in attenuation due to the water vapor absorption at the on-line wavelength.

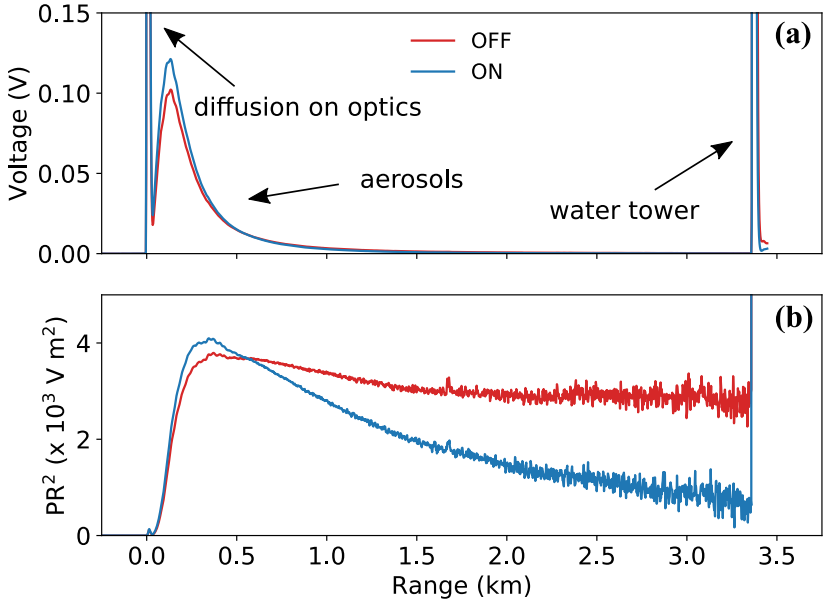

Figure 5.6: (a) Backscattered on- and off-line lidar signals of the horizontal H_2O measurement averaged over 30 min (ca. 73 000 valid on/off-shot pairs). (b) Range-corrected (PR^2) representation of the lidar signals shown in panel (a).

5.3.3 Estimation of the wavelength bias

Due to the fact that the wavelength meter was not calibrated correctly, an a- posteriori-correction of the measured wavelengths needs to be applied for the mixing ratio retrieval. In the following, the wavelength

bias is estimated by comparing the optical depth derived from the measured on- and off-line signals with optical depths obtained by simulation. The simulated optical depths are calculated on the basis of temperature, pressure and humidity data from the SIRTA observatory (Site Instrumental de Recherche par Télédétection Atmosphérique (Haeffelin et al., 2005), 48.71° N, 2.21° E) located only 2 km to the west of ONERA. This approach is based on the assumption that the atmospheric water vapor concentration is the same at the SIRTA point sensor and along the lidar line of sight.

Figure 5.7a shows the DIAL-measured differential optical depth (DOD) between 300 m and 1000 m range and two simulated cases (linear functions of range due to the assumed constant mixing ratio). The first case (grey line) assumes that the wavelength meter reading is unbiased. This leads to the case in which the on-line wavelength is positioned close to the peak of the H_2O absorption line in Fig. 5.7b. However, the measured DOD has a substantially smaller slope leading to an underestimation in the retrievals if no wavelength correction is applied. As shown by the second simulated case in Fig. 5.7a, simulating the DOD with a wavelength correction of -10 pm (red line) leads to good agreement with the measured DOD. This means that during the H_2O DIAL measurement, the on-line wavelength was positioned on the flank of the absorption line as shown in Fig. 5.7b. The following retrievals of the H_2O and HDO mixing ratios thus take into account for this wavelength correction.

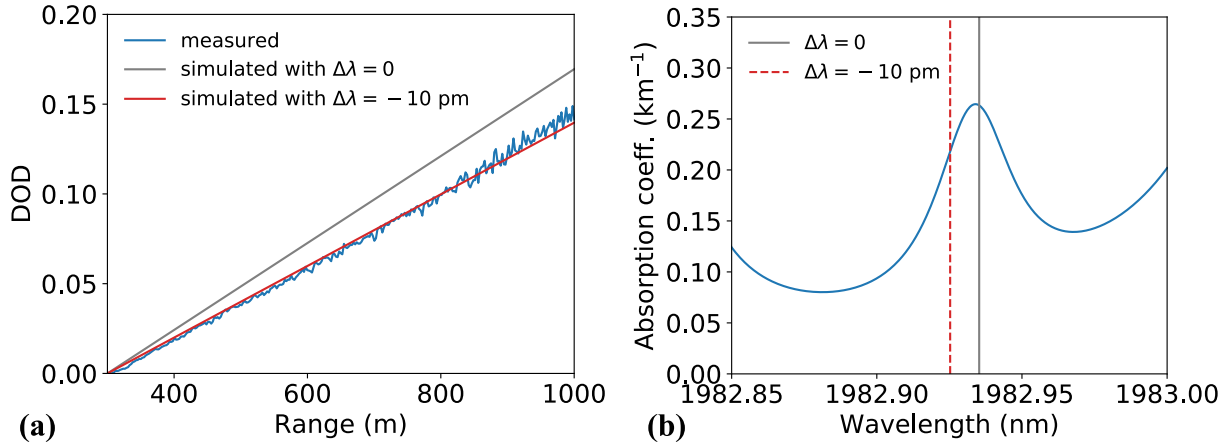

Figure 5.7: (a) DIAL-measured differential optical depth compared to simulated cases with no wavelength correction and a correction of -10 pm with respect to the wavelength meter measurements. (b) Spectrum of the H_2O absorption coefficient. Grey line indicates positioning of the on-line wavelength at the H_2O absorption line as measured by the wavelength meter. Red dashed line shows on-line wavelength position after bias correction of -10 pm for which measured and simulated DOD agree as shown in (a).

It is worth noting that the sign of the wavelength correction cannot be determined using the above described method alone. A fit of the calculated and measured DOD is also possible for an on-line wavelength positioned on the other flank of the absorption line. The negative sign of the bias correction was in fact determined a postiori in the laboratory in the framework of measurement campaign 3 presented in section 5.5. This was done by utilizing a laser diode emitting at 1560 nm which was locked to a hyperfine transition of rubidium-87 atoms. By comparing the wavelength meter reading with the locked diode laser wavelength, it was found that the wavelength meter systematically added a positive bias which was also on the order of 10 pm.

5.3.4 Retrieval of the H_2O and HDO volume mixing ratios

Figure 5.8 shows the results of two separate DIAL measurements of the water vapor isotopologues H_2O and HDO. For each sounding, lidar signals were accumulated and then averaged over a duration of 30 min. After passing through the data post-processing, ca. 73 000 valid on/off-shot pairs were selected for the H_2O retrieval and around 77 000 in the case of HDO. The lidar post-processing first screens each single-shot signal to check if its associated wavelength falls into a pre-specified wavelength interval. This eliminates all laser shots which are not emitted close to the DIAL wavelengths such as cavity mode hops of the NesCOPO. A second filter then only selects consecutive on-line and off-line laser shots, i.e. two shots separated by around 7 ms (inverse of the laser repetition rate of 150 Hz), in order to minimize the effects of fluctuations of the atmospheric backscatter coefficient.

The upper panels of Fig 5.8 show the signal-to-noise ratios of the on- and off-line signals. The SNR is calculated by dividing the received signal voltage by the standard deviation of a pre-trigger signal (usually -5 µs to -1 µs), thus only accounting for detection noise which is the major noise source given the amplifier

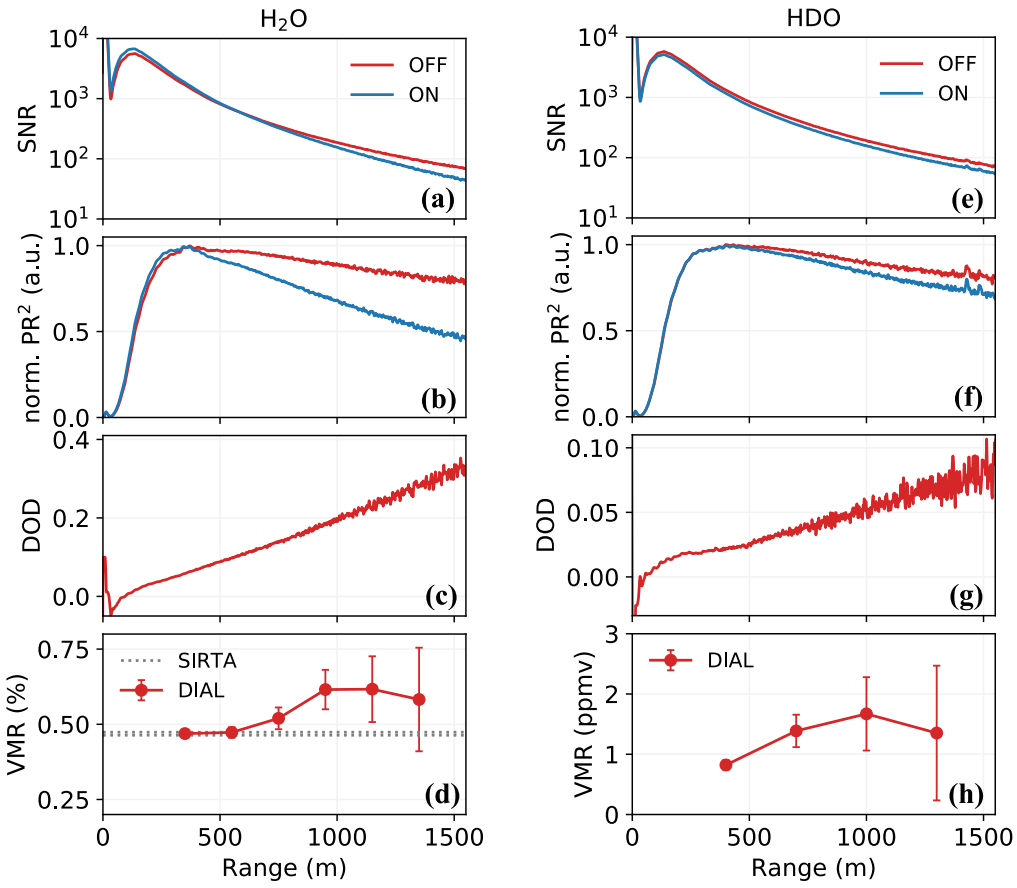

Figure 5.8: Results from DIAL measurements of H_2O (right) and HDO (left) on 16.04.2021 along a horizontal line of sight. Signals are averaged over 30 min (ca. 73 000 valid on/off-shot pairs for H_2O and ca. 77 500 for HDO). (a/e) Raw-data (no energy normalization) signal-to-noise ratios evaluated from detection noise. (b/f) Normalized range-corrected lidar signals. (c/g) Differential optical depth derived from the on/off lidar signals. (d/h) Isotopologue volume mixing ratio retrieved from the DIAL-measured DOD. Range bins of 200 m and 300 m were used for the retrieval of H_2O and HDO mixing ratios, respectively. Error bars indicate standard error due to detection noise.

NEP of 1.3 pW $Hz^{-1/2}$. From the measured on-line and off-line SNR the DOD standard error is calculated according to Eq. 2.37

Figures 5.8b and 5.8f depict the range-corrected lidar signals of the H_2O and HDO measurements, respectively. The signals are normalized to account for differences in the emitted energies of the on-line and off-line cavity modes. The comparison between both PR^2 plots clearly demonstrates the difference in absorption between H_2O and HDO.

The differential optical depths derived from the measured on- and off-line signals are shown in Figs. 5.8c and 5.8g. From the DOD and in the range between 250 m and 1500 m, the volume mixing ratios of H_2O and HDO are retrieved using range bins of 200 m and 300 m, respectively. A larger range bin is used for HDO because of its lower absorption and thus more noise in the measured DOD. The volume mixing ratio at a given range is calculated from the slope of the DOD in each range bin (see Eq. 2.26). To evaluate the derivative of the DOD a linear least-square estimator is used and the local mixing ratio is then calculated from the slope of the linear regression and its random error is determined by the standard error of the regression weighted by the DOD variance obtained from the on-line and off-line SNR. The horizontal line in Fig. 5.8d indicates the H_2O volume mixing ratio measured by the humidity sensor of the SIRTA observatory. The agreement of the first two DIAL points with the SIRTA value is not surprising since it served as a calibration when the wavelength bias was identified by simulation as described earlier.

5.3.5 Conclusion

The preliminary DIAL tests in horizontal configuration from the rooftop of an ONERA building demonstrated for the first time range-resolved measurements of both water vapor isotopologues H_2O and HDO using a single lidar instrument. It was also shown that signal averaging over 20–30 min and range resolutions between 100–300 m are necessary in order to achieve a meaningful precision in the retrieved mixing ratios and that the HDO measurement is particularly challenging due to weaker absorption.

5.4 Measurement campaign 2: vertical DIAL measurements of H_2O and HDO in the framework of a multi-instrument field campaign

This section summarizes the experimental results that were obtained with the WaVIL instrument in the framework of a ground validation field campaign carried out during the EU H2020 LEMON project. The measurement campaign took place at the Aubenas air field (44.54° N, 4.37° E, 281 m above sea level) in the Ardèche region, southern France, between 13 and 24 September 2021. It brought together researchers from the French laboratories ONERA, CNRS, LATMOS, LSCE, Aix-Marseille University and from the University of Bergen, Norway. To participate in this field campaign with the WaVIL instrument assembled at ONERA, the laser bench was transferred from the laboratory into a lidar truck operated by the LSCE laboratory. The main objective of this field campaign was to test the WaVIL system in such an environment and to compare the DIAL measurements with data obtained from auxiliary measurement platforms which helped to identify limitations and biases in the conducted measurements.

5.4.1 Context and approach

The DIAL measurements conducted with the WaVIL instrument during the 2021 field campaign in Aubenas were subject to a range of technical uncertainties. First and foremost, the receiver telescope which was installed in the lidar truck in zenith-looking orientation was never tested before in lidar configuration. A pre-alignment of the telescope was done at ONERA, but no alignment after installation and transport to the field campaign was possible. During the pre-alignment in the laboratory it was also noticed that the position of the field stop aperture could not be adjusted properly. It is also worth noting that it is far from trivial to transfer a laboratory laser bench into a truck. Due to the mechanical shocks and vibrations from the transport of the lidar to the field campaign site, the laser setup needed to be realigned from the start as the pump laser had moved completely out of position. Furthermore, large temperature fluctuations in the lidar truck easily exceeding 5 K between the morning the and afternoon resulted in significant drifts of the pump laser pointing which in turn necessitated a regular realignment of the NesCOPO and the OPA amplification line. And finally, the wavelength meter used for the monitoring of the emitted laser wavelengths was not calibrated correctly which was confirmed after the field campaign through additional tests in the laboratory (same type of calibration error as already discussed in section 5.3.3).

The approach followed in this section essentially consists in using the available experimental data from the conducted DIAL measurements to get an understanding of the limitations and biases. Due to the availability of auxiliary measurements of atmospheric state parameters and both water vapor isotopologues H_2 and HDO with high vertical resolution, it was possible to simulate the experimental conditions and compare calculated signals with the lidar signals that were obtained experimentally in order to identify eventual measurement errors.

(a) (b) (c)

Figure 5.9: Measurement platforms of the field campaign. (a) Lidar truck with both the WaVIL and the WALI instruments. (b) Example of an instrumented ULA. (c) Launch of a radiosonde balloon

5.4.2 Auxiliary measurement platforms

5.4.2.1 Ground-based instrumentation

Besides the DIAL instrument WaVIL, other ground-based instruments included the Raman lidar WALI (Weather and Aerosol Lidar, Chazette et al., 2014) to measure the vertical water vapor field and aerosol distribution and a point sensor for meteorological parameters (pressure, temperature, relative humidity) 5 m above the ground next to the lidars. Figure 5.9a shows the lidar truck in which both lidars were integrated and the meteorological probe on top of the truck.

5.4.2.2 Airborne instrumentation

The deployed airborne platforms included two ultra light aircraft (ULA, see Fig. 5.9b) to monitor meteorological parameters (humidity, temperature, pressure), water vapor isotopic composition, clouds, and aerosols in the lower troposphere. The first ULA (ULA-1) was equipped with a polarized Rayleigh–Mie lidar to infer the aerosol scattering structure of the lower troposphere, a Global Positioning System (GPS) device and a meteorological probe for sampling data of pressure, temperature and relative humidity. The second ULA (ULA-2) carried a CRDS analyzer (Picarro L2130-i) dedicated to the measurement of the water vapor isotopologues , $H_2{}^{18}O$ and and $HD^{16}O$, a meteorological probe (pressure, temperature and relative humidity), a GPS device and a cloud water collector. Finally, the availability of balloon radiosondes provided an additional in-situ instrumentation to measure vertical profiles of pressure, temperature and relative humidity.

5.4.3 Analysis of the in situ measurements

On 23 September 2021, the WaVIL instrument was operational from around 09:50 am to 12:45 pm (CET). The main isotopologue was addressed with two separate measurements with the first conducted between 09:50 am and 10:20 am and the second from 12:15 pm to 12:45 pm. HDO measurements were performed from 10:40 am to 11:50 am. Figure 5.10 illustrates the availability of the auxiliary in situ measurements during the operation of WaVIL. For the first H_2O measurement, reference profiles from simultaneous observations were obtained by both ULAs. Additionally, a first radiosonde was launched at around 10:45 am. During the HDO DIAL measurement, reference profiles were obtained by the CRDS-equipped ULA-2.

A second radiosonde was launched at 12:05 pm serving as an in situ reference for the second H_2O DIAL experiment.

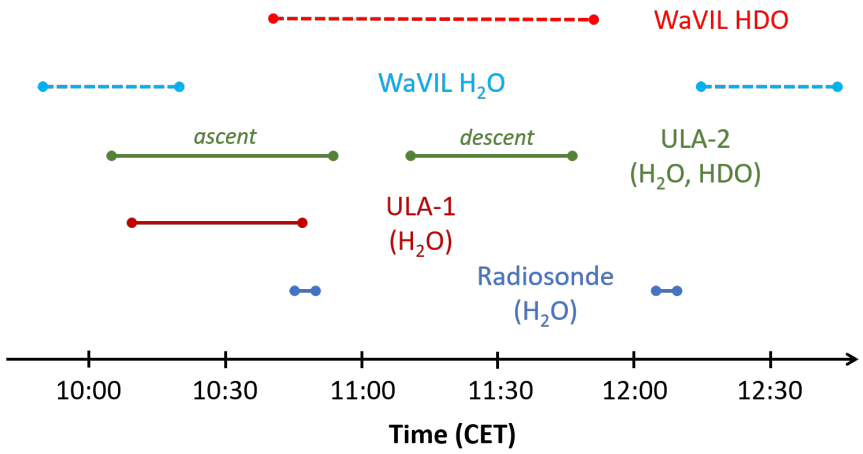

Figure 5.10: Data availability from different instruments for the morning of 23 September 2021. For ULAs, only data within the first 1.5 km are considered.

Using the ULAs to obtain vertical in situ profiles as a reference for the WaVIL measurement, data were sampled in the first kilometer of the troposphere above the lidar using a spiral flight path as illustrated in 5.11a. At different height levels spaced by 50–100 m, the ULA flew rectangular loops around the ground position of the lidar extending ca. 2 km and 3 km in latitudinal and longitudinal direction, respectively. Using this flight path strategy, it took around 20 min to obtain a single profile up to a height of 1 km.

Figure 5.11b shows the H_2O profiles measured by the CRDS onboard the ULA-2 for its ascent (dark

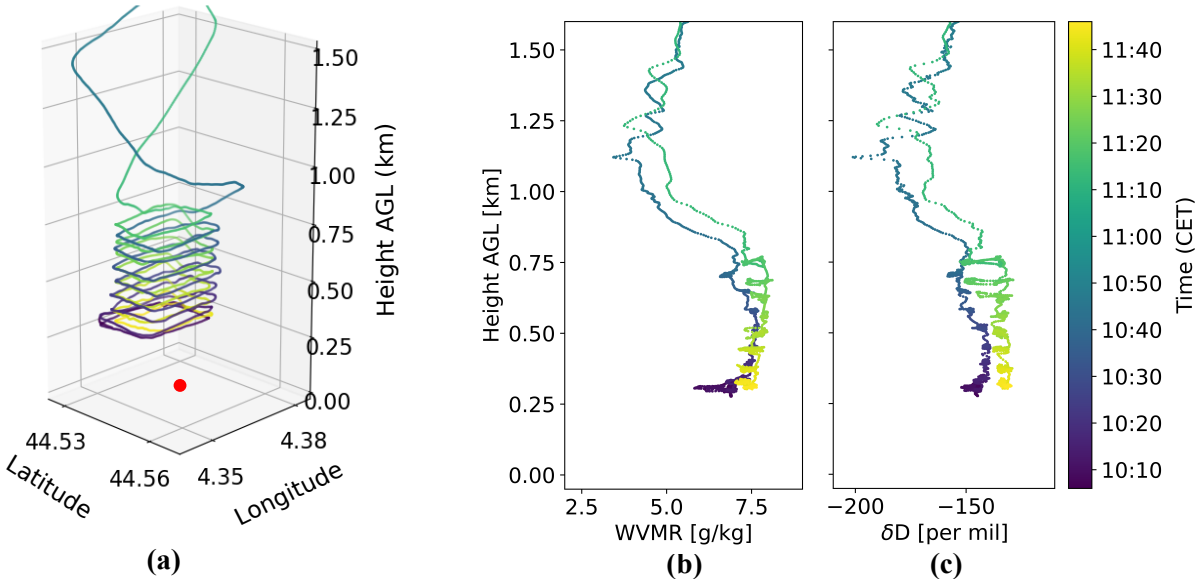

Figure 5.11: Measurement of water isotopologues by CRDS mounted on ULA-2. (a) Ascending (violet/ blue colors) and descending (green/yellow colors) spiral flight paths of the ULA above the lidar truck (red dot). Dimension of the spiral in the horizontal plane is roughly $2 \times 3\,\mathrm{km}^2$. (b) Ascent and descent profiles of the water vapor mixing ratio. (c) Ascent and descent profiles of HDO isotopic abundance δD.

colors) and its descent (green/yellow colors). The resulting profiles of the HDO isotopic abundance are shown in Fig. 5.11c. Both measurements show an increase of the concentration of H_2O and HDO between the ascent and the descent measurement which is consistent with the increasing water vapor content measured by the meteorological probe on the ground plotted in Fig. 5.12a. The observed horizontal variability at a single height level can be attributed to the rectangular flight pattern of kilometer-dimension where differences in the measured water vapor content and δD can be explained by topographic differences or thermal winds.

A comparison of all in situ measured water vapor profiles is given in Fig. 5.12b. It shows relatively good agreement on the overall structure of the vertical water vapor field, but it also shows the difficulty of such inter-comparisons as the measured profiles strongly depend on timing and the exact flight paths of the airborne platforms.

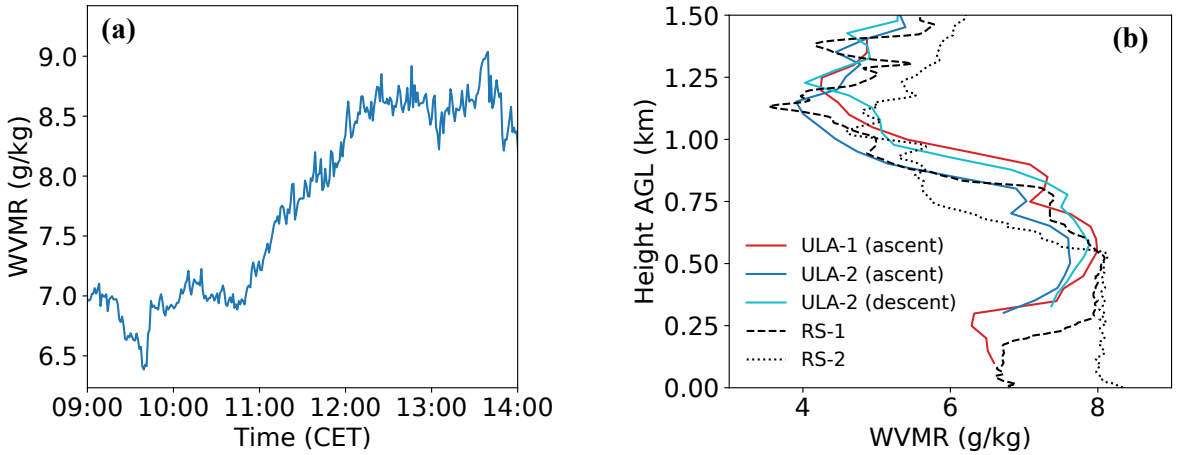

Figure 5.12: (a) Evolution of the water vapor mixing ratio on the ground. (b) Comparison of vertical in situ profiles of the water vapor mixing ratio measured onboard the ULAs and via balloon-borne radiosoundings (RS). ULA data are spatially averaged with a vertical resolution of 50 m.

5.4.4 Lidar setup

The lidar setup used in the framework of the field campaign consisted of the WaVIL laser bench integrated into the mobile lidar truck and the vertically oriented 40 cm-aperture Cassegrain telescope (telescope configuration 2, see section 5.2). Key system parameters of the lidar operation during this field campaign are summarized in Tab. 5.4. Figure 5.13 shows two photographs of the complete lidar system integrated in the lidar truck. Laser output energies at 1.98 µm ranged from 3 mJ to 5 mJ depending on the alignment which was very challenging to maintain due to a continuous increase in room temperature in the lidar truck despite air conditioning. The wavelength meter was incorrectly calibrated with the commercial 852 nm calibration source leading to differences between the wavelength meter reading and the actual wavelength at 1.98 µm of close to 10 pm. Section 5.4.5.3 presents an approach to estimate the wavelength bias by comparing the measured optical depth to a simulated case based on auxiliary measurement data.

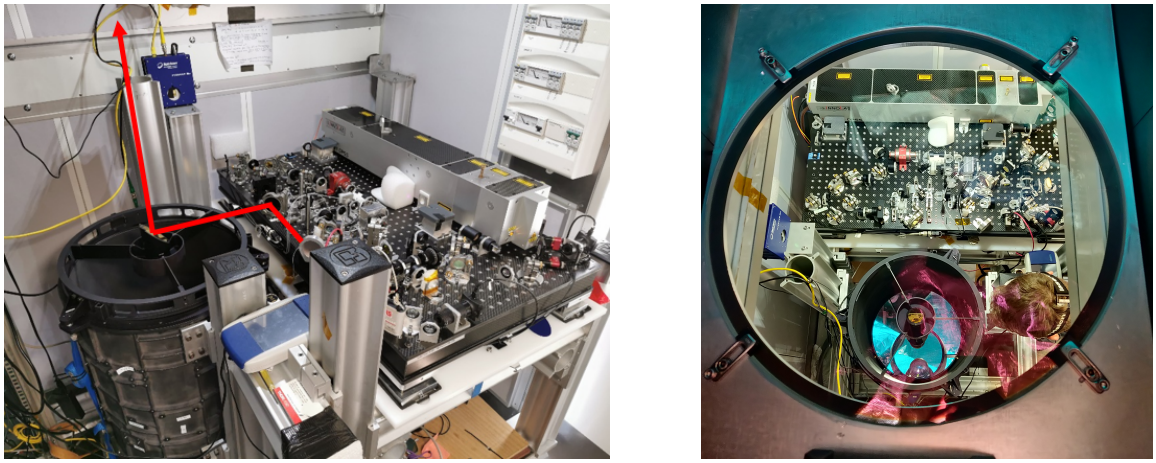

(a) (b)

Figure 5.13: Photographs of the WaVIL instrument setup integrated in the lidar truck. (a) Side view of the laser bench and the telescope from the interior of the lidar truck. Red arrow represents the final path of the laser beam. (b) Top view of the setup through the ceiling window.

Table 5.4: DIAL system parameters for measurement campaign 2

Laser energy	3–5 mJ
Telescope configuration	Telescope 2 (40 cm Cassegrain-type)
Detector	InGaAs PIN
Gain / bandwidth setting	10^6 V/A / 3.5 MHz
Wavelength calibration	852 nm (erroneous)

5.4.5 DIAL measurements of H_2O and HDO

5.4.5.1 Selected absorption lines

Table 5.5 lists the spectroscopic parameters of the absorption lines that were addressed for the DIAL measurements of H_2O and HDO. It is important to note that for H_2O the water vapor absorption line at around 1982.66 nm was targeted for the DIAL measurement. It is an absorption line which was not considered for DIAL sensing in the sensitivity analysis in chapter 3 as it has a considerably stronger temperature sensitivity (high lower-state energy E") than the originally proposed absorption line at 1982.93 nm. This was a choice out of technical necessity as the NesCOPO did not operate stably enough due to misalignment caused by the transport to allow for a wavelength switching between the on- and off-line wavelengths over the entire parametric gain bandwidth (ca. 1 nm). Consequently, the absorption line at 1982.66 nm was chosen so that an off-line wavelength at 1982.59 nm could be accessed via mode hop by a single free spectral range. The on-line wavelength for HDO is at 1982.47 nm which corresponds to one of the proposed wavelength options. However, a bias correction stemming from an H_2O absorption feature at this wavelength has to be taken into account.

Table 5.5: Spectroscopic parameters for selected DIAL absorption lines from the HITRAN2020 database. ν: wavenumber, λ: vacuum wavelength, S: line intensity at 296 K, γ_{air}: air-broadened half width at half maximum (HWHM) at 296 K and reference pressure of 1 atm (1013.25 hPa), E": lower-state energy

	ν	λ	S	γ_{air}	E"
	cm^{-1}	nm	$cm^{-1}(molec \cdot cm^{-2})^{-1}$	$cm^{-1}atm^{-1}$	cm^{-1}
H_2O	5043,7377	1982.657	3.55×10^{-24}	0.0291	2246.89
HDO	5044.2277	1982.464	1.17×10^{-24}	0.1036	91.33

5.4.5.2 Lidar signal analysis

Figure 5.14a shows the time averaged off-line signals for all DIAL measurements conducted on 23 September 2021. For H_2O, signals were averaged over ca. 30 min. HDO DIAL signals were acquired over a duration of 1.5 h, but for analysis two data sets of 45 min are considered here. The depicted lidar returns all show the characteristic initial peak caused by diffusion of laser light at the optics, however its intensity is relatively small and it does not saturate the detector or the signal digitizer. A significant difference can be observed between the lidar signal of the second H_2O measurement and the rest of the signals. This is due to a strong angular misalignment between the laser beam and the central axis of the telescope field of view. The misalignment is even better illustrated in the range-corrected representation of the off-line signals shown in Fig. 5.14b. Since such misalignment can lead to strong bias due to incomplete overlap between laser beam and telescope field of view, the H_2O (2) data set will not be further analyzed or used for the mixing ratio retrieval. For the remaining data, the range-corrected plots indicate a significant loss of signal towards a range (height) of 1 km which is either due to the absence of aerosols in the upper part of the boundary layer and the free troposphere or an alignment issue related to the positioning of the field stop aperture in the telescope setup. An investigation of this problem is presented in section 5.4.6 by comparing observed signals with simulated cases.

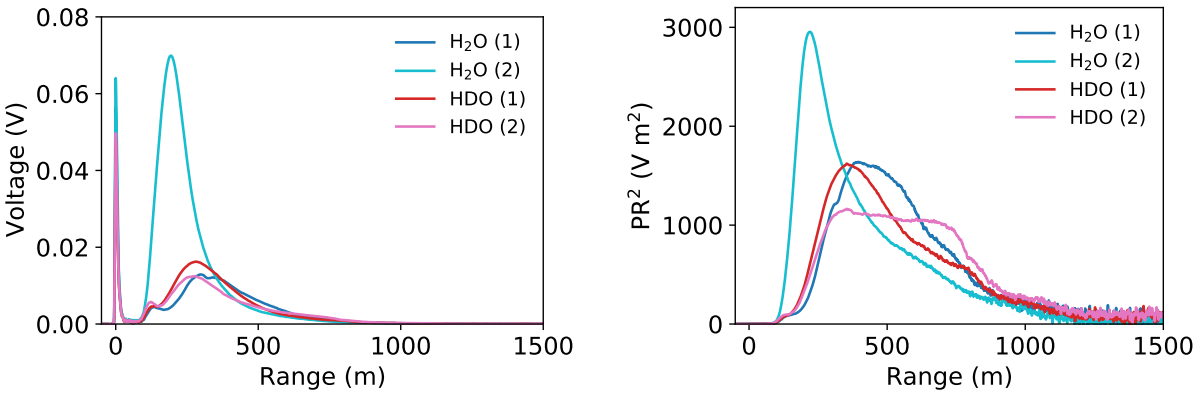

(a) **(b)**

Figure 5.14: Off-line signals for two sets of H_2O and HDO DIAL measurements. Signals are time averages over 30 min and 45 min for H_2O and HDO, respectively. (a) Average voltages of the off-line lidar signals. (b) Range-corrected signals

5.4.5.3 Estimation of the wavelength meter error

Due to the improper wavelength meter calibration method applied during the field campaign, all DIAL measurements were conducted with a substantial wavelength bias. In the following, simulated atmospheric transmissions for the laser beam at the on- and off-line wavelengths are utilized to give an estimate of this wavelength bias. The simulations are based on the CRDS-obtained H_2O and HDO profiles as well as temperature and pressure data measured onboard the ULA-2 during the H_2O (1) and HDO (1) DIAL measurements. The approach consists in simulating the differential optical depth (DOD) for different wavelength detunings from the initial DIAL wavelengths and comparing the thus obtained DOD with the measured DOD based on the off- and on-line signals. When simulated and measured DOD coincide, the corresponding wavelength detuning is the wanted wavelength bias.

Figure 5.15a depicts two cases of simulated DOD for H_2O. The first case (grey line) is based on the assumption that the wavelength meter reading is unbiased. This leads to the case in which the on-line wavelength is positioned close to the peak of the H_2O absorption line in Fig. 5.15b. However, the measured DOD is substantially lower leading to an underestimation in the retrievals if no wavelength correction is applied. As shown in Fig. 5.15a, simulating the DOD with a wavelength correction of -10 pm (red line) leads to good agreement with the measured DOD. This means that during the H_2O DIAL measurement, the on-line wavelength was positioned quite significantly away from the absorption peak as shown in Fig. 5.15b.

Again, as already discussed in section 5.3 for the preliminary tests conducted at ONERA, the negative sign of the wavelength correction was determined a posteriori in the laboratory by comparison with a laser diode emitting at 1560 nm which was locked to a hyperfine transition of rubidium-87 atoms. The wavelength bias of 10 pm is coherent with the value found in the frame of the preliminary measurements at ONERA.

Figures 5.15c and 5.15d show the same approach applied to the HDO measurement. Due to the absorption feature of H_2O at the HDO line at 1982.47 nm, both contributions to the DOD must be taken into account. Again, simulation with the on-line wavelength at the absorption peak leads to a higher than observed DOD. Similarly to the H_2O case, the DOD was calculated for wavelength correction of -10 pm which in the case of HDO is however not sufficient to achieve an agreement between measurement and simulation. As shown in Fig. 5.15c, a wavelength correction of -18 pm would be needed instead to result in a match between measurement and simulation. That the value found by this approach corresponds to the wavelength meter bias during the HDO measurement at the field campaign is highly unlikely. First, the HDO DIAL measurement was conducted directly after the H_2O measurement meaning that the wavelength meter bias should not have changed drastically within the time frame of 30 min despite a change in temperature in the lidar truck, for example. And second, when using the same simulation approach based on the H_2O (2) data set which was the last measurement on 23 September 2021, the same wavelength detuning of 10 pm is found similar to the H_2O (1) data. A possible explanation could be that there are additional biases, for example spectral impurities caused by unstable operation of the NesCOPO during the HDO measurement.

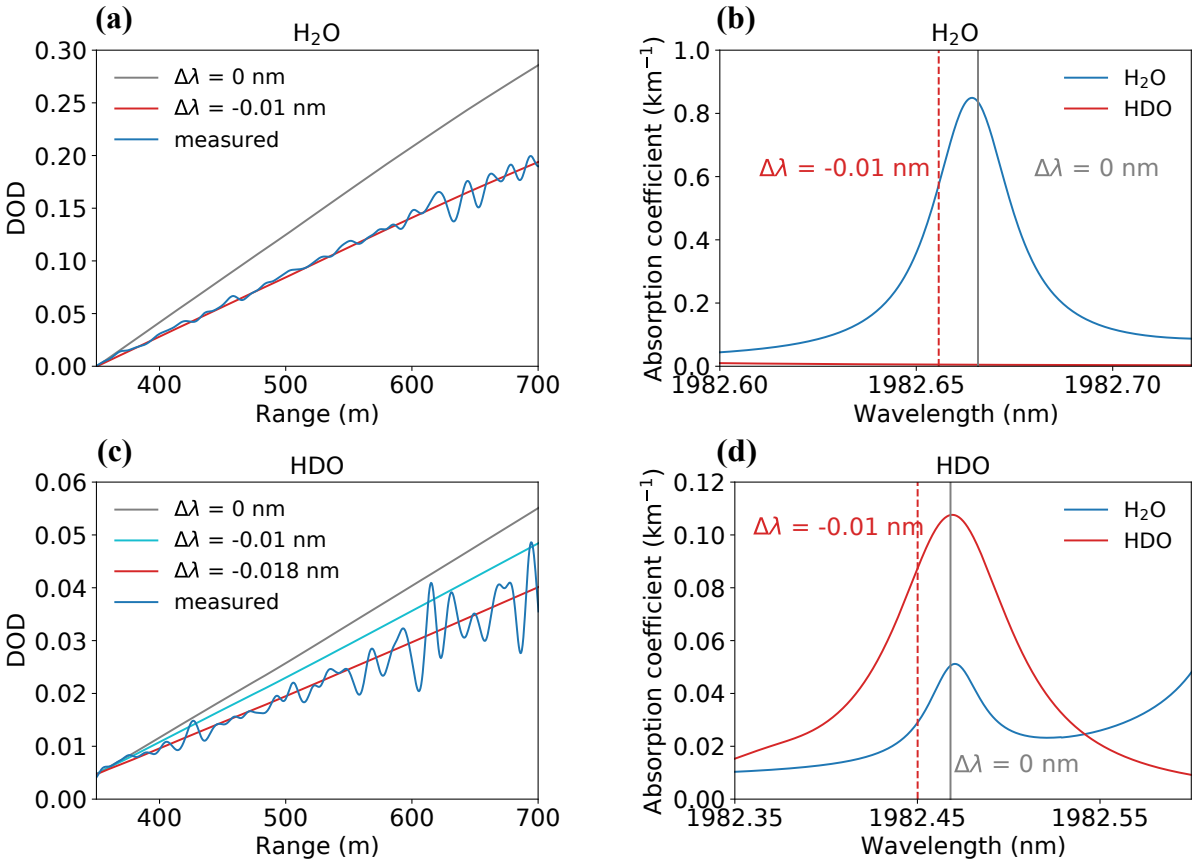

Figure 5.15: Estimation of the wavelength bias by comparing simulated with measured differential optical depths. (a) Measured and simulated differential optical depth (DOD) of the H_2O (1) DIAL measurement. Grey line shows simulated case for the DIAL wavelengths monitored by the wavelength meter. Red line corresponds to DOD with a wavelength correction of -10 pm. (b) Spectrum of the H_2O absorption coefficient (ground level) around the H_2O on-line wavelength of 1982.665 nm. Grey line indicates on-line wavelength as measured by the wavelength meter. Dashed red line is the the resulting on-line wavelength corrected by -10 pm estimated in (a). (c) Same as (a) but for the HDO (1) measurement and an additional simulation using a -18 pm correction. (d) Spectrum of the H_2O/HDO absorption coefficient (ground level) around the HDO on-line wavelength of 1982.470 nm.

5.4.5.4 H_2O/HDO retrieval results and comparison with in situ data

A vertical profile of the water vapor mixing ratio was retrieved using the H_2O (1) data set. Figure 5.16a shows the water vapor absorption spectrum and the distribution of the on- and off-line DIAL wavelengths (corrected for 10 pm wavelength bias) selected for the mixing ratio retrieval. The histograms of the wavelengths are used to calculate the effective absorption cross-sections used for the retrieval. The time averaged on- and off-line signals are depicted in Fig. 5.16b. Signals were averaged over roughly 78 000 selected laser shots over a duration of ca. 30 min. The signal-to-noise ratios are determined from the standard deviation of a pre-trigger signal.

Figure 5.16c shows the raw differential optical depth which is utilized for the mixing ratio retrieval. In this case, the retrieval is restricted to heights < 800 m due to the fast deteriorating SNR. Range bins of 150 m are used and the weight function is calculated based on temperature and pressure data from the meteorological probe onboard ULA-2. The resulting H_2O profile is shown in Fig. 5.16d where it is

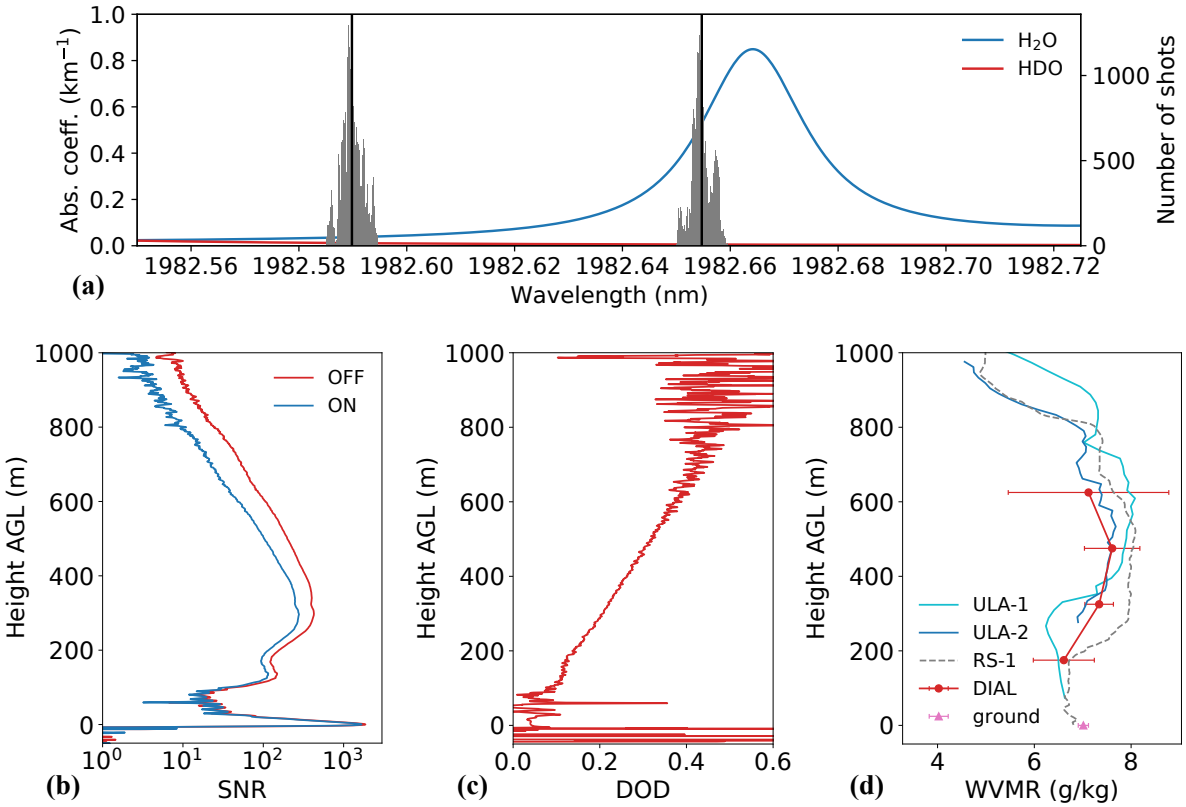

Figure 5.16: Results of the H_2O (1) DIAL measurement. Signals averaging over ca. 30 min (78 296 selected laser shots) (a) Absorption coefficient spectrum (ground level) with the bias-corrected (-10 pm) mean on-and off-line wavelengths (vertical lines). Histograms in grey show the distribution of the on-and off-line wavelengths. (b) Signal-to-noise ratios (averaged, no energy normalization) for the on- and off-line signals. (c) Raw data differential optical depth calculated from the on/off lidar signals. (d) Profiles of the water vapor mixing ratio obtained by DIAL (150 m range bins) compared to different in situ measurements.

compared to several auxiliary in situ measurements showing relatively good agreement but with large error bars due low signal-to-noise ratios.

For the HDO retrieval, the second half of the HDO DIAL measurement period is used since it coincides perfectly with the ascent of the CRDS-equipped ULA-2. Lidar signals were averaged over ca. 185 000 shots (45 min). Figure 5.17a shows the distribution of DIAL wavelengths (again with -10 pm bias correction) and the absorption spectrum of HDO and H_2O. The H_2O absorption feature at the on-line wavelength has to be taken into account in the retrieval by relying on an auxiliary measurement of the water vapor profile and correcting the measured total DOD, which is shown in Fig. 5.17c, by the calculated H_2O optical depth. Figure 5.17d shows the DIAL-retrieved mixing ratio between 200 m and 900 m. Due to low SNR, the entire height interval was used as a 700 m range bin for the determination of the slope using the least-squared estimator method. The retrieval of a range-resolved profile with reasonable error bars is simply impossible for this case characterized by low signal-to-noise ratios. Comparison with the CRDS-measured in situ profile for this height interval reveals a biased DIAL measurement. However, this is expected as detailed previously since the applied wavelength correction of -10 pm does not lead to an agreement between measurement and simulation and therefore additional sources of bias are likely the cause of the observed deviation.

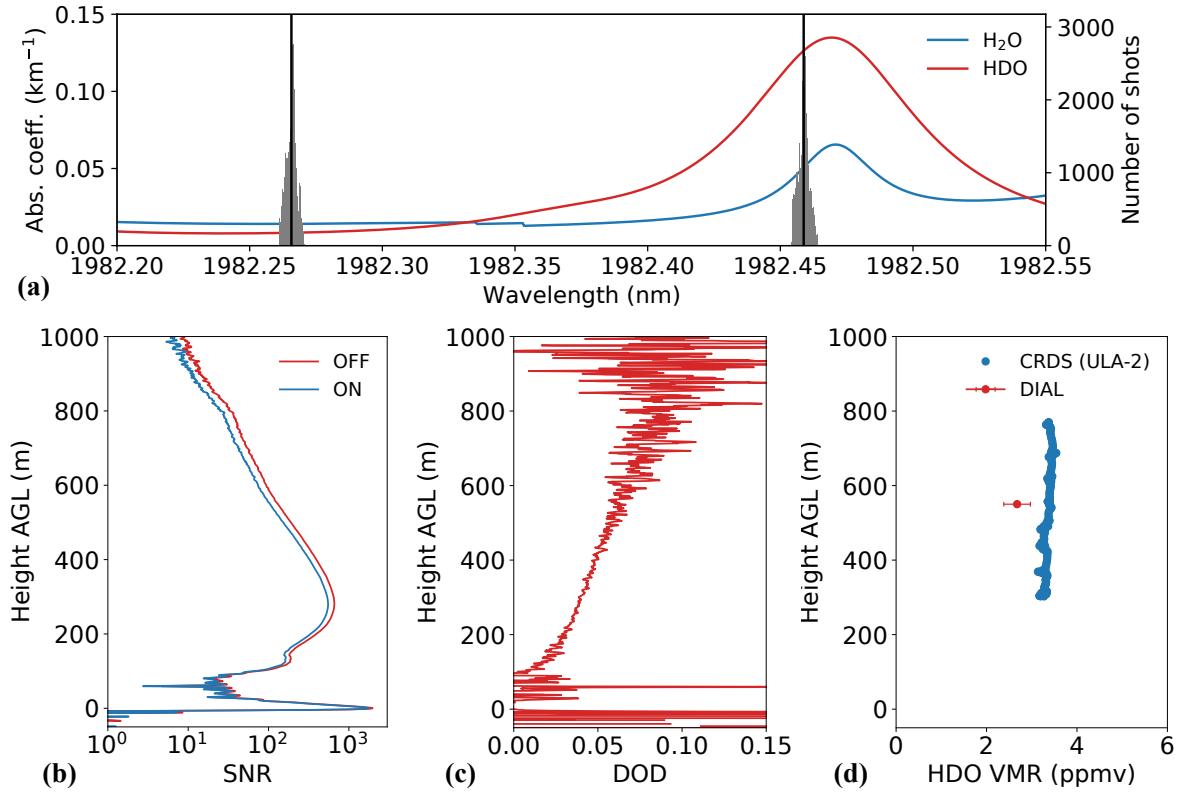

Figure 5.17: Results of the HDO (2) DIAL measurement. Signals averaging over ca. 45 min (185 076 selected laser shots) (a) Absorption coefficient spectrum (ground level) with the bias-corrected (-10 pm) mean on- and off-line wavelengths (vertical lines). Histograms in grey show the distribution of the on- and off-line wavelengths. (b) Signal-to-noise ratios (averaged, no energy normalization) for the on- and off-line signals. (c) Raw data differential optical depth calculated from the on/off lidar signals. (d) HDO volume mixing ratio obtained by DIAL (700 m range bin) compared to CRDS-measured in situ profile.

5.4.6 Additional alignment test after the field campaign

To further investigate the alignment issue of the receiver telescope, i.e. if the field stop diaphragm is positioned improperly with respect to the telescope focal plane, additional tests were carried out after the field campaign at the site of the LSCE laboratory. By using a plane mirror positioned on the roof of the lidar truck in a 45°position and by aiming the emission and reception axis on a water tower at a distance of ca. 2.5 km, a better controlled alignment was achieved in comparison to the field campaign. Furthermore, due to the horizontal configuration, the aerosol backscatter coefficient can be assumed as constant along the line of sight which simplifies the comparison with simulated signals. Assuming that the laser beam axis and telescope field of view are perfectly aligned, the in the following presented analysis compares a measured off-line signal (averaged over ca. 74 000 shots) with simulated cases with varying positions of the field stop (as outlined in paragraph 5.4.4, a potential problem in positioning the field stop was already noticed during the pre-alignment in the laboratory before the field campaign).

Figure 5.18a shows the effect of different field stop positions relative to the focal plane of the telescope on the lidar overlap function. In the ideal case, a diaphragm of 1.2 mm in diameter is positioned 5 mm behind the focus resulting in a full overlap at around 450 m. The two other cases correspond to deviations from the ideal position of 2 mm and 4 mm, i.e. positions of the field stop at 7 mm and 9 mm from the focal

plane. As demonstrated by the simulated overlap functions, a field stop positioned further away from the focal plane favors shorter distances with the overlap reaching unity at shorter ranges. However, at longer ranges the overlap decreases again. In the simulated signals depicted in Fig. 5.18b (off-line signals, i.e. no significant attenuation due to absorption), this is reflected by a loss of signal at long ranges additional to the attenuation due to aerosol extinction. In addition to the simulated cases, Fig. 5.18b also shows a measured off-line signal obtained for a horizontal line of sight. First, the distance at which full overlap is achieved is located at significantly longer distances compared to the simulation. And second, the overlap function seems to have a more complex shape than represented by the simulated cases because a local minimum can be observed in the measured range-corrected signal between 250 m and 500 m. However, an altered overlap function can also be caused by the plane mirror that was positioned on the rooftop of the lidar truck. At least in one direction, the mirror did not cover the entire telescope diameter which could be the cause of the observed behavior in the signal at short ranges. Indeed, a signal which was measured in vertical configuration supports this assumption as it shows no such local minimum (but still a full overlap further away than expected based on the simulations).

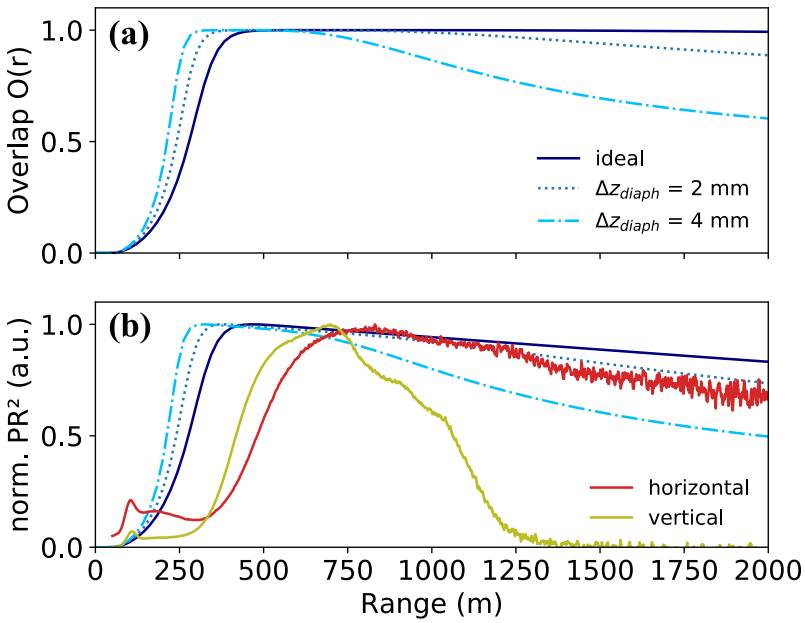

Figure 5.18: (a) Simulated lidar overlap functions for different positions of the field stop. The ideal positioning is 5 mm behind the telescope focal plane. Two other cases represent deviations from the ideal position. (b) Comparison between simulated and measured lidar signals (off-line signals, no significant absorption). Simulations (in blue) are for horizontal line of sight (constant aerosol backscatter coefficient).

All in all, the presented additional test confirmed that the telescope is not properly aligned since its full overlap is reached at distances far greater than simulations suggest. However, to derive a quantitative estimate of the misalignment, which might be due to the positioning of the field stop aperture, by comparing measurement and simulation is not possible because too many parameters influencing the lidar geometry are unknown or not well enough controlled in the experiment.

5.4.7 Conclusion

The multi-instrument field campaign in the southern French region of Ardèche was a valuable opportunity to test the WaVIL instrument under challenging experimental conditions. The rare possibility of having multiple auxiliary in situ measurements, especially an airborne CRDS sensor capable of measuring range-resolved profiles of water vapor isotopologues with high accuracy, were helpful to identify limitations and biases in the conducted DIAL measurements. Unfortunately, the WaVIL system was operational only at the end of the field campaign and this with major issues concerning the receiver telescope alignment, laser stability due to strong temperature gradients and an incorrect wavelength calibration procedure giving rise to a significant wavelength bias. All these factors led to signal-to-noise ratios that were lower than expected for this setup even after long time averaging (more than 30 min). Due to the variety of auxiliary measurements with high vertical resolution, it was possible to gain an insight on the wavelength meter bias. However, it was not to derive quantitative conclusions on the telescope misalignment from the acquired lidar signals as there are too many unknown parameters. Nevertheless, the insights and results from this field campaign helped to significantly improve the WaVIL setup for the subsequent measurement campaign which is presented in the next section.

5.5 Measurement campaign 3: vertical DIAL measurements of H_2O and HDO

After the field campaign of September 2021 and some additional tests at LSCE in November 2021, the mobile lidar truck containing the WaVIL system was still available until May 2022 and was relocated to the ONERA site in Palaiseau for this period. Due to the alignment issues with the Cassegrain telescope used in the field campaign, the most convenient solution consisted in replacing that telescope with the less complex Newton-type telescope which was already utilized in the framework of the first horizontal lidar tests presented in section 5.3. This section presents a selection of vertical measurements of the water vapor isotopologues H_2O and HDO in the boundary layer which were conducted within a time frame from February to April 2022 at ONERA. Random and systematic errors are discussed in the form of an error budget. Using the lidar simulator described in chapter 3, the measured signals and the obtained signal-to-noise ratios are compared to simulated cases.

Parts of the content in this section were the subject of an article submitted to *Optics Express* which was accepted for publication in October 2022.

5.5.1 Lidar setup and DIAL wavelength selection

In the framework of the third measurement campaign, the lidar setup consisted of the WaVIL laser bench and telescope configuration 1. Table 5.6 gives a short overview of key instrument characteristics relevant for the here presented measurement campaign. A major improvement compared to the two previously described measurement campaigns is the wavelength calibration procedure. The wavelength meter was first calibrated using a laser diode at 1579 nm and before and after each DIAL measurement the wavelength meter reading was compared to a reference wavelength provided by a laser diode tuned to a CO_2 absorption line at 2051 nm. The calibration procedure is described in more detail in section 5.5.2.

Figure 5.19 shows the spectrum of the H_2O and HDO optical depths calculated for a 1 km path under the atmospheric conditions during the DIAL measurements on 23 March 2022 ($T = 16°C$, $p = 1010.4$ hPa, RH = 28%) using the line parameters of the HITRAN2020 database (Gordon et al., 2022). The H_2O on-line wavelength is located at 5043.0475 cm^{-1} (1982.93 nm) and the off-line wavelength at 1982.25 nm. HDO is sounded at 5040.4937 cm^{-1} (1983.93 nm) with an off-line wavelength close to 1983.80 nm. Sounding HDO at this wavelength was chosen to avoid the H_2O bias correction which is needed if HDO is targeted at 1982.47 nm. As shown in Fig. 5.19, the differential absorption is significantly higher for H_2O (0.27 over 1 km with constant mixing ratio of 3.1 g/kg) compared to the differential absorption of HDO (0.04 over

Table 5.6: DIAL system characteristics for measurement campaign 3

Laser energy	5–7 mJ
Telescope configuration	Telescope 1 (25 cm Newton-type)
Detector	InGaAs PIN
Gain / bandwidth setting	10^6 V/A / 3.5 MHz
Wavelength calibration	calibrated at 1579 nm and verified at 2051 nm (see section 5.5.2)

1 km assuming $\delta D = 0$). This has implications on the range bin size used for the DIAL retrieval as the random error is inversely proportional to the differential absorption cross-section.

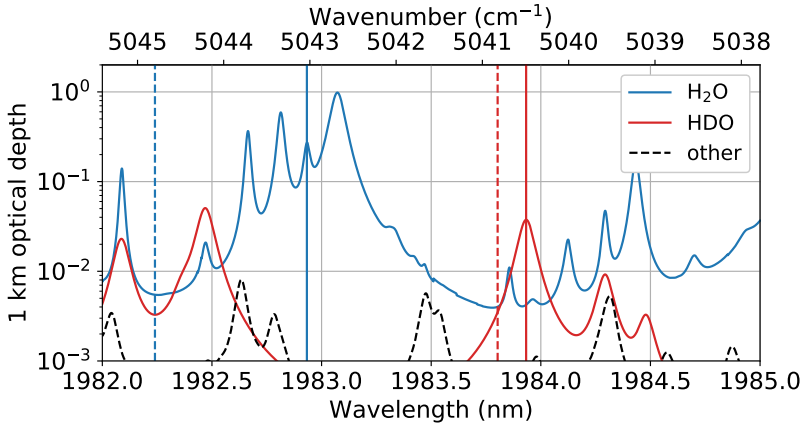

Figure 5.19: Spectrum of the optical depth over a 1 km path with uniform mixing ratios of H_2O and HDO corresponding to the atmospheric conditions during the DIAL measurements on 23 March 2022 ($T = 16$°C, $p = 1010.4$ hPa, $RH = 28\%$) ($\delta D = 0$ assumed for HDO). Dashed black line: other trace gases (CO_2, CH_4, N_2O) assuming typical atmospheric concentrations. Solid and dashed vertical lines: positions of on-line and off-line wavelengths.

Table 5.7 provides an overview of key spectroscopic parameters from the HITRAN2020 database for the H_2O and HDO absorption lines of interest. Note the difference in the lower-state energy E" between H_2O and HDO. A higher value for H_2O gives rise to a higher temperature sensitivity. This implies some a priori knowledge of the temperature profile along the lidar line of sight in order to limit retrieval biases (see error budget in section 5.5.6).

Table 5.7: Spectroscopic parameters for selected DIAL absorption lines from the HITRAN2020 database. ν: wavenumber, λ: vacuum wavelength, S: line intensity at 296 K, γ_{air}: air-broadened half width at half maximum (HWHM) at 296 K and reference pressure of 1 atm (1013.25 hPa), E": lower-state energy

	ν	λ	S	γ_{air}	E"
	cm^{-1}	nm	cm^{-1}(molec·cm^{-2})$^{-1}$	cm^{-1}atm^{-1}	cm^{-1}
H_2O	5043.0476	1982.928	2.17×10^{-24}	0.0367	920.21
HDO	5040.4937	1983.933	9.38×10^{-25}	0.1003	116.46

5.5.2 Wavelength meter calibration and stability

Because the mixing ratio retrieval depends on the absorption cross-sections at the on- and off-line wavelengths, an accurate knowledge of the laser-emitted wavelengths is crucial to limit biases. Therefore, care has to be taken to calibrate the wavelength meter and to estimate the uncertainty related to the wavelength reading during DIAL operation.

Measurements by wavelength meters can be subject to drifts induced by temperature and pressure changes in the instrument environment which cannot always be accounted for in the wavelength calculation (König et al., 2020). To gain an insight into the magnitude of this type of wavelength deviation,

the wavelength meter was used to record the wavelength of a laser diode emitting at 1560 nm locked to a hyperfine transition of rubidium-87 atoms (^{87}Rb). Figure 5.20a shows the observed wavelength drift over a duration of 90 min. The recording was performed under temperature-stabilized laboratory conditions and shows wavelength fluctuations of 30 MHz (peak to peak) which is in line with the accuracy of 40 MHz stated in the wavelength meter data sheet. However, wavelength monitoring under less temperature-stable conditions such as field campaigns is expected to induce larger drifts. It is thus important to calibrate the wavelength meter regularly.

With no calibration source at hand at the DIAL wavelength around 1983 nm and the calibration software requiring wavelengths below 2000 nm, in a first step, a laser diode locked to a CO_2 absorption line at 1579 nm was used to calibrate the wavelength meter. Since this wavelength is over 400 nm below the water vapor DIAL wavelengths, an additional laser diode locked to a CO_2 absorption line at 2051 nm (closest to the DIAL wavelength of 1983 nm) is used to quantify the difference between the theoretical wavelength of the absorption peak and the wavelength meter reading, which is in the order of 2.7±0.6 pm at 2051 nm (see Fig. 5.20b). Assuming a linear increase for the observed differences in wavelength meter measurement and transition-locked diode wavelength, a wavelength correction term of -2.4 pm was estimated that has to be applied to all wavelength meter readings at the DIAL wavelengths around 1983 nm. As a final estimate of the wavelength uncertainty for the error budget a value of 1 pm (75 MHz) is used. This accounts for possible wavelength drifts during the DIAL measurement and the uncertainty related to the procedure of determining the described wavelength correction applied to all DIAL wavelengths around 1983 nm.

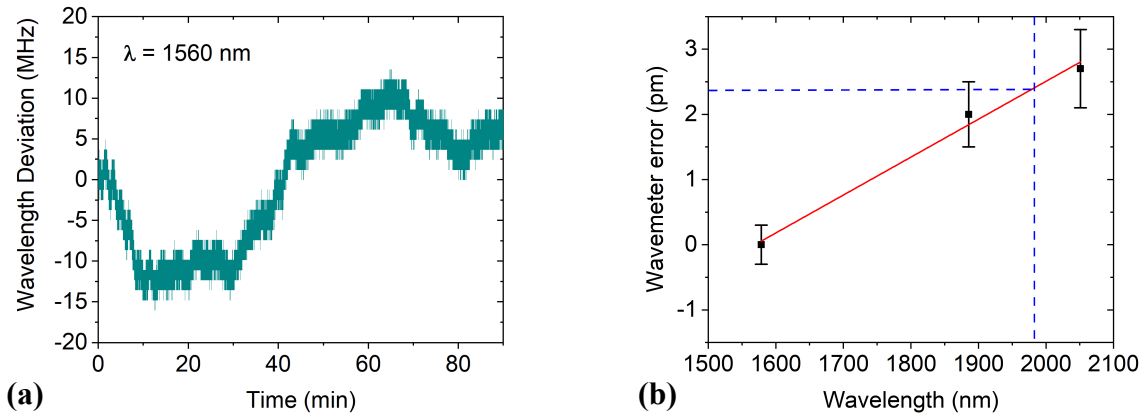

Figure 5.20: (a) High Finesse WS6 IR wavelength meter stability over 90 min determined by monitoring the wavelength of a 1560 nm laser diode locked to a hyperfine transition of ^{87}Rb atoms. (b) Difference between wavelength meter reading and actual wavelength of a laser diode locked to a CO_2 or H_2O absorption line after calibration at 1579 nm. Error bars indicate uncertainty due to the laser diode locking stability.

5.5.3 Measurement conditions and auxiliary instruments

DIAL measurements of the two stable water vapor isotopologues were performed on 23 March 2022 at the facilities of ONERA (48.71° N, 2.23° E) located on the Saclay plateau approximately 15 km south of Paris (see Fig. 5.21). With a water vapor mixing ratio of 3.5 g kg^{-1} measured on the ground, the atmosphere was relatively dry. Figure 5.22 shows the aerosol backscatter signal over the entire day of 23 March 2022

obtained by a cloud and aerosol ceilometer (1064 nm) operated by the SIRTA observatory (Haeffelin et al., 2005, 48.71° N, 2.21° E) also located on the Saclay plateau only 2 km to the west of ONERA. It indicates cloud-free conditions with aerosols trapped in the boundary layer stretching up to a height of 2 km. Apart from a sensor for meteorological parameters such as temperature, pressure and humidity next to the lidar at ground level, the DIAL-retrieved H_2O profile is compared with a measurement obtained by balloon-borne radio sounding launched at 12:00 UTC at the Météo-France site of Trappes (48.77° N, 2.01° E) which is located about 17 km to the north-west of ONERA.

Figure 5.21: Overview map of the different observation locations at the Saclay plateau in the south-western Paris region. The DIAL instrument was located the ONERA site. Aerosol backscatter profiles were measured at the SIRTA observatory. A vertical humidity profile was measured at the Météo France station of Trappes. Map credit: © Google Maps 2022

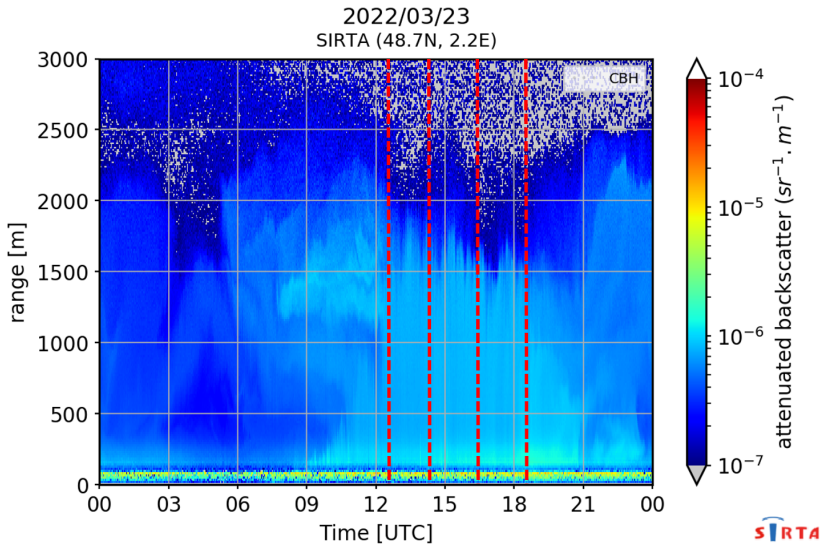

Figure 5.22: Ceilometer measurement of the attenuated backscatter coefficient at the SIRTA observatory on 23 March 2022. Vertical dashed lines indicate time windows during which DIAL measurements of H_2O and HDO were performed at ONERA. Figure credit: © SIRTA 2022

5.5.4 Retrieved vertical profiles of H_2O and HDO

Figures 5.23 and 5.25 show examples of two separate measurements of H_2O and HDO performed consecutively between 12:25 and 13:20 UTC on 23 March 2022. A 5 min-long interruption separates both measurements due to routine checks and the need to adjust the NesCOPO operating temperature in order to switch from the H_2O to the HDO spectral range. In both figures, panel (a) shows the received on- and off-line lidar signals expressed as signal-to-noise ratios (SNR) resulting from time averaging over 25 min (ca. 60 000 and 70 000 valid on/off laser shot pairs for H_2O and HDO, respectively). With the dominant noise contribution related to the transimpedance amplifier (1.3 pW $Hz^{-1/2}$ noise-equivalent power), the reported SNRs take account for detection noise only. The SNR is calculated by dividing the received signal voltage by the standard deviation of a pre-trigger signal. The lower off-line SNR in Fig. 5.23a is the consequence of a less energetic cavity mode emitted by the NesCOPO at the off-line wavelength. Figure 5.23b presents the H_2O raw-data differential optical depth (DOD) derived from the on- and off-line signals

The retrieved vertical profile of the H_2O mixing ratio is plotted in Fig. 5.23c. The depicted profile was derived from the measured DOD using range cells of 150 m and a sampling of 75 m. As a first validation of the obtained profile, the DIAL measurement is compared with a radiosonde in situ measurement launched 17 km away from the WaVIL operation site. The DIAL-retrieved profile compares fairly well to the radiosounding and also to the water vapor content measured by a humidity sensor directly at the lidar on the ground (accuracy ca. 0.25 g/kg).

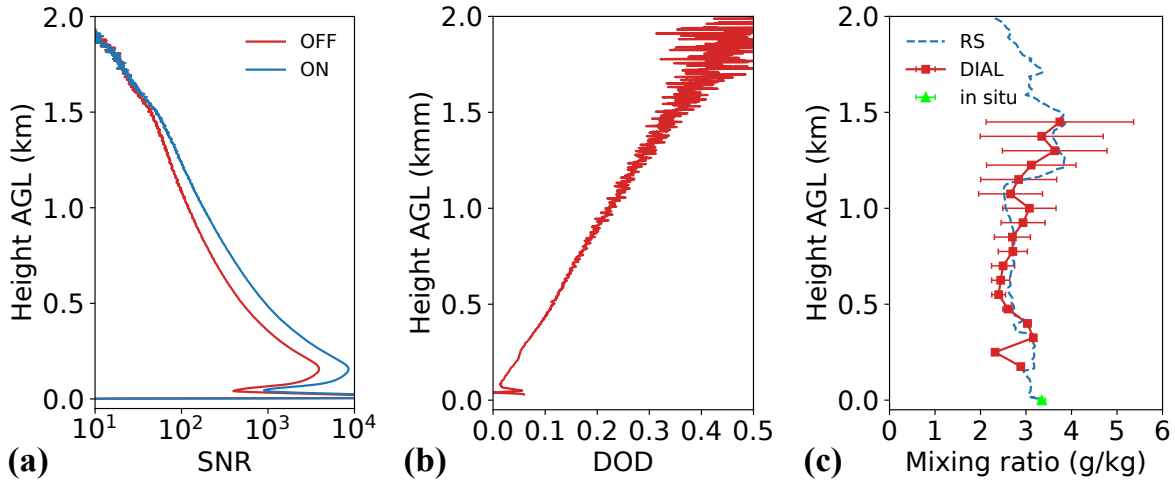

Figure 5.23: DIAL measurement results for H_2O from 12:25 to 12:50 UTC (ca. 60 000 valid on/off shot pairs). (a) Raw (no energy normalization) signal-to-noise ratios of the on- and off-line lidar returns. (b) Recorded differential optical depth. (c) DIAL-retrieved profile of the H_2O mixing ratio (150 m range cells and 75 m sampling) compared to radiosonde (RS) profile and ground-based in situ sensor

In a second validation experiment, the lidar was operated continuously over two hours from 16:30 UTC to 18:30 UTC on the same day to measure the time evolution of the vertical profile of H_2O with a time resolution of 8 min. Figure 5.24 shows the resulting time series for the first point of the DIAL-retrieved profiles at 175 m above ground level (a.g.l.) compared to the in situ point sensor located on the ground. The observed difference between both measurements can most likely be explained by the fact that the water vapor concentration is slightly higher in the surface layer where the in situ probe is located as it is also

the case in the H_2O profile measured earlier on that day shown in Fig. 5.23c. Despite the difference in the measured mixing ratios at ground level and at 175 m a.g.l., a clear correlation is apparent between the in situ and the DIAL measurements proving well the H_2O sensitivity of the WaVIL instrument to small variations in the atmospheric water vapor concentration.

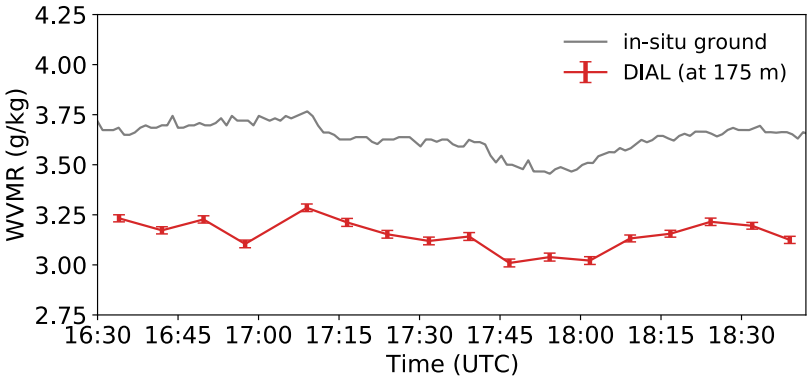

Figure 5.24: Two-hour continuous H_2O DIAL measurement from 16:30 UTC to 18:30 UTC (8 min time resolution) and comparison between water vapor mixing ratio measured in situ on the ground and the first DIAL measurement point at 175 m above ground level. The accuracy of the point sensor is 0.25 g/kg.

Figure 5.25c depicts the retrieved profile of the HDO volume mixing ratio. Due to the significantly lower differential absorption of HDO, and thus more noise in the obtained DOD, the range bin size of the retrieval has to be significantly increased in order to limit the resulting random error at the cost of range resolution. In the presented HDO profile range cells of 600 m and a spatial sampling of 300 m are used. With no reference measurement of HDO available during the operation of the WaVIL instrument, the retrieved HDO profile is compared to an estimated range of the HDO mixing ratio calculated from the

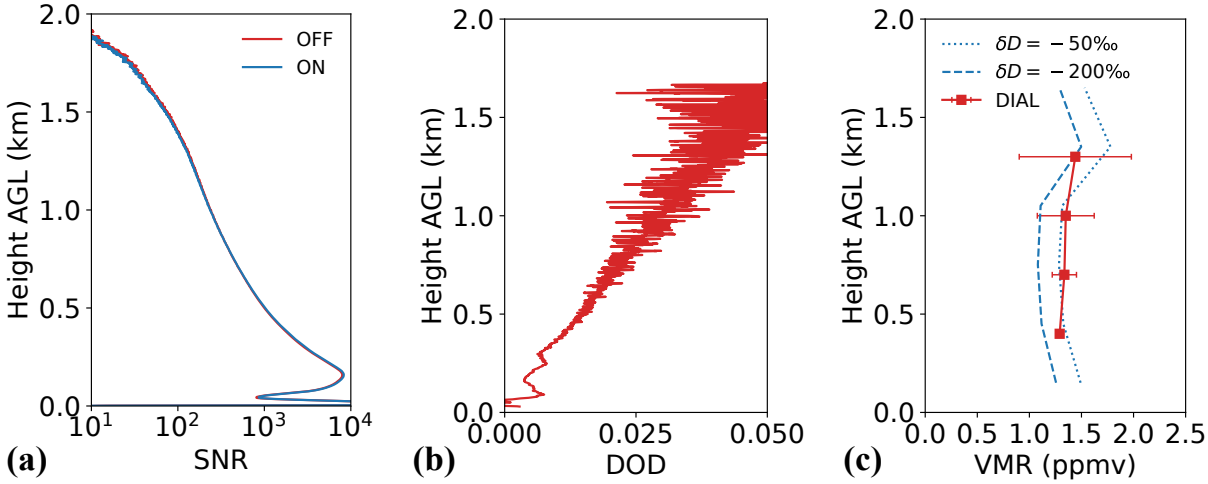

Figure 5.25: DIAL measurement results for HDO from 12:55 to 13:20 UTC (ca. 70 000 valid on/off shot pairs). (a) Raw (no energy normalization) signal-to-noise ratios of the on-line and off-line lidar returns. (b) Recorded differential optical depth. (c) DIAL-retrieved profile of the HDO volume mixing ratio (600 m range cells and 300 m sampling). Dotted and dashed lines are drawn to guide the eye, indicating calculated HDO profiles based on the H_2O radiosonde profile (spatially averaged using 300 m range bins) and uniform δD values of -50‰ and -200‰.

H_2O radiosonde profile (spatially averaged using 300 m range bins) and assuming uniform values for δD between -50‰ and -200‰, which are typical values to be found in the lower troposphere (Chazette et al., 2021; Sodemann et al., 2017; Zeng et al., 2022; Dyroff et al., 2015). The profiles obtained this way are plotted in Fig. 5.25c alongside the DIAL-retrieved profile showing good agreement to within the retrieval standard errors. The error bars in the retrieved profiles result from the standard error of the regression used to evaluate the slope of the differential optical depth. Altitude-dependent absorption cross-sections are calculated based on vertical profiles of temperature (lapse rate of -6.5 K km^{-1}) and pressure calibrated to ground sensor measurements next to the lidar.

5.5.5 Estimation of the isotopic abundance δD

Using the DIAL-measured mixing ratio profile of HDO and the profile of H_2O retrieved earlier with the same vertical resolution (600 m range bins and 300 m sampling), the HDO isotopic abundance δD was derived from the two measurements according to Eq. 1.1. The resulting values of δD range from -51‰ at 0.4 km a.g.l. to -119‰ at 1.3 km a.g.l. with absolute random errors of 20‰ and 337‰, respectively. It is worth noting that δD is not determined from simultaneous measurements of H_2O and HDO but from two consecutive and independent measurements. Due to the fact that for each sounding lidar signals are accumulated over a duration of 25 min, any change in the atmospheric water vapor content between both measurements results in a biased δD calculation. For instance, the H_2O mixing ratio measured by the point sensor at ground level decreased slightly by ca. 1.5% within 30 min between the H_2O and the HDO DIAL measurement. Assuming that the water vapor content within the first few hundreds of meters is correlated to changes at ground level (see Fig. 5.24), the 1.5% change in the H_2O mixing ratio would lead to a 15‰ bias in δD.

The isotopic abundance δD is an indicator of phase change conditions in the atmosphere that occur during the transport of air parcels at various scales, evidencing processes such as mixing, evaporation and condensation since the fractionation degree depends on the meteorological conditions, e.g. temperature and level of saturation (Sodemann et al., 2017). For instance, low δD values (typically -150‰) in atmospheric water vapor at the surface indicate low air mass temperatures and strong rainout of air parcels (Yoshimura et al., 2010; Jacob and Sonntag, 1991), whereas high δD (typically -80‰) values indicate high air mass temperatures and recent mixture of fresh ocean evaporate. Using an airborne CRDS analyzer above an alpine mountain lake, Chazette et al. (2021) reported δD observations ranging between -80‰ near the surface and -335‰ around 3.5 km above mean sea level. Over the Mediterannean, Sodemann et al. (2017) reported airborne δD observations between -97‰ near the sea surface and -225‰ in the free troposphere around 3.5 km above sea level. At mid-latitudes, increasing depletion with height is also generally observed based on airborne in situ observations (Schneider et al., 2015; Sodemann et al., 2017; Chazette et al., 2021).

5.5.6 Error budget analysis

Table 5.8 gives a summary of different error sources contributing to the total error budget in the H_2O and HDO DIAL measurements, and finally δD, over a 1.5 km range under the meteorological and instrumental conditions of the DIAL tests on 23 March 2022. Random errors are principally due to noise in the detection unit. For an integration time of 25 min, the precision in the water vapor mixing ratio was estimated as

0.1 g kg^{-1} (2.5% relative error) at 0.4 km above the ground and 0.6 g kg^{-1} (20%) at 1 km for 150 m range bins. For HDO and with 600 m range bins, the relative error at the first DIAL point at 0.4 km a.g.l. is 2% and grows to 37% at 1.3 km. Using this range bin size for the retrieval of H_2O yields a 0.5% relative error at 0.4 km and 8.4% at 1.3 km. With respect to δD this amounts to absolute random errors of 20‰ and 337‰ at 0.4 km and 1.3 km a.g.l., respectively.

Systematic errors arise from uncertainties in the knowledge of spectroscopic, atmospheric and instrument parameters used to compute the weight function WF (see Eq. 2.24) for the mixing ratio retrieval. Using the same approach as outlined in the theoretical sensitivity study (see section 3.3.3), systematic errors were estimated by calculating the sensitivity of WF to the uncertainty in each parameter of interest.

The first category of systematic errors is related to uncertainties in the spectroscopic line parameters from the HITRAN2020 database. If stated therein, line parameter uncertainties are used for the error estimation. With respect to line position, the stated uncertainty of 0.001 cm^{-1} translates into a relative error of 0.2% in the retrieved H_2O mixing ratio. For HDO, the stated uncertainty is even smaller so that the resulting systematic error is negligible. For both H_2O and HDO, a 2% uncertainty is assumed for the line intensity parameter giving rise to relative errors of 1.6% for both isotopologues resulting in a 22‰ absolute error in δD. Uncertainties for the air-broadened width stated in HITRAN2020 differ with 2% for H_2O and 10% for HDO. While this leads to an error of 0.5% in the retrieved H_2O mixing ratio, the HDO retrieval is very sensitive to the high uncertainty leading to an error of 9.3% and an absolute error in δD of 89‰. This makes it the largest systematic δD error and the dominant error contribution in the lower boundary layer up to the point where the random error begins to dominate at around 0.7 km a.g.l. With respect to the temperature exponent of the air-broadened width, an uncertainty of 10% results in relative errors of 0.1% and 0.4% for H_2O and HDO, respectively. This translates into an error in δD of 4‰. Uncertainties for the pressure shift parameters are not stated in HITRAN2020. A conservative assumption of 20% leads to 0.4% relative error for H_2O and a negligible error for HDO.

The next category includes systematic errors due to uncertainties in the a priori profiles of atmospheric pressure and temperature used for the isotopologue retrieval. Because the presented DIAL measurements rely on temperature and pressure model profiles calibrated only to the point sensor measurement on the ground, we use relatively conservative uncertainties of 3 K and 5 hPa for temperature and pressure, respectively. For the more temperature-sensitive H_2O isotopologue this leads to a relative error of 1.9% and a pressure error of 0.2%. HDO is less sensitive to uncertainties in the temperature and pressure profiles with relative errors of 0.9% and 0.1%. This leads to errors in δD of 20‰ and 2‰ due to temperature and pressure, respectively.

An instrument-related systematic error stems from the uncertainty of the wavelength meter reading at the on-line wavelength. As described in section 5.5.2, this error is principally determined by the accuracy of the wavelength meter and the uncertainty related to the calibration process which is estimated to be 1 pm (75 MHz). The resulting relative errors are around 0.5% and 0.1% for H_2O and HDO, respectively, which translates into an absolute error in δD of 5‰.

An additional wavelength-related systematic error can arise from the position of the on-line wavelength at the absorption peak and eventual fluctuations thereof. Figure 5.26 shows histograms of the measured on-line wavelengths for both the H_2O and HDO measurement. For the H_2O measurement, the on-line wavelengths have a standard deviation of 0.1 pm (11 MHz), which is close to the wavelength meter resolu-

Table 5.8: Budget of random and systematic errors for DIAL measurements of H_2O and HDO up to a height of 1.5 km with the WaVIL instrument. Random errors for 600 m range bins for H_2O and HDO. Assumed uncertainties of spectroscopic parameters from HITRAN2020 database if stated therein. (*) marks uncertainties with no estimates in HITRAN2020 for which case an assumed value is used. Systematic errors were calculated using a random-seeding approach (see text for details).

Error source	**H_2O**		**HDO**		**δD**
	Uncertainty	Rel. error	Uncertainty	Rel. error	Abs. error
Detection (random)					
at 400 m		0.5%		2.0%	20‰
at 700 m		2.5%		8.7%	92‰
at 1000 m		4.6%		20.2%	192‰
at 1300 m		8.4%		37.4%	337‰
Transmitter					
Wavelength accuracy	±1 pm (75 MHz)	0.5%	±1 pm (75 MHz)	0.1%	5‰
Spectroscopy					
Line position	±0.001 cm^{-1}	0.2%	±0.0001 cm^{-1}	negligible	2‰
Line intensity	±2%	1.6%	±2%	1.6%	22‰
Air-broadened width γ_{air}	±2%	0.5%	±10%	9.3%	89‰
T-exponent of γ_{air}	±10%*	0.1%	±10%	0.4%	4‰
Pressure shift	±20%*	0.4%	±20%*	negligible	4‰
Atmosphere					
Temperature	±3 K	1.9%	±3 K	0.9%	20‰
Pressure	±5h Pa	0.2%	±5h Pa	0.1%	2‰
Total systematic error		2.6%		9.5%	94‰

tion. Similarly for HDO, the on-line wavelengths have a standard deviation of 0.2 pm (16 MHz). Variations in the emitted on-line wavelengths of this order induce only very small variations in absorption (0.1% for H_2O and 0.02% for HDO) which are negligible compared to the aforementioned uncertainty due to the accuracy of the wavelength meter and calibration procedure.

The total systematic error for the H_2O mixing ratio is under 3% ($< 0.12\,g\,kg^{-1}$) and can be further reduced by limiting the uncertainty in the a priori temperature profile by the means of auxiliary measurements if available. A possible total systematic error of nearly 10% was estimated for HDO which is largely due to the uncertainty in the air-broadened width parameter stated in the HITRAN2020 database and which is the most significant contribution to the total error in the isotopic abundance δD in the first few hundreds of meters until the random error begins to dominate at around 0.7 km.

It should be noted that the position of the on-line wavelength was controlled manually during the DIAL measurements by adjusting the piezo voltages of the NesCOPO. A further improvement of the wavelength stability – and also a step towards autonomous lidar operation – could be achieved by the implementation of a stabilization scheme which was already tested in the laboratory with the WaVIL NesCOPO and which is presented in chapter 6.

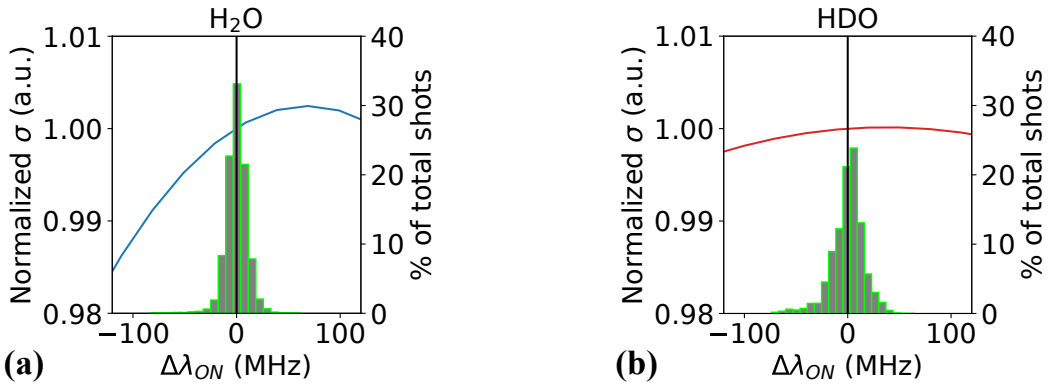

Figure 5.26: Absorption cross-section σ (left y-axis) and histogram of on-line wavelengths (right y-axis) expressed as differences $\Delta\lambda_{ON}$ from mean on-line wavelengths for H_2O (a) and HDO (b). Absorption cross-sections are normalized to their values at the mean on-line wavelengths.

5.5.7 Comparison between measurement and simulation

The simulation of lidar signals is based on many assumptions concerning a range of instrument-related and atmospheric parameters which are often not exactly known. Due to the proximity of the SIRTA observatory to ONERA, it is possible to access information about aerosol structure and aerosol optical depth which are representative for the atmospheric conditions during the DIAL experiments. These independent data sets were used as the basis to simulate the signals of the DIAL measurements on 23 March 2022 in order to compare the simulation outcome with the experiments. Such a cross-validation can be useful to identify eventual issues in the experimental setup (alignment, wavelength stability and calibration), but it also provides a feedback on the simulation method used and the model assumptions made therein.

5.5.7.1 Model of aerosol distribution

A model of the vertical distribution of the aerosol extinction coefficient representative of the measurement conditions is constructed using auxiliary measurements from the nearby SIRTA observatory. Figure 5.27a shows the aerosol optical depths (AOD) for different wavelengths during the day of 23 March 2022. The data were obtained from the AERONET sun photometer of Palaiseau located at the SIRTA observatory. With the two DIAL measurements of H_2O and HDO conducted between 12:25 and 13:20 UTC, only the AOD averages from this time frame at the wavelengths from 340 to 1640 nm are considered. The AOD-wavelength dependence is plotted in Fig. 5.27b. In order to derive the AOD at the DIAL wavelength of 1.98 µm, a power law fit of the form:

$$\mathrm{AOD}(\lambda) = \mathrm{AOD}(\lambda_0)\left(\frac{\lambda}{\lambda_0}\right)^{-\alpha} \tag{5.1}$$

is applied to the AERONET AOD data, where α is the Angstrom exponent (Ångström, 1929). With $\alpha = 1.38$ from the fit, the AOD at 1.98 µm is determined as 0.027. To build a vertical profile of the aerosol extinction coefficient, in a first step the backscatter profile of the 1064 nm ceilometer of the SIRTA obervatory is used to determine qualitatively the distribution of aerosols. In a second step, the profile of the extinction coefficient is constructed from this distribution by constraining its values to the estimated AOD

at 1.98 µm, so that the following condition is fulfilled:

$$\int_0^{2.5\,km} \gamma_{ext}(z)\,dz = 0.027. \tag{5.2}$$

The resulting profile of aerosol extinction is shown in Fig. 5.27c. From the profile of the the extinction coefficient, the backscatter coefficient is calculated assuming a constant extinction-to-backscatter ratio (lidar ratio) of 45 sr.

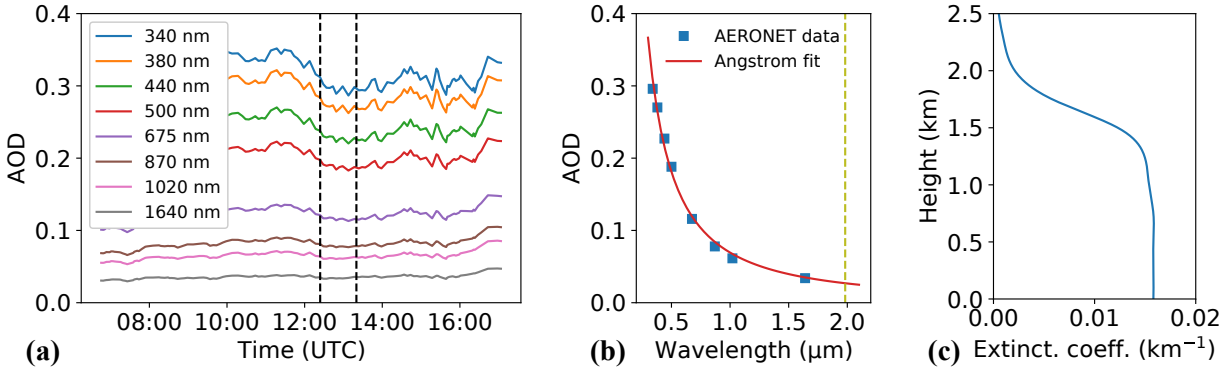

Figure 5.27: (a) Aerosol optical depth (AOD) for different wavelengths measured at the AERONET station of Palaiseau on 23.03.2022. Dashed vertical lines indicate the time window in which DIAL measurements were conducted. (b) AOD (average calculated from values within the DIAL time window) as function of wavelength with power law fit according to Eq. 5.1. Vertical dashed line indicates the DIAL wavelength region at 1.98 µm (c) Profile of the aerosol extinction coefficient calculated for 1.98 µm.

5.5.7.2 Simulated lidar signals and signal-to-noise ratios

The on- and off-line lidar signals are calculated using the lidar equation (Eq. 2.16). The calculation of the atmospheric transmission due to absorption is based on the radiosonde data from 23 March 2022. To simulate the HDO DIAL measurement, a vertical HDO profile is derived from the H_2O radiosonde data assuming a constant HDO isotopic abundance δD of -100‰. Aerosol extinction and backscatter coefficients are calculated using the aerosol model described in paragraph 5.5.7.1. The laser pulse energies are not exactly known, since they are not monitored during the DIAL operation. Based on routine laser energy checks conducted prior to the DIAL experiments and the ratio of the measured on- and off-line signals of the H_2O DIAL measurement, pulse energies of 5 mJ and 2.2 mJ for the on- and off-line pulses are used for the simulation. Figure 5.28a shows both the measured and the simulated range-corrected signals for the H_2O DIAL indicating good agreement between the measurement and the model. Signal-to-noise ratios are calculated by taking into account for detector/amplifier noise defined by the noise-equivalent power (NEP), which represents the major noise contribution, as well as shot noise and laser speckle. Panels (b) and (c) of Fig. 5.28 show a comparison between the measured SNR (detection noise evaluated from the pre-trigger part of the lidar signal) and two simulated cases for different values of the receiver transmission term of the lidar equation. The overall receiver transmission is difficult to determine experimentally. Comparing measured SNR with the simulated cases with receiver transmissions between 0.3 and 0.5, a value of around 0.35 is found to be the parameter for which measured and simulated SNR profiles are of the same order. An overall transmission of the lidar receiver of 35% is plausible as it depends on the quality of the telescope

mirrors, the efficiency of coupling into the multimode fiber and the quality of the anti-reflection coatings of filters and lenses used in the detection setup. A similar value for the receiver transmission is found for the HDO measurement, where on-and off-line pulse energies differ by only a few percent as observed from the averaged lidar signals. Fig. 5.29 shows the comparison between measurement and simulation for HDO assuming respective on- and off-line laser energies of 5 mJ and 4.7 mJ. The simulated lidar signals shown in Fig. 5.29a agree slightly less with the measured signals which can simply be due to a change in the aerosol distribution which is not reflected in the model.

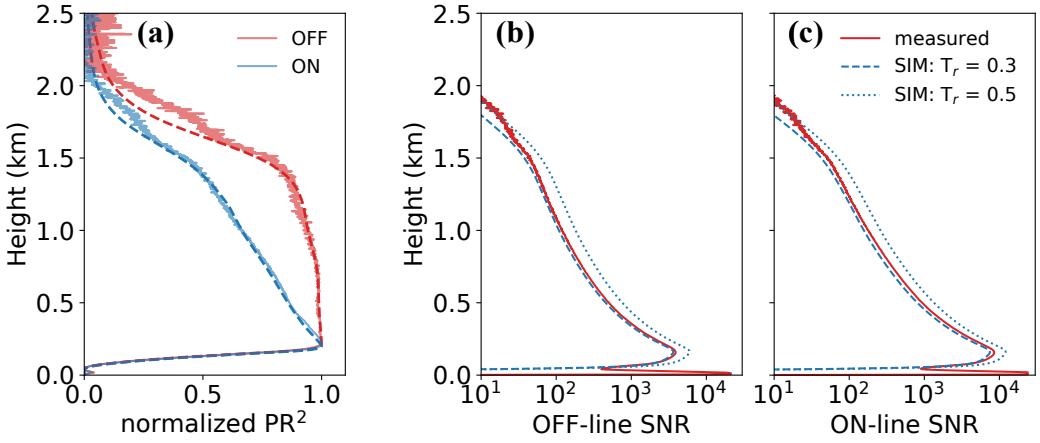

Figure 5.28: Comparison between measured and simulated H_2O DIAL signals: (a) normalized range-corrected on/off signals (simulation represented as dashed lines). (b) off-line signal-to-noise ratio obtained by measurement versus simulated cases with different receiver transmission parameters T_r. (c) same as (b) but for the on-line signal.

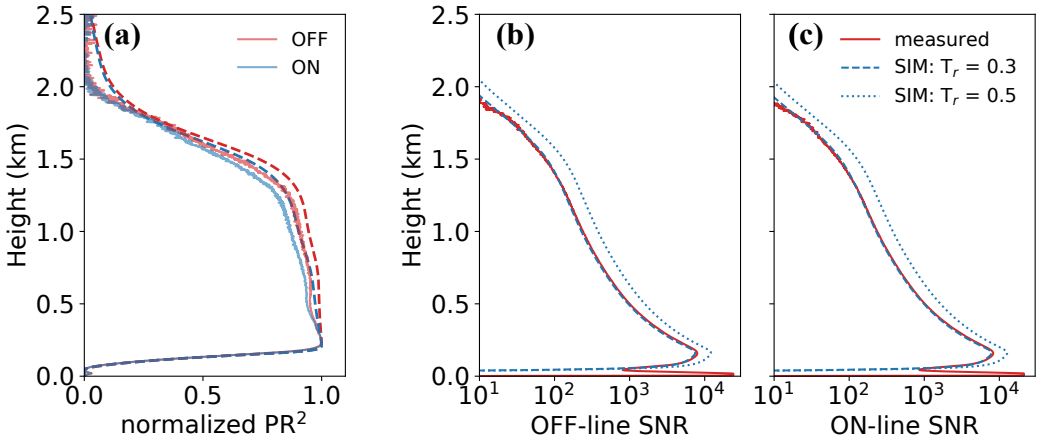

Figure 5.29: Comparison between measured and simulated HDO DIAL signals: (a) normalized range-corrected on/off signals (simulation represented as dashed lines). (b) off-line signal-to-noise ratio obtained by measurement versus simulated cases with different receiver transmission parameters T_r. (c) same as (b) but for the on-line signal.

All in all, it was found that the constructed atmospheric model represents quite well the measurement conditions during the DIAL experiments and that simulated and measured signal-to-noise ratios are in good agreement considering that there are still parameters, such as the transmission of the receiver or the exact value of the lidar ratio, which have to be estimated.

5.5.8 Five-hour IP-DIAL measurement of the column-averaged boundary layer isotopic ratio

This last section presents a data set obtained from a five-hour long operation of the WaVIL instrument during which H_2O and HDO were addressed alternately using the integrated-path DIAL technique in order to calculate the column-averaged isotopic abundance δD from each H_2O/HDO measurement pair. The derivation of column-averaged values was chosen here in order to achieve higher measurement precision compared to range-resolved measurements which was enabled by favorable aerosol backscatter conditions. Additionally, the IP-DIAL method uses an integrated weight function which results in a more accurate evaluation of the mixing ratio for atmospheric columns of hundreds of meters. The presented data set is the largest continuous measurement obtained in the framework of this thesis and presents thus an opportunity to demonstrate the measurement stability over several hours. The experiments were conducted on 11 February 2022 at ONERA using the instrument configuration as described in section 5.5.1.

5.5.8.1 Measurement conditions and DIAL wavelength selection

The atmospheric conditions are illustrated by the attenuated backscatter time series measured at the nearby SIRTA observatory shown in Fig. 5.30. Typical for winter, the atmospheric boundary layer is shallow (< 500 m) and it is topped by a residual aerosol layer at night and rises to a depth of around 1 km in the afternoon when it is well mixed. As indicated by the vertical lines in Fig. 5.30, DIAL measurements were conducted in a time window from 12:20 to 17:45 UTC (13:20 to 18:45 CET local time) during which the boundary layer was mostly topped by clouds. Low backscatter signal from the free troposphere (when not blocked by clouds) indicates the absence of aerosols in that zone. Consequently, even during cloud-free moments DIAL measurements were restricted to the boundary layer only.

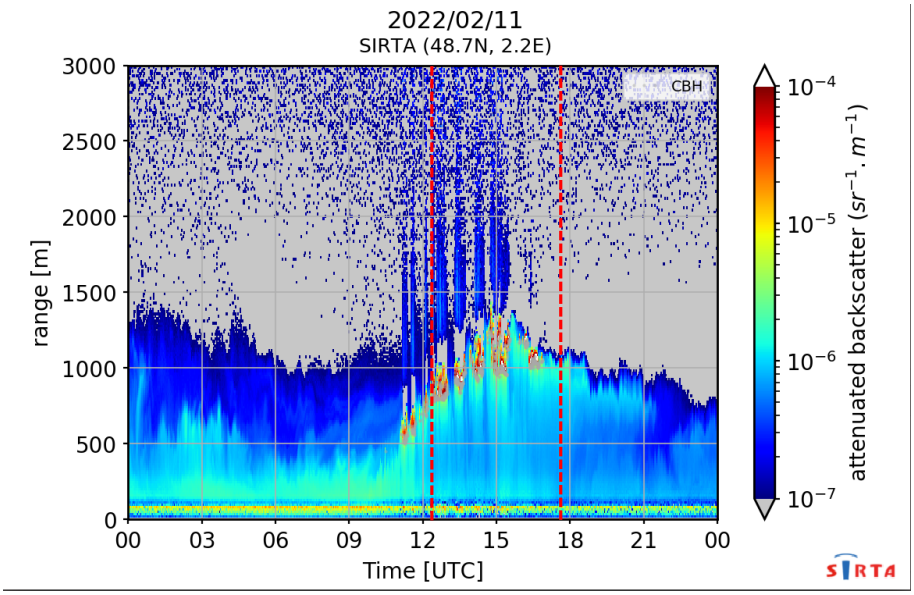

Figure 5.30: Ceilometer measurement of the attenuated backscatter coefficient at the SIRTA observatory on 11 February 2022. Vertical dashed lines indicate time window during which vertical DIAL measurements of H_2O and HDO were conducted at ONERA.

Figure 5.31 shows the absorption spectra of H_2O and HDO and the on- and off-line DIAL wavelengths. The HDO on-line wavelength is tuned to 1982.47 nm where the main isotopologue adds a non-negligible absorption contribution which has to be corrected for in the retrieval. The correction of this H_2O bias is done for each HDO measurement using the retrieved H_2O concentration of the preceding H_2O DIAL measurement.

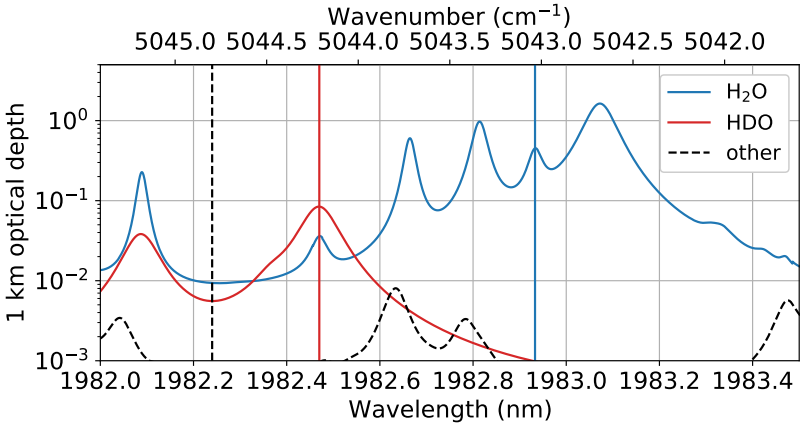

Figure 5.31: (a) Spectrum of the H_2O and HDO optical depths over 1 km under standard atmospheric conditions (15°C and 1013.25 hPa) and 50% relative humidity ($\delta D = 0$ assumed for HDO). Vertical solid lines indicate the DIAL on-line wavelengths, the vertical dahsed line the off-line wavelength.

5.5.8.2 IP-DIAL measurement results and estimation of δD

During the five-hour measurement period, H_2O and HDO were addressed alternately on average every 15 min. Figure 5.32 provides an example of the first measurement sets of H_2O and HDO. In fact, atmospheric conditions were quite favorable on 11 February 2022. The range-corrected signals of panels (b) and (e) show an increase with range which is even the case for the more strongly absorbed on-line signals. This is due to an increasing aerosol backscatter coefficient towards the boundary layer top resulting in a slower decline of the signal-to-noise ratios with range and thus reduced noise in the measured differential optical depth which are depicted in panels (c) and (f) of Fig. 5.32.

The principle of the IP-DIAL measurement which was applied to all H_2O and HDO data sets is illustrated in Fig. 5.32c. The column-averaged mixing ratio is calculated from the measured DOD evaluated at 250 m and 700 m. To reduce effects of noise, the DOD at both ranges is evaluated from the mean of all values within a 50 m window indicated by the vertical lines in Fig. 5.32c. Figure 5.32f shows the same approach applied to the DOD of the HDO DIAL measurement which was corrected by the absorption contribution of H_2O at 1982.47 nm. The correction was calculated using the H_2O mixing ratio from the preceding H_2O IP-DIAL measurement and a vertical profile of temperature and pressure based on the respective values measured at ground level by the weather station of the lidar truck. For the first H_2O measurement depicted in Fig. 5.32, the IP-DIAL-retrieved column-averaged volume mixing ratio of H_2O is estimated as 0.55% (3.39 g/kg) with an absolute random error due to detection noise of 0.01% (0.05 g/kg). The retrieved column-averaged volume mixing ratio of HDO is 1.49 ppmv with a random error of 0.10 ppmv. From this

H_2O/HDO measurement pair, the HDO isotopic abundance δD is calculated as -125‰ with a precision of 60‰.

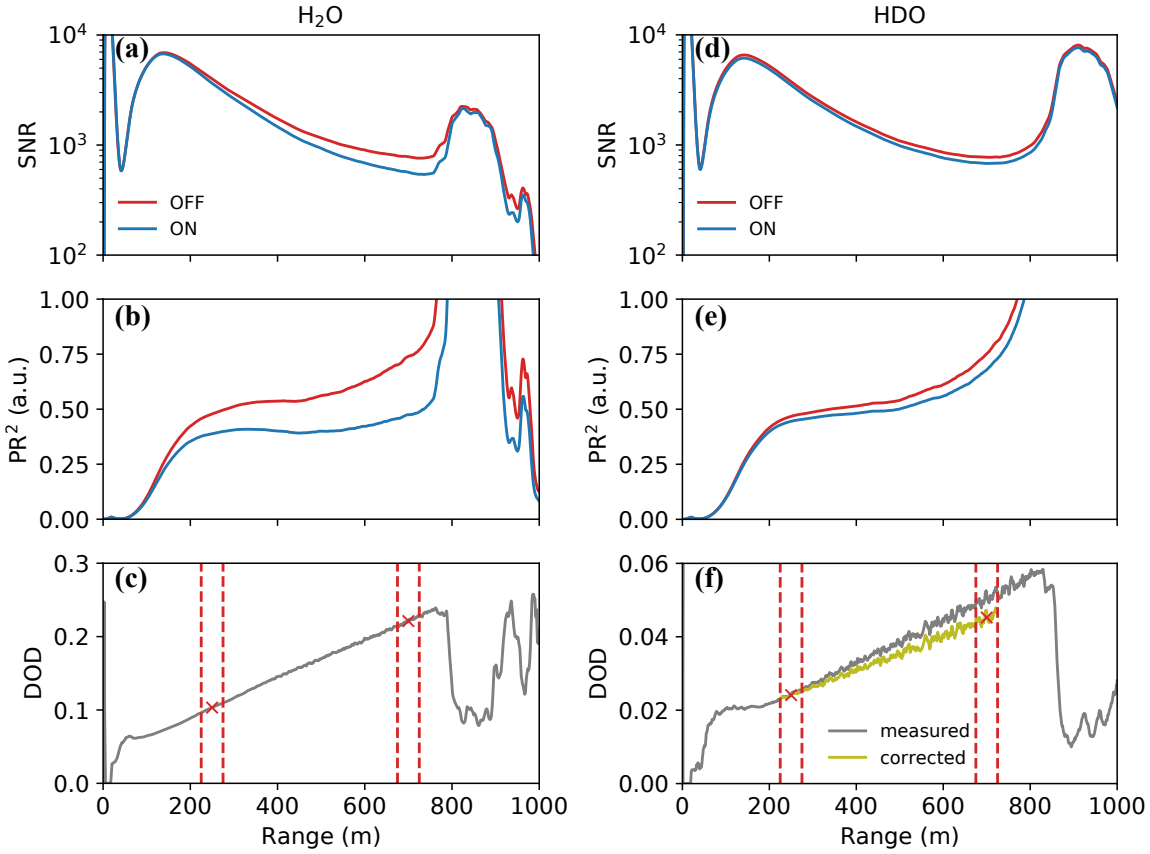

Figure 5.32: First set of H_2O/HDO DIAL measurements on 11.02.2022. Time averaging over 15 min (ca. 40 000 valid shot pairs) for H_2O and 12 min (ca. 35 000 valid shot pairs) for HDO. (a/d) Signal-to-noise ratios of the on- and off-line signals. (b/e) Range-corrected signals. (c/f) Measured differential optical depth. For the IP-DIAL measurement, the DOD was evaluated at 250 m and 700 m by calculating the mean value within a 50 m window indicated by the vertical dashed lines. For HDO, the measured DOD was corrected by the H_2O bias calculated from the IP-DIAL-retrieved H_2O concentration.

Figure 5.33 shows a time series of the measured lidar signals and the IP-DIAL-retrieved quantities over the entire measurement duration. Panel (b) depicts the time evolution of the range-corrected off-line signals indicating an increase in aerosol backscattering towards the boundary layer top as already discussed for the first measurement set above. Fig. 5.33c shows the IP-DIAL-derived H_2O volume mixing ratio as the column-average between 250 m and 700 m a.g.l. measured approximately every 30 min with signal averaging over 15 min. Compared to the in situ mixing ratio measured at ground level, the IP-DIAL-derived concentration is lower but also shows some correlation to the ground sensor measurement.

Similar to H_2O, the column-averaged volume mixing ratio of the HDO isotopologue was measured approximately every 30 min with a signal acquisition time of 15 min per measurement. The resulting time series of the HDO mixing ratio is shown in Fig. 5.33d and features some variations with time which are however within the standard error due to detection noise. Finally, the time evolution of δD is plotted in Fig. 5.33e. It should be noted that for the calculation of δD, both combinations of alternate measurements are used, i.e. the first δD value in panel (e) is derived from the first measurements of H_2O and HDO and

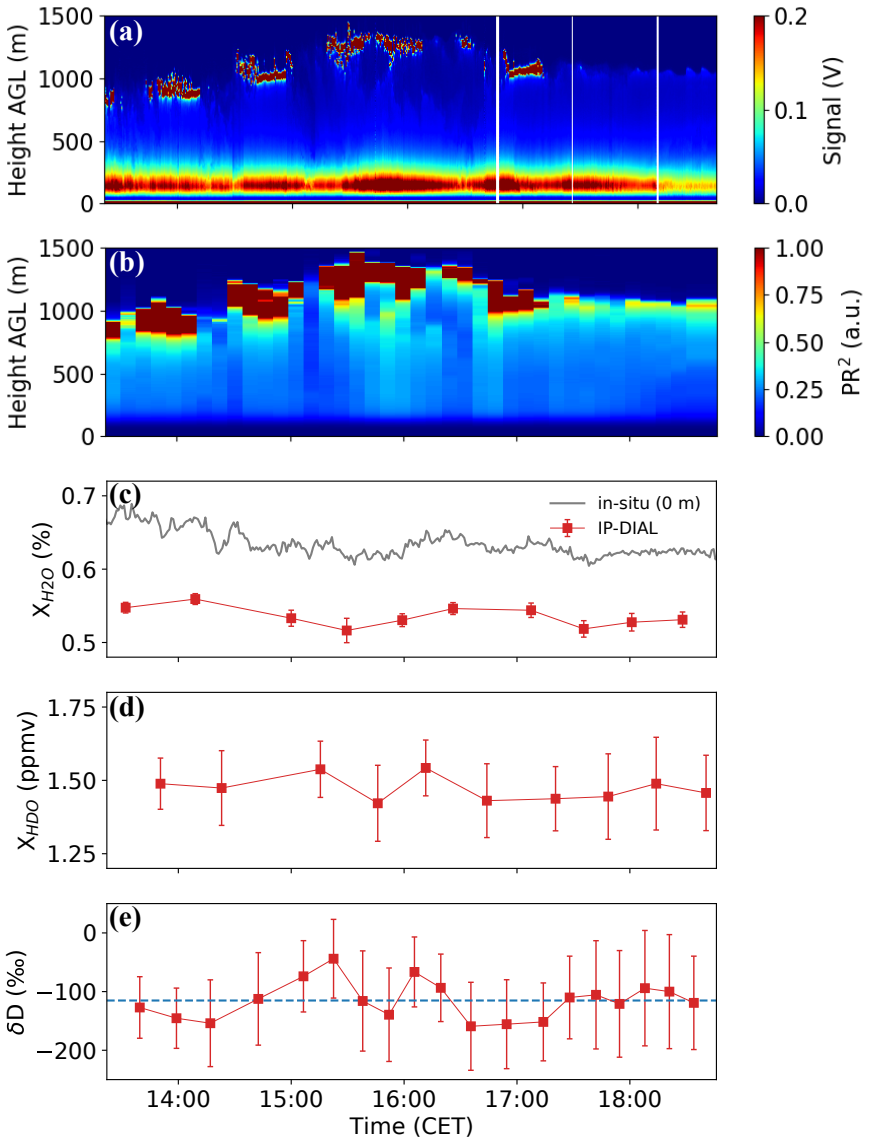

Figure 5.33: Five-hour DIAL operation on 11.02.2022: (a) Detected off-line signals (1000 shot averages). (b) Range-corrected off-line signals (7 min time resolution). (c) Column-averaged H_2O volume mixing ratio measured by IP-DIAL between 250 m and 700 m a.g.l. and mixing ratio measured by in-situ probe at ground. (d) Column-averaged HDO volume mixing ratio measured by IP-DIAL between 250 m and 700 m a.g.l. (e) Column-averaged HDO abundance δD calculated from two consecutive H_2O/HDO or HDO/H_2O measurement pairs. Horizontal dashed line indicates average value of δD from all points.

the second δD value is calculated from the same HDO data set with the next (second) H_2O data set, and so forth. The observed variations with time in δD from -159‰ to -45‰ are mostly the result of the limited precision in the HDO measurements (up to 10% relative error) which is reflected by the standard error bars in the δD time series.

A physically meaningful estimation of δD could be obtained by calculating the mean and standard deviation values of all δD measurement points yielding -115$\pm$30‰, which of course would have to be verified with an auxiliary in situ instrument, but is consistent with typical δD values in mid-latitude regions. In general, lower values of δD are observed during winter months. For instance, Jacob and Sonntag (1991)

monitored the atmospheric HDO abundance over an eight-year-long period in Heidelberg, Germany, and measured monthly mean values of δD ranging between -140‰ and -180‰ in winter months.

5.5.9 Conclusion

A significant improvement in the quality of the conducted DIAL measurements was achieved in the framework of the third measurement campaign at ONERA. First, the improvement comes from the implemented wavelength calibration protocol which uses a calibration source closer to the DIAL operation wavelength and an additional verification using a laser diode tuned to a CO_2 absorption line at 2.05 µm. And second, a well aligned and stable laser setup enabled the operation of the lidar instrument over several hours at a time to acquire more data sets to analyze than in previous measurement campaigns.

In the framework of this third measurement campaign it was demonstrated that vertical DIAL measurements of the water vapor main isotopologue H_2O can be realized with the WaVIL instrument within the atmospheric boundary layer with a vertical resolution of 100–200 m and temporal resolutions of 20–30 min. With those parameters and a laser pulse energy typically around 5 mJ, the random error in the water vapor mixing ratio was estimated as 0.1 g kg^{-1} (2.5% relative error) at 400 m above ground level and 0.6 g kg^{-1} (20% relative error) at a height of 1 km under relatively dry conditions (mixing ratios of 3–5 g kg^{-1}). This compares to an estimated total systematic error of under 3% in relative terms. The demonstrated performance in terms of temporal and spatial resolution, noise error and systematic error is very close to the requirements needed for operational weather forecasting (Wulfmeyer et al., 2015), but it is restricted to the atmospheric boundary layer in the absence of free-tropospheric aerosols or in the presence of clouds at the boundary layer top. A validation experiment was demonstrated with an in situ radiosonde reference launched around 15 km away from ONERA, which showed good agreement between both profiles over the entire vertical lidar range of 1.5 km. Additionally, measurements over a few hours clearly showed the correlation with an in situ ground sensor despite relatively small changes in the atmospheric water vapor content proving the high sensitivity of the DIAL method.

The derivation of vertical HDO profiles is more challenging owing to the lower absorption of HDO. Meaningful relative precision similar to H_2O for similar averaging times can only be achieved at the cost of spatial resolution (range bins of ca. 500 m). As a consequence, measurements of the HDO abundance δD must have a similarly coarse resolution. The experiments showed that only for the first range bin corresponding to the first few hundred meters of the atmosphere the noise error is sufficiently low (few tens of ‰) to allow for a meaningful characterization of the variations in δD. Despite the relatively large noise error, the δD values derived from the DIAL-measured profiles of H_2O and HDO mostly lied within the expected range for mid-latitude conditions from -50‰ to -200‰. A validation was not possible since no isotopologue-capable CRDS analyzer was available during the measurement campaign.

An additional bias in δD can be caused by changes in the water vapor content between the independent H_2O and HDO measurements which typically lasted between 15 and 30 min for each isotopologue due to the need for time averaging in order to achieve sufficient signal-to-noise ratios. In the future, this could be addressed by implementing a multiple-wavelength DIAL technique to measure both isotopologues simultaneously. This would be possible by using spectral lines within a 1 nm-window and by implementing a more complex wavelength-switching scheme with at least three wavelengths switched on a pulse-to-pulse

basis.

Finally, it is worth mentioning that the presented measurements were conducted under rather dry conditions with water vapor mixing ratios of 3–5 $g\,kg^{-1}$. Such values correspond to the least favorable mid-latitude scenario used in in the sensitivity analysis in chapter 3 which implies that the precision would increase with the same instrument setup under more favorable conditions with higher water vapor content.

5.6 Measurement campaign 4: vertical DIAL measurements of carbon dioxide at 2.05 µm

To demonstrate the versatility of the parametric laser source, a vertical DIAL measurement of CO_2 in the atmospheric boundary layer was obtained with the WaVIL instrument adapted to a signal output wavelength of 2.05 µm. This was achieved by changing the quasi-phase-matching period of the PPLN crystal of the NesCOPO and by adapting the operation temperature of the PPKTP crystals in the amplification line. The DIAL measurement was conducted at ONERA on 29 April 2022 with the WaVIL instrument still integrated in the LSCE lidar truck with the same telescope configuration (telescope 1, 25 cm-diameter Newton-type telescope combined with 900 µm-diameter multi-mode fiber) used for the H_2O/HDO DIAL measurements at ONERA presented in section 5.5.

5.6.1 Spectroscopy and line selection

For the in the following presented DIAL measurement of CO_2, the spectral window around the R30 absorption line at 4875.7487 cm^{-1} (close to 2051 nm) is used. The spectroscopic parameters of this absorption line are relatively well studied because of the interest of this spectral region for space-based integrated-path-DIAL sensing of CO_2. The R30 line offers an optimal optical depth close to unity when tuning the on-line wavelength to the wing of the absorption line which minimizes the statistical error for space-based IP-DIAL measurements and it is rather insensitive to temperature variations (Ehret et al., 2008). Table 5.9 lists some of the R30 line parameters from the HITRAN2020 database. Indeed, the lower-state energy E" of 362.79 cm^{-1} indicates a low temperature sensitivity.

Table 5.9: Spectroscopic parameters of the CO_2 R30 absorption line from the HITRAN2020 database. ν: wavenumber, λ: vacuum wavelength, S: line intensity at 296 K, γ_{air}: air-broadened half width at half maximum (HWHM) at 296 K and reference pressure of 1 atm, E": lower-state energy

	ν [cm^{-1})]	λ [nm]	S [cm^{-1}(molec·cm^{-2})$^{-1}$]	γ_{air} [cm^{-1}]	E" [cm^{-1}]
CO_2 (R30)	4875.7487	2050.9670	1.51×10^{-22}	0.0689	362.79

Figure 5.34a shows the spectrum of optical depth over 1 km for the wavelength range around the R30 absorption line calculated for a CO_2 volume mixing ratio of 400 ppmv under standard atmospheric conditions. For the ground-based DIAL measurement, the on-line wavelength is tuned to the peak of the R30 absorption line at 2050.969 nm and the off-line wavelength is set to 2051.246 nm to achieve maximum differential absorption in the boundary layer. In this wavelength configuration, both the on- and off-line signals experience the same (very small) absorption due to water vapor so that no further bias correction is needed.

5.6.2 Lidar setup

The lidar setup is very similar to the one used for H_2O/HDO at 1.98 µm except that the PPLN quasi-phase-matching period was changed to 14.26 µm by laterally translating the crystal inside the NesCOPO. The resulting signal wavelength is at 2.05 µm and the idler at 2.21 µm. For this wavelength range, the PPKTP

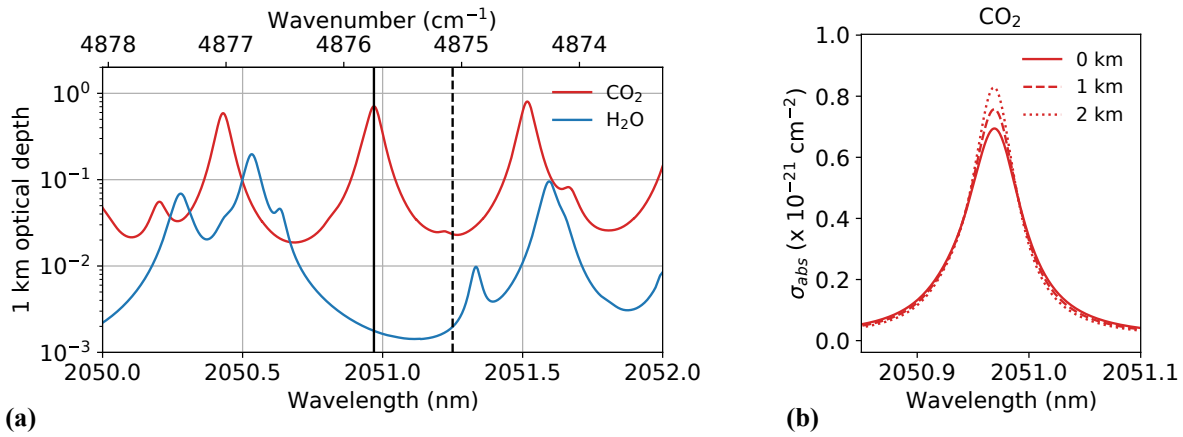

Figure 5.34: (a) Spectrum of the CO_2 and H_2O optical depths over 1 km under standard atmospheric conditions (15°C and 1013.25 hPa), 50% relative humidity and a constant CO_2 VMR of 400 ppmv. Vertical solid and dashed lines indicate the DIAL on- and off-line wavelengths. (b) CO_2 absorption cross-section around the on-line wavelength for different altitudes.

crytals of the OPA line need to be operated at a temperature of ca. 45°C in order to achieve optimal phase matching which was achieved by placing them in mounts with thermoelectric heating. Using a combination of three 12-mm-long PPKTP crystals and an idler out-coupler behind the second crystal, signal output energies of 6–9 mJ were achieved. This is slightly more than what was possible for the H_2O/HDO DIAL experiments at 1.98 µm, probably due to the fact that by heating the PPKTP crystals an optimum of the QPM condition was achieved. Figure 5.35 shows a schematic of the entire lidar setup. The receiver part is the same as the one described in section 5.5 consisting of a 10-inch Newton telescope coupled to a 900 µm-diameter multimode fiber and an amplified commercial InGaAs PIN photodiode.

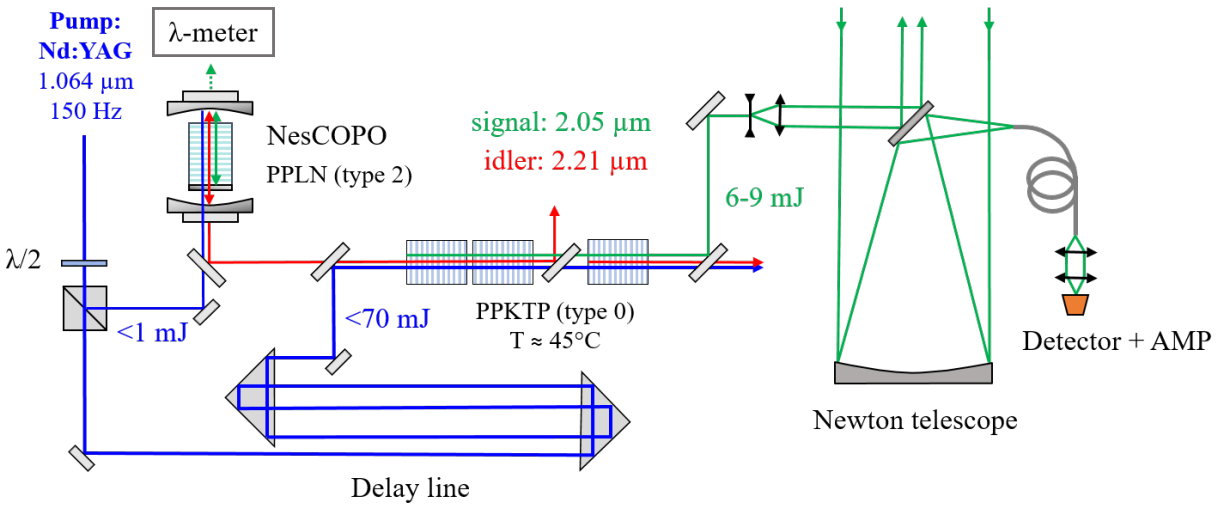

Figure 5.35: Schematic lidar instrument architecture for DIAL measurements of CO_2. NesCOPO: nested-cavity optical parametric oscillator with type-0-PPLN crystal (14.26 µm QPM-period). OPA stage with three PPKTP crystals (38.85 µm QPM-period), DET + AMP: detector and amplifier.

Table 5.10 provides a summary of key parameters of the DIAL system adapted to the measurement of CO_2. As described in section 5.5, the wavelength meter was calibrated using a laser diode at 1579 nm stabilized (manually) to a CO_2 absorption line. Then in a second step, a laser diode tuned to the CO_2 absorption line at 2051 nm was used to compare the wavelength meter reading with the actual wavelength of the molecular transition. The observed wavelength difference (usually around 2.5 pm) was then used as a correction to be applied in the mixing ratio derivation. Again, this was done because the wavelength meter used cannot be calibrated with wavelengths greater than 2 µm. As a conservative estimate an uncertainty of 1 pm (70 MHz) related to this procedure is assumed for the error budget.

Table 5.10: System parameters of the WaVIL instrument adapted to the measurement of CO_2 at 2.05 µm

On-line / off-line wavelength	2050.969 nm / 2051.25 nm
Laser energy	6–9 mJ
Telescope configuration	Telescope 1 (25 cm Newton-type)
Detector	InGaAs PIN
Gain / bandwidth setting	10^6 V/A / 3.5 MHz
Wavelength calibration	calibrated at 1579 nm and verified at 2051 nm (see section 5.5.2)

5.6.3 Measurement conditions and auxiliary instruments

Figure 5.36 shows the aerosol backscatter signal over the entire day of 29 April 2022 obtained by the cloud and aerosol ceilometer (1064 nm) of the SIRTA observatory located 2 km to the west of ONERA (see map of Fig. 5.21 in section 5.5). It shows a dynamically increasing boundary layer height from 9:00 UTC (11:00 local time) to 18:00 UTC (20:00 local time). The DIAL measurement was conducted in the time window from 15:15 UTC to 16:00 UTC during which aerosols were trapped in the boundary layer up to a height of 1.6 km. Also visible in the ceilometer backscatter plot are the return signals of small clouds at the top of the boundary layer.

An auxiliary measurement of the CO_2 mixing ratio was provided by a CRDS analyzer (Picarro G2301) which was placed on the rooftop of the J3 building at ONERA approximately 20 m above the lidar. The CRDS analyzer measures the dry air mixing ratio which is defined as:

$$X_{\mathrm{CO_2,dry}} = \frac{1}{1 - X_{\mathrm{H_2O}}} X_{\mathrm{CO_2}}, \tag{5.3}$$

where $X_{\mathrm{CO_2}}$ is the CO_2 mixing ratio in a volume of air including water vapor and $X_{\mathrm{H_2O}}$ is the H_2O volume mixing ratio. In the following, all DIAL-retrieved mixing ratios are given for dry air. The H_2O mixing ratio is calculated from temperature and humidity measurements on the ground.

Figure 5.37 shows the evolution of the measured CO_2 mixing ratio over the course of 24 hours on 29 April 2022. The time series shows the typical diurnal cycle characterized by a peak in the CO_2 concentration in the morning and the minimum of the cycle in the afternoon. The time series also shows higher-frequency fluctuations of up to 10 ppm occurring on the time scale of minutes. High concentrations of CO_2 in the morning hours can be explained by the shallow boundary layer (see Fig. 5.36), respiration of vegetation and the occurrence of rush hour traffic whereas low concentrations in the afternoon are due to a

deep and well mixed boundary layer as well as increased photosynthesis of vegetation (Xueref-Remy et al., 2018). Indeed, the influence of the boundary layer dynamics on the diurnal cyle of the CO_2 concentration is qualitatively well reflected by the correlation of the boundary layer height measured by the aerosol backscatter ceilometer shown in Fig. 5.36 with the in situ measured CO_2 mixing ratio depicted in Fig. 5.37. The observed diurnal pattern is very similar to the ones observed by other research groups on the Saclay plateau in the Southern Paris region (see for example Gibert et al. (2008) or Xueref-Remy et al. (2018)).

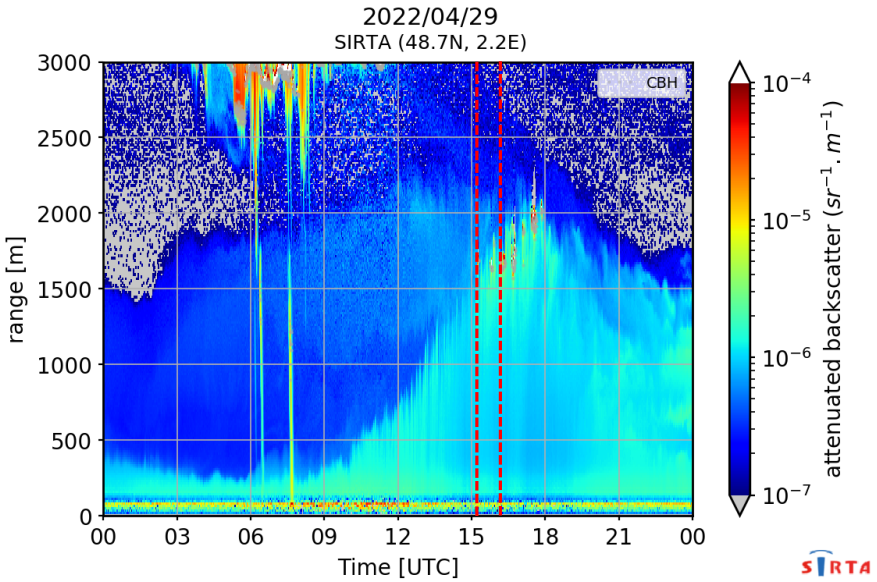

Figure 5.36: Ceilometer measurement of the attenuated backscatter coefficient at the SIRTA observatory on 29 April 2022. Vertical dashed lines indicate time window during which DIAL measurement of CO_2 were performed at ONERA. Local time is UTC+2.

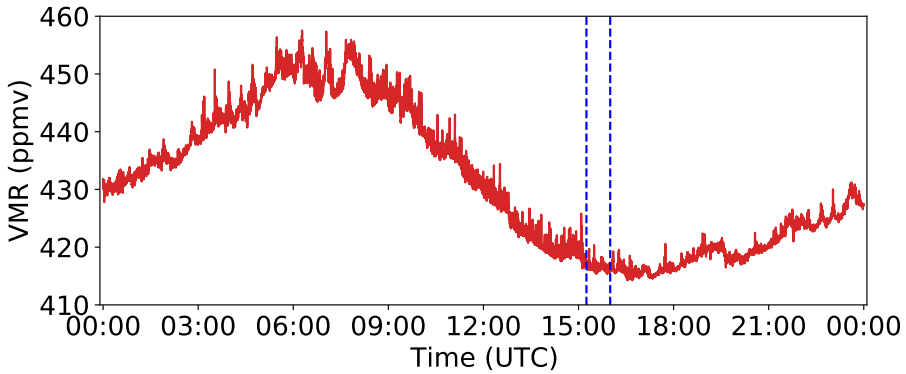

Figure 5.37: CO_2 dry air mixing ratio measured by CRDS analyzer (Picarro G2301) located on the rooftop of the J3 building at ONERA over 24 hours on 29.04.2022. Vertical dashed lines indicate time window during which DIAL measurement of CO_2 was performed. Local time is UTC+2

5.6.4 Example of a range-resolved DIAL measurement of CO_2

The presented vertical DIAL measurement of CO_2 is the result of time averaging over a duration of 20 min (ca. 48 000 valid shot pairs) from 15:35 UTC to 15:55 UTC. Figure 5.38 depicts the averaged raw-data on- and off-line signals showing both the aerosol returns and backscatter signals from clouds at the boundary layer top. The range-corrected signals in the lower panel of Fig. 5.38 clearly indicate the strong attenuation of the on-line signal due to high absorption at the on-line wavelength tuned to the center of the R30 line.

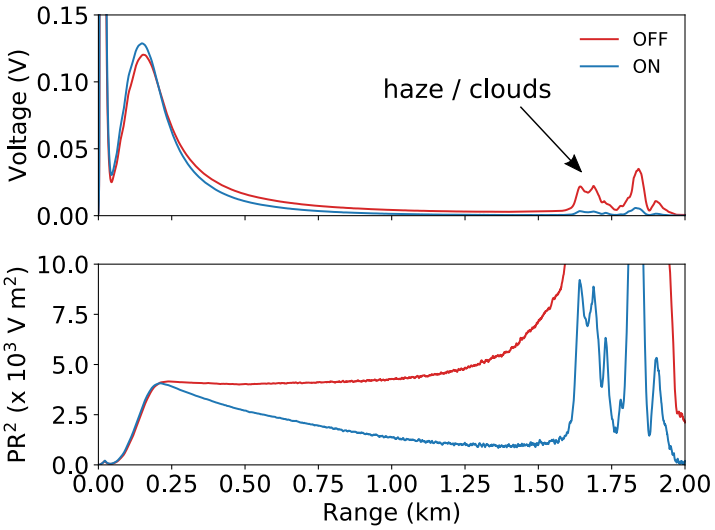

Figure 5.38: Raw lidar signals of the CO_2 DIAL measurement (averaged over ca. 48 000 valid shot pairs within 20 min). Upper panel: detected signal voltage. Lower panel: range-corrected signals.

Figure 5.39a depicts the signal-to-noise ratios of the on- and off-line lidar returns (no energy normalization) for the signal accumulation time of 20 min. The SNR is over 100 in the first kilometer of atmosphere even for the strongly absorbed on-line signal. The differential optical depth calculated from the lidar signals is shown in panel (b) of Fig. 5.39 and the retrieved profile of the dry-air CO_2 volume mixing ratio is depicted in panel (c). For the retrieval, DOD data from 0.2 km to 1.5 km above ground was used with range bins of 200 m and a 100 m sampling. Restricting the retrieval to below 1.5 km ensures that no cloud returns are included. For the presented DIAL measurement, a maximum number of valid shot pairs was selected in order to achieve high SNR. Consequently, also laser shots were selected in the data post-processing which saturated the digitizer card which would lead to biases at ranges with saturation.

The retrieved profile of the CO_2 mixing ratio shows large vertical variations ranging from 401±2 ppm at 0.3 km to 499±51 ppm at 1.1 km above ground level. The mean volume mixing ratio measured by the in situ sensor located on the top of a building around 20 m above the lidar is 416.5 ppm with a standard deviation over 20 min of 0.5 ppm. There is thus relatively good agreement between the first DIAL point at 0.3 km above the ground and the in situ measurement considering that CO_2 concentrations can vary locally by a few ppm, especially in the vicinity of buildings. However, values close to 500 ppm measured at around 1 km above ground level give reason to belief that the measurement is biased since no such gradient in the CO_2 concentration would be expected in the well mixed afternoon boundary layer.

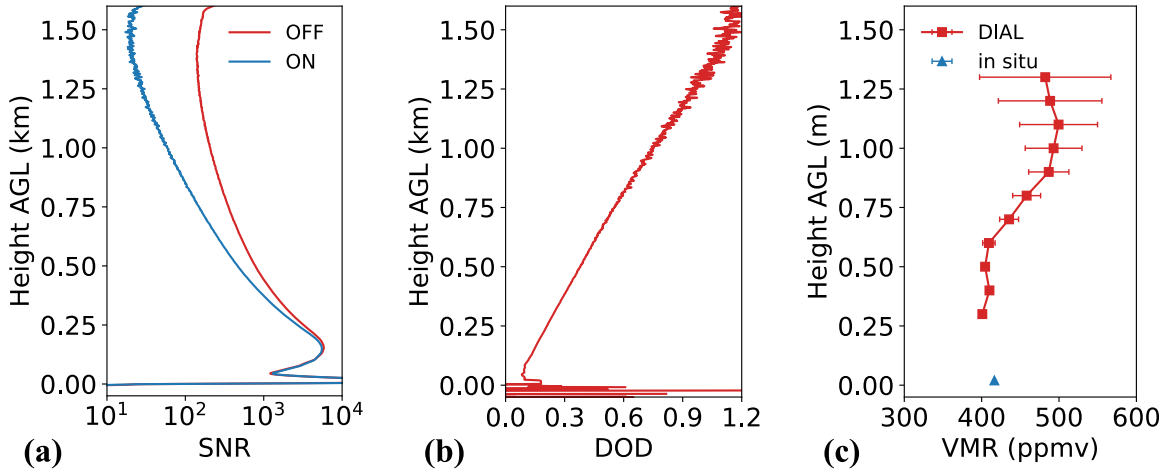

Figure 5.39: DIAL measurement results for CO_2 on 29.04.2022 (ca. 48 000 valid shot pairs, 20 min time averaging). (a) Raw (no energy normalization) signal-to-noise ratios of the on- and off-line lidar returns. (b) Recorded differential optical depth. (c) DIAL-retrieved profile of the CO_2 volume mixing ratio (200 m range cells and 100 m sampling) and in situ reference provided by CRDS analyzer (Picarro G2301, placed on a rooftop ca. 20 m above the lidar). Error bars evaluated from detection noise only.

5.6.5 Error analysis

Table 5.11 provides a list of systematic errors associated with the CO_2 DIAL measurement. The errors are calculated in the same way as for the H_2O/HDO DIAL measurements in section 5.5 by using a random seeding approach to estimate the sensitivity of the weight function to the uncertainty in the parameter of interest. Using this method, the total systematic error in the retrieved CO_2 mixing ratio is determined as 1.9% (in relative terms).

The main contribution to the error budget stems from uncertainties in the spectroscopic line parameters from the HITRAN2020 database. The uncertainties listed in Table 5.11 are the uncertainties stated in the error code of HITRAN2020. For example, the uncertainties for line intensity and air-broadened width of 1% and 2% result in relative errors in the CO_2 mixing ratio of 0.8% and 1.6%, respectively.

Because the DIAL retrieval relies on a model for the altitude-dependent atmospheric parameters of temperature and pressure for which the ground-level data is taken from the point sensor measurement next to the lidar, conservative uncertainties of 3 K and 5 hPa for temperature and pressure are used. Since the R30 absorption line is relatively temperature insensitive, the estimated relative error is 0.3%. The contribution of the pressure error to the error budget is negligible.

A relative error of 0.2% stems from the uncertainty related to the wavelength measurement. An uncertainty of 1 pm (70 MHz) is assumed accounting for the uncertainty related to the determination of the wavelength correction described in paragraph 5.6.2 and possible wavelength drifts over the course of a typical DIAL measurement duration of a few minutes. Figure 5.40 shows a histogram of the recorded on-line wavelengths of the DIAL measurement. Fluctuations of the on-line wavelength on the absorption line can represent another systematic error source if the wavelength distribution spreads out to the flanks of the absorption line. This is however not the case here as the on-line wavelengths are positioned narrowly (29 MHz standard deviation) at the peak of the R30 line and the more significant systematic error still stems from the accuracy of the wavelength meter.

Table 5.11: Budget of systematic errors for DIAL measurements of CO_2 up to a height of 1.5 km. Assumed uncertainties of spectroscopic parameters from HITRAN2020 database. Errors were calculated using a random-seeding approach (see section 5.5.6).

Systematic error source	Uncertainty	Relative error
Transmitter		
Wavelength accuracy	1 pm (70 MHz)	0.2%
Spectroscopy		
Line position	0.001 cm^{-1}	0.1%
Line intensity	1%	0.8%
Air-broadened width γ_{air}	2%	1.6%
T-exponent of γ_{air}	5%	0.2%
Pressure shift	0.001 cm^{-1}	negligible
Atmosphere		
Temperature	3 K	0.3%
Pressure	5h Pa	negligible
Total systematic error		1.9%

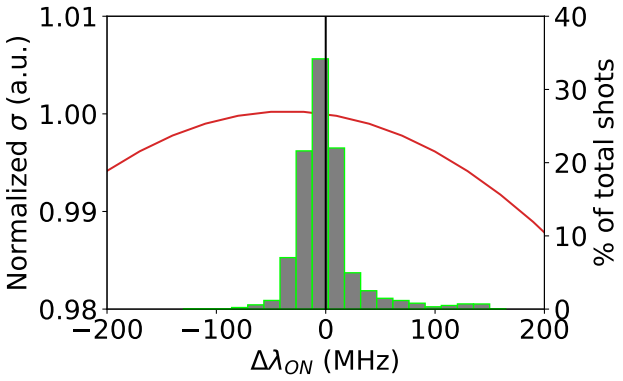

Figure 5.40: CO_2 absorption cross-section σ (left y-axis) and histogram of on-line wavelengths (right y-axis) expressed as differences $\Delta\lambda_{ON}$ from the mean on-line wavelength. Absorption cross-section is normalized to its value at the mean on-line wavelength.

5.6.6 OFF/OFF DIAL experiment

An experimental approach to check the DIAL retrieval for eventual biases due to misalignment, shot-to-shot laser beam pointing variations or fluctuations of the aerosol backscatter coefficient between two laser shots consists in conducting a DIAL measurement with two wavelengths with low and equal absorption. In theory, such a "ghost" measurement should yield a flat differential optical depth with slope zero and any deviations from that can be quantified as eventual bias in the mixing ratio retrieval.

Such an experiment was conducted after the above presented CO_2 DIAL measurement by using two equally absorbed off-line wavelengths at 2051.18 nm and 2051.32 nm. Figure 5.41a shows both lidar signals averaged over a duration of 5 min during which roughly 18 000 valid off/off shot pairs were accumulated.

The difference in the measured signals is related to slightly different energies of the NesCOPO cavity modes at both wavelengths. From both off-line signals, the differential optical depth was calculated which is shown in Fig. 5.41b. As expected, the measured DOD is mostly flat over the range of 1.5 km with only minor deviations in the first 300 m which can be due to the effect of laser beam pointing fluctuations in the zone of incomplete overlap between laser beam and receiver field of view. In order quantify potential biases on the mixing ratio retrieval, the DOD from the two off-line signals was then processed as if a CO_2 DIAL measurement was conducted, i.e. the second off-line wavelength at 2051.32 nm was treated as if it was the on-line wavelength at 2050.696 nm for the calculation of the absorption cross-sections. Fig. 5.41c shows the retrieved mixing ratio bias using 300 m range bins and a 150 m sampling. Indeed, the retrieved mixing ratios are close to zero accounting for their standard errors, except for the first DIAL point for which the mixing ratio differs from the expected value of zero by roughly 7 ppm which might be caused by laser depointing fluctuations in the zone of incomplete overlap or parasitic signal offsets from the Pockels cell of the Q-switched pump laser.

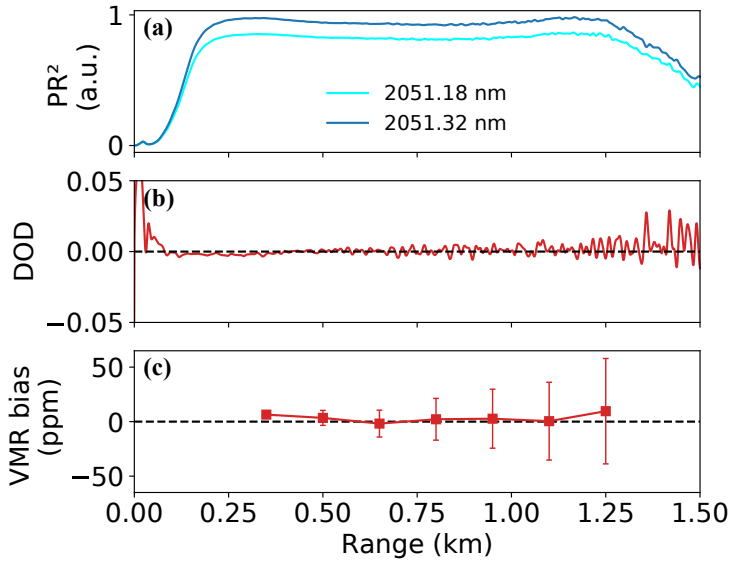

Figure 5.41: DIAL experiment with two off-line wavelengths at 2051.18 nm and 2051.32 nm. (a) Averaged range-corrected signals (5 min averaging, ca. 18 000 valid shot pairs). (b) Differential optical depth calculated from both off-line lidar signals. (c) Volume mixing ratio bias retrieved from the DOD in (b) by using the absorption cross-section at the CO_2 on-line wavelength for one of the two off-line wavelengths in order to simulate a DIAL measurement for which the expected retrieved concentration would be zero. Retrieval with 300 m range bins and 150 m sampling.

5.6.7 Comparison to other atmospheric CO_2 measurements close to Paris

Thanks to the high density of research laboratories on the Saclay plateau, several measurements of atmospheric CO_2 that were conducted close to ONERA are reported in the literature. In a comprehensive study for the whole Paris region, Xueref-Remy et al. (2018) used CO_2 in situ sensors at five locations in and around Paris to produce a continuous one-year long data set in 2010/2011. One of the peri-urban measurement stations was in Gif-sur-Yvettes (48.71° N, 2.15° E) located approximately 6 km west of ONERA. For the month of April 2011, the monthly mean and standard deviation are 408.7 ppm and 15.3 ppm, respectively. Much larger variability of CO_2, with concentrations occasionally exceeding 500 ppm, has been

observed at the site of Gonesse (48.99° N, 2.46° E) located ca. 20 km to the north of the Paris city center which is subject to the influence of a highway with heavy traffic during rush hour, two airports in proximity, as well as industrial sources.

Closer to ONERA at the Laboratoire de Météorologie Dynamique (LMD) facility at École Polytechnique (48.72° N, 2.21° E), Gibert et al. (2008) used a heterodyne-detection DIAL system operating at 2064 nm for horizontal and vertical measurements of the mean CO_2 mixing ratio in the lower troposphere in June 2005. The mean concentration was calculated over the entire observation range (0.2–1.2 km a.g.l.) using a single linear fit of the optical depth measurement, i.e. no range-resolved profile was retrieved. In that particular study, the measured mean CO_2 mixing ratio in the boundary layer was very similar to the measurement by an in situ sensor on the ground, which was even located a few kilometers away from the lidar, suggesting a well mixed boundary layer.

Comparing directly the obtained results by the WaVIL CO_2 DIAL with measurements reported in the literature is difficult because locations and measurement conditions are different. What the presented examples show is that indeed mixing ratios up to 500 ppm were measured before in the boundary layer in the Greater Paris region. However, a vertical gradient of almost 100 ppm within 1 km is rather unlikely in the afternoon when the boundary layer is usually well mixed.

5.6.8 Conclusion

By changing the operation wavelength from the H_2O/HDO window at 1.98 µm to 2.05 µm the versatility of the developed parametric laser source was demonstrated and a vertical range-resolved measurement of the atmospheric boundary layer CO_2 content was performed. While the near-range points of the DIAL-measured CO_2 profile compare well with a reference sensor on the ground, values measured towards 1 km above the ground are around 25% higher. Such a vertical gradient of close to 100 ppm seems rather unlikely in a well-mixed boundary layer suggesting that additional biases might be present in the measurement. The hypothesis of a systematic error due to a non-uniform overlap function could be rejected experimentally by conducting a "ghost"-DIAL measurement using two equally absorbed off-line wavelengths. Another potential source of error could be attributed to the response of the detector or the linearity of detection and acquisition unit. Compared to the water vapor DIAL measurements presented in the previous sections, the CO_2 on-line wavelength is absorbed more strongly giving rise to effects which were not observed for water vapor since the on- and off-line signals were more similar. Given the limited time frame of this last measurement campaign, this hypothesis was not further investigated. An interesting experimental approach to test this hypothesis would be to compare two consecutive DIAL measurements: one with the on-line wavelength tuned to the peak of the CO_2 absorption line as presented here and another with the on-line wavelength tuned to the wing reducing the attenuation of the on-line signal which should reduce any effect due to the detector response or detection nonlinearity.

5.7 Conclusion of the DIAL measurement campaigns

The developed lidar instrument was tested in various experimental environments. This strategy was helpful to gain a better understanding of limitations and biases. This has finally led to a net improvement in the quality of the conducted lidar experiments over time. One such improvement concerns the calibration of the wavelength meter. The calibration method which was used initially and relied on a commercial calibration source led to a wavelength bias of ca. 10 pm due to the large gap between calibration wavelength close to 0.85 µm and the DIAL wavelength range at 1.98 µm. This was overcome by calibrating the wavelength meter at 1.58 µm and by applying an additional wavelength correction which was estimated with the help of a 2.05 µm laser diode locked to a CO_2 absorption line.

With the final configuration of the WaVIL instrument, it was possible to obtain for the first time ever range-resolved measurements of the stable water vapor isotopologues H_2O and HDO along the vertical using a lidar. However, rather coarse range resolutions (ca. 500 m) have to be used in order to reduce the noise error of the HDO measurement due to weak absorption. This limits the HDO retrieval, and thus the estimation of the isotopic abundance δD, to a low number of 2–4 points in the atmospheric boundary layer. Due to the more favorable absorption of H_2O, DIAL soundings with vertical resolutions of 100–200 m and a temporal resolution of 20–30 min were demonstrated with relative random errors ranging from a few percent close to the surface to 20–30% towards the boundary layer top. The total systematic error was estimated to be under 3%. However, these values are derived from the measured SNR and essentially from a theoretical model. For a more rigorous derivation of quantitative estimates of precision and bias, measurements over a longer duration (a few days) and a better validation strategy with a higher density of reference measurements in space and time are needed, which takes a lot of effort to realize.

Finally, the potential of the developed parametric source to serve as transmitter of a multi-species DIAL instrument was demonstrated with an additional DIAL measurement of CO_2 at 2.05 µm.

Chapter 6

Perspectives for the development of a high-energy multi-species DIAL instrument

This chapter presents the instrumental improvements undertaken in the framework of the development of the LEMON lidar which is aimed to demonstrate the characteristics required for a space-borne instrument. This concerns the improvement in terms of laser energy to levels >30 mJ realized by the implementation of a double-stage OPA setup based on high-aperture PPKTP similar to the crystals which were characterized experimentally in chapter 4. Furthermore, an improvement in frequency stability towards a few hundred kHz over 10 s integration time is envisioned by the use of a frequency-locking scheme developed in the framework of this thesis project and a referencing technique based on a stabilized optical frequency comb developed by an industrial partner. With respect to the receiver of the future LEMON lidar, an improvement in measurement sensitivity is expected due to a larger telescope and a slightly more sensitive detector. Finally, taking these new developments into account, the expected precision for ground-based DIAL measurements of H_2O and HDO is compared to the performance of the WaVIL instrument and the sensitivity for an airborne measurement scenario is discussed.

Parts of this chapter were the subject of a peer-reviewed article in the MDPI journal *Atmosphere* published in March 2021.

6.1 Improvement of the transmitter OPA line

This section provides a solution for an improved OPA architecture which will be implemented in the LEMON lidar transmitter in order to increase the pulse energy of the signal wavelength. The achievable output energies for the improved design were estimated based on numerical simulations that were initialized with the OPA test results obtained on the WaVIL laser bench presented in section 4.4.1.

6.1.1 Two-stage OPA setup for increased output energy

The OPA experiments conducted on the WaVIL laser bench showed that the achievable output energy was limited by the damage threshold of the anti-reflection coating of the PPKTP crystals. As a consequence, less than half of the available pump energy was used for the amplification process. In order to overcome this issue, an architecture based on two successive OPA stages each consisting of two amplifiers was investigated

in the frame of the LEMON lidar development. Figure 6.1 schematically illustrates the envisioned OPA setup which enables a separation of the total available pump energy and a disposal of the depleted pump behind the first amplifier stage. The idler is coupled out after each amplifier to reduce gain saturation effects.

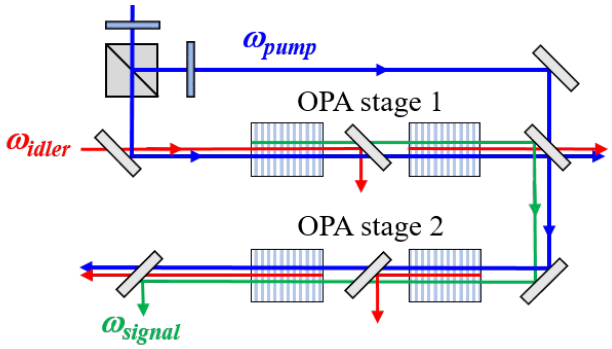

Figure 6.1: Schematic of the envisioned two-stage OPA setup

The QPM period chosen for the PPKTP crystals of the LEMON transmitter is 38.75 µm and thus slightly different to the PPKTP crystals used in the WaVIL OPA setup. The choice results from the need to reach the target spectral bands within a convenient temperature range of 20–80°C. Figure 6.2 shows the gain spectra of a 10 mm-long PPKTP crystal with a 38.75 µm poling period at two operation temperatures corresponding to the gain optima for the 1.98 µm and the 2.05 µm spectral windows.

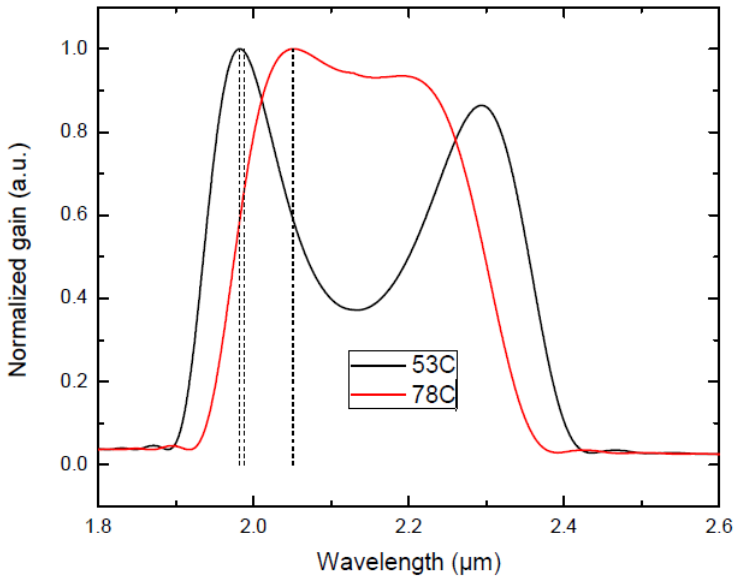

Figure 6.2: Calculated gain spectra in 10 mm long PPKTP with 38.75 µm poling period at temperatures of 53°C and 78°C. Dashed vertical lines indicate the H_2O/HDO spectral window at 1.98 µm and the CO_2 spectral window at 2.05 µm.

6.1.2 Expected output energy based on experiment-initialized simulations

The expected output energy of a two-stage OPA setup was estimated using numerical simulations which were conducted by LEMON project collaborators at Fraunhofer ILT in Germany. In a first step, the numerical model was used to simulate the OPA experiment conducted with the WaVIL laser bench presented in section 4.4.1. The calculated signal energies were compared with the measured values and the simulation parameters were adapted to best fit the experimental data. In a second step, the simulations were run with the adjusted simulation parameters for the two-stage OPA design of the LEMON transmitter.

6.1.2.1 Experiment-based initiation of the numerical model

Figure 6.3 depicts in red the measured signal energy as a function of pump energy for an OPA configuration consisting of three 12 mm-long PPKTP crystals with an idler filter between the second and third crystal (configuration (c) of Fig. 4.14). In the experiment on the WaVIL laser bench, the OPA setup was seeded with 10–20 µJ of idler radiation at 2.30 µm and it was pumped at 1.064 µm by 15 ns pulses at a repetition rate of 150 Hz. The pump beam diameter ($1/e^2$-value) was determined as 2.8 mm.

The black curve of Fig. 6.3 shows the numerical result with modified simulation parameters to best fit the experimental data. Good agreement between experiment and simulation is achieved for a reduction in the gain which can be modelled by reducing the effective nonlinearity of the PPKTP crystals by a factor of 1.69. Indeed, a gain reduced by a factor of 1.5 is also reported in a previous study for the case that the pump laser is switched from multi- to single-longitudinal-mode operation (Elsen et al., 2017). Table 6.1 provides an overview over the parameters that were adapted to best fit the experimental data. A combination of reduced gain and reflection losses at the crystal facets are thus assumed to account for the actual experimental outcome. A gain reduction might be also be linked to slight misalignments in the experiment leading to non-optimal overlap between the pump and idler waves.

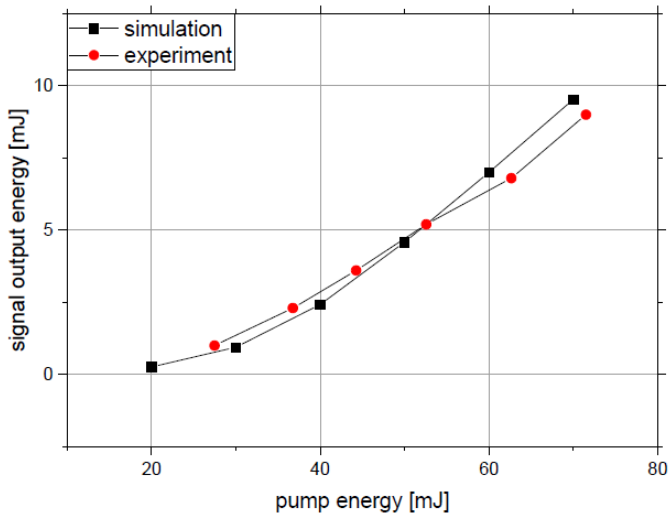

Figure 6.3: Measurement (obtained with WaVIL OPA configuration (c), see section 4.4.1) and simulation of the signal output energy as a function of pump energy for an OPA setup with three PPKTP crystals and an idler outcoupler behind the second crystal. Simulation parameters were adjusted as indicated in Table 6.1 to fit the experimental data. Calculations by Fraunhofer ILT. Figure from Hamperl et al. (2021b)

Table 6.1: Simulation values leading to best fit the experimental results.

Parameter	Nominal value	Simulation value
d_{eff} (pm/V)	9.3	5.5 (= $d_{\text{eff}}/1.69$)
Losses at crystal facets	n.a.	3%
Idler seed energy (µJ)	10–20	11

6.1.2.2 Simulation of output energy for a two-stage OPA setup

Using the the experiment-initiated simulation parameters, an OPA design consisting of four PPKTP crystals in two successive amplification stages with filtering of the idler wave behind each crystal was investigated. Indeed, distributing the available pump pulse energy between two stages and removal of the idler result in an optimization of the extracted signal and beam quality. Figure 6.4 shows the simulated signal output energy and beam quality factor M^2 after the second amplification stage dependent on the lengths of the two crystals of the second amplifier stage. The resulting energies were obtained for 12 mm-long crystals in the first amplifier stage pumped with pulse energies of 90 mJ and 110 mJ for the second stage.

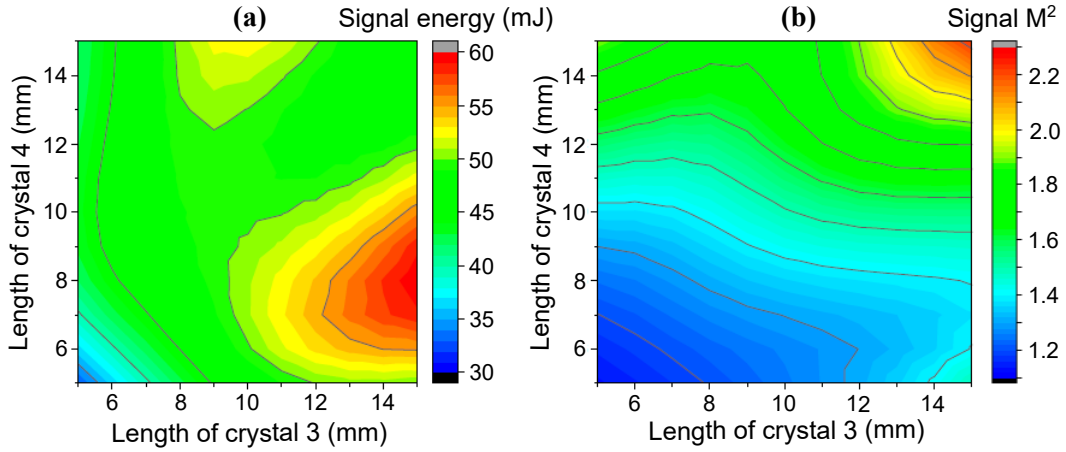

Figure 6.4: Calculated output pulse energy (a) and beam quality factor (b) after the second PPKTP amplification stage in dependency of crystal lengths between 5 and 15 mm for an idler-seeded OPA and a pump energy of 90 mJ in stage 1 and 110 mJ in stage 2. The first stage consists of two 12 mm-long PPKTP crystals and the idler wavelength is coupled out in between all four crystals for improved conversion efficiency. Calculations by Fraunhofer ILT. Figure from Hamperl et al. (2021b)

As a trade-off between achievable output pulse energy and beam quality, a design with 12 mm-long PPKTP crystals in the first stage and crystals with lengths of 12 mm and 6 mm in the second stage was chosen. For this configuration a signal pulse energy of > 50 mJ with a beam quality factor < 1.3 is expected for an incident pump energy of 90 mJ in the first OPA stage and 110 mJ in the second stage. Such high pump energies should in principle be possible without causing damage to the anti-reflection coatings of the PPKTP crystals as it was observed in the OPA experiments with the WaVIL system. The limitation to 70 mJ in the experiments was a rather conservative choice taking into account the degraded beam quality of the pump. The beam quality of the LEMON pump laser will be significantly improved so that pump beam diameter and fluence can be managed more efficiently.

6.2 Improvement of laser transmitter frequency stability

In the context of DIAL measurements, high stability of the emitted laser wavelengths is desired in order to sound the atmospheric gas of interest at a fixed spectral position during the entire measurement duration. Frequency stability is especially critical for prospective IP-DIAL measurements of greenhouse gases from space. A laser frequency stability close to 200 kHz (for averaging over 10 s) is needed in the case of an IP-DIAL system dedicated to CO_2 sounding from space in order to achieve the required accuracy in the measured column-averaged dry-air mixing ratio (Ingmann et al., 2008).

This section presents an active frequency control scheme which was implemented for the WaVIL NesCOPO and first test results for frequency locking over a duration of 10 min. Since the developed approach relies on a feedback loop using a commercial wavelength meter to monitor the emitted laser frequency, the achievable stability is thus only as good as the frequency stability of the wavelength meter. In the framework of the LEMON instrument, an absolute frequency reference based on a GPS-stabilized optical frequency comb will be realized.

6.2.1 Implementation of a NesCOPO-frequency control scheme

Deviations in the NesCOPO-emitted wavelengths are due to drifts of the coincidence between signal and idler frequency combs within the parametric gain bandwidth. These drifts can be caused by (i) changes in the signal and idler cavity lengths due to thermal deformations or vibrations, (ii) variations in the phase matching condition due to fluctuations of the crystal temperature and (iii) fluctuations of the pump wavelength. By properly adjusting the signal and idler cavity lengths using piezoelectric transducers, it is possible to maintain the overlap of the signal and idler cavity modes at a fixed position within the parametric gain bandwidth, thus locking the signal and idler wavelengths.

In the framework of this thesis, an active frequency control scheme was developed and tested for the WaVIL NesCOPO. Figure 6.5 schematically illustrates the feedback loop to stabilize the signal wavelength. A part of the signal at 1.98µm serves as error signal and is coupled into the wavelength meter (High Finesse WS-6-200-IR) which determines the wavelength on a shot-to-shot basis. The measured wavelength is sent to a computer which runs a stabilization algorithm. Depending on the difference between measured wavelength (the average wavelength of multiple laser shots is used in the algorithm) and a specified target value, the algorithm calculates the voltages needed to be applied to the piezoelectric transducers (PZT) controlling the translation of mirrors M1 and M3 of the NesCOPO to adjust the signal and idler cavity lengths. Parameters such as the proportionality factor between wavelength error and the required PZT voltage as well as the ratio of the PZT voltages for mirrors M1 and M3 were optimized experimentally.

6.2.2 Measurement of frequency stability

The active frequency control of the NesCOPO was tested over a duration of 10 min which corresponds to a typical signal averaging duration for ground-based DIAL measurements. Figure 6.6a compares the deviation of the NesCOPO-emitted signal wavelength (1.98 µm) in free-running mode with the closed-loop operation. The wavelength was measured by the wavelength meter which is in the feedback loop and provides the error signal for the stabilization algorithm. With no active stabilization, the measured signal

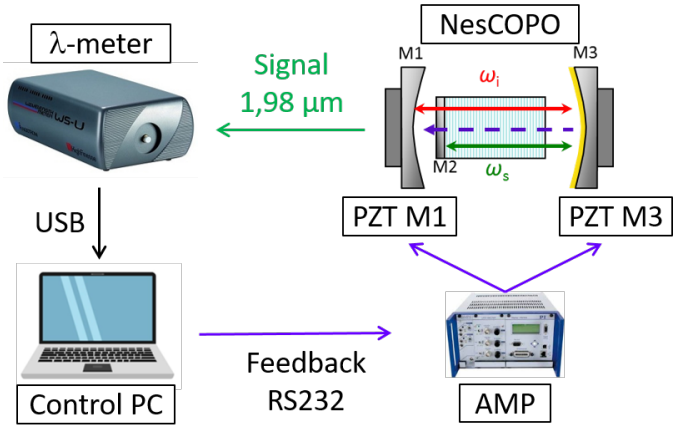

Figure 6.5: Schematic of the NesCOPO-stabilizing feedback loop. The signal wavelength is measured by the wavelength meter (High Finesse WS-6-200-IR) and is sent to a computer running the stabilization algorithm. Depending on the error signal, a feedback is sent to an amplifier module (AMP) generating the corresponding voltages for the piezoelectric transducers (PZT) of the NesCOPO cavity mirrors M1 and M3.

wavelength exhibits low-frequency fluctuations within a range of roughly 100 MHz over several minutes which can be attributed to variations in the room temperature of the laboratory and drifts in the pump laser pointing (which is highly correlated to the room temperature). In closed-loop operation, the fluctuations in the measured signal wavelength are well suppressed. In Fig. 6.6b the Allan standard deviations are plotted for both measurements shown in Fig. 6.6a. Although the active frequency control causes slightly increased standard deviations for averaging times <1 s (which could probably still be reduced by fine-tuning the algorithm parameters), it leads to sub-MHz frequency stability for averaging over more than 10 s. This clearly demonstrates the potential of the presented NesCOPO-stabilization technique in order to meet the stringent frequency stability requirements for IP-DIAL measurements from space.

The presented closed-loop measurement shown in Figs. 6.6a and 6.6b was obtained by the wavelength meter which is part of the feedback loop. However, the wavelength meter measurement can also be subject to drifts caused by temperature and pressure changes in the instrument environment. In order to asses the frequency stability by a measurement independent of the feedback loop, a simultaneous measurement with second wavelength meter was performed. Because this second wavelength meter (High Finesse WSU-10) is designed for the 1 µm spectral range, the NesCOPO-emitted idler wave was used to seed a PPKTP OPA stage and the generated signal wave was subsequently frequency-doubled to 991 nm using a second-harmonic setup. And indeed, the Allan standard deviation in closed-loop mode plotted in Fig. 6.6d does not show the same decrease with increasing averaging time. The frequency stability measured by the second wavelength meter outside the feedback loop remains in the MHz-range due to the relative measurement drift between the two wavelength meters.

A measurement of the IR-wavelength meter (W6-6-200-IR2) stability was already presented in section 5.5.2 (see page 104). Although obtained independently on a different day, Figure 6.6b also shows the Allan deviation of the experimentally measured wavelength meter stability (see Fig. 5.20a) for the purpose of demonstration. It clearly illustrates the problematic of drifts in the measured frequency at time scales of tens of seconds to minutes, hindering to reach an absolute frequency stability of a few hundreds of kHz over those time scales.

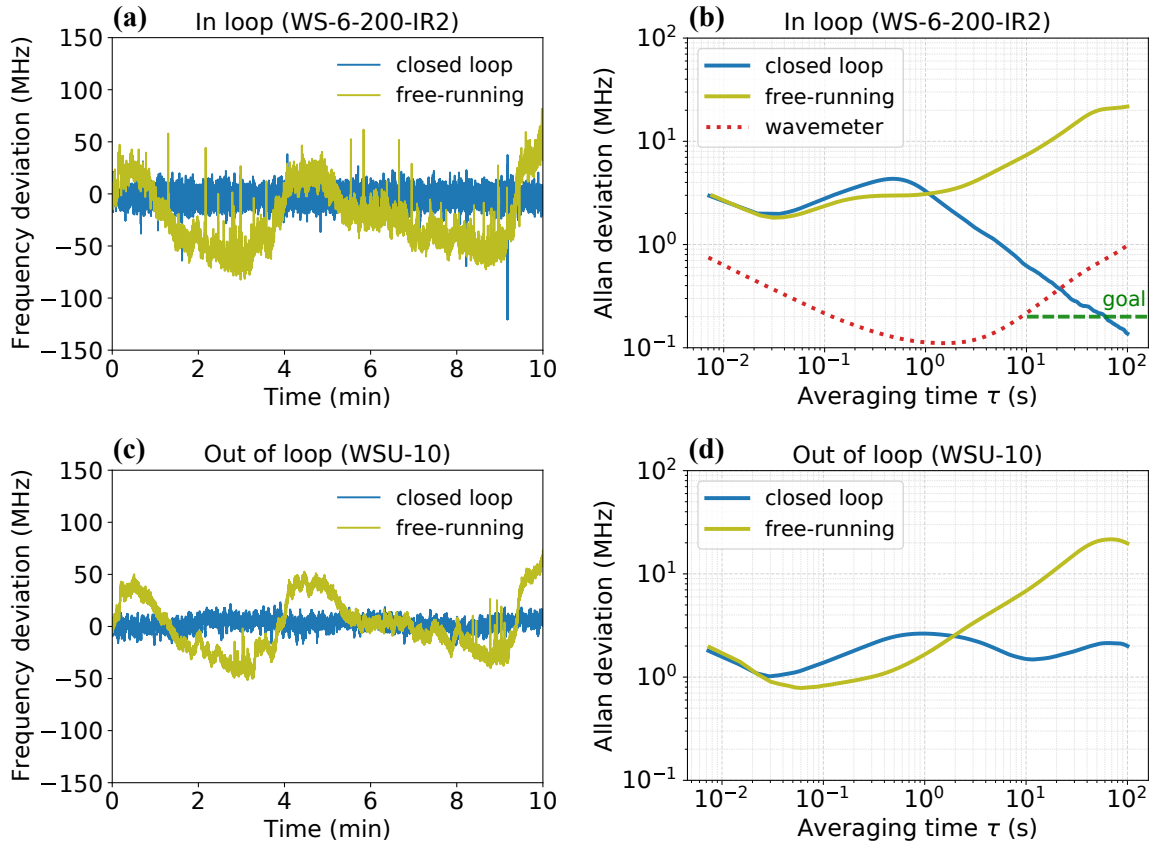

Figure 6.6: NesCOPO frequency stability over 10 min measured with a wavelength meter inside the feedback loop (top panels) and one out of the control loop (bottom panels). (a) NesCOPO signal (1.98 µm) frequency deviation over 10 min in free-running and closed-loop operation measured by the wavelength meter inside the feedback loop. (b) Allan deviations of the of the in-loop measurements shown in (a) and wavelength meter stability measured independently as described in section 5.5.2 (see page 104). Horizontal dashed line indicates stability requirement of 200 kHz for space-borne IP-DIAL sensing of CO_2. (c) Frequency stability in free-running and closed-loop mode measured by a wavelength meter outside the control loop. (d) Allan deviations of measurements shown in (c).

The presented measurement examples have demonstrated that sub-MHz frequency stability is achievable using a relatively simple feedback control scheme to stabilize the NesCOPO-emitted wavelengths by adjusting the cavity lengths using piezoelectric transducers. However, care has to be taken to lock the frequency to a stable reference.

6.2.3 Frequency referencing based on an optical frequency comb

A common approach for frequency referencing of a DIAL instrument is to use an absorption cell containing the gas of the species to be measured (Amediek et al., 2008). This allows for absolute calibration of the emitted wavelength but restricts the locking scheme to a narrow spectral band. For the broad spectral range required for the multi-species LEMON lidar, a solution based on an optical frequency comb was chosen to reference the laser transmitter wavelength and to transfer the stability and accuracy of a GPS-disciplined oscillator into the optical domain.

Today, the bidirectional transfer between the radio-frequency and optical domains is a well established technology. For the last two decades, it has been predominantly used in the laboratory in the context of

atomic and optical clock comparisons (Hollberg et al., 2005). More recently, frequency combs have also been deployed on satellites (Lezius et al., 2016) and novel applications such as field-deployed dual comb spectrometers for gas sensing have been demonstrated (Coburn et al., 2018). A stabilized frequency comb will also serve as the absolute frequency reference unit of the future space-borne Methane Remote Sensing LIDAR Mission (MERLIN) instrument (Schaefer et al., 2019).

6.3 Architecture of the future LEMON lidar

The overall LEMON instrument architecture is schematically depicted in Fig. 6.7. It is composed of: (i) a laser transmitter module consisting of two separate housings, which emits the laser radiation to probe the targeted gas absorption lines; (ii) a frequency reference unit (FRU), which provides the frequency of the emitted laser radiation with high accuracy; (iii) an acquisition and receiver module to detect and acquire the DIAL signals; (iv) a software and electronic control system to control the emitter unit, record, and analyze the data.

6.3.1 Lidar transmitter

In order to achieve the laser transmitter specifications based on the requirements for space-based IP-DIAL measurements and to benefit from the maturity and know-how on the development of 1.064 µm pump lasers, the LEMON laser transmitter architecture is based on a nested-cavity OPO (NesCOPO), followed by parametric amplifier stages. For enhanced thermo-mechanical stability, pump laser, NesCOPOs, and amplifiers are separated into two different housings, placed on a common base plate. The first housing is dedicated to the 1.06 µm pump laser and two NesCOPOs (NesCOPO 1 for H_2O/HDO and NesCOPO 2 for CO_2). The pump laser is a diode-pumped, injection-seeded Nd:YAG laser in MOPA configuration. The pump pulse duration is 15 ns with an energy of close to 200 mJ at a repetition rate of 150 Hz. A special pumping scheme will allow the operation in "quasi-75 Hz mode", meaning that pairs of pulses with a delay of 500 µs are emitted at a repetition rate of 75 Hz. Short pulse separation is especially critical for space-borne and airborne measurements in which the target reflectivity can change rapidly between the on- and off-line pulses due to the velocity of the satellite or aircraft. Around 0.5–1 mJ of the Nd:YAG oscillator is coupled out to pump the two NesCOPOs. The amplified pump beam is guided to the second housing which contains the double-stage PPKTP parametric amplifier setup presented in section 6.1.

6.3.2 Frequency reference unit

The frequency reference unit (FRU) consists of a femtosecond laser generating the optical frequency comb and the equipment necessary for the comb stabilization and beat note detection. Prior to the beat note measurement, the OPA signal is up-converted to the 1 µm spectral range in a second-harmonic stage to enable the use of standard silicon detectors. The wavelength determined from the beat note measurement between the nanosecond SHG pulse and an isolated line of the frequency comb serves as error signal for the active wavelength control of the NesCOPO and is recorded with the lidar signals on a shot-to-shot basis for data analysis in the DIAL retrieval.

6.3.3 Lidar receiver

The LEMON lidar receiver consists of a commercial PIN photodiode (same or similar to the one used in the WaVIL setup) coupled to a 350 mm diameter commercial telescope via multi-mode optical fiber. Great care was taken with respect to mechanical adaptations to ensure the stability of the receiver design with respect to aircraft vibration levels for airborne validation campaigns.

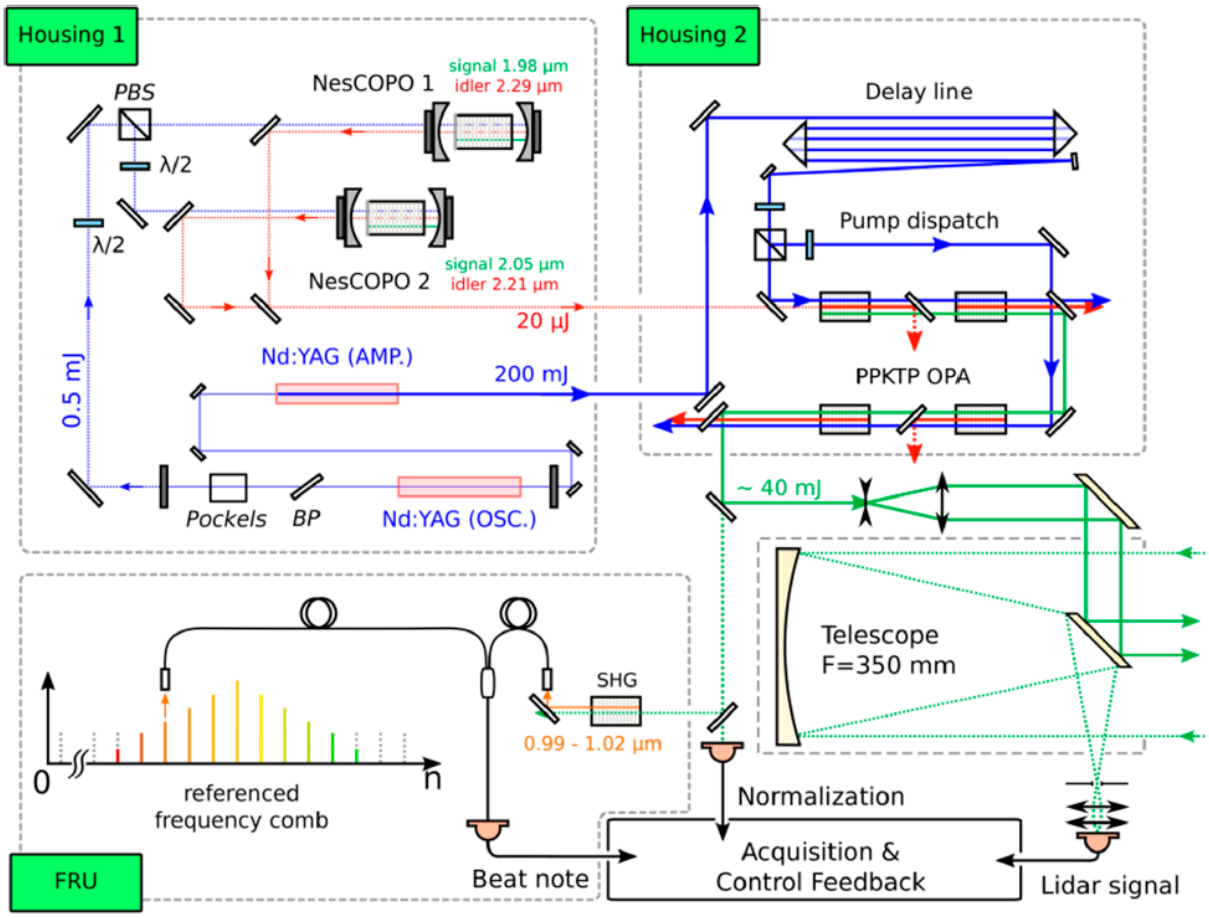

Figure 6.7: Schemaitc setup of the LEMON instrument architecture. Housing 1 with Nd:YAG pump laser (1.06 µm) in master-oscillator power amplifier (MOPA) configuration and two nested-cavity optical parametric oscillators (NesCOPO) for wavelength generation around 2.05 µm and 1.98 µm. Housing 2 contains two periodically poled Potassium Titanyle Phosphate crystals (PPKTP) amplification stages and a delay line to compensate for the pulse build-up time in the NesCOPOs. PBS: polarizing beam splitter, OSC: master oscillator, AMP: amplifier, SHG: second harmonic generation, FRU: frequency reference unit.

6.4 Expected sensitivity for ground-based and airborne DIAL measurements of H_2O and HDO

Taking the instrumental improvements realized with the future LEMON lidar into account, this section provides some estimates of the expected measurement precision following the approach outlined in the sensitivity analysis of chapter 3. The expected precision of ground-based measurements of H_2O and HDO is compared to the current WaVIL system. An overarching objective in the development of the LEMON instrument is a demonstration in the frame of an airborne measurement campaign. To provide a first estimate of the sensitivity which can be expected from such a measurement scenario, simulations were also performed for a nadir-looking airborne DIAL system.

6.4.1 Simulation parameters

The following calculations are based on the mid-latitude baseline atmospheric model (vertical profiles of pressure, temperature and water vapor mixing ratio) which was used in the sensitivity analysis in chapter 3. A vertical profile of the HDO isotopologue was calculated from the H_2O mixing ratio profile shown in Fig. 6.8a assuming a constant δD value of -100‰. Figure 6.8b shows the two different aerosol distributions used in the simulations. Model 1 is representative for conditions with aerosols confined to the atmospheric boundary layer (baseline model derived from median AOD, see section 3.2.2). Model 2 represents a more DIAL-favorable scenario with higher aerosol load and with the presence of a second aerosol layer in the free troposphere (derived from highest-decile AOD, see section 3.2.2). From the profiles of the aerosol extinction coefficient, the backscatter coefficient is calculated assuming a lidar ratio of 50 sr.

Besides a ground-based zenith-looking measurement configuration, an airborne nadir-looking measurement scenario is also investigated assuming an aircraft altitude of 4 km. Figure 6.8c shows the calculated optical depth spectrum for the first 2 km of atmosphere corresponding to the situation of a ground-based

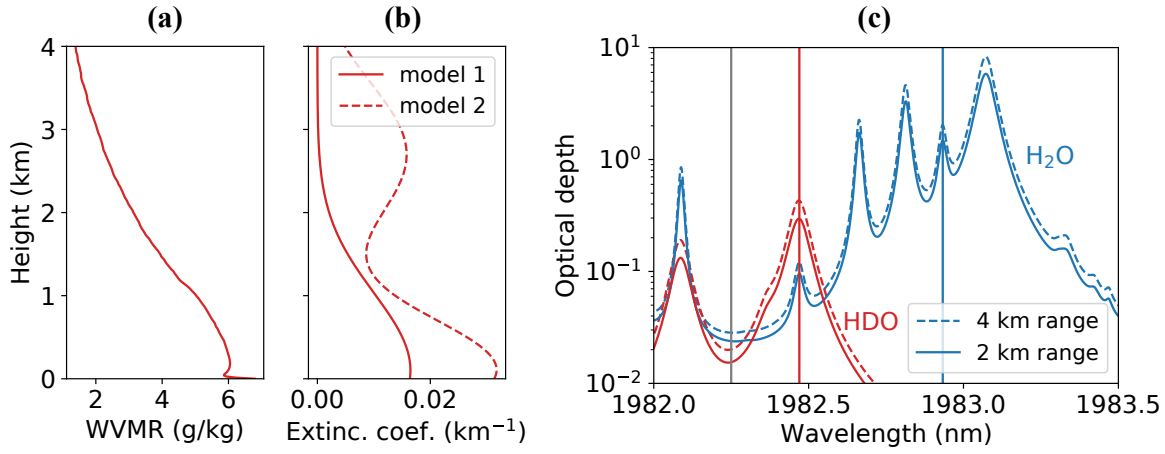

Figure 6.8: Vertical profiles of (a) water vapor mixing ratio (WVMR) and (b) aerosol extinction coefficient representative for mid-latitude atmospheric conditions. Model 1 is representative for aerosols confined to the atmospheric boundary layer, model 2 represents an additional layer aerosols in the free troposphere. (c) Optical depth spectrum calculated for the WVMR profile shown in (a) assuming a uniform δD of -100‰. Solid lines: ground-based measurement scenario (4 km total path length). Dashed lines: airborne scenario (8 km total path length).

measurement in the atmospheric boundary layer, and for 4 km of atmosphere corresponding to ground-based or airborne soundings of the boundary layer and lower free troposphere. For the sake of simplicity, only the on-line wavelengths of 1982.93 nm and 1982.47 nm are considered for H_2O and HDO, respectively.

Table 6.2 provides an overview of the instrumental parameters used in the simulations. Compared to the WaVIL instrument configuration with which the DIAL experiments were conducted in the framework of this thesis project, the future LEMON lidar will be significantly improved in terms of laser energy and will benefit from a larger telescope. For the following calculations, a laser pulse energy of 35 mJ (compared to typically 5 mJ for the current WaVIL instrument) and a telescope diameter of 35 cm (compared to 25 cm) are assumed. With respect to detection, the LEMON instrument will rely on a similar amplified InGaAs PIN photodiode. The calculations are based on a bandwidth of 1 MHz (150 m range resolution) and a NEP of 0.6 pW $Hz^{-1/2}$. This compares to the 3.5 MHz bandwidth setting (85 m range resolution) and a NEP of 1.3 pW $Hz^{-1/2}$ which were used for the DIAL experiments conducted with the WaVIL system. However, spatial averaging was typically applied in the retrieval to reduce the random error. Consequently, range bins of 150 m are used in the following for the calculation of random errors with the WaVIL instrument which makes it better comparable to the 150 m range resolution of the LEMON system. For both instruments, a total receiver transmission of 50% is assumed.

Table 6.2: Instrumental parameters used in the simulations

Instrument	**WaVIL (this work)**	**LEMON**
Pulse energy	5 mJ	35 mJ
Pulse length	12 ns	12 ns
Full beam divergence	0.3 mrad	0.3 mrad
Telescope diameter	25.4 cm	35 cm
Field of view	1.2 mrad	1.0 mrad
Detection bandwidth	3.5 MHz	1 MHz
NEP	1.3 pW $Hz^{-1/2}$	0.6 pW $Hz^{-1/2}$
Receiver transmission	0.5	0.5

6.4.2 Improvement of the ground-based measurement sensitivity

The expected measurement sensitivity of the future LEMON lidar system is compared with the DIAL of this thesis for a ground-based measurement scenario using aerosol model 1. For both systems, calculations were performed for 45 000 laser shots per wavelength which corresponds to time averaging over 10 min per isotopologue. Figure 6.9a depicts the resulting relative random error in the mixing ratio of H_2O for a range resolution of 150 m. The calculated precision for the WaVIL system is indeed in line with the precision typically achieved in the DIAL experiments of a few percent in the lower part of the boundary layer and a few tens of percent towards the boundary layer top at around 1.5 km above the ground. With the improvements brought about by the LEMON instrument, the precision would improve by roughly an order of magnitude allowing for the derivation of the H_2O mixing ratio with a relative precision better than 1% within the first 1.5 km.

The precision in the estimation of the HDO abundance δD will also increase significantly as shown in Fig. 6.9b. For the same averaging time of 10 min per isotopologue and a range resolution of 150 m, the absolute precision in δD is in the order of a few per mil in the lower boundary layer and reaches 20–40‰ towards the boundary layer top. This should make the LEMON system capable of monitoring the spatio-temporal variability of δD in the atmospheric boundary layer.

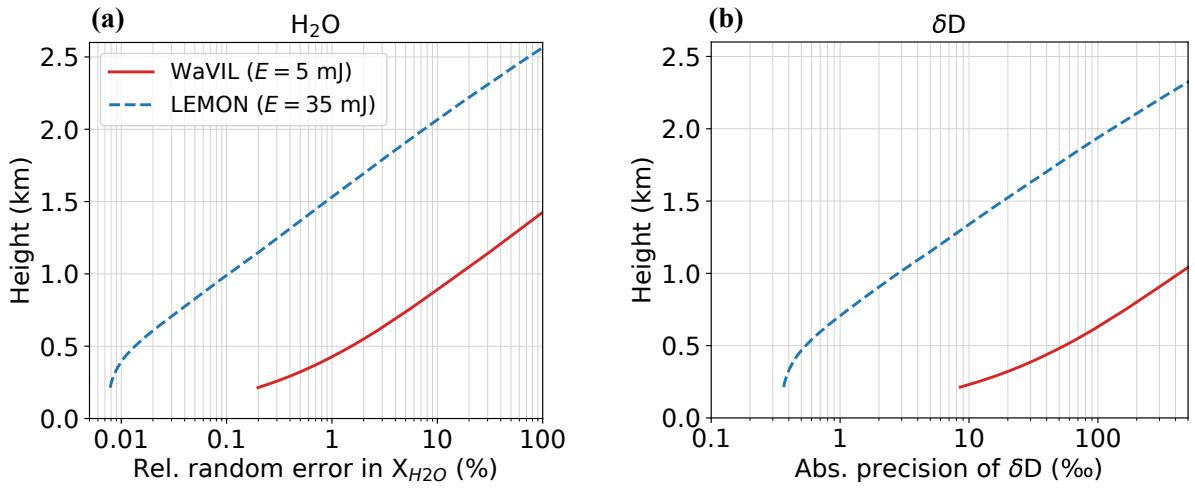

Figure 6.9: Expected precision from the future LEMON instrument compared to the current WaVIL system: (a) Relative random error in the mixing ratio of H_2O. (b) Absolute precision in δD calculated from independent measurements of H_2O and HDO. Calculations based on 45 000 shots per wavelength (10 min averaging per isotopologue), range resolution of 150 m and mid-latitude conditions (aerosol model 1).

6.4.3 Sensitivity for an airborne measurement scenario

In addition to the ground-based measurement scenario, simulations were also performed for the case of a nadir-looking measurement from an altitude of 4 km. The calculations are very simplified and do not take into account the effects of changing profiles of water vapor and aerosols due the movement of the aircraft. In reality, the aircraft would have to follow a flight pattern restricted to the desired horizontal dimensions of the sounded atmospheric column.

Figure 6.10 shows the calculated signal-to-noise ratios for different DIAL wavelengths of an airborne measurement compared the ground-based scenario with the same instrumental parameters averaged over the same number of laser shots. Panels (a) and (b) depict the vertical dependency of the lidar signals for the case of aerosols being confined to the boundary layer and for the case of a second aerosol layer in the free troposphere, respectively.

The corresponding relative random errors of the H_2O and HDO mixing ratios are shown in Fig. 6.11 calculated for a range resolution of 150 m. In the case where aerosols are confined to the boundary layer, the precision in the lower part of the atmosphere is, as expected, better when measured from the ground. However, an airborne measurement under these conditions would still be able to provide a vertical profile of H_2O with a relative error close to 1% in the boundary layer and around 10% in the free troposphere, which might be sufficient depending on the scientific objectives. The advantage of an airborne sounding is even more evident in Fig. 6.11b, which shows the relative random errors for the second case with aerosols also

present in the free troposphere. For that specific case, the simulations indicate a relative precision better than 1% for H_2O in the entire atmospheric column. The precision of the HDO mixing ratio would be a few percent in the atmospheric boundary layer and better than 1% in the free troposphere.

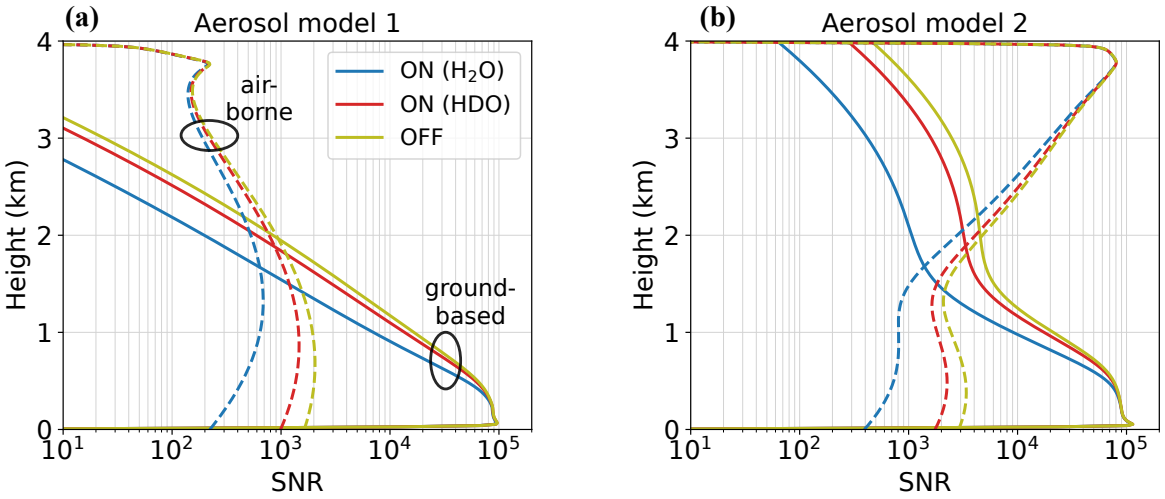

Figure 6.10: Signal-to-noise ratios at the on-line wavelengths of H_2O (blue) and HDO (red), and the off-line wavelength (gold) for a zenith-looking ground-based DIAL measurement (solid lines) and a nadir-looking measurement from an aircraft at an altitude of 4 km (dashed lines). (a) Medium aerosol load and aerosols confined to the boundary layer. (b) High aerosol load and additional free-tropospheric aerosol layer. 45 000 shots per wavelength.

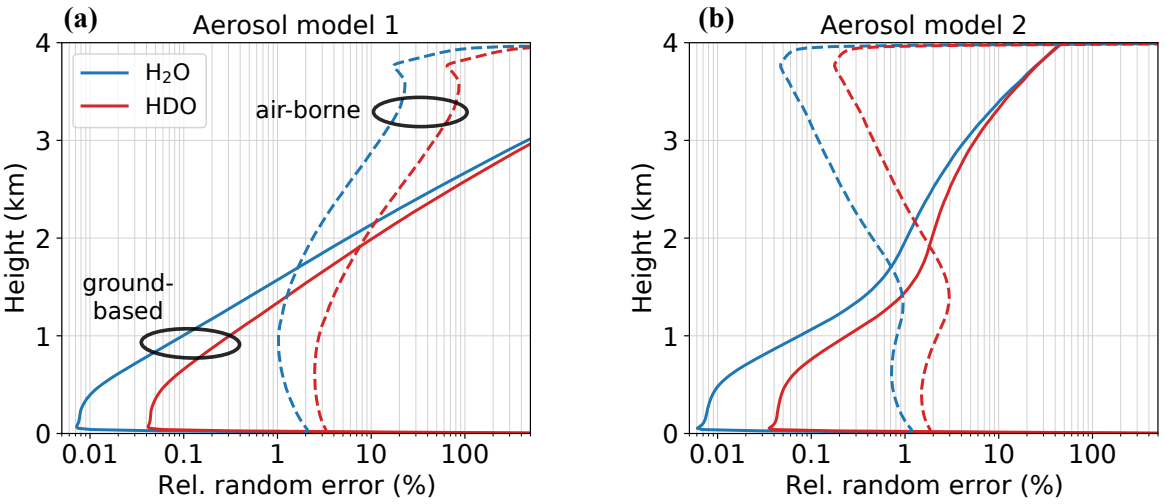

Figure 6.11: Relative random error in the mixing ratios of H_2O (blue) and HDO (red) for a zenith-looking ground-based DIAL measurement (solid lines) and a nadir-looking measurement from an aircraft at an altitude of 4 km (dashed lines). (a) Medium aerosol load and aerosols confined to the boundary layer. (b) High aerosol load and additional free-tropospheric aerosol layer. 45 000 shots per wavelength, range resolution of 150 m.

Finally, the precision in the isotopic abundance δD was calculated from two independent measurements of H_2O and HDO. Figure 6.12a depicts the comparison between ground-based and airborne measurements for the case of aerosols trapped in the atmospheric boundary layer. Under these conditions, an absolute δD precision of a few tens of per mil can be expected in the boundary layer when measured from an aircraft. Due to weak backscatter signals in the free troposphere, the precision deteriorates significantly with height making measurements of atmospheric δD in this zone with reasonable precision not possible. This changes for conditions with aerosols present in the free troposphere as indicated in Fig. 6.12b. In the presented case, the precision of δD is better than 10‰ for the majority of the free troposphere and reaches values of around 20‰ in the boundary layer when measured from an altitude of 4 km. The situation is reversed for the ground-based measurement where sub-10‰ precision can be expected in the boundary layer and a slightly larger noise error in the free troposphere. This shows clearly that in order to achieve even better precision over the entire 4 km range, in any measurement configuration, a more sensitive detector (avalanche photodiode) is required as outlined in the sensitivity analysis of chapter 3.

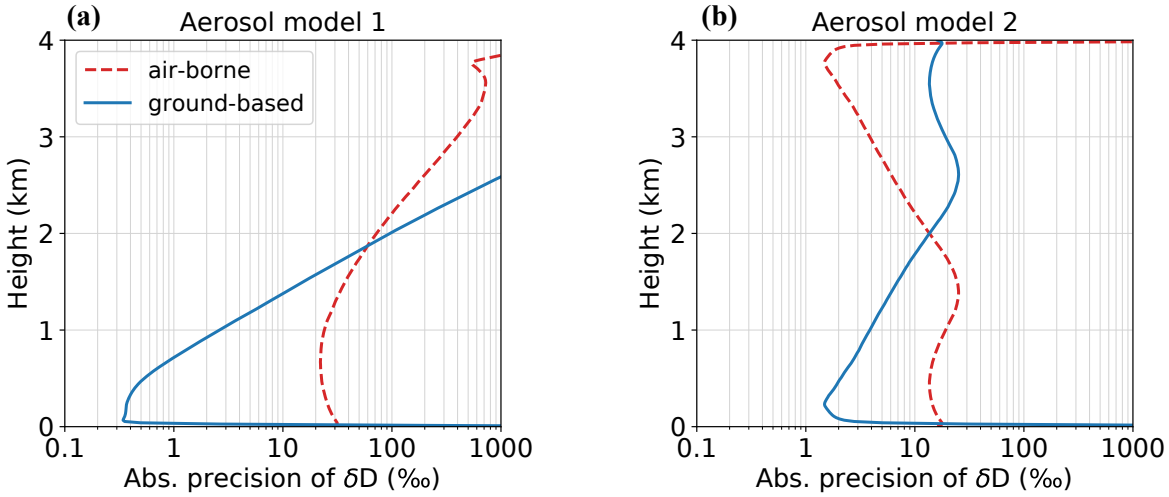

Figure 6.12: Absolute precision of the HDO abundance δD for a zenith-looking ground-based DIAL measurement (dashed line) and a nadir-looking airborne measurement from an altitude of 4 km. (a) Medium aerosol load and aerosols confined to the boundary layer. (b) High aerosol load and additional free-tropospheric aerosol layer. 45 000 shots per wavelength, range resolution 150 m.

6.5 Conclusion

With the realization of the future LEMON instrument, significant improvements compared to the current WaVIL system are to be expected. Thanks to the proposed double-stage amplification architecture based on high-aperture PPKTP crystals and the potential of using higher pump energies enabled by a higher-quality pump beam, it should be possible to achieve the desired output energies >40 mJ in line with the goal for future space-borne DIAL measurements of CO_2. It was also shown that sub-MHz frequency stability can be achieved with the parametric source by implementing a stabilization scheme for the NesCOPO-emitted signal wavelength. Furthermore, the use of a stabilized frequency comb as absolute frequency reference will eliminate issues with drift and calibration encountered with the use of standard wavelength meters.

Simulations conducted with the expected parameters of the future LEMON instrument showed that a significant improvement (ca. 1 order of magnitude) in the H_2O/HDO measurement sensitivity can be realized with the future LEMON instrument in comparison to the WaVIL setup tested in the framework of this thesis project. With laser energies > 30 mJ, a larger telescope diameter and slightly reduced detection noise, the LEMON lidar should enable range-resolved measurements of δD in the atmospheric boundary layer with a precision suitable for capturing variations in δD of a few tens of per mil. Calculations for an airborne nadir-looking measurement from an altitude of 4 km and with a range resolution of 150 m showed that the sensitivity depends largely on the vertical distribution of aerosols. If aerosols are present solely in the atmospheric boundary layer, DIAL measurements with reasonable precision are limited to H_2O only for which relative noise errors in the order of a few percent can be expected in the boundary layer and errors in the range of 10–20% in the free troposphere. For the more favorable case of higher aerosol load and an aerosol layer in the free troposphere, high signal-to-noise ratios can also be reached in the free troposphere which should even allow for the estimation of the HDO abundance δD.

General conclusions

The work presented in this thesis investigated the feasibility to measure vertical profiles of the stable water vapor isotopologues H_2O and HDO in the lower troposphere by using a differential absorption lidar. Stable isotopologues of water and their ratios act like natural tracers in the hydrological cycle and thus provide valuable information to improve the understanding of atmospheric processes such as cloud formation, moist convection and vertical mixing. Compared to passive remote sensors and in situ observations, lidar remote sensing offers the potential to deliver both continuous and highly resolved vertical profiles in the atmospheric boundary layer where the majority of atmospheric water vapor is concentrated and which is highly sensitive to exchange processes near the surface.

The potential of measuring H_2O and HDO by DIAL was first investigated theoretically by simulation. The numerical analysis took account of instrumental and environmental parameters to estimate the achievable precision in the HDO abundance δD. On the instrument side, calculations were performed for a commercial InGaAs PIN photodiode, which was utilized in the framework of this thesis project, and for a state-of-the-art low-noise HgCdTe avalanche photodiode to provide an estimation of the maximally achievable precision with current detector technology. The sensitivity to environmental factors was investigated for mid-latitude, arctic and tropical environments accounting for both vertical water vapor and aerosol variability. A DIAL-suitable wavelength window was identified between 1982 nm and 1984 nm where both water isotopologues possess well separated absorption features. The HDO absorption lines are substantially weaker which has to be mitigated by coarser range-resolution or stricter requirements on the laser source (higher pulse energy) and the lidar receiver (low-noise detector) if a relative precision similar to H_2O is required. With the commercial photodiode and for laser energies of 20 mJ, a range resolution of 150 m and time averaging over 10 min, the calculated precision (noise error) in δD is better than 10‰ in the first kilometer of atmosphere and reaches 20–40‰ towards the boundary layer top at 1.5 km under the mid-latitude and tropic model. The estimated values are in the order of or better than columnar measurements obtained by passive remote sensors but with much better vertical resolution. However, they are only partly sufficient to fully capture the vertical variability of δD of a few tens of per mil in the lower troposphere. With detection noise reduced by roughly an order of magnitude, the investigated HgCdTe avalanche photodiode can overcome this limitation for which calculations indicate a δD precision better than 10‰ within the entire boundary layer. The analysis also revealed a significantly reduced precision under arctic conditions due to low water vapor content and reduced aerosol load. An analysis of systematic errors identified the uncertainties in the spectroscopic line parameters of HDO as major contributions to the total systematic error of δD which highlights the importance of additional spectroscopic laboratory measurements in the 1.98 µm region.

A first experimental part of this thesis project consisted in the implementation of a parametric laser source capable of delivering high-energy (mJ-level) nanosecond pulses suitable for range-resolved DIAL measurements at 1.98 µm. The developed laser source is based on a nested-cavity OPO (NesCOPO) and an optical parametric amplifier stage. The NesCOPO serves as frequency converter of the 1.06 µm pump wavelength to tunable signal and idler wavelengths covering a spectral window from 1.95 to 2.30 µm. With the aim of developing a compact and broadband amplification setup, which can operate at 1.98 µm for H_2O/HDO but also at 2.05 µm for CO_2 DIAL sensing, an approach based on quasi-phase-matched nonlinear materials was tested. Therefore, state-of-the-art high-aperture ($5 \times 7\,mm^2$) PPKTP crystals were used as this material offers a high effective nonlinear coefficient, high resistance to optical damage as well as favorable mechanical and thermal properties. The final, optimized amplifier configuration is based on three 12 mm-long PPKTP crystals with an idler outcoupler after the second crystal to reduce gain saturation effects. Signal energies at 1.98 µm up to 9 mJ were demonstrated when pumped with 70 mJ. Higher pump energies could not be realized due to potential damage to the anti-reflection coatings on the crystal facets.

The developed 2 µm-laser was integrated into a lidar architecture in order to assess the feasibility of range-resolved DIAL measurements of the water vapor isotopologues H_2O and HDO experimentally in the frame of several measurement campaigns. With the final lidar configuration, vertical range-resolved measurements of both isotopologues were demonstrated in the atmospheric boundary layer above the ONERA site of Palaiseau. With signal averaging over roughly half an hour and a vertical resolution of 100–200 m, profiles of the H_2O mixing ratio were obtained with relative noise errors of a few percent in the first 500 m and 20–30% towards the boundary layer top at 1.5 km above the ground. This compares to a total systematic error of under 3% estimated from uncertainties related to atmospheric and spectroscopic parameters as well as the accuracy of the DIAL wavelength measurement. Good agreement between a DIAL-measured H_2O profile and an in situ profile obtained by a nearby radiosounding indicated no major bias over the entire range of 1.5 km. DIAL measurements of HDO are more challenging due to its weaker absorption. Coarser range resolutions were needed in order to reduce the noise error to a meaningful level. This limits the HDO retrieval, and thus the estimation of δD, to 2–4 points in the atmospheric boundary layer. The obtained values of δD in different experiments were most of the time in a range which would be expected for mid-latitude conditions (-50‰ to -200‰), however no validation with reference sensors was possible in the framework of the last measurement campaign in which the DIAL system was fully operational.

Figure 6.13 shows how the WaVIL instrument in its current state compares to space-borne and ground-based passive sensors as well as to the initially envisaged WaVIL instrument (notably with higher laser energy and a larger telescope). Although with range bins close to 0.5 km and rapidly decreasing precision with height, the current WaVIL instrument still offers a multi-level measurement of δD in the atmospheric boundary layer. In terms of time resolution, it is still better than passive space-borne sounders, but has a lower temporal resolution (ca. 1 h due to signal averaging) compared to ground-based FTIR spectrometers (a few minutes).

The conducted proof-of-concept experiments clearly illustrated the high instrumental demands for obtaining vertically resolved water isotopologue measurements using the DIAL method. The two key instrumental parameters of laser pulse energy (around 5 mJ in DIAL experiment conditions) and detector sensitivity (NEP of $1.3\,pW\,Hz^{-1/2}$ for the utilized InGaAs PIN detector and current amplifier) do not yet

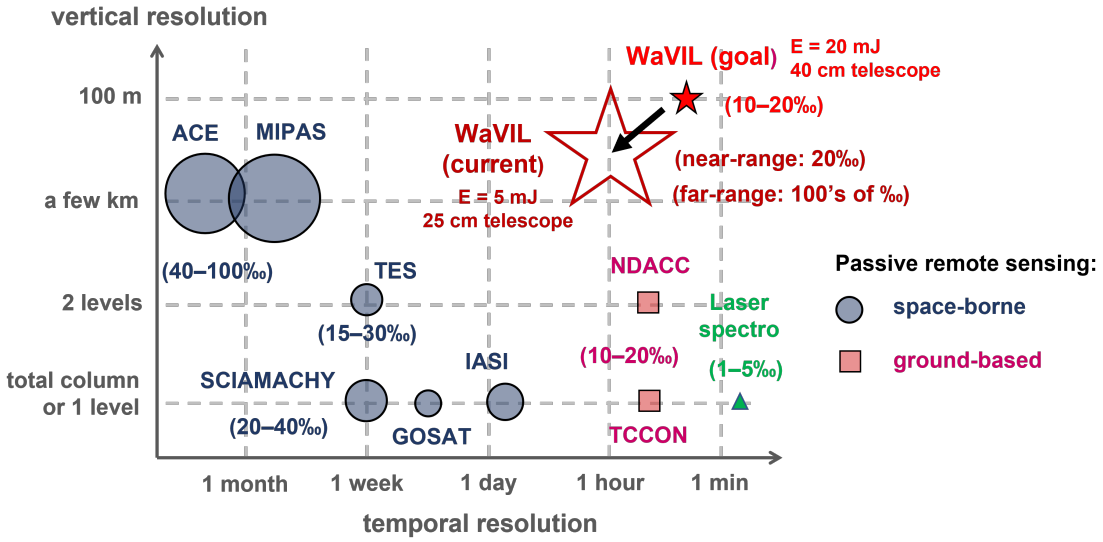

Figure 6.13: Performance in terms of vertical (y-axis) and temporal resolution (x-axis) as well as δD precision (values in parentheses; symbol size inversely proportional to precision) of the current WaVIL instrument compared to the initial goal and other measurement methods.

fully allow for δD profiling with the desired range-resolution and precision. Based on the conducted sensitivity analysis, the laser energy needs to be improved by a factor of 4–5 and the detector sensitivity ideally by a factor of 10 in order to be able to capture δD variations of a few tens of per mil in the entire boundary layer.

Furthermore, the versatility of the developed lidar transmitter was demonstrated with the measurement of a vertical profile of CO_2 at 2.05 µm.

An approach to scale the laser pulse energy was presented which is based on a double-stage parametric amplification setup. Using this improved architecture based on high-aperture PPKTP crystals, output energies are expected to reach up to 50 mJ. This would allow for significantly increased precision in range-resolved DIAL measurements of H_2O/HDO at 1.98 µm. Moreover, a 2 µm laser source emitting pulses with tens of mJ is also of interest in the context of future integrated-path-DIAL sensing of CO_2 from space. Such a measurement also requires sub-MHz frequency stability which was demonstrated with the developed laser setup by locking the NesCOPO-emitted wavelength using a simple stabilization scheme. The combination of large tuning range around 2 µm, potential pulse energies of tens of mJ, sub-MHz frequency stability and robustness enabled by quasi-phase-matched PPKTP crystals make the presented laser a unique transmitter platform for future multi-species greenhouse gas sensing.

References

A. Amediek, A. Fix, M. Wirth, and G. Ehret. Development of an OPO system at 1.57 µm for integrated path DIAL measurement of atmospheric carbon dioxide. 92(2):295–302, 2008.

A. Amediek, G. Ehret, A. Fix, M. Wirth, C. Büdenbender, M. Quatrevalet, C. Kiemle, and C. Gerbig. CHARM-F – a new airborne integrated-path differential-absorption lidar for carbon dioxide and methane observations: measurement performance and quantification of strong point source emissions. *Appl. Opt.*, 56(18):5182–5197, 2017.

A. Ansmann, J. Bösenberg, A. Chaikovsky, A. Comerón, S. Eckhardt, R. Eixmann, V. Freudenthaler, P. Ginoux, L. Komguem, H. Linné, M. L. Márquez, V. Matthias, I. Mattis, V. Mitev, D. Müller, S. Music, S. Nickovic, J. Pelon, L. Sauvage, P. Sobolewsky, M. K. Srivastava, A. Stohl, O. Torres, G. Vaughan, U. Wandinger, and M. Wiegner. Long-range transport of Saharan dust to northern Europe: The 11–16 October 2001 outbreak observed with EARLINET. *Journal of Geophysical Research: Atmospheres*, 108 (D24), 2003.

R. A. Anthes. Exploring earth's atmosphere with radio occultation: contributions to weather, climate and space weather. *Atmospheric Measurement Techniques*, 4(6):1077–1103, 2011.

G. Arisholm, Ø. Nordseth, and G. Rustad. Optical parametric master oscillator and power amplifier for efficient conversion of high-energy pulses with high beam quality. *Opt. Express*, 12(18):4189–4197, 2004.

A. Bailey, D. Noone, M. Berkelhammer, H. C. Steen-Larsen, and P. Sato. The stability and calibration of water vapor isotope ratio measurements during long-term deployments. *Atmospheric Measurement Techniques*, 8(10):4521–4538, 2015.

J. Barrientos-Barria. *Développement de deux instruments LIDAR multi-longueurs d'onde et multi-espèces à base de sources paramétriques*. PhD thesis, Université Pierre et Marie Curie, 2014.

J. Barrientos Barria, D. Mammez, E. Cadiou, J. B. Dherbecourt, M. Raybaut, T. Schmid, A. Bresson, J. M. Melkonian, A. Godard, J. Pelon, and M. Lefebvre. Multispecies high-energy emitter for CO_2, CH_4, and H_2O monitoring in the 2 µm range. *Opt. Lett.*, 39(23):6719–6722, 2014.

J. Beck, T. Welch, P. Mitra, K. Reiff, X. Sun, and J. Abshire. A highly sensitive multi-element HgCdTe e-APD detector for IPDA lidar applications. *Journal of Electronic Materials*, 43(8):2970–2977, 2014.

J. Bjorkholm and H. Danielmeyer. Frequency control of a pulsed optical parametric oscillator by radiation injection. *Applied Physics Letters*, 15(6):171 – 173, 1969.

S. Bony and J.-L. Dufresne. Marine boundary layer clouds at the heart of tropical cloud feedback uncertainties in climate models. *Geophysical Research Letters*, 32(20), 2005.

S. Bony, R. Colman, V. M. Kattsov, R. P. Allan, C. S. Bretherton, J.-L. Dufresne, A. Hall, S. Hallegatte, M. M. Holland, W. Ingram, D. A. Randall, B. J. Soden, G. Tselioudis, and M. J. Webb. How Well Do We Understand and Evaluate Climate Change Feedback Processes? *Journal of Climate*, 19(15):3445–3482, 2006.

J. Bösenberg. Ground-based differential absorption lidar for water-vapor and temperature profiling: methodology. *Appl. Opt.*, 37(18):3845–3860, 1998.

J. Bösenberg. Differential-Absorption Lidar for Water Vapor and Temperature Profiling. In *Lidar – Range-Resolved Optical Remote Sensing of the Atmosphere*, pages 213–239. Springer-Verlag, 2005.

D. Bruneau, P. Quaglia, C. Flamant, M. Meissonnier, and J. Pelon. Airborne lidar LEANDRE II for water-vapor profiling in the troposphere. I. System description. *Appl. Opt.*, 40(21):3450–3461, 2001.

D. Bruneau, F. Gibert, P. H. Flamant, and J. Pelon. Complementary study of differential absorption lidar optimization in direct and heterodyne detections. *Appl. Opt.*, 45(20):4898–4908, 2006.

M. Buchwitz, M. Reuter, O. Schneising, H. Boesch, S. Guerlet, B. Dils, I. Aben, R. Armante, P. Bergamaschi, T. Blumenstock, H. Bovensmann, D. Brunner, B. Buchmann, J. Burrows, A. Butz, A. Chédin, F. Chevallier, C. Crevoisier, N. Deutscher, C. Frankenberg, F. Hase, O. Hasekamp, J. Heymann, T. Kaminski, A. Laeng, G. Lichtenberg, M. De Mazière, S. Noël, J. Notholt, J. Orphal, C. Popp, R. Parker, M. Scholze, R. Sussmann, G. Stiller, T. Warneke, C. Zehner, A. Bril, D. Crisp, D. Griffith, A. Kuze, C. O'Dell, S. Oshchepkov, V. Sherlock, H. Suto, P. Wennberg, D. Wunch, T. Yokota, and Y. Yoshida. The Greenhouse Gas Climate Change Initiative (GHG-CCI): Comparison and quality assessment of near-surface-sensitive satellite-derived CO_2 and CH_4 global data sets. *Remote Sensing of Environment*, 162: 344–362, 2015.

R. L. Byer and R. L. Herbst. Parametric oscillation and mixing. In Y. R. Shen, editor, *Nonlinear Infrared Generation*, Topics in Applied Physics, pages 81–137. Springer, 1977.

E. Cadiou. *LIDAR DIAL multi espèces à base de sources paramétriques optiques pour la détection des gaz à effet de serre depuis l'espace.* PhD thesis, Université Paris-Saclay, 2017.

E. Cadiou, D. Mammez, J.-B. Dherbecourt, G. Gorju, J. Pelon, J.-M. Melkonian, A. Godard, and M. Raybaut. Atmospheric boundary layer CO_2 remote sensing with a direct detection LIDAR instrument based on a widely tunable optical parametric source. *Opt. Lett.*, 42(20):4044–4047, 2017.

B. J. Carroll, A. R. Nehrir, S. A. Kooi, J. E. Collins, R. A. Barton-Grimley, A. Notari, D. B. Harper, and J. Lee. Differential absorption lidar measurements of water vapor by the High Altitude Lidar Observatory (HALO): retrieval framework and first results. *Atmospheric Measurement Techniques*, 15(3):605–626, 2022.

N. Cezard. *Etude de faisabilité d'un lidar Rayleigh-Mie pour des mesures à courte portée de la vitesse de l'air, de sa température et de sa densité*. PhD thesis, Ecole polytechnique, Palaiseau, 2008.

P. Chazette and P. Royer. Springtime major pollution events by aerosol over Paris Area: From a case study to a multiannual analysis. *Journal of Geophysical Research: Atmospheres*, 122(15):8101–8119, 2017.

P. Chazette, F. Marnas, and J. Totems. The mobile Water vapor Aerosol Raman LIdar and its implication in the framework of the HyMeX and ChArMEx programs: application to a dust transport process. *Atmospheric Measurement Techniques*, 7(6):1629–1647, 2014.

P. Chazette, J.-C. Raut, and J. Totems. Springtime aerosol load as observed from ground-based and airborne lidars over northern Norway. *Atmospheric Chemistry and Physics*, 18:13075–13095, 2018.

P. Chazette, C. Flamant, H. Sodemann, J. Totems, A. Monod, E. Dieudonné, A. Baron, A. Seidl, H. C. Steen-Larsen, P. Doira, A. Durand, and S. Ravier. Experimental investigation of the stable water isotope distribution in an Alpine lake environment (L-WAIVE). *Atmospheric Chemistry and Physics*, 21(14): 10911–10937, 2021.

S. Coburn, C. B. Alden, R. Wright, K. Cossel, E. Baumann, G.-W. Truong, F. Giorgetta, C. Sweeney, N. R. Newbury, K. Prasad, I. Coddington, and G. B. Rieker. Regional trace-gas source attribution using a field-deployed dual frequency comb spectrometer. *Optica*, 5(4):320–327, 2018.

I. Coddington, N. Newbury, and W. Swann. Dual-comb spectroscopy. *Optica*, 3(4):414, 2016.

R. S. Coetzee, S. Duzellier, J. B. Dherbecourt, A. Zukauskas, M. Raybaut, and V. Pasiskevicius. Gamma irradiation-induced absorption in single-domain and periodically-poled $KTiOPO_4$ and Rb:$KTiOPO_4$. *Opt. Mater. Express*, 7(11):4138–4146, 2017.

R. T. H. Collis and P. B. Russell. Lidar measurement of particles and gases by elastic backscattering and differential absorption. In *Laser Monitoring of the Atmosphere*, pages 71–151. Springer Berlin Heidelberg, 1976.

H. Craig. Standard for reporting concentrations of deuterium and oxygen-18 in natural waters. *Science*, 133(3467):1833–1834, 1961.

C. Crevoisier, C. Clerbaux, V. Guidard, T. Phulpin, R. Armante, B. Barret, C. Camy-Peyret, J.-P. Chaboureau, P.-F. Coheur, L. Crépeau, G. Dufour, L. Labonnote, L. Lavanant, J. Hadji-Lazaro, H. Herbin, N. Jacquinet-Husson, S. Payan, E. Péquignot, C. Pierangelo, P. Sellitto, and C. Stubenrauch. Towards IASI-New Generation (IASI-NG): impact of improved spectral resolution and radiometric noise on the retrieval of thermodynamic, chemistry and climate variables. *Atmospheric Measurement Techniques*, 7(12):4367–4385, 2014.

W. Dansgaard. Stable isotopes in precipitation. *Tellus*, 16(4):436–468, 1964.

M. De Mazière, A. M. Thompson, M. J. Kurylo, J. D. Wild, G. Bernhard, T. Blumenstock, G. O. Braathen, J. W. Hannigan, J.-C. Lambert, T. Leblanc, T. J. McGee, G. Nedoluha, I. Petropavlovskikh, G. Seckmeyer, P. C. Simon, W. Steinbrecht, and S. E. Strahan. The network for the detection of atmospheric

composition change (NDACC): history, status and perspectives. *Atmospheric Chemistry and Physics*, 18 (7):4935–4964, 2018.

P. Di Girolamo, D. Summa, R.-F. Lin, T. Maestri, R. Rizzi, and G. Masiello. UV Raman lidar measurements of relative humidity for the characterization of cirrus cloud microphysical properties. *Atmospheric Chemistry and Physics*, 9(22):8799–8811, 2009.

P. Di Girolamo, B. De Rosa, C. Flamant, D. Summa, O. Bousquet, P. Chazette, J. Totems, and M. Cacciani. Water vapor mixing ratio and temperature inter-comparison results in the framework of the Hydrological Cycle in the Mediterranean Experiment—Special Observation Period 1. *Bulletin of Atmospheric Science and Technology*, 1(2):113–153, 2020.

M. Di Pierro, L. Jaeglé, E. W. Eloranta, and S. Sharma. Spatial and seasonal distribution of Arctic aerosols observed by the CALIOP satellite instrument (2006–2012). *Atmospheric Chemistry and Physics*, 13(14): 7075–7095, 2013.

T. Dinoev, V. Simeonov, Y. Arshinov, S. Bobrovnikov, P. Ristori, B. Calpini, M. Parlange, and H. van den Bergh. Raman Lidar for Meteorological Observations, RALMO - Part 1: Instrument description. *Atmospheric Measurement Techniques*, 6(5):1329–1346, 2013.

V. G. Dmitriev, G. G. Gurzadyan, and D. N. Nikogosyan. *Handbook of Nonlinear Optical Crystals*, volume 64 of *Springer Series in Optical Sciences*. Springer Berlin, Heidelberg, 1999.

A. Dumas, J. Rothman, F. Gibert, D. Édouart, G. Lasfargues, C. Cénac, F. L. Mounier, J. Pellegrino, J.-P. Zanatta, A. Bardoux, F. Tinto, and P. Flamant. Evaluation of a HgCdTe e-APD based detector for 2 µm CO_2 DIAL application. *Appl. Opt.*, 56(27):7577–7585, 2017.

C. Dyroff, D. Fütterer, and A. Zahn. Compact diode-laser spectrometer ISOWAT for highly sensitive airborne measurements of water-isotope ratios. *Applied Physics B*, 98(2-3):537–548, 2010.

C. Dyroff, S. Sanati, E. Christner, A. Zahn, M. Balzer, H. Bouquet, J. B. McManus, Y. González-Ramos, and M. Schneider. Airborne in situ vertical profiling of HDO / $H_2{}^{16}O$ in the subtropical troposphere during the MUSICA remote sensing validation campaign. *Atmospheric Measurement Techniques*, 8(5): 2037–2049, 2015.

D. H. Ehhalt. Vertical profiles of HTO, HDO, and H_2O in the troposphere. *NCAR Tech. Note NCAR–TN/STR–100*, page 131 pp., 1974.

D. H. Ehhalt, F. Rohrer, and A. Fried. Vertical profiles of HDO/H_2O in the troposphere. *Journal of Geophysical Research*, 110(D13), 2005.

G. Ehret, C. Kiemle, M. Wirth, A. Amediek, A. Fix, and S. Houweling. Space-borne remote sensing of CO_2, CH_4, and N_2O by integrated path differential absorption lidar: a sensitivity analysis. *Applied Physics B*, 90(3):593–608, 2008.

F. Elsen, M. Livrozet, M. Strotkamp, J. Wüppen, B. Jungbluth, R. Kasemann, J. Löhring, A. Meissner, R. Meyer, H.-D. Hoffmann, and R. Poprawe. Demonstration of a 100-mJ OPO/OPA for future lidar

applications and laser-induced damage threshold testing of optical components for MERLIN. *Optical Engineering*, 57(2):021205, 2017.

European Space Agency. ARMA Reference Model of the Atmosphere. 1999.

M. Fejer, G. Magel, D. Jundt, and R. Byer. Quasi-phase-matched second harmonic generation: tuning and tolerances. *IEEE Journal of Quantum Electronics*, 28(11):2631–2654, 1992.

R. A. Ferrare, E. V. Browell, S. Ismail, S. A. Kooi, L. H. Brasseur, V. G. Brackett, M. B. Clayton, J. D. W. Barrick, G. S. Diskin, J. E. M. Goldsmith, B. M. Lesht, J. R. Podolske, G. W. Sachse, F. J. Schmidlin, D. D. Turner, D. N. Whiteman, D. Tobin, L. M. Miloshevich, H. E. Revercomb, B. B. Demoz, and P. Di-Girolamo. Characterization of Upper-Troposphere Water Vapor Measurements during AFWEX Using LASE. *Journal of Atmospheric and Oceanic Technology*, 21(12):1790 – 1808, 2004.

A. Fix, G. Ehret, C. Kiemle, V. Klein, G. Mileti, J. P. do Carmo, M. Quatrevalet, R. Matthey, A. Amediek, and F. Gruet. Investigations on frequency and energy references for a space-borne integrated path differential absorption lidar. In B. Cugny, Z. Sodnik, and N. Karafolas, editors, *International Conference on Space Optics — ICSO 2014*. SPIE, 2017.

C. Frankenberg, K. Yoshimura, T. Warneke, I. Aben, A. Butz, N. Deutscher, D. Griffith, F. Hase, J. Notholt, M. Schneider, H. Schrijver, and T. Röckmann. Dynamic Processes Governing Lower-Tropospheric HDO/H_2O Ratios as Observed from Space and Ground. *Science*, 325(5946):1374–1377, 2009.

C. Frankenberg, D. Wunch, G. Toon, C. Risi, R. Scheepmaker, J.-E. Lee, P. Wennberg, and J. Worden. Water vapor isotopologue retrievals from high-resolution GOSAT shortwave infrared spectra. *Atmospheric Measurement Techniques*, 6(2):263–274, 2013.

J. Galewsky, H. C. Steen-Larsen, R. D. Field, J. Worden, C. Risi, and M. Schneider. Stable isotopes in atmospheric water vapor and applications to the hydrologic cycle. *Reviews of Geophysics*, 54(4):809–865, 2016.

J. Geng and S. Jiang. Fiber Lasers: The 2 μm Market Heats Up. *Optics and Photonics News*, 25(7):34–41, 2014.

F. Gibert, P. H. Flamant, J. Cuesta, and D. Bruneau. Vertical 2 μm Heterodyne Differential Absorption Lidar Measurements of Mean CO_2 Mixing Ratio in the Troposphere. *Journal of Atmospheric and Oceanic Technology*, 25(9):1477–1497, 2008.

F. Gibert, D. Edouart, C. Cénac, F. L. Mounier, and A. Dumas. 2-μm Ho emitter-based coherent DIAL for CO_2 profiling in the atmosphere. *Opt. Lett.*, 40(13):3093–3096, 2015.

F. Gibert, A. Dumas, J. Rothman, D. Edouart, C. Cénac, and J. Pellegrino. Performances of a HgCdTe APD based direct detection lidar at 2 μm. Application to DIAL measurements. *EPJ Web of Conferences*, 176: 01001, 2018a.

F. Gibert, J. Pellegrino, D. Edouart, C. Cénac, L. Lombard, J. L. Gouët, T. Nuns, A. Cosentino, P. Spano, and G. D. Nepi. 2-μm double-pulse single-frequency Tm:fiber laser pumped Ho:YLF laser for a space-borne CO_2 lidar. *Appl. Opt.*, 57(36):10370–10379, 2018b.

A. Godard. Infrared (2–12 μm) solid-state laser sources: a review. *Comptes Rendus Physique*, 8(10): 1100–1128, 2007.

A. Godard, M. Raybaut, and M. Lefebvre. Nested cavity optical parametric oscillators – a tunable frequency synthesizer for gas sensing. In *Encyclopedia of Analytical Chemistry*, pages 1–35. John Wiley Sons, Ltd, 2017.

J. E. M. Goldsmith, F. H. Blair, S. E. Bisson, and D. D. Turner. Turn-key Raman lidar for profiling atmospheric water vapor, clouds, and aerosols. *Appl. Opt.*, 37(21):4979–4990, 1998.

S. P. Good, D. Noone, and G. Bowen. Hydrologic connectivity constrains partitioning of global terrestrial water fluxes. *Science*, 349(6244):175–177, 2015.

J. W. Goodman. Some fundamental properties of speckle. *J. Opt. Soc. Am.*, 66(11):1145–1150, 1976.

I. Gordon, L. Rothman, R. Hargreaves, R. Hashemi, E. Karlovets, F. Skinner, E. Conway, C. Hill, R. Kochanov, Y. Tan, P. Wcisło, A. Finenko, K. Nelson, P. Bernath, M. Birk, V. Boudon, A. Campargue, K. Chance, A. Coustenis, B. Drouin, J. Flaud, R. Gamache, J. Hodges, D. Jacquemart, E. Mlawer, A. Nikitin, V. Perevalov, M. Rotger, J. Tennyson, G. Toon, H. Tran, V. Tyuterev, E. Adkins, A. Baker, A. Barbe, E. Canè, A. Császár, A. Dudaryonok, O. Egorov, A. Fleisher, H. Fleurbaey, A. Foltynowicz, T. Furtenbacher, J. Harrison, J. Hartmann, V. Horneman, X. Huang, T. Karman, J. Karns, S. Kassi, I. Kleiner, V. Kofman, F. Kwabia–Tchana, N. Lavrentieva, T. Lee, D. Long, A. Lukashevskaya, O. Lyulin, V. Makhnev, W. Matt, S. Massie, M. Melosso, S. Mikhailenko, D. Mondelain, H. Müller, O. Naumenko, A. Perrin, O. Polyansky, E. Raddaoui, P. Raston, Z. Reed, M. Rey, C. Richard, R. Tóbiás, I. Sadiek, D. Schwenke, E. Starikova, K. Sung, F. Tamassia, S. Tashkun, J. Vander Auwera, I. Vasilenko, A. Vigasin, G. Villanueva, B. Vispoel, G. Wagner, A. Yachmenev, and S. Yurchenko. The HITRAN2020 molecular spectroscopic database. *Journal of Quantitative Spectroscopy and Radiative Transfer*, 277: 107949, 2022.

I. E. Gordon, L. S. Rothman, C. Hill, R. V. Kochanov, Y. Tan, P. F. Bernath, M. Birk, V. Boudon, A. Campargue, K. V. Chance, B. J. Drouin, J. M. Flaud, R. R. Gamache, J. T. Hodges, D. Jacquemart, V. I. Perevalov, A. Perrin, K. P. Shine, M. A. H. Smith, J. Tennyson, G. C. Toon, H. Tran, V. G. Tyuterev, A. Barbe, A. G. Császár, V. M. Devi, T. Furtenbacher, J. J. Harrison, J. M. Hartmann, A. Jolly, T. J. Johnson, T. Karman, I. Kleiner, A. A. Kyuberis, J. Loos, O. M. Lyulin, S. T. Massie, S. N. Mikhailenko, N. Moazzen-Ahmadi, H. S. P. Müller, O. V. Naumenko, A. V. Nikitin, O. L. Polyansky, M. Rey, M. Rotger, S. W. Sharpe, K. Sung, E. Starikova, S. A. Tashkun, J. V. Auwera, G. Wagner, J. Wilzewski, P. Wcisło, S. Yu, and E. J. Zak. The HITRAN2016 molecular spectroscopic database. *Journal of Quantitative Spectroscopy and Radiative Transfer*, 203:3–69, 2017.

M. R. Gunson, M. M. Abbas, M. C. Abrams, M. Allen, L. R. Brown, T. L. Brown, A. Y. Chang, A. Goldman, F. W. Irion, L. L. Lowes, E. Mahieu, G. L. Manney, H. A. Michelsen, M. J. Newchurch, C. P. Rinsland,

R. J. Salawitch, G. P. Stiller, G. C. Toon, Y. L. Yung, and R. Zander. The Atmospheric Trace Molecule Spectroscopy (ATMOS) Experiment: Deployment on the ATLAS space shuttle missions. *Geophysical Research Letters*, 23(17):2333–2336, 1996.

M. Haeffelin, L. Barthès, O. Bock, C. Boitel, S. Bony, D. Bouniol, H. Chepfer, M. Chiriaco, J. Cuesta, J. Delanoë, P. Drobinski, J.-L. Dufresne, C. Flamant, M. Grall, A. Hodzic, F. Hourdin, F. Lapouge, Y. Lemaître, A. Mathieu, Y. Morille, C. Naud, V. Noël, W. O'Hirok, J. Pelon, C. Pietras, A. Protat, B. Romand, G. Scialom, and R. Vautard. SIRTA, a ground-based atmospheric observatory for cloud and aerosol research. *Annales Geophysicae*, 23(2):253–275, 2005.

J. Hamperl, C. Capitaine, J.-B. Dherbecourt, M. Raybaut, P. Chazette, J. Totems, B. Grouiez, L. Régalia, R. Santagata, C. Evesque, J.-M. Melkonian, A. Godard, A. Seidl, H. Sodemann, and C. Flamant. Differential absorption lidar for water vapor isotopologues in the 1.98 µm spectral region: sensitivity analysis with respect to regional atmospheric variability. *Atmospheric Measurement Techniques*, 14(10):6675–6693, 2021a.

J. Hamperl, J. F. Geus, K. M. Mølster, A. Zukauskas, J.-B. Dherbecourt, V. Pasiskevicius, L. Nagy, O. Pitz, D. Fehrenbacher, H. Schaefer, D. Heinecke, M. Strotkamp, S. Rapp, P. Denk, N. Graf, M. Dalin, V. Lebat, R. Santagata, J.-M. Melkonian, A. Godard, M. Raybaut, and C. Flamant. High Energy Parametric Laser Source and Frequency-Comb-Based Wavelength Reference for CO_2 and Water Vapor DIAL in the 2 µm Region: Design and Pre-Development Experimentations. *Atmosphere*, 12(3), 2021b.

B. Hardy, A. Berrou, S. Guilbaud, M. Raybaut, A. Godard, and M. Lefebvre. Compact, single-frequency, doubly resonant optical parametric oscillator pumped in an achromatic phase-adapted double-pass geometry. *Opt. Lett.*, 36(5):678–680, 2011.

B. Hardy-Baransky. *Façonnage du contenu spectral d'un OPO doublement résonnat par maîtrise de la phase relative, applications pour la spectroscopie*. PhD thesis, Ecole Polytechnique, 2011.

H. Herbin, D. Hurtmans, C. Clerbaux, L. Clarisse, and P.-F. Coheur. $H_2{}^{16}O$ and HDO measurements with IASI/MetOp. *Atmospheric Chemistry and Physics*, 9(24):9433–9447, 2009.

D. I. Herman, G. J. Mead, N. A. Malarich, F. R. Giorgetta, E. Baumann, B. R. Washburn, N. R. Newbury, I. Coddington, and K. C. Cossel. Open-path measurement of water isotopologues with mid-infrared dual-comb spectroscopy. In *Optical Sensors and Sensing Congress 2022 (AIS, LACSEA, Sensors, ES)*, page EM2D.4. Optica Publishing Group, 2022.

L. Hollberg, S. Diddams, A. Bartels, T. Fortier, and K. Kim. The measurement of optical frequencies. *Metrologia*, 42(3):S105–S124, 2005.

P. Ingmann, P. Bensi, Y. Duran, A. Griva, and P. Clissold. A-SCOPE Advanced Space Carbon and Climate Observation of Planet Earth. In *ESA Report for Assessment SP-1313/1 Candidate Earth Explorer Core Missions*. European Space Agency, 2008.

H. Ishizuki and T. Taira. High-energy quasi-phase-matched optical parametric oscillation in a periodically poled MgO:$LiNbO_3$ device with a 5 mm × 5 mm aperture. *Opt. Lett.*, 30(21):2918–2920, 2005.

H. Jacob and C. Sonntag. An 8-year record of the seasonal variation of ^{2}H and ^{18}O in atmospheric water vapour and precipitation at Heidelberg, Germany. *Tellus B*, 43(3):291–300, 1991.

L. R. Johnson, Z. D. Sharp, J. Galewsky, M. Strong, A. D. Van Pelt, F. Dong, and D. Noone. Hydrogen isotope correction for laser instrument measurement bias at low water vapor concentration using conventional isotope analyses: application to measurements from Mauna Loa Observatory, Hawaii. *Rapid Communications in Mass Spectrometry*, 25(5):608–616, 2011.

A. Kabacinski, J. Armougom, J.-M. Melkonian, M. Raybaut, J.-B. Dherbecourt, A. Godard, R. Vasilyeu, and V. Smirnov. Wavelength tunable, single-longitudinal-mode optical parametric oscillator with a transversally chirped volume Bragg grating. *Opt. Lett.*, 45(3):607–610, 2020.

S. R. Kawa, J. B. Abshire, D. F. Baker, E. V. Browell, D. Crisp, S. M. R. Crowell, J. J. Hyon, J. C. Jacob, K. W. Jucks, B. Lin, R. T. Menzies, L. E. Ott, and T. S. Zaccheo. Active Sensing of CO_2 Emissions over Nights, Days, and Seasons (ASCENDS): Final Report of the ASCENDS Ad Hoc Science Definition Team. *NASA/TP*, 2018.

J. T. Kiehl and K. E. Trenberth. Earth's Annual Global Mean Energy Budget. *Bulletin of the American Meteorological Society*, 78(2):197 – 208, 1997.

D. K. Killinger and N. Menyuk. Effect of turbulence-induced correlation on laser remote sensing errors. *Applied Physics Letters*, 38(12):968–970, 1981.

G. J. Koch, J. Y. Beyon, B. W. Barnes, M. Petros, J. Yu, F. Amzajerdian, M. J. Kavaya, and U. N. Singh. High-energy 2-μm Doppler lidar for wind measurements. *Optical Engineering*, 46(11):116201, 2007.

G. J. Koch, J. Y. Beyon, F. Gibert, B. W. Barnes, S. Ismail, M. Petros, P. J. Petzar, J. Yu, E. A. Modlin, K. J. Davis, and U. N. Singh. Side-line tunable laser transmitter for differential absorption lidar measurements of CO_2: design and application to atmospheric measurements. *Appl. Opt.*, 47(7):944–956, 2008. doi: 10.1364/AO.47.000944.

L. B. Kreuzer. Single mode oscillation of a pulsed singly resonant optical parametric oscillator. *Applied Physics Letters*, 15(8):263–265, 1969.

A. Kuze, H. Suto, K. Shiomi, S. Kawakami, M. Tanaka, Y. Ueda, A. Deguchi, J. Yoshida, Y. Yamamoto, F. Kataoka, T. E. Taylor, and H. L. Buijs. Update on GOSAT TANSO-FTS performance, operations, and data products after more than 6 years in space. *Atmospheric Measurement Techniques*, 9(6):2445–2461, 2016.

K. König, P. Imgram, J. Krämer, B. Maaß, K. Mohr, T. Ratajczyk, F. Sommer, and W. Nörtershäuser. On the performance of wavelength meters: Part 2—frequency-comb based characterization for more accurate absolute wavelength determinations. *Applied Physics B*, 126(5):86, 2020.

J. Lahyani. *Lidar 2 μm à source hybride fibrée/solide pour la télédétection du CO_2 atmosphérique*. PhD thesis, Institut Polytechnique de Paris, 2022.

J. Lahyani, J. L. Gouët, F. Gibert, and N. Cézard. 2.05-µm all-fiber laser source designed for CO_2 and wind coherent lidar measurement. *Appl. Opt.*, 60(15):C12–C19, 2021.

D. Lange, A. Behrendt, and V. Wulfmeyer. Compact Operational Tropospheric Water Vapor and Temperature Raman Lidar with Turbulence Resolution. *Geophysical Research Letters*, 46(24):14844–14853, 2019.

M. Lezius, T. Wilken, C. Deutsch, M. Giunta, O. Mandel, A. Thaller, V. Schkolnik, M. Schiemangk, A. Dinkelaker, A. Kohfeldt, A. Wicht, M. Krutzik, A. Peters, O. Hellmig, H. Duncker, K. Sengstock, P. Windpassinger, K. Lampmann, T. Hülsing, T. W. Hänsch, and R. Holzwarth. Space-borne frequency comb metrology. *Optica*, 3(12):1381–1387, 2016.

G. L. Liberti, D. Dionisi, F. Cheruy, and C. Risi. Feasibility study to measure HDO/H_2O atmospheric profiles through a Raman Lidar. *EPJ Web of Conferences*, 176:05032, 2018.

M. G. Littman. Single-mode operation of grazing-incidence pulsed dye laser. *Opt. Lett.*, 3(4):138–140, 1978.

A. Maity, S. Maithani, and M. Pradhan. Cavity ring-down spectroscopy: recent technological advances and applications. In *Molecular and Laser Spectroscopy*, pages 83–120. Elsevier, 2020.

V. Matthias, D. Balis, J. Bösenberg, R. Eixmann, M. Iarlori, L. Komguem, I. Mattis, A. Papayannis, G. Pappalardo, M. R. Perrone, and X. Wang. Vertical aerosol distribution over Europe: Statistical analysis of Raman lidar data from 10 European Aerosol Research Lidar Network (EARLINET) stations. *Journal of Geophysical Research: Atmospheres*, 109(D18), 2004.

S. H. Melfi, J. D. Lawrence, and M. P. McCormick. Observation of Raman scattering by water vapor in the atmosphere. *Applied Physics Letters*, 15(9):295–297, 1969.

G. Mennerat and P. Kupecek. High-energy narrow-linewidth tunable source in the mid infrared. In *Advanced Solid State Lasers*, page FC13. Optica Publishing Group, 1998.

G. Mie. Beiträge zur Optik trüber Medien, speziell kolloidaler Metallösungen. *Annalen der Physik*, 330 (3):377–445, 1908.

K. Mizutani, S. Ishii, M. Aoki, H. Iwai, R. Otsuka, H. Fukuoka, T. Isikawa, and A. Sato. 2 µm Doppler wind lidar with a Tm:fiber-laser-pumped Ho:YLF laser. *Opt. Lett.*, 43(2):202–205, 2018.

A. S. Moore, K. E. Brown, W. M. Hall, J. C. Barnes, W. C. Edwards, L. B. Petway, A. D. Little, W. S. Luck, I. W. Jones, C. W. Antill, E. V. Browell, and S. Ismail. Development of the Lidar Atmospheric Sensing Experiment (LASE) – An Advanced Airborne DIAL Instrument. In A. Ansmann, R. Neuber, P. Rairoux, and U. Wandinger, editors, *Advances in Atmospheric Remote Sensing with Lidar*, pages 281–288, Berlin, Heidelberg, 1997. Springer Berlin Heidelberg.

S. K. Muppa, A. Behrendt, F. Späth, V. Wulfmeyer, S. Metzendorf, and A. Riede. Turbulent Humidity Fluctuations in the Convective Boundary Layer: Case Studies Using Water Vapour Differential Absorption Lidar Measurements. *Boundary-Layer Meteorology*, 158(1):43–66, 2016.

G. Myhre, D. Shindell, F.-M. Bréon, W. Collins, J. Fuglestvedt, J. Huang, D. Koch, J.-F. Lamarque, D. Lee, B. Mendoza, T. Nakajima, A. Robock, G. Stephens, T. Takemura, and H. Zhang. Anthropogenic and Natural Radiative Forcing. In T. F. Stocker, D. Qin, G.-K. Plattner, M. Tignor, S. K. Allen, J. Boschung, A. Nauels, Y. Xia, V. Bex, and P. Midgley, editors, *Climate Change 2013: The Physical Science Basis. Contribution of Working Group I to the Fifth Assessment Report of the Intergovernmental Panel on Climate Change*. Cambridge University Press, Cambridge, United Kingdom and New York, NY, USA, 2013.

N. Pougatchev, T. August, X. Calbet, T. Hultberg, O. Oduleye, P. Schlüssel, B. Stiller, K. S. Germain, and G. Bingham. IASI temperature and water vapor retrievals – error assessment and validation. *Atmospheric Chemistry and Physics*, 9(17):6453–6458, 2009.

M. Raybaut, T. Schmid, A. Godard, A. K. Mohamed, M. Lefebvre, F. Marnas, P. Flamant, A. Bohman, P. Geiser, and P. Kaspersen. High-energy single-longitudinal mode nearly diffraction-limited optical parametric source with 3 MHz frequency stability for CO_2 DIAL. *Opt. Lett.*, 34(13):2069–2071, 2009.

T. F. Refaat, U. N. Singh, J. Yu, M. Petros, R. Remus, and S. Ismail. Double-pulse 2-μm integrated path differential absorption lidar airborne validation for atmospheric carbon dioxide measurement. *Appl. Opt.*, 55(15):4232–4246, 2016.

J. Reichardt, U. Wandinger, V. Klein, I. Mattis, B. Hilber, and R. Begbie. RAMSES: German Meteorological Service autonomous Raman lidar for water vapor, temperature, aerosol, and cloud measurements. *Appl. Opt.*, 51(34):8111–8131, 2012.

G. B. Rieker, F. R. Giorgetta, W. C. Swann, J. Kofler, A. M. Zolot, L. C. Sinclair, E. Baumann, C. Cromer, G. Petron, C. Sweeney, P. P. Tans, I. Coddington, and N. R. Newbury. Frequency-comb-based remote sensing of greenhouse gases over kilometer air paths. *Optica*, 1(5):290–298, 2014.

C. Risi, D. Noone, J. Worden, C. Frankenberg, G. Stiller, M. Kiefer, B. Funke, K. Walker, P. Bernath, M. Schneider, D. Wunch, V. Sherlock, N. Deutscher, D. Griffith, P. O. Wennberg, K. Strong, D. Smale, E. Mahieu, S. Barthlott, F. Hase, O. García, J. Notholt, T. Warneke, G. Toon, D. Sayres, S. Bony, J. Lee, D. Brown, R. Uemura, and C. Sturm. Process-evaluation of tropospheric humidity simulated by general circulation models using water vapor isotopologues: 1. Comparison between models and observations. *Journal of Geophysical Research: Atmospheres*, 117:D05303, 2012.

L. Régalia, C. Capitaine, B. Grouiez, and S. Mikhailenko. Absorption of deuterated water vapor in the 1.98 μm spectral region. *Journal of Quantitative Spectroscopy and Radiative Transfer*, 276:107915, 2021.

B. Saleh. *Photoelectron Statistics: With Applications to Spectroscopy and Optical Communication*. Springer-Verlag Berlin Heidelberg GmbH, 1978.

A. Sato, M. Aoki, S. Ishii, R. Otsuka, K. Mizutani, and S. Ochiai. 7.28-W, High-Energy, Conductively Cooled, Q-Switched Tm,Ho:YLF Laser. *IEEE Photonics Technology Letters*, 29(1):134–137, 2017.

H. Schaefer, D. Heinecke, T. Liebherr, D. Battles, K. Schleisiek, D. Fehrenbacher, M. Herding, A. Baatzsch, C. Dahl, and K. Nicklaus. Flight design of the absolute frequency reference unit for the methane-sensing LIDAR Mission MERLIN. In Z. Sodnik, N. Karafolas, and B. Cugny, editors, *International Conference on Space Optics — ICSO 2018*, volume 11180, page 111802L. International Society for Optics and Photonics, SPIE, 2019.

R. A. Scheepmaker, C. Frankenberg, N. M. Deutscher, M. Schneider, S. Barthlott, T. Blumenstock, O. E. Garcia, F. Hase, N. Jones, E. Mahieu, J. Notholt, V. Velazco, J. Landgraf, and I. Aben. Validation of SCIAMACHY HDO/H_2O measurements using the TCCON and NDACC-MUSICA networks. *Atmospheric Measurement Techniques*, 8(4):1799–1818, 2015.

J. J. Scherer, J. B. Paul, A. O'Keefe, and R. J. Saykally. Cavity Ringdown Laser Absorption Spectroscopy: History, Development, and Application to Pulsed Molecular Beams. *Chemical Reviews*, 97(1):25–52, 1997.

S. Schiller. Spectrometry with frequency combs. *Optics Letters*, 27(9):766, 2002.

A. Schneider, T. Borsdorff, J. aan de Brugh, H. Hu, and J. Landgraf. A full-mission data set of H_2O and HDO columns from SCIAMACHY 2.3 µm reflectance measurements. *Atmospheric Measurement Techniques*, 11(6):3339–3350, 2018.

A. Schneider, T. Borsdorff, J. aan de Brugh, F. Aemisegger, D. G. Feist, R. Kivi, F. Hase, M. Schneider, and J. Landgraf. First data set of H_2O/HDO columns from the Tropospheric Monitoring Instrument (TROPOMI). *Atmospheric Measurement Techniques*, 13(1):85–100, 2020.

A. Schneider, T. Borsdorff, J. aan de Brugh, A. Lorente, F. Aemisegger, D. Noone, D. Henze, R. Kivi, and J. Landgraf. Retrieving H_2O/HDO columns over cloudy and clear-sky scenes from the Tropospheric Monitoring Instrument (TROPOMI). *Atmospheric Measurement Techniques*, 15(7):2251–2275, 2022.

M. Schneider and F. Hase. Optimal estimation of tropospheric H_2O and δD with IASI/METOP. *Atmospheric Chemistry and Physics*, 11(21):11207–11220, 2011.

M. Schneider, S. Barthlott, F. Hase, Y. González, K. Yoshimura, O. E. García, E. Sepúlveda, A. Gomez-Pelaez, M. Gisi, R. Kohlhepp, S. Dohe, T. Blumenstock, A. Wiegele, E. Christner, K. Strong, D. Weaver, M. Palm, N. M. Deutscher, T. Warneke, J. Notholt, B. Lejeune, P. Demoulin, N. Jones, D. W. T. Griffith, D. Smale, and J. Robinson. Ground-based remote sensing of tropospheric water vapour isotopologues within the project MUSICA. *Atmospheric Measurement Techniques*, 5(12):3007–3027, 2012.

M. Schneider, Y. González, C. Dyroff, E. Christner, A. Wiegele, S. Barthlott, O. E. García, E. Sepúlveda, F. Hase, J. Andrey, T. Blumenstock, C. Guirado, R. Ramos, and S. Rodríguez. Empirical validation and proof of added value of MUSICA's tropospheric δD remote sensing products. *Atmospheric Measurement Techniques*, 8(1):483–503, 2015.

Z. Sharp. Principles of stable isotope geochemistry, 2nd edition. 2017.

U. N. Singh, B. M. Walsh, J. Yu, M. Petros, M. J. Kavaya, T. F. Refaat, and N. P. Barnes. Twenty years of Tm:Ho:YLF and LuLiF laser development for global wind and carbon dioxide active remote sensing. *Opt. Mater. Express*, 5(4):827–837, 2015.

U. N. Singh, M. Petros, T. F. Refaat, J. Yu, C. W. Antill, B. D. Taylor, S. C. Bowen, A. M. Welters, R. G. Remus, T.-H. Wong, K. Reithmaier, J. Lee, and S. Ismail. Progress on development of an airborne two-micron IPDA lidar for water vapor and carbon dioxide column measurements. In U. N. Singh, editor, *Lidar Remote Sensing for Environmental Monitoring 2017*, volume 10406, page 1040603. International Society for Optics and Photonics, SPIE, 2017a.

U. N. Singh, T. F. Refaat, S. Ismail, K. J. Davis, S. R. Kawa, R. T. Menzies, and M. Petros. Feasibility study of a space-based high pulse energy 2 µm CO_2 IPDA lidar. *Applied Optics*, 56(23):6531–6547, 2017b.

H. Sodemann, F. Aemisegger, S. Pfahl, M. Bitter, U. Corsmeier, T. Feuerle, P. Graf, R. Hankers, G. Hsiao, H. Schulz, A. Wieser, and H. Wernli. The stable isotopic composition of water vapour above Corsica during the HyMeX SOP1 campaign: insight into vertical mixing processes from lower-tropospheric survey flights. *Atmospheric Chemistry and Physics*, 17(9):6125–6151, 2017.

F. Späth, A. Behrendt, S. K. Muppa, S. Metzendorf, A. Riede, and V. Wulfmeyer. 3-D water vapor field in the atmospheric boundary layer observed with scanning differential absorption lidar. *Atmospheric Measurement Techniques*, 9(4):1701–1720, 2016.

S. M. Spuler, K. S. Repasky, B. Morley, D. Moen, M. Hayman, and A. R. Nehrir. Field-deployable diode-laser-based differential absorption lidar (DIAL) for profiling water vapor. *Atmospheric Measurement Techniques*, 8(3):1073–1087, 2015.

S. M. Spuler, M. Hayman, R. A. Stillwell, J. Carnes, T. Bernatsky, and K. S. Repasky. MicroPulse DIAL (MPD) – a diode-laser-based lidar architecture for quantitative atmospheric profiling. *Atmospheric Measurement Techniques*, 14(6):4593–4616, 2021.

H. C. Steen-Larsen, S. J. Johnsen, V. Masson-Delmotte, B. Stenni, C. Risi, H. Sodemann, D. Balslev-Clausen, T. Blunier, D. Dahl-Jensen, M. D. Ellehøj, S. Falourd, A. Grindsted, V. Gkinis, J. Jouzel, T. Popp, S. Sheldon, S. B. Simonsen, J. Sjolte, J. P. Steffensen, P. Sperlich, A. E. Sveinbjörnsdóttir, B. M. Vinther, and J. W. C. White. Continuous monitoring of summer surface water vapor isotopic composition above the Greenland Ice Sheet. *Atmospheric Chemistry and Physics*, 13(9):4815–4828, 2013.

J. Steinwagner, M. Milz, T. von Clarmann, N. Glatthor, U. Grabowski, M. Höpfner, G. P. Stiller, and T. Röckmann. HDO measurements with MIPAS. *Atmospheric Chemistry and Physics*, 7(10):2601–2615, 2007.

B. Stevens and S. Bony. Water in the atmosphere. *Physics Today*, 66(6):29–34, 2013a.

B. Stevens and S. Bony. What Are Climate Models Missing? *Science*, 340(6136):1053–1054, 2013b.

X. Sun, J. B. Abshire, J. D. Beck, P. Mitra, K. Reiff, and G. Yang. HgCdTe avalanche photodiode detectors for airborne and spaceborne lidar at infrared wavelengths. *Opt. Express*, 25(14):16589–16602, 2017.

C. H. Tan, A. Velichko, L. W. Lim, and J. S. Ng. Few-photon detection using InAs avalanche photodiodes. *Opt. Express*, 27(4):5835–5842, 2019.

C. Tomasi, A. A. Kokhanovsky, A. Lupi, C. Ritter, A. Smirnov, N. T. O'Neill, R. S. Stone, B. N. Holben, S. Nyeki, C. Wehrli, A. Stohl, M. Mazzola, C. Lanconelli, V. Vitale, K. Stebel, V. Aaltonen, G. de Leeuw, E. Rodriguez, A. B. Herber, V. F. Radionov, T. Zielinski, T. Petelski, S. M. Sakerin, D. M. Kabanov, Y. Xue, L. Mei, L. Istomina, R. Wagener, B. McArthur, P. S. Sobolewski, R. Kivi, Y. Courcoux, P. Larouche, S. Broccardo, and S. J. Piketh. Aerosol remote sensing in polar regions. *Earth-Science Reviews*, 140:108–157, 2015.

K. E. Trenberth and L. Smith. The Mass of the Atmosphere: A Constraint on Global Analyses. *Journal of Climate*, 18(6):864 – 875, 2005.

U. Wandinger. Raman lidar. In C. Weitkamp, editor, *Lidar: Range-Resolved Optical Remote Sensing of the Atmosphere*, pages 241–271. Springer New York, 2005.

C. R. Webster and A. J. Heymsfield. Water Isotope Ratios D/H, $^{18}O/^{16}O$, $^{17}O/^{16}O$ in and out of Clouds Map Dehydration Pathways. *Science*, 302(5651):1742–1745, 2003.

T. M. Weckwerth, V. Wulfmeyer, R. M. Wakimoto, R. M. Hardesty, J. W. Wilson, and R. M. Banta. NCAR–NOAA lower-tropospheric water vapor workshop. *Bulletin of the American Meteorological Society*, 80(11):2339–2357, 1999.

D. N. Whiteman, S. H. Melfi, and R. A. Ferrare. Raman lidar system for the measurement of water vapor and aerosols in the Earth's atmosphere. *Appl. Opt.*, 31(16):3068–3082, 1992.

D. M. Winker, J. L. Tackett, B. J. Getzewich, Z. Liu, M. A. Vaughan, and R. R. Rogers. The global 3-D distribution of tropospheric aerosols as characterized by CALIOP. *Atmospheric Chemistry and Physics*, 13(6):3345–3361, 2013.

M. Wirth, A. Fix, P. Mahnke, H. Schwarzer, F. Schrandt, and G. Ehret. The airborne multi-wavelength water vapor differential absorption lidar WALES: system design and performance. *Applied Physics B*, 96(1):201, 2009.

J. Worden, K. Bowman, D. Noone, R. Beer, S. Clough, A. Eldering, B. Fisher, A. Goldman, M. Gunson, R. Herman, S. S. Kulawik, M. Lampel, M. Luo, G. Osterman, C. Rinsland, C. Rodgers, S. Sander, M. Shephard, and H. Worden. Tropospheric Emission Spectrometer observations of the tropospheric HDO/H_2O ratio: Estimation approach and characterization. *Journal of Geophysical Research*, 111(D16), 2006.

J. Worden, , D. Noone, and K. Bowman. Importance of rain evaporation and continental convection in the tropical water cycle. *Nature*, 445(7127):528–532, 2007.

J. R. Worden, S. S. Kulawik, D. Fu, V. H. Payne, A. E. Lipton, I. Polonsky, Y. He, K. Cady-Pereira, J.-L. Moncet, R. L. Herman, F. W. Irion, and K. W. Bowman. Characterization and evaluation of AIRS-based estimates of the deuterium content of water vapor. *Atmospheric Measurement Techniques*, 12(4): 2331–2339, 2019.

V. Wulfmeyer. Investigation of Turbulent Processes in the Lower Troposphere with Water Vapor DIAL and Radar–RASS. *Journal of the Atmospheric Sciences*, 56(8):1055 – 1076, 1999.

V. Wulfmeyer, R. M. Hardesty, D. D. Turner, A. Behrendt, M. P. Cadeddu, P. Di Girolamo, P. Schlüssel, J. Van Baelen, and F. Zus. A review of the remote sensing of lower tropospheric thermodynamic profiles and its indispensable role for the understanding and the simulation of water and energy cycles. *Reviews of Geophysics*, 53(3):819–895, 2015.

D. Wunch, G. C. Toon, J.-F. L. Blavier, R. A. Washenfelder, J. Notholt, B. J. Connor, D. W. T. Griffith, V. Sherlock, and P. O. Wennberg. The Total Carbon Column Observing Network. *Phil. Trans. R. Soc. A.*, 369:2087–2112, 2011.

D. Wunch, P. O. Wennberg, G. Osterman, B. Fisher, B. Naylor, C. M. Roehl, C. O'Dell, L. Mandrake, C. Viatte, M. Kiel, D. W. T. Griffith, N. M. Deutscher, V. A. Velazco, J. Notholt, T. Warneke, C. Petri, M. De Maziere, M. K. Sha, R. Sussmann, M. Rettinger, D. Pollard, J. Robinson, I. Morino, O. Uchino, F. Hase, T. Blumenstock, D. G. Feist, S. G. Arnold, K. Strong, J. Mendonca, R. Kivi, P. Heikkinen, L. Iraci, J. Podolske, P. W. Hillyard, S. Kawakami, M. K. Dubey, H. A. Parker, E. Sepulveda, O. E. García, Y. Te, P. Jeseck, M. R. Gunson, D. Crisp, and A. Eldering. Comparisons of the Orbiting Carbon Observatory-2 (OCO-2) XCO_2 measurements with TCCON. *Atmospheric Measurement Techniques*, 10 (6):2209–2238, 2017.

I. Xueref-Remy, E. Dieudonné, C. Vuillemin, M. Lopez, C. Lac, M. Schmidt, M. Delmotte, F. Chevallier, F. Ravetta, O. Perrussel, P. Ciais, F.-M. Bréon, G. Broquet, M. Ramonet, T. G. Spain, and C. Ampe. Diurnal, synoptic and seasonal variability of atmospheric CO_2 in the Paris megacity area. *Atmospheric Chemistry and Physics*, 18(5):3335–3362, 2018.

K. Yoshimura, M. Kanamitsu, and M. Dettinger. Regional downscaling for stable water isotopes: A case study of an atmospheric river event. *Journal of Geophysical Research*, 115(D18), 2010.

S. Yu, Z. Zhang, H. Xia, X. Dou, T. Wu, Y. Hu, M. Li, M. Shangguan, T. Wei, L. Zhao, L. Wang, P. Jiang, C. Zhang, L. You, L. Tao, and J. Qiu. Photon-counting distributed free-space spectroscopy. *Light: Science & Applications*, 10(1), 2021.

Z.-C. Zeng, O. Addington, T. Pongetti, R. L. Herman, K. Sung, S. Newman, A. Schneider, T. Borsdorff, Y. L. Yung, and S. P. Sander. Remote sensing of atmospheric HDO/H_2O in southern California from CLARS-FTS. *Journal of Quantitative Spectroscopy and Radiative Transfer*, 288:108254, 2022.

A. Zukauskas, N. Thilmann, V. Pasiskevicius, F. Laurell, and C. Canalias. 5 mm thick periodically poled Rb-doped KTP for high energy optical parametric frequency conversion. *Opt. Mater. Express*, 1(2): 201–206, 2011.

A. Ångström. On the atmospheric transmission of sun radiation and on dust in the air. *Geografiska Annaler*, 11(2):156–166, 1929.

List of publications

Peer-reviewed articles

J. Hamperl, J. F. Geus, K. M. Mølster, A. Zukauskas, J.-B. Dherbecourt, V. Pasiskevicius, L. Nagy, O. Pitz, D. Fehrenbacher, H. Schaefer, D. Heinecke, M. Strotkamp, S. Rapp, P. Denk, N. Graf, M. Dalin, V. Lebat, R. Santagata, J.-M. Melkonian, A. Godard, M. Raybaut, and C. Flamant. High Energy Parametric Laser Source and Frequency-Comb-Based Wavelength Reference for CO_2 and Water Vapor DIAL in the 2 µm Region: Design and Pre-Development Experimentations, *Atmosphere*, 12 (3), 402, 2021

J. Hamperl, C. Capitaine, J.-B. Dherbecourt, M. Raybaut, P. Chazette, J. Totems, B. Grouiez, L. Régalia, R. Santagata, C. Evesque, J.-M. Melkonian, A. Godard, A. Seidl, H. Sodemann, and C. Flamant. Differential absorption lidar for water vapor isotopologues in the 1.98 µm spectral region: sensitivity analysis with respect to regional atmospheric variability. *Atmospheric Measurement Techniques*, 14 (10), pp. 6675–6693, 2021

J. Hamperl, J.-B. Dherbecourt, M. Raybaut, J. Totems, P. Chazette, L. Régalia, B. Grouiez, N. Geyskens, O. Aouji, N. Amarouche, J.-M. Melkonian, R. Santagata, A. Godard, C. Evesque, V. Pasiskevicius, C. Flamant. Range-resolved detection of boundary layer stable water vapor isotopologues using a ground-based 1.98 µm differential absorption lidar. *Optics Express*, accepted for publication on 10 October 2022 (in production)

Conference proceedings and presentations

J. Hamperl, C. Capitaine, R. Santagata, J.-B. Dherbecourt, J.-M. Melkonian, A. Godard, M. Raybaut, L. Régalia, B. Grouiez, F. Blouzon, N. Geyskens, C. Evesque, P. Chazette, J. Totems, and C. Flamant. "WaVIL : a Differential Absorption LIDAR for Water Vapor and Isotope HDO Observation in the Lower Troposphere - Instrument Design," in *Optical Sensors and Sensing Congress*, OSA Technical Digest (Optica Publishing Group, 2020), paper LM4A.4.

J. Hamperl, M. Raybaut, J.-B. Dherbecourt, P. Chazette, J. Totems, and C. Flamant. Differential absorption lidar for water vapor isotopologues in the 1.98 µm spectral region: sensitivity analysis with respect to regional atmospheric variability, EGU General Assembly 2021, online, 19–30 April 2021, EGU21-8792 (oral presentation)

J. Hamperl, J. F. Geus, K. M. Mølster, A. Zukauskas, J.B. Dherbecourt, V. Pasiskevicius, M. Strotkamp, S. Duzellier, M. Dalin, V. Lebat, R. Santagata, J.M. Melkonian, A. Godard, M. Raybaut. Parametric source for future space DIAL sounding of greenhouse gases in the 2 µm region, Optique Dijon 2021, Dijon, 05-09 July 2021 (oral presentation)

J. Hamperl, M. Raybaut, J.-B. Dherbecourt, J.-M. Melkonian, R. Santagata, A. Godard, C. Capitaine, L. Régalia, B. Grouiez, F. Blouzon, N. Geyskens, O. Aouji, C. Evesque, P. Chazette, J. Totems, and C. Flamant. WaVIL: Differential absorption lidar for water vapor isotope remote sensing in the lower troposhere, Optique Dijon 2021, Dijon, 05–09 July 2021 (poster)

J. Hamperl, P. Chazette, J. Totems, J.-B. Dherbecourt, J.-M. Melkonian, P. Nicolas, M. Raybaut, A. Clémençon, N. Geyskens, P. Geneau, C. Flamant, D. Zannoni, H. Sodemann, H. C. Steen-Larsen, A. Monod, A. Durand, S. Ravier, and A. Schwarzenboeck. Demonstration of water vapor and Isotopes measurement from lidar using a multi-platform, multi-instrumental approach, EGU General Assembly 2022, online, 23–27 May 2022, EGU22-12076 (oral presentation)

J. Hamperl, J.-B. Dherbecourt, M. Raybaut, J. Totems, R. Santagata, J.-M. Melkonian, A. Godard, P. Chazette, C. Flamant. Demonstration of range-resolved detection of stable water isotopologues by differential absorption lidar. 2022 Conference on Lasers and Electro-Optics (CLEO), May 2022, San Jose, CA, United States (oral presentation)